WARWICK
THE UNIVERSITY OF WARWICK

A Thesis Submitted for the Degree of PhD at the University of Warwick

Permanent WRAP URL:
http://wrap.warwick.ac.uk/98510

Copyright and reuse:
This thesis is made available online and is protected by original copyright.
Please scroll down to view the document itself.
Please refer to the repository record for this item for information to help you to cite it.
Our policy information is available from the repository home page.

For more information, please contact the WRAP Team at: wrap@warwick.ac.uk

warwick.ac.uk/lib-publications

Optical Spectra and Energy Levels of Divalent Ytterbium and Samarium Ions in Some Alkali Halides

by

Ihebrodike Maurice Mejeha

A thesis submitted to

the University of Warwick

for admission to the degree of

Doctor of Philosophy

Department of Physics

January 1988

Declaration

This thesis is submitted to the University of Warwick in support of my application for admission to the degree of Doctor of Philosophy. It contains an account of my own research work carried out at the University of Warwick under the general supervision of Dr M.J.A. Smith from October 1983 to September 1987. No part of it has previouly been used in a degree thesis submitted to this or any other University. The work described in this thesis are the result of my own independent research except where specifically acknowledged in the text.

January 1988 Ihebrodike M. Mejeha

To my father

The late Mazi Mejeha Innocent (Nwoeke) Obila

who motivated my quest for learning

Summary

This study is concerned with the measurement and analysis of the optical absoprtion spectra of divalent samarium (Sm^{2+}) and ytterbium (Yb^{2+}) ions in potassium and rubidium halide crystals. To incorporate the ions into the crystals, the latter were heated in (the appropriate) metal vapour. The optical absorption spectra of the impurity-doped crystals were measured and are ascribed to $4f^{N+1} \rightarrow 4f^N 5d$ electronic transitions. For the first time, the optical spectra of Sm^{2+} and Yb^{2+} ions in $RbBr$ and RbI crystals are reported.

In the case of Yb^{2+} ions in RbX, $(X = Cl, Br, I)$ crystals, intermediate coupling calculations using J_1j- coupled basis functions give a satisfactory agreement between experimental and theoretical energy levels of the ions, by assuming that the effective site symmetry of the substitutional impurity ions is octahedral. However, the Slater-Condon and spin-orbit parameters that give the best fit between theory and experiment are reduced by up to 44% from the free-ion values.

In the case of Sm^{2+} ions in KX and RbX crystals, theoretical calculation of the energy levels (assuming octahedral approximation) was based on a model in which the $4f^5$ core electron states, best described in terms of LS-coupled basis functions, are coupled to the $5d$ electron states which are strongly perturbed by the crystal field. In this model, the agreement between theoretical and experimental energy levels is also quite satisfactory.

Also found, are sets of absorption bands whose spectral positions and behaviour can best be explained by assuming electronic transitions from the ground states of the ions to the bonding molecular orbitals formed by the overlap of the $6s$ atomic orbitals of the impurity ions and the $(n+1)s$ atomic orbitals of the ligand ions.

Preliminary investigations of the effect of thermal ageing on the optical spectra of $RbBr : Yb^{2+}$ crystals suggest that the Yb^{2+} ions exist in three separate phases (in the crystals) among which is the Suzuki phase.

Acknowledgements

I would like to put on record, my indebtedness and gratitude to Dr M. J.A. Smith, my supervisor, for the invaluable guidance, encouragement and support he gave me during the period this research was carried out. Also I would like to thank Mr Cliff Randle, who gave me a lot of technical assistance and masterfully constructed many of the pieces of apparatus used in the study.

The illuminating discussions I held with Dr J. M. Dixon on the theoretical models adopted in the analysis of the experimental data and with Dr S. W. Bland on some of the experimental techniques cannot go unappreciated. My gratitude also goes to the academic and technical staff of the Department of Physics for various types of assistance and encouragement at one time or another. In particular, I would like to thank Dr H. Mykura and Mr Roy McLeod. The latter carefully prepared most of the diagrams and photographs.

It would have been very difficult for me to do the theoretical analysis reported here were it not for the assistance I received from the Computing Services Centre of the University of Warwick. In this respect, I register my gratitude to Dr R. Parkins, Messrs. J. M. Hicks and Bal Dhesi who started me off on the use of the IBM 4381 mainframe computer. Dr Parkins' immense help at the production stage of this thesis is highly appreciated. I would also like to thank Mrs G. Buxton who skillfully typed the thesis.

It was the Scholarship Division of the Federal Ministry of Education, Lagos, Nigeria that provided me with financial support. Financial assistance also came from the Peter MacMillan Fund and the Department of Physics. To these, as well as the Anambra State College of Education, Awka, Nigeria, that granted me study leave for purpose this work, my immense gratitudes go.

Finally, I would like to thank my wife and children who patiently endured my long absence from home and who together with my mother, brothers and sisters gave me encouragement and support throughout the period of study.

January 1988 **Ihebrodike M. Mejeha**

Contents

List of Figures

List of Tables

Chapter 1

Introduction

1.1 General Introduction

1.1.1 Rare–earth metal ions

Ytterbium and samarium are rare–earth metals. The rare–earths form two series of metallic elements in the periodic table. Starting with cerium, with atomic number $Z = 58$,the first series ends with lutecuim ($Z = 71$). They are known as the lanthanides. Metallic elements lying between and including thorium ($Z = 90$) and lawrencium ($Z = 103$) constitute the second series known as the actinides [1,2].

A neutral lanthanide atom has an electronic configuration of the form $(Xe)f^N6s^2$ or $(Xe)f^N5d6s$ where (Xe) refers to the electronic configuration of the zenon atom and $1 \leq N \leq 14$. Configurations with 5d subshells include those of cerium, gadolinium ($Z = 64$) and lutecium. In the case of actinides, the electronic configuration of a neutral atom is of the form $(Rn)5f^N7s^2$ or $(Rn)5f^N6d7s^2$ where (Rn) is the electronic structure of the radon atom ($Z = 86$). It should be noted however that normal thorium atom has completely empty 5f subshell.

Evidently, the two elemental series are similar in having partially filled $4f$ or $5f$ subshells, the electrons of which are shielded by the outer shell electrons owing to the contraction of the f subshells [2]. It is this remarkable similarity, with its attendant consequences on the properties of these elements, and their compounds that has prompted the classification of the two groups of elements as rare–earths. Many authors [3-6] have tended to regard the lanthanides as the true rare–earths.

In this work, whenever reference is made to rare–earths it shall be understood as elements in the lanthanide series.

The lanthanides exhibit appreciable similarity in their chemical, magnetic and some other physical properties such as specific heats. In general there, is a tendency for them to form trivalent compounds. However samarium ($Z = 62$), europium ($Z = 63$) and ytterbium ($Z = 70$) easily exist also in the divalent state. For the last two elements, this tendency has been explained by the assumption that at the ground state, both are S–state ions, because of the half-filled (as in the case of divalent europium Eu^{2+} ($4f^7$)) or completely filled (as in the case of divalent ytterbium Yb^{2+} ($4f^{14}$)) nature of the $4f$ subshells. The above explanation cannot however apply to the case of divalent samarium, Sm^{2+}, with $4f^6$ subshell. Nevertheless, the other lanthanides can be made to exist in the divalent state under specially arranged conditions [7-13]. The rare- earths appear to be strongly paramagnetic at low temperatures and some are ferromagnetic or antiferromagnetic [3].

Many of the properties of the rare–earths either in solid or ionised state, or in combination with other elements as in compounds of rare–earths or in crystals as impurities have been ascribed to the small radial extension of the $4f$ subshell in comparison with the $5s$,$5p$,$5d$ or $6s$ subshells. It is this comparatively small spatial extension of the radial part of the wavefunctions of the $4f$ electrons as seen in Fig 1.1, that causes the shielding of the $4f$ electrons from the environment by the electrons of the outer $5s$, $5p$ and $6s$ atomic orbitals.

In an isolated free rare–earth ion, the $4f$ electrons exhibit strong mutual repulsion and considerable magnetic interaction between the magnetic dipole associated with spin angular momentum and the magnetic field resulting from their motion around the nucleus (spin-orbit interaction). Consequently, there exists in typical rare earth ions a very large number of quantum states. Excitations of these ions cause electronic transitions from the ground state to these quantum states resulting in very weak and sharp absorption. The observed absorption lines are weak because the transitions are not allowed on grounds of parity selection rule. This rule, due to Laporte, says that electronic transitions, under electric dipole approximation, are forbidden between quantum states of same parity [30]. Therefore $4f^N \leftrightarrow 4f^N$

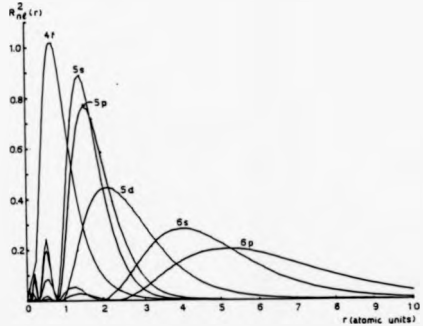

Fig 1.1 Distribution of radial density $R^2_{nl}(r)$ for the $4f, 5s, 5p, 5d, 6s$,and $6p$ electrons of CsI as a fuction of radial extension r (after Goldschmidt [29])

transitions are parity forbidden.

Electronic transitions from the ground state to low–lying excited configurations such as $4f^N5d$ and $4f^N6s$ are parity allowed although transitions to the latter configuration are forbidden on grounds of a different selection rule. The resulting absorption lines are generally strong in intensity. These configurations are more complex because of the additional interactions such as Coulomb and exchange interactions between the $4f^N$ core electrons and the single electron in an outer orbital. In many cases, the number of resulting energy levels run into thousands. Indeed, the observed optical spectra of various rare–earth ions in triply or doubly ionised state show in some cases thousands of sharp lines, interpretation to which becomes very difficult. The task of interpreting the observed spectra often becomes complicated by the fact that electronic states belonging to different configurations do sometimes overlap, resulting in the mixing of states from different configurations (configuration interaction). Inclusion of considerations of this kind in doing energy level calculations have greatly improved the fit between the experimentally observed spectra and theoretically computed energy levels [31-37].

1.1.2 Rare earth ions in crystalline environments

For many decades, there have been intensive and extensive studies of the optical, electrical, paramagnetic and magnetic properties of rare–earths ions in crystalline solids. One strategy has been to investigate the properties of rare–earth compounds where availabe [38,51–58] while another has been to introduce rare–earth ions into crystals [9 - 28, 39–50,59–70]. In many of these studies, optical (both absorption and fluorescence) spectroscopy has proved a very powerful tool in obtaining experimental data, analyses of which have led to a deeper understanding of the optical properties of the ions. Because many of the ions are paramagnetic, electron spin resonance (ESR) technique and Zeeman spectroscopy have also proved very useful in gathering data on the paramagnetic and magnetic behaviour of the ions. Among the many objectives of these studied is the understanding of the precise nature of the perturbation interactions that determine the observed physical properties. For instance, as has earlier been pointed out, in free ion state, the structure of the

energy levels of rare–earth ions is determined by electrostatic interactions between pairs of optically active electrons as well as by spin-orbit interaction What then is the role of these interactions in determining the structure of the energy levels of ions in crystalline environment? Equally important are the class of interactions between the rare–earth ions in crystals (which are here perceived as occupying substitutional lattice sites and regarded as central ions) and the surrounding ligand ions. Again, what is the effect of this latter class of interactions on the structure of the energy levels and paramagnetic properties of the rare–earth ions in crystals? Answers to questions such as these make possible a clear understanding of the properties of these ions and the possible use to put them to.

Correlation of the observed energy levels of rare–earth ions in crystals as determined from the optical absorption and fluorescence spectra of crystals containing these ions with the emission spectra of the same ions in free space has led to an understanding of the effect of crystalline environment on the electronic states of the low–lying configurations. As an example, the weak, sharp spectral lines exhibited by many trivalent and divalent rare–earth ions in crystals in both absorption, and fluorescence resemble very closely in energy levels positions the spectral lines characteristic of $4f^N$-$4f^N$ transitions of free rare–earth ions [38,59,61– 69,73]. This has led to the conclusion that the interaction between 4f electrons and the ligand ions is weak compared with inter-electronic interactions within the $4f^N$ electron system. In fact, for some rare earth ions, the known free ion energy levels of the $4f^N$ configuration are inferred from studies of the ions in crystals [72,74].

Direct correlation between the free ion energy levels of mixed configurations such as $4f^N5d$ or $4f^N6s$ with observed optical spectra of rare–earth ions in crystals is more difficult to make. In the first place, optical spectra of rare–earth ions in crystals ascribable to $4f^{N+1} \leftrightarrow 4f^N5d$ transitions usually consist of strong broad bands. For divalent rare–earth ions, the optical absoprtion spectra generally extend from the infra red to the ultra-violet, the onset of absorption beginning at energies characteristic of each rare–earth ion [6 - 10,40 - 43,62,75 - 89], while for the trivalent ions, the spectral bands are generally located in the vacuum ultra–violet [79].

One of the difficulties in the direct correlation pertains to the broad nature of

the spectral bands, the half–width of which sometimes is as large as 2000 cm^{-1}, even at low temperatures [62]. The broadening of the bands can be explained by assuming that the states of the outer 5d or 6s (optically active) electron are more easily perturbed by the charge distribution of the ligand ions since electrons in these outer subshells extend further into space than electrons in the $4f$ subshell. In other words, the 5d or 6s electrons are more strongly coupled to the ligand ions than the $4f$ electrons. In any theoretical analysis of the observed spectra therefore, the relative magnitudes of the interactions within the system of optically active electrons on the one hand and between them and the ligand ions on the other become of paramount importance. Another aspect of the problem presented by the large width of the bands is that usually, the $4f^N5d$ configuration consists of very large number of quantum states which may be very close in energy terms. Most of the observed absorption bands of some rare–earth ions in crystals may in fact be connected to overlap of bands connected to states of different multiplets of the free ion.

In the analysis of the observed $4f^N(5d + 6s)$ spectra of rare–earth ions in crystalline environments, some approximations become inevitable. Some investigators have tended to ignore the effect of the interaction between the $4f^N$ electrons and the ions in the crystal lattice while others work on the model that the direct Coulomb and exchange interactions between the $4f^N$ electrons and the outer $5d$ or $6s$ electron can be ignored [10,70,80,90]. Authors like Eremin [91], Piper and his collaborators [86] and Yanase and Kasuya [92] see no point in making the latter assumption, since in their view many of these interactions are of comparable magnitude. If issues such as this are to be resolved, a large number of experimental data on rare–earth ions in a wide variety of crystalline solids and theoretical analyses of these is required. Admittedly, a large amount of experimental data on the optical spectra ascribable to $4f^{N+1} \rightarrow 4f^N5d$ electronic transitions of rare–earth ions exist [10,40 - 43,75 - 92] but there are only a comparatively few detailed theoretical analyses of these spectra [6,76,77,86,91,92,228].

Whatever the assumptions and (or) approximations used in studying the inter–communications, through electronic transitions, between the ground and excited configurations of rare–earth ions in crystals, there are some strategies and techniques

central to most approaches. Firstly, the energy level structure of the free ions has to be clearly understood. This requires an adequate understanding of the theory of complex spectra. Among of the most powerful tools in studying complex atomic spectra are the Racah's tensor operator techniques [93 - 95] and are very commonly used by many investigators. Secondly, the influence of the crystalline environment on the free ion energy levels is considered. In this respect, the application of the theory of finite groups to the problem of the splitting of the free ion energy levels as the ion enters a crystalline environment has proved very useful. It was Bethe [96] who first explained how the splitting of energy levels of a free ion introduced into a crystal depends on the symmetry of the site occupied by the ion and on the magnitude of the electrostatic interaction between the ion and the ligand ions.

Successful as Bethe's theory has been in offering a qualitative (and to some extent quantitative) understanding of the experimental data for ions in ionic crystals, a rival molecular orbital (MO) theory exists which explains the situation in covalent crystals [97,98]. Essentially, the latter theory applies the same basic symmetry principles as Bethe's theory but proposes that atomic orbitals of both the central and ligand ions overlap to form molecular orbitals (MO's). The degree of overlap determines the extent of the splitting of the energy levels of the central ions.

This study is concerned, in the main with the optical properties of Sm^{2+} and Yb^{2+} ions in potassium and rubidium halide crystals. In particular, measurements of optical absorption spectra of the crystals containing these ions will be made and analysed. The high ionicity of alkali halides and the high symmetry of the cation site of their crystals make them attractive hosts for substituting the ions being studied. As a result, the basic symmetry principles embodied in Bethe's crystal field theory can be readily applied to the problem. All these considerations also necessitate short reviews of the properties of ytterbuim and samaruim ions in crystals which are included in a later section of this chapter.

Since a variety of crystal imperfections can easily be introduced into alkali halide crystals during the process of incorporating the intentional impurity ions a short review of the major structural defects in alkali halide crystals is also given. The objective is to keep these imperfections and their optical properties in focus throughout

the investigations.

In the first part of Chapter 2 of this work are introduced the theoretical formulations essential for calculating the energy levels of free rare–earth ions in crystalline environments, the major tools being quantum mechanical and group theretical principles and Racah's tensor operator techniques. Because all the computer programs and subroutines used in calculating the energy levels of the ions being studied were designed, developed and tested by the author, it is instructive to discuss the major computational strategies and algorithms adopted in doing these tasks. Such a discussion constitutes the second and larger part of Chapter 2. Application of the major concepts introduced in that chapter to the problem of Yb^{2+} and Sm^{2+} ions in alkali halide crystals is detailed in two separate chapters; (Chapters 4 and 5). Finally, the main findings of this work and the conclusions are summarised in Chapter 7.

1.2 Preliminary comments on Yb^{2+} and Sm^{2+} ions in crystals

1.2.1 Ytterbium ions in crystals

A neutral ytterbuim atom has the electronic structure (Xe)$4f^{14}6s^2$. In vacuum ytterbuim can exist quite easily in triply ionised ($YbIV$) doubly ionised ($YbIII$) or singly ionised ($YbII$) states. $YbIV$ (or Yb^{3+} ion) has a ground configuration of $4f^{13}$ while $YbIII$ (or Yb^{2+} ion) has ground configuration of $4f^{14}$. The free ion spectra of these ions have been investigated both experimentally and theoretically [99]. One notable result of the study is the strong spin-orbit interactions that perturb the states of the 4f electrons. Thus in considering electronic transitions from the ground configuration $4f^{14}$ to an excited configuration such as $4f^{13}5d$ of Yb^{2+} (or $4f^{13}6s6p$ of Yb^{+}) ions, spin-orbit interaction within the states of $4f^{13}$ core over-rides the electrostatic interaction betwen the $4f^{13}$ electrons and the outer 5d (or 6p) electron in importance. As will be made clear in a latter chapter, it is the relative strength of these perturbation interactions that determine the choice of wavefunctions with which to describe the electronic states of the free ions. Another important result is that the energy levels of free Yb^{2+} ions ascribable to $4f^{13}$ - $4f^{12}5d$ -electronic

transitions are higher than the corresponding $4f^{14}$ - $4f^{12}5d$ of free Yb^{2+} ions.

On incorporating Yb^{3+} ions into crystals of well-defined point symmetry, the various features of the energy levels of the ions can be studied by an analysis of optical absorption and emission spectra of the ions in crystals, and ESR studies. These studies reveal that although the electronic levels of the $4f^{12}5d$ configuration are lowered by the crystal field they are located at spectral positions greater than 50 000 cm^{-1} above the ground state of Yb^{3+} ions and therefore outside the region of optical transparency of most alkali halide crystals. Also revealed in these studies is the fact that the spin-orbit split ^2F term of $4f^{13}$ configuration couple weakly to the crystal field levels. Electronic transitions between the energy levels of this configuration are parity forbidden and optical absorption and emission measurements show that the spectra consist of weak but sharp bands, the spectral energies being located in the infra-red [100].

Divalent ytterbuim ions in crystals on the other hand do not show corresponding low-lying levels since the ground configuration consists of a single $^1S_0$ state. However inter-communication through electronic transitions between the $4f^{14}$ configuration and the first excited configuration $4f^{13}5d$ is possible since it is parity allowed. A number of studies have shown that in crystals of CaF_2 structure which contain Yb^{2+} ions, such transitions are manifested in a number of strong broad absorption bands located mainly in the ultra violet or in broad emission bands in the visible region [42]. Theoretical studies of the energy level structure based on these experimental findings have been limited in their success. Two most widely quoted studies were done by Piper, Brown and McClure [86] and Eremin [91]. These authors rightly acknowledge the relative importance of the main perturbation interactions operative on the electronic states of the ions but proceed to assume that the best description of the states of the ions consists in coupling the total spin (S) and total orbital (L) angular momenta to obtain the total angular momenta (J) of the electrons. Such a description, even though it could give reasonably good energy level structure, gives incorrect wavefunctions for the ions since it ignores the fact that spin orbit interaction within the states of the $4f^{13}$ core is far more important than the electrostatic interaction between the core electrons and the outer $5d$ electron.

In their study of electronic states of Yb^{2+} ions in potassium and sodium halides, Bland and Smith [101] acknowledge the drawback in the above-mentioned studies and use J_1j coupling scheme which more closely describes the physical coupling situation between $4f$ and $5d$ electrons in Yb^{2+} ions. In the next chapter, the important features of these coupling schemes will be more fully explained. Also revealed in these later studies is the fact that electrostatic coupling (both the Coulomb and exchange type) between the $4f^{13}$ and $5d$ electrons is an important interaction to consider in determining the energy levels of Yb^{2+} ions in crystals, although the coupling strength is reduced from free ion values.

One remarkable aspect of the Bland and Smith study is that Yb^{2+} ions were incorporated into the crystals by vapour phase diffusion technique in which the crystals were heated in ytterbium metal vapour. It was the first time such a technique has been successfully used for implanting Yb^{2+} ions in potassium and sodium halide crystals.

It will be interesting therefore to extend the study to Yb^{2+} ions in rubiduim halide crystals and using the same doping technique. As far as the author knows, optical studies of RbX:Yb^{2+} ($X = Cl, Br, I$) systems have not previously been reported. The only study done with a rudibium halide crystal system was done with RbCl host [64]. In that study, attention was focussed on vibronic transitions involving the lowest energy band of the $4f^{13}5d$ configuration at 4.2 K. It is reasonable, therefore, to assume that the experimental and theoretical studies of the $4f^{13}5d$ configuration of Yb^{2+} ions in RbX crystals have not been done before. This is one of the tasks undertaken in this study.

1.2.2 Samaruim ions in crystals

The electronic configuration of a neutral samaruim atom is $(Xe)4f^66s^2$. For the free trivalent samaruim ion ($SmIV$), it is $4f^5$ while that of the doubly ionised free ion, ($SmIII$) is $4f^6$. Most of what is known about the free ion states of $SmIV$ comes from comparisons of experimental data obtained in the study of optical absorption and fluorescence spectra of Sm^{3+} ions in $LaCl_3$ crystals [74]. Results of the studies show that the lowest energy levels originate from the multiplets ^6FH and

are separated from the next higher groups of energy levels by about 12 000 cm^{-1} as shown in Fig 1.2. The energy levels of the free Sm^{2+} ions, on the other hand, have been obtained experimentally by identification, characterisation and analysis of the spark emission spectra of the ions by Dupont [102]. His analysis shows that the $4f^6$ configuration of Sm^{2+} comprises a ground multiplete ^7F term, separated from the next higher multiplet, ^5D by about 18 000 cm^{-1} which in turn is fairly well separated from the 230 multiplet terms above it. These latter group of levels are characterised by admixed wavefunctions.

However, the high purity of the ^7F and ^5D multiplet levels of the $4f^6$ configuration makes fairly easy the theoretical analysis of the experimental data corresponding to the lower energy levels of Sm^{2+} ions in crystalline environments. Many of such studies exist [62,64,67,71,140]. As a result of these studies the energy level structure of the $4f^6$ configuration of Sm^{2+} ions in alkali halide crystals is now well understood. Fig 1.3 shows the energy level structure developed using data obtained by analysing the fluorescence spectra of Sm^{2+} ions in these crystals.

The free ion states of the first excited configuration of Sm^{2+} ions are equally complex. An analysis of this configuration by Dupont [102] who incorporates the preliminary calculations by Becher [103] gives rise to the identification by most of the energy levels originating from $4f^5(^6PFH)5d$ sub-configuration. Identified levels lie in the energy range 26 283.55 - 55 149.58 cm^{-1} above the ground state of the $4f^6$ configuration. In crystalline environment, the centre of gravity of the $4f^55d$ configuration is lowered relative to the ground state of $4f^6$ configuration. Evidence of this is provided by the observation that the absorption spectra of Sm^{2+} ions in alkaline-earth fluorite and alkali halide crystals consist of strong broad bands in both the visible and ultra-violet, the lowest of these lying between 15 380 and 16 420 cm^{-1} in $CaF_2 : Sm^{2+}$ crystals at 4.2 K [43,63]. The location of corresponding band in other alkaline fluorite and alkali halide crystals containing Sm^{2+} are not markedly different [62,80,64].

What is of interest in the present study is that despite the large amount of experimental data on the properties of Sm^{2+} ions in various crystals, not much interest has been shown on the theoretical analysis of the structure of the $4f^55d$ configura-

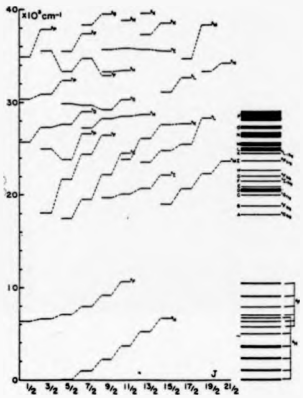

Fig 1.2 Theorectical and experimental energy levels of $4f^5$ configuration of Sm^{3+} ions. Experiment levels were obtained from studies of trivalent samarium salts. (after Wybourne [74])

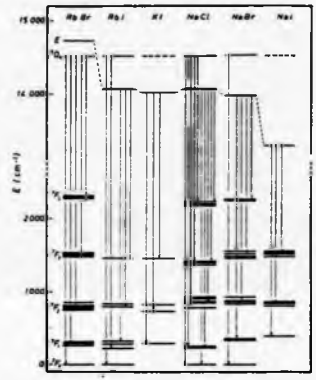

Fig 1.3 Energy level scheme for for $4f^6$ configuration of Sm^{2+} ions in some alkali halide crystals developed from fluoresence data. (after Guzzi and Baldini [69])

tion of the ions in crystals. It is true however that there have been some attempts at qualitative and semi-quantitative assignments of the observed energy bands in the absorption spectra of Sm^{2+} ions ascribable to this configuration through recourse to group theory [62,80]. The only attempt at a detailed calculation up to date was made by Yanase [104]. In it he tries to fit the coarse structure of the experimentally determined spectra of $CaF_2 : Sm^2$ crystals to theoretical energy levels based on a coupling scheme suggested by Yanase and Kasuya [92]. The coupling formalism is assumes that even though the 5*d* electron states are strongly perturbed by the crystal field, the total angular momentum J obtained by the coupling of total spin angular momentum S and orbital angular momentum $\mathbf{L}_f$ derived from the $4f^6$ configuration is still a good quantum number. In order to explain the main features of the absorption spectra of Sm^{2+} ions in alkali halide crystals, it appears reasonable to apply the above coupling scheme in the calculation of the energy levels of the ions.

Worthy of note is the fact that absorption spectra, in the visible and ultra violet, of Sm^{2+} ions in potassuim halide and rubidium chloride crystals have earlier, been reported [50,64,80] but that those of the ions in rubidium bromide and iodide crystals have not. In some reported cases, the spectra were measured at room, liquid nitrogen and liquid helium temperatures but only room temperature spectra were published, except for $KCl : Sm^{2+}$ spectrum at 10K. In all these studies, the doping techniques adopted are the conventional methods in which a trivalent samarium salt is added to the host crystal in molten form and the Sm^{3+} ions reduced to the divalent state.Single crystals of the solid solution is then grown using one of the standard methods such as the Bridgman, Kryopolous or Czochralski techniques [15-17,64,84-86]. It will be interesting to see if Sm^{2+} ions could be implanted into potassuim and rubiduim halide crystals through vapour phase diffusion process as has been successfully done for Yb^{2+} ions [6,101].

1.3 Structural imperfections in alkali halides

1.3.1 Alkali halides

Alkali halides are chemical compounds of alkali metals and halogens. They can be represented in the form MX, with M denoting an alkali metal ion (cation) and X, a halogen ion (anion). Alkali halides are ionic and sixteen of the twenty salts crystallise in the sodium chloride structure with each cation co-ordinated with six ions of opposite kind. Cesium halides (excepting the fluoride) are different in that they form crystals in which the cations experience eight-fold co-ordination [105,121]. This study shall be concerned only with alkali halides that crystallise in sodium chloride structure.

Halides of alkali metals are wide band gap materials and are optically transparent, exhibiting a wide range of spectral transparency. The absorption spectra of pure crystals of these materials occur generally in the infra-red (corresponding to lattice vibrational spectra) and in the far end of the ultra-violet (corresponding to electronic transitions from the valence band to the conduction band) [105,121]. It is this property of alkali halides, together with high symmetry of the lattice sites that make them attractive as host materials for the study of impurity ions in solids. The optical properties of impurity defects and other absorbing centres in alkali halides whose spectral energies fall within the region of optical transparency can easily be studied.

1.3.2 Intrinsic point defects in alkali halides

Ideal crystalline solids are thought of as consisting of periodic array of identical unit cells. Normal solids however depart from this idealised structure. Thermodynamic considerations establish the hypothesis that there arise in crystals which are in thermodynamic equilibrium vacant lattice sites. In ionic solids, intrinsic lattice vacancies consist of equal numbers of cation and anion vacancies. They could be Frenkel type or Schottky type defects [106].

Apart from these point defects and the possibilities of their aggregation, some extended defects such as dislocation lines, grain boundaries and even internal cracks

and surfaces could exist in alkali halide crystals [140]. These other defect structures are not of immediate interest in this work.

1.3.3 Electron– and hole– excess centres

Another class of point defects in alkali halides are electron–excess centres. The most important of this is formed when a halogen ion vacancy, which has an effective positive charge traps an electron to form an electrically neutral entity known as the F-centre [106]. The presence of the electron could result from an irradiation of the crystal with energetic photons such as X–rays or γ–rays or with fast moving particles such as electrons or protons [113,115,121]. In these processes not only are electrons and holes injected into the crystals, lattice vacancies are created as well. Other methods of defect structure formation include electrolytic injection of electrons and holes and chemical addition [6,113,115 ,121,130].

The F-centre is a highly localized point defect and its presence in alkali halide crystals makes available localized energy levels in the band gap region of the crystals. The electron of the F-centre can absorb a characteristic photon energy and make a transition from the 1*s*–like ground state of the centre to the 2*p*–like excited state. Thus the presence of F-centres in an alkali halide crystal is made manifest by the occurrence of a broad intense band in the optical absorption spectrum of the crystal. This strong optical absorption at a frequency characteristic of the host crystal gives the crystal a characteristic colouration. The broad nature of the F-centre absorption band is attributed to the interaction of the F-centre with surrounding ions of the crystal [107,108].

On the high energy side of the F-band, there could arise some broad low intensity bands which are attributed to transitions of the F-centre electron to higher excited states. These bands include the K,L_1, L_2 and L_3 bands [115-116]. Other absorption bands associated either with an F-centre linked with other defect centres or F-centre aggregates include the β- and α- bands on the long wavelength tail of the fundamental absorption edge of the crystal and the F', R_1, R_2, M and N- bands on the low energy side of the F-band. Fig 1.4(a) illustrates the relative spectral positions of these bands.

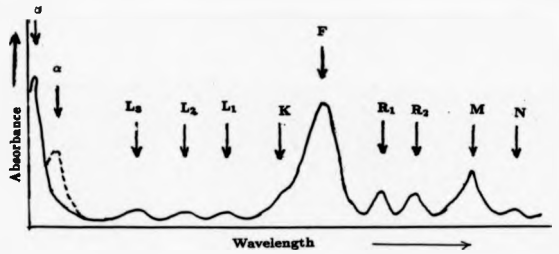

(a)

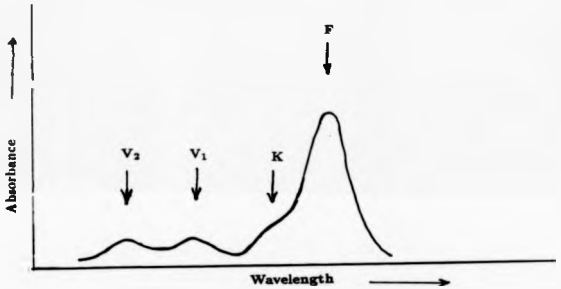

(b)

Fig 1.4(a) Schematic representation of the relative positions of some electron–excess colour centre bands in the absorption spectrum of a typical alkali halide crystal containing these centres.

Fig 1.4(b) Schematic representation of the relative positions of some absorption bands in th spectrum of hole–excess centres in a typical alkali halide crystal.

Hole-excess centres belong to another category of point imperfections that occur in alkali halide crystals. In the absorption spectrum of an alkali halide crystal, bands due to hole trapping centres generally occur to the short wavelength side of the F-band. The best understood of these centres is the V_k– and H-centres [115,119 - 121]. In Fig 1.4(b) the positions of the absorption bands due to these centres relative to the F-band are shown.

1.3.4 Impurity defect structures

Appreciable quantities of hydroxyl (OH^-) and hydride (H^-) ions can easily be incorporated into the alkali halide crystals during preparation. These impurities give rise to definite defect centres some of which are now well understood. Among these are the U–,U_1– and U_2– centres which are associated with characteristic absorption bands in various host crystals, usually occuring in the ultra violet [123–1252].

Certain categories of impurity centres give rise to perturbed F-centres. If an alkali impurity ion is introduced into a crystal of a halide of a different metal, the impurity ion occupies a substitutional lattice site thereby distorting the symmetry at the site of any of the nearest neighbour halogen ions. A perturbation of the electronic states of the F-centre results if a substitutional impurity is situated adjacent to the F-centre. Owing to the lowering of symmetry at the site of the F-centre, there arise a splitting of the energy levels of the centre. In the case of monovalent impurity ions, additional absorption bands known as the F_{A1}- and F_{A2}- bands arise [126,127].

Similarly divalent impurities situated at lattice sites close to F-centres or other electron-excess centres could cause some perturbation in the energy states of these centres. There are many types of centres in this category and are known as the Z_i-centres (i=1,2,..) [128 - 131].

Substitutional cation impurities in alkali halide crystals could be isolated from other point defects. Excitation of these impurities cause electronic transitions as manifested in characteristic absorption and emission bands obtained in optical studies of alkali halide crystals doped with these ions [132-133]. In the cases where atomically dispersed divalent cation impurities occupy substitutional sites in alkali halides cation vacancies are introduced at a next nearest neighbour lattice point in

a < 110 > direction in order to maintain the local charge neutrality in the neighbourhood of the cation impurity site. The creation of the impurity-vacancy complex lowers the local point symmetry at the site of the impurity ion from the octahedral (O_h) to orthorombic (C_{2v}) symmetry. Fig 1.5 schematically illustrates an isolated divalent metal ion in association with a cation vacancy in an alkali halide crystal. This model has been established with data obtained from dielectric loss measurements [134 - 137], optical and electron spin resonance (ESR) studies [134,138-143] of alkali halide doped with divalent cation impurities. As a result of the lowering of the point symmetry at the site of the impurity ion, it is expected that those impurity energy levels which exhibit some degeneracy (with the exception of cases of Kramer's degeneracy) will be split. Consequently many more spectral bands characteristic of the impurity ions could be observed in absorption and luminescence studies of these impurity-doped crystals.

1.3.5 Precipitate phases of divalent impurity ions in alkali halide single crystals

The presence of divalent impurity cations have other effects in the properties of host crystals than those mentioned above. There could occur precipitate structures which vary in size, morphology, or complexity depending on the history of the doped crystals. A wide range of data about the formation kinetics, phase transformations, microstructural compositions and attendent effects on the electrical, paramagnetic, optical and mechanical properties of the host crystals have accumulated over the years. Dielectric loss and ionic thermoconductivity measurements [134 - 137], ESR and optical spectroscopic studies (140 - 144) and X–ray diffraction and electron microscopy [143-153] have added to the understanding of the nature of the precipitate structures.

To appreciate how the precipitate structures and other complexes identified in alkali halide crystals containing divalent impurity ions arise, it is important to note that the formation of divalent impurity–cation vacancy complex (which is dipolar in nature and therefore known as 1-V dipole) in the nearest neighbour cation site is only one of the many possible mechanisms of charge compensation. As has been

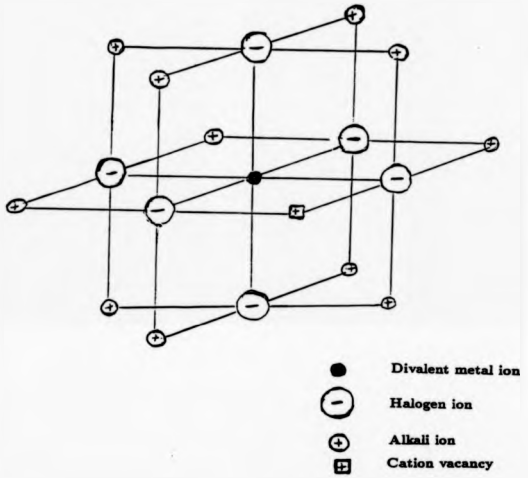

Fig 1.5 Schematic illustration of a divalent metal impurity ion at a cation site in an alkali halide crystal and in which it enters into association with a cation vacancy situated in one of the twelve possible nearest neighbour cation sites.

pointed out by Watkins [134], the cation vacancies which are created to maintain the charge neutrality of the crystal system could even occupy next nearest neighbour (nnn) cation sites. Results of dielectric loss measurements on NaCl:$CaCl_2$ and $KCl : SrCl_2$ solid solutions, suggest that two, three or more dipoles could aggregate to form dimers, trimers or higher order complexes respectively [135,137].

Another possibility is that the divalent impurity ions and the cation vacancies could exist independent of each other. In this latter case divalent ions could form solid solutions of dihalide of the impurity ions [$MeHaI_2$, Me = divalent impurity, HaI = halide ion] within the host crystal matrix. This is the situation in NaCl:$CaCl_2$ crystal system in which small metastable plate-like precipitates called plate zones and made up of smaller units known as platelets are observed to be formed parallel to the (111) and (310) planes of the crystal matrix [145,146]. According to Suzuki [146] who, with Miyake, first observed the above precipitation phenomenon, using X-ray diffraction techniques, the arrangement of the Ca^{2+} ions in the platelets is similar to that expected for the crystal structure of $CaCl_2$. However in this model, layers of vacancies are thought to exist within the platelets. Also found in the same crystal matrix are stable precipitates identified as $CaCl_2$, which have grown out of the metastable (111) plate zones after some heat treatment of the crystal sample. Precipitation of stable crystallites of the dihalides of divalent impurities has been reported in other crystal systems such as $NaCl : SrCl_2$ [151], $LiF : MgF_2$ [149], $NaF : Eu^{2+}$, $NaF : Yb^{2+}$ [6], $NaCl : EuCl_2$ [153], $KBr : EuBr_2$ [154], $NaBr : EuCl_2$ [137,155].

Interestingly, X-ray diffraction analysis also reveals that precipitate structures which are metastable and known as the Suzuki phase, exist in $NaCl : CdCl_2$ solid solutions [148]. Structurally and compositionally, the Suzuki phase is fairly complex since it is built up from super unit cells having face-centred cubic (fcc) structure but a lattice constant almost twice that of the host crystal. The most suitable model of the structure assumes is stiochiometry to be $6NaCl : CdCl_2$, with four of these chemical units in a unit cell. However, the arrangement of the ions in the unit cell is such that the 4 Cd^{2+} ions, and the 24 Na^+ ions occupy normal cation sites; the 32 Cl^- ions occupy anion sites but slightly displaced towards the positive ions while the

remaining 4 cation sites are vacant. Fig 1 6 illustrates schemically the arrangement of the ions in a two dimensional plane. Suzuki phase precipitates have also been identified in a number of alkali halide solid solutions including $NaCl : MgCl_2$[152], $NaCl : MnCl_2$ [150], $LiF : MgF_2$ [149], $RbBr : EuBr_2$ [156], $KBr : EuBr_2$ [154], $RbCl : EuCl_2$ [156] and $KCl : EuCl_2$ [157,158].

The results of these studies underlie the need for care in handling impurity–doped crystals and in interpreting data from studies made with them. Their relevance is appreciated in the thermal annealing experiments reported in Chapter 6 of this work.

1.4 Statement of the problem

The main objective of this study is to construct the energy level scheme for divalent samarium, Sm^{2+} and ytterbuim Yb^{2+} ions in some alkali halide crystals. To do this use will be made of optical absorption spectra of these ions in alkali halide hosts. Since Bland and Smith [101] have developed the energy level structure of Yb^{2+} ions in potassium and sodium halides attention will be concentrated on Yb^{2+} ions in rubidium chloride, bromide, and iodide crystals. Host crystals for Sm^{2+} ions shall be restricted to the chlorides, bromides and iodides of potassium and rubudium.

The problem is therefore divided into the following stages:

(a) measurement of optical absorption spectra of Yb^{2+} and Sm^{2+} ions in the host crystals (b) identification of the origin of the observed absorption bands, (c) theoretical calculation of the energy levels of the ions in crystals of appropriate point symmetry and (d) parametrisation the observed crystal energy levels by the process of fitting these energy levels with the theoretically predicted ones.

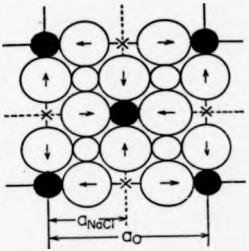

Fig 1.6 Arrangement of ions in the (100) plane of the unit cell of the Suzuki phase of $NaCl : CdCl_2$ solid solution. Small solid circle circles are Cd^{2+} ions, open circles Na^+ ions, and large open circles Cl^- ions. Vacancies are shown in crosses. Arrows indicate the displacement of Cl^- ions. (after Suzuki [148])

Chapter 2

Theoretical Background and Computational Techniques.

2.1 Introduction

A systematized procedure for calculating the energy level of free rare–earth ions has evolved over the years through the efforts of Slater [159,160], Condon and Shortley [30] and Racah [93 - 95,161 - 163]. Racah's irreducible tensor operator techniques (which have been elaborated by Judd [165-171], Wybourne [172 -176] and Fano and Racah [197]) together with concepts from the theory of finite groups [96 - 98,202 - 207,215,318,324] shall be used in this work to construct the energy matrices of the major interactions perturbing the electronic states of rare–earth ions in crystalline environments. In this chapter, therefore, a short statement on how this is done shall be given. In addition, the chapter contains an elaboration of the computational techniques employed in obtaining the energy levels as well as the wavefunctions of Yb^{2+} and Sm^{2+} ions in octahedral crystals field.

2.2 Theory of rare–earth ions in crystalline environment

2.2.1 System Hamiltonian

For a system of N+1 optically active electrons in the excited configuration $nl^N n'l'$ of an ion in a crystalline environment, the Hamiltonian can be written as

$$H = H_0 + H_0' + H_{el} + H_{so} + H_{cr} \qquad (2.1)$$

where H_0 is the central filed Hamiltonian under the central field approximation [1,29,30,159,160] and H_0' is an interaction term which makes no contribution to the energy level structure of the electronic configuration. H_{el} represents the electrostatic interaction between pairs of electrons in the system, H_{so} is the spin–orbit interaction Hamiltonian while H_{cr} represents the electrostatic interaction between the N+1 electrons of the ion and those of the ligand ions. Some other interactions such as configuration interaction, spin–other–orbit and spin–spin interactions [1,186] have been neglected since their effects are small in comparison to those of the interactions listed above. Use of the central field approximation ignores all interaction terms in Eqn. (2.1) except H_0 and solution of the Schrodinger's equation $H_0\Psi = E_0\Psi$ yields the energy levels, E_0, of the electronic configurations and zero–order wavefunctions, Ψ, which are seen to be perturbed by a composite perturbation interaction H'. For an analysis of the energy level structure of a given configuration, H' is usually taken to be the sum of H_{el}, H_{so} and H_{cr}.

Each component of H' can be partitioned to reflect the subspace of the electronic wavefuctions on which they act. In this connection $H_{el} = H_{el}(l,l) + H_{el}(l,l')$. The first term to the right of the expression is the electrostatic interaction between pairs of electrons in the core configuration l^N while the second refers to that between the lone electron in the $n'l'$ outer subshell and the electrons in the nl^N core subshell. Also the expression $H_{so} = H_{so}(l) + H_{so}(l')$ in which the argument (l) or (l') indicates the orbits of the electrons, is valid. In a similar manner, the operator H_{cr} consists of two the components $H_{cr}(l)$ and $H_{cr}(l')$. The precise definitions of these operators in terms of electron co-ordinates and charge distribution within the system have been

well documented [1,2,29,30,93 - 95,159,160,165,223 - 225].

It is possible to express some of these operators in terms of linear combinations of functions which have the same transformation properities with respect to rotation and inversion oprations as spherical harmonic functions Y_L^M and hence as angular momentum operators $\mathbf{J}_z$, $\mathbf{J}_\pm$, $\mathbf{L}_z$, $\mathbf{L}_\pm$ and so on [2,93,165,178,183,197]. For example, $H_{ss}(l,l')$ can be written as

$$H_{ss}(l,l') = \sum_{k=0}^{\infty}[Of_k(l,l')F^k(nl,n'l') + Og_k(l,l')G^k(nl,n'l')] \qquad (2.2)$$

where $F^k(nl,n'l')$ and $G^k(nl,n'l')$ are Slater integrals [1,2,29,30,93,159,160] and $Of_k(l,l')$ and $Og_k(l,l')$ are respectively the effective direct Coulomb and exchange interaction operators acting between pairs of electrons in the nl and $n'l'$ subshells. They can be shown to be [2]

$$Of_k(l,l') = (-1)^{l-l'}[l,l']\begin{pmatrix} l & k & l \\ 0 & 0 & 0 \end{pmatrix}\begin{pmatrix} l' & k & l' \\ 0 & 0 & 0 \end{pmatrix}\mathbf{U}_l^{(k)}.\mathbf{u}_{l'}^{(k)} \qquad (2.3)$$

and

$$\begin{aligned} Og_k(l,l') &= -\frac{1}{2}[l,l']\begin{pmatrix} l & k & l' \\ 0 & 0 & 0 \end{pmatrix}^2\sum_{r=0}^{\min(2l,2l')}(-1)^r[r]\begin{Bmatrix} l & l & r \\ l' & l' & k \end{Bmatrix} \\ &\quad\times[\mathbf{U}_l^{(r)}.\mathbf{u}_{l'}^{(r)} + 4\mathbf{V}_l^{(1r)}.\mathbf{v}_{l'}^{(1r)}] \end{aligned} \qquad (2.4)$$

where the symbol [a,b,...] represents (2a+1)(2b+1)... and the symbols with six arguments enclosed in parenthesis ( ) and curly brackets { } are respectively the the 3-j and 6-j symbols of Wigner [1,2,165]. Their symmetry and orthogonality properties have been well documented [2,165,177 - 182] and their values tabulated [179]. The operator $\mathbf{U}_l^{(r)}$ with $(2q+1)$ components $U_q^{(lr)}$ is a multi–electron unit irreducible tensor operator acting on the electrons in the nl subshell [2,93,165,287]. If $\mathbf{u}_l^{(r)}$ is the unit irreducible tensor operator acting on an electron in the nl subshell, then $U_q^{(lr)} = \sum_{i=1}^{N} u_q^{(r)}(i)$ where the summation is over all the electrons in the subshell. Analogously if $\mathbf{V}_l^{lr}$ is the many–electron unit double tensor operator acting on the N equivalent electrons of the nl^N subshell, its $(2\pi+1)(2q+1)$ components can be defined as [2] $V_{\pi q}^{(1r)} = \sum_{i=1}^{N} v_{\pi q}^{(1r)}(i)$ where $\mathbf{v}^{(1r)} = \mathbf{s}^{(1)}\mathbf{u}^{(r)}$ is the unit double tensor operator for a single electron and $\mathbf{s}^{(1)}$ is its spin angular momentum operator.

For the $H_{ss}(l,l')$ operator and in the case of $4f^N$ configuration, Racah [95] using some generalised tensor operators has shown that the electrostatic energy can be written as

$$E = \sum_{k=0}^{3} e_k E^k \qquad (2.5)$$

where e_k are the linear combination of scalar operators of the form $\mathbf{u}_f^{(k)}.\mathbf{u}_f^{(k)}$ and E^k can be shown to be linear combinations of $F_k(f,f)$ or $F^k(f,f)$ integrals [1,95,165,196].

The spin–orbit operators $H_{so}(l)$ and $H_{so}(l')$ can, infact, be connected to the unit double tensor opreators $\mathbf{V}_f^{(11)}$ and $\mathbf{v}_F^{(11)}$ respectively [1,2,165]. However, $H_{cr}(l)$ and $H_{cr}(l')$ under the point–ion crystal field model [1,3,4,209,220,223 - 225,228 - 230] are conveniently expressed in terms of irreducible tensor operators $\Theta_\Gamma^{(k)}$ which transform as the irreducible representation, Γ, of the point group symmetry of the site of the ion [6,71,206,224,228]. In the particular case of rare–earth ions in octahedral crystal field in which the electronic states of the $4f^N5d$ configuration are being perturbed, $\Theta_\Gamma^{(k)}$ are linear combinations of the operators $\mathbf{U}^{(k)}$ which transform as the identity representation, Γ_1, of the octahedral (O_h) point group [6,71,91,228]. It can be shown [6] that

$$H_{cr}(d) = 6\sqrt{30}Dq\Theta_{\Gamma_1}^{(4)} \qquad (2.6)$$

$$H_{cr}(f) = 16\sqrt{\frac{6}{11}}B_4^0\Theta_{\Gamma_1}^{(4)} + 320\sqrt{\frac{14}{429}}B_6^0\Theta_{\Gamma_1}^{(6)} \qquad (2.7)$$

where Dq is the crystal parameter which represents the strength of splitting of the d–electron states by the crystal field. More specifically, in an octahedral or cubic crystal field, the states of a single d–electron are split into γ_3 and γ_5 states and the energy separation between the crystal levels associated with them is given by $10Dq$ [97,204,207 - 209,228,229]. The other parameters B_k^0 ($k = 4,6$) are the fourth and sixth order crystal field parameters for electrons in the $4f^N$ subshell [6,19,26,59,101,165,206,221,224,228 - 230].

2.2.2 Basis functions

As has been pointed out [86,91], for the $4f^N5d$ configurations of the rare–earth ions in crystal field, the interactions H_{el}, H_{so} and H_{cr} are best treated on the same footing in any perturbation calculation scheme since their energies are generally of

the same order of magnitude. In calculating the perturbation interaction matrices for Yb^{2+} and Sm^{2+} ions, therefore, intermediate coupling scheme is preferred [1,6,76,86,91,101,228,271]. The problem revolves round the choice of starting set of basis functions which best describe the electronic states of the ions.

One variant of the intermediate coupling scheme applies to divalent rare–earth ions towards the end of the lanthanide series, particularly Tm^{2+} and Yb^{2+} ions for which spin–orbit interaction within the $4f^N$ subshell is about as large as the crystal field splitting of the 5*d*–electron states [2,6,82,86,101]. From point of view of the physical coupling of the electronic states, it is more realistic to choose $J_1 j$–coupled basis functions [1,6,99,162,170] of the form

$$|\psi_1 J_1, sl'j', J_2 M_2^{\alpha_2} \Gamma_i \gamma_i\rangle \qquad (2.8)$$

In Eqn. (2.8), $\psi_1 J_1$ ($\equiv \tau S_1 L_1 J_1$) represents a set of angular momentum quantum numbers that uniquely defines the states of the $4f^N$ electrons in the LS coupling scheme [1,6,170]. The arguments $sl'j'$ are the set of quantum numbers that describe the coupling of the states of the 5*d* electron, J_2, M_2 refer to coupled states of the $4f^N 5d$ configuration while Γ_i is a quantum number indicating that the coupled basis functions have the same transformation properties as the irreducible representation Γ_i of the point group symmetry at the site of the ion [206,209,215,228]. α_2 is an index that differentiates between irreducible representations of the same type but associated with the same J_2 while γ_i identifies the row of the irreducible representation to which the basis function belongs.

Another variant of the intermediate coupling scheme pertains to those divalent rare–earth ions for which the effect of $H_{so}(f)$ (although large enough to play a significant role in determining the energy level structure of the ions) is not as large as that of $H_{cr}(d)$. In this latter case, the coupling of the low–lying states of the $4f^N$ configuration approximates to LS coupling. These electronic states then couple to the strongly perturbed 5*d*–electron states, definable in terms of crystal wavefunctions, $|\Gamma_\beta \gamma_\mu\rangle$, which reflect the point group symmetry of the site of the ion [75,76,92,104,217,218]. Accordingly, Yanase and Kasuya [92] suggest the above coupling scheme for Eu^{2+} ions in EuF_2 crystals. Hence the basis functions describing

electronic states coupled in such a manner are of the form [75,76,104]

$$| f^N[(S_1 s)S_2 L_1]J_2, \Gamma_F \; {}^{2S+1}\Gamma_\gamma \rangle \qquad (2.9)$$

In the case of rare–earth ions in an octahedral or cubic crystal field, $\Gamma_F = \Gamma_d = \Gamma_3, \Gamma_5$ and $\Gamma = \Gamma_i$ $(i = 1,2,...,5)$. This coupling scheme referred to in this work as the Yanase – Kasuya coupling scheme has been applied with some measure of success to the problem of Eu^{2+} ions in alkaline earth chalcogenides [76,219] and to the low–lying states of Sm^{2+} ions in some alkaline earth halide crystals [104].

2.2.3 Matrix elements of perturbation interaction operators

In order to calculate the matrix elements of the perturbation operators between the basis functions defined by Eqns. (2.8) and (2.9) some recoupling of the basis functions is necessary. For example, the basis function (2.8) can be expanded into the sum of products of the coefficients $\langle J_2 M_2 \; | {}^{2s}\Gamma_i \gamma_i \rangle$ and the $J_1 j$–coupled basis functions for free ions $|\psi_1 J_1, sl'j', J_2 M_2 >$. The matrix elements of $H_{sl}(l,l')$, $H_{ss}(l)$ and $H_{ss}(l')$ between the basis functions (2.8) are the same as would be obtained if the calculation were done as for free ions. The procedure for doing this has been clearly explained by Judd [170]. For the case of Yb^{2+} ions, the problem is simplified by noting that the $4f^{13}5d$ configuration can be regarded as a two electron system [6,86,99,101,228]. To construct the crystal field energy matrices for Yb^{2+} ions, the matrix elements of the operators $\Theta^{(k)}_{\Gamma_\gamma}$ have to be taken between basis functions (2.8). This is achieved by the application of the Wigner–Eckart theorem [2,165,182] and the repeated use of Eqns. (11.38) and/or (11.39) of the book by Cowan [2] to simplify the resulting reduced matrix element, RME. As a consequence of the processes, a generalised Clebsch–Gordon (CG) or vector coupling coefficients, designated as $\langle k\Gamma_1, J_4^{2s+1}\Gamma_j \; | \; J_2^{2s}\Gamma_i \rangle$ appears in the result [71,91,228]. Their values have been tabulated for integral [228] and half–integral [71] J–values.

Yanase [104] and Asano [75] have elaborated on the procedures for obtaining the matrix elements of the major perturbation operators between basis functions (2.9). The method adopted in this study follows closely those of Asano. As shown by the latter author, the matrix elements of the scalar operators $\mathbf{U}_i^{(r)}.\mathbf{u}_F^{(r)}$ and $\mathbf{V}_i^{(1r)}.\mathbf{v}_F^{(1r)}$

involve the block coefficients W[ ] ($\equiv W[l^r(\Gamma_r)J_2, l'^r(\Gamma'_r)J_4 : {}^{\alpha_3\alpha_4}\ \Gamma_T]$). In calculating the matrix elements of $H_{ss}(l')$ between the basis functions (2.9), it is necessary to introduce the block coefficients S[ ] ($\equiv S[\Gamma_r J_2 \Gamma'_r J_3 : {}^{\alpha_2\alpha_3}\ \Gamma_S]$) which are analogous to the block coefficients W( ) defined by Eqn. (31) of reference [75]. In a similar way, the matrix elements of the irreducible operaters, $\Theta^{(k)}_{\Gamma_1}$ associated with crystal field have block coefficients X[ ] ($\equiv X[J_2 J_4(\Gamma_r) : k\Gamma_1\ {}^{\alpha_2\alpha_4}\ \Gamma]$). Although analogous to the Y–coefficients of Asano [75], the X[ ] coefficients differ from the latter through a set of expansion factors $\langle kq \mid \Gamma_1 a_1 \rangle$ consistent with the definitions of $\Theta^{(k)}_{\Gamma_1}$.

By applying the above techniques to the case of $4f^N 5d$ configurations of rare-earth ions it was possible to express the elements of the energy matrices of the major perturbation interactions in terms of energy parameters. For example, the matrix elements of $H_{el}(f,d)$ were expressed in terms of sum of the products : $f^k(f,d)F_k(f,d)$ and $g^k(f,d)G_k(f,d)$. $f^k(f,d)$ and $g^k(f,d)$ are the angular parts of the matrix elements of the direct Coulomb and exchange interaction energy matrices respectively (they are real numbers) while $F_k(f,d)$ ($= \frac{F^k(f,d)}{D_k}$) and $G_k(f,d)$ ($= \frac{G^k(f,d)}{D_k}$) are Slater–Condon parameters [30]. D_k are denominators introduced by Condon and Shortley [30]. (In the above definitions, the n and n' in $F^k(nl, n'l')$ and $G^k(nl, n'l')$ are ignored since it is understood the case at hand is the $4f^N 5d$ configuration). Similarly, the spin–orbit energy matrices are expressed in terms of products of angular parts (real numbers) and radial parts (the spin–orbit parameters ζ_{4f} and ζ_{5d}) while the crystals field energy matrices are in terms of the parameters Dq (in the case of $H_{cr}(d)$ operator) and B^q_4 and B^q_6 (in the case of $H_{cr}(f)$).

2.3 Introductory comments on computational techniques

The composite energy matrix for each of the systems studied is simply the sum of the various perturbation energy matrices. It was there an easy matter to set up secular equations of the type

$$det|\langle \Psi \mid H' \mid \Psi \rangle - E_n| = 0 \qquad (2.10)$$

Solution of such equations gives the eigenvalues of the matrix and its eigenvectors can then be determined.

To do these tasks, it was found necessary to design, develop and test a self-contained set of libraries of computer program units or subroutines modelled to the problems. Each library of subroutines was designed for specific aspects of the problems. There resulted therefore specialised libraries for the calculation of elements of the interaction matrices and of the commonly re-occurring quantities such as the 3n-j symbols, the generalised CG or vector coupling coefficients and the block coefficients encountered in the last section. In the remaining sections of this chapter, the computational techniques and algorithms adopted for the different tasks will be highlighted.

There are a number of algorithims which can be used in developing the subroutines for solving the secular equations and for determining the eigenvectors of the composite matrices. But the requirements of numerical stability, efficiency and speed demand very careful choice of algorithms. For this reason, the algorithms used in developing the eigenvalue subroutines shall be discussed and their unique properties highlighted. In the last section of the chapter, the inter-relationship between one subroutine and another will be specified.

In addition to these, there was developed a procedure for fitting the experimentally observed energy levels with the theoretically determined ones with a view to minimising the differences between them. The theoretical basis for the procedure is included in this chapter together with elements of the computer program and subroutines that execute the minimisation process.

2.4 Calculation of energy matrices

2.4.1 Introduction

The calculation of the energy matrices for the $4f^{13}5d$ configuration of Yb^{2+} ions was done by free hand and the elements expressed in terms of energy parameters $F_k(f,d)$,$G_k(f,d)$, ζ_{nl} and B_q^0. But free hand calculation of the elements of the energy matrices for $4f^{6}5d$ configuration of Sm^{2+} ions was not feasible. Besides many coefficients such as the W[ ], S[ ] and X[ ] block coefficients, which in themselves are very difficult to calculate by hand, were involve in the calculation of the matrix

elements.

In view of the above, two stages were adopted in calculating the energy matrices. The first stage consists in computing the 3n-j and block coefficients while the second is the actual calculation of the matrix elements

2.4.2 Calculation of the 3n-j symbols, and block coefficients W[ ], S[ ] and X[ ]

It is well known that tables of 3-j and 6-j symbols exist but to knowledge of the author, tables of W[ ], S[ ] and X[ ] block coefficients are not available in literature. The use of available tables of 3-j and 6-j symbols was considered infeasible, however since an extremely large number of such quantities was involved in the calculation. Use of those tables would therefore require keying in the whole tables into the computer. For this reason, a library of subroutines was designed, developed and thoroughly tested for the calculation of the 3-j and 6-j symbols. In all cases tested, the values returned by the computer were exactly the same as the values in tables by Rotenberg and his co-workers[179].

One formidable problem encountered in calculating either the block coefficients or the 3n-j symbols was that of computational precision. An early decision was taken to use integer arithmetic for the computing task in order to retain their exact values at that computational stage. However, this could not be done by using straightfoward arithmetical procedure. The strategy adopted is to express the square of each of the numbers involved in the calculation as the product of a phase factor p, an integer array $\{q_{ij}\}$, $(i = 1, 2, 3, \ldots; j = 1, 2, \ldots, 12)$ of the exponents of the first twelve prime numbers, a_j, $(j = 1, 2, \ldots 12)$ and a positive integral factor, b. Therefore any non-decimal real number can be expressed as the product

$$(p).\sqrt{\prod_{j=1}^{12} a_j^{q_{ij}} b}$$

with $p = 0, \pm 1$.

Another library of subroutines was developed for computing the block coefficients in integer arithmetic. Results obtained were also expressed in terms of p, a_j and b factors and constituted into (n x 14) matrices where n could be as large as 900,

depending on the rank r (or k) of the tensor operator associated with the block matrix. The important point is that each row of such a matrix represents an exact number, the single coefficient being calculated. The matrices were stored in the computer from where they were later accessed .

Two advantages were gained by adopting the above arithmetic strategy. Firstly, the often encountered problem of dealing with very large integers which cannot be accurately stored in the computer was avoided. For the computer system used, IBM 4381, the maximum integer number that can be stored accurately is in the order of 2.2×10^9. Secondly, a system of checks built into the subroutines that detected when two unequal surds were being added helped to locate either incorrect input numbers or errors in the computer subroutines.

2.4.3 Calculation of elements of energy matrices

A library of computer subroutines was developed for the purpose of calculating the elements of the energy matrices. Some of the subroutines were specifically designed to access specific block coefficients required in the calculation. In order to minimise computational errors, the calculations were done in integer arithmetic but the elements were converted to double precision quantities at the final stage of the computation.

Energy matrices corresponding to each of the parameters $F_k(f,d)$, $G_k(f,d)$, ζ_{4f} ζ_{5d} Dq and B_k^q were then constructed and their elements stored as sixteen digit numbers in the computer work disk from where they were accessed when required.

2.5 Determination of eigenvalues of composite energy matrices

2.5.1 Introduction

The composite energy matrix for each of the systems is real and symmetric. In order to solve the secular equations (2.10), it is advantageous to reduce the matrix to a tridiagonal form so that all its elements excepting the diagonal, subdiagonal and super-diagonal elements are zero. Tridiagonalisation of the matrices was

achieved through a sequence of Householder orthogonal similarity transformations. The eigenvalues of the resulting tridiagonal matrices were determined by using the Sturm sequence property and the method of bisection. In this section, the algorithms for these processes will be highlighted.

2.5.2 Tridiagonalisation of a real symmetric matrix

Householder orthogonal transformations have been acknowledged as being numerically very stable and computationally economical [236-237]. Given a real symmetric matrix A of order n, a sequence of orthogonal similarity transformations can be used to reduce A to a tridiagonal form such that

$$\begin{aligned} a_{ii} &= a_i \\ a_{i,i+1} &= a_{i+1,i} \\ &= b_i \\ a_{ij} &= 0 \ , \ j \neq i, i+1 \end{aligned} \qquad (2.11)$$

To do this, a set of $n-2$ real symmetric matrices $P_1 P_2, ..., P_{n-2}$ can be defined such that they are connected to the $n-1$ matrices $A(= A_0), A_1, A_2, ..., A_{n-2}$ through the similarity transformation of the form [236]

$$\begin{aligned} A_r &= P_r A_{r-1} P_r^T \\ &= P_r A_{r-1} P_r \end{aligned} \qquad (2.12)$$

where

$$P_r = I - 2\mathbf{w}_r \mathbf{w}_r^T \qquad (2.13)$$

and $\mathbf{w}_r$ are n–component unit vectors defined by

$$\mathbf{w}_r \mathbf{w}_r^T = 1 \qquad (2.14)$$

P_r^T and $\mathbf{w}_r^T$ are the respective transpose of P_r and $\mathbf{w}_r$. The matrices P_r are Householder matrices and Equation 4.2 is a statement of the Householder transformations. The vectors $\mathbf{w}_r$ are chosen so that at the r^{th} step in the reduction process, zeros are introduced into the r^{th} row and column of A_{r-1}. In so doing however, the zeros introduced in the preceeding steps are left intact. To accomplish this, $\mathbf{w}_r$ are

defined such that the first r elements are zero. The rest of the problem reduces to that of suitably defining $\mathbf{w}_r$. How this is done has been discussed by many authors [236-239].

However the symmetry of the problem can be exploited so as to reduce computational errors, computation time and storage space requirements by using a strategy suggested by Wilkinson [236]. This consists on redefining the matrices P_r in terms of vectors $\mathbf{u}_r$. Thus

$$P_r = I - \frac{\mathbf{u}_r \mathbf{u}_r^T}{2K_r^2} \tag{2.15}$$

where $\mathbf{u}_r$ are n-component vectors whose elements are:

$$\begin{aligned} u_{rj} &= 0\ ,\ j = 1,2,\ldots,r \\ u_{r+1,r} &= a_{r,r+1}^{r-1} \mp S_r^{\frac{1}{2}} \\ u_{jr} &= a_{rj}^{r-1}\ ,\ j = r+2, r+3, \ldots, n \end{aligned} \tag{2.16}$$

where

$$2K_r^2 = S_r \mp a_{r,r+1}^{r-1} S_r^{\frac{1}{2}} \tag{2.17}$$

Using these definitions, Eqn (4.2) becomes

$$A_r = (I - \frac{\mathbf{u}_r \mathbf{u}_r^T}{2K_r^2}) A_{r-1} (I - \frac{\mathbf{u}_r \mathbf{u}_r^T}{2K_r^2})$$

Defining the vectors

$$\begin{aligned} \mathbf{p}_r &= A_{r-1} \frac{\mathbf{u}_r^T}{2K_r^2} \\ \mathbf{q}_r &= \mathbf{p}_r - \frac{1}{2} \mathbf{u}_r (\frac{\mathbf{u}_r^T \mathbf{p}_r}{2K_r^2}) \end{aligned} \tag{2.18}$$

one obtains [236]

$$A_r = A_{r-1} - \mathbf{u}_r \mathbf{q}_r^T - \mathbf{q}_r \mathbf{u}_r^T \tag{2.19}$$

The use of the last set of definitions (2.15)–(2.19) reduces the number of computational operations. They constitute the set of equations for writing the program subroutine used in this work to obtain the final tridiagonal matrix A_{n-2}.

Since matrices connected by similarity transformations are similar, the matrices A_r $(r = 0, 1, 2..n-2)$ are similar and therefore have the same eigenvalues. This also means that the traces of the matrices are equal. One strategy adopted in the design

of the program unit to tridiagonalise the energy matrices was to compare the traces of the matrices A_r for equality at each stage of the reduction process.

As will be realised later, the matrices P_r will be needed for the determination of the eigenvectors of A. Even though a record of P_r is required, it was enough to record the elements of the vectors u_r and the numbers $2K_r^2$, with which P_r could be reconstructed, at the appropriate stage.

2.5.3 Determination of eigenvalues of a symmetric tridiagonal matrix

Determination of the eigenvalues of the matrix A therefore reduces to that of evaluating the eigenvalues of the tridiagonal matrix A_{n-2}. The secular equations can be rewritten as

$$det|A_{n-2} - \lambda I| = 0 \qquad (2.20)$$

where λ_i are the roots of the characteristic equation. Solution of the latter equation proceeds by constructing a sequence of recurrence relations known as the Sturm sequence which connect the polynomial $p_i(\lambda)$. These polynomials are defined as [236–238]

$$\begin{aligned} p_0(\lambda) &= 1 \\ p_1(\lambda) &= a_1 - \lambda \\ p_i(\lambda) &= (a_i - \lambda)p_{i-1}(\lambda) - b_{i-1}p_{i-2}(\lambda)\ ,\ i = 2, 3, \ldots, n \end{aligned} \qquad (2.21)$$

In order to find the roots of the characteristic polynomial $p_n(\lambda)$ (and hence the eigenvalues of A_{n-2}), use is made of the Sturm sequence property. This means that if λ' is some value in the interval within which the roots of p_n are located, the number of agreements in sign $v(\lambda')$ between consecutive terms in the sequence

$$p_0(\lambda'), p_1(\lambda'), p_2(\lambda'), \ldots, p_n(\lambda')$$

is the number of roots of $p_n(\lambda)$ equal to or greater than λ'. Therefore $v(\lambda')$ corresponds to the number of eigenvalues of A greater than λ'. Overflow and underflow problems do sometimes result in the calculation of the polynomials $p_i(\lambda')$, particularly for large matrices. To ameliorate this difficulty, it is instructive to define the

following sequence [237].

$$\begin{aligned} r_1(\lambda) &= p_1(\lambda) \\ &= a_1 - \lambda \\ r_i(\lambda) &= a_i - \lambda - b_{i-1}^2 \frac{p_{i-2}(\lambda)}{p_{i-1}(\lambda)}, \; i = 2, 3, \ldots, n \\ &= a_i - \lambda - b_{i-1}^2 \frac{1}{r_{i-1}(\lambda)} \end{aligned} \qquad (2.22)$$

The number of non-negative terms in the sequence $r_1(\lambda), r_2(\lambda), \ldots, r_n(\lambda)$ is equal to $v(\lambda)$ [237]. This feature of the Sturm sequence which enables the roots of the characteristic equation to be separated is known as the Sturm sequence property.

The actual isolation of the roots of $p_n(\lambda)$ is achieved by the method of bisection. Suppose $[l, u]$ is the interval within which all the eigenvalues of A_{n-2} lie. In this case, l and u are the lower and the upper bounds of the interval respectively. Both are real numbers. Again, suppose η_1 is the midpoint of the interval. The procedure is to compute $v(\eta_1)$, the number of roots of $p_n(\lambda)$ in the interval $[\eta_1, u]$. If we are interested in computing the r^{th} eigenvalue and $v(\eta_1) \geq r$, then $\lambda_r \in [\eta_1, u]$, otherwise $\lambda_r \in [l, \eta_1]$. Suppose actually $\lambda_r \in [\eta_1, u]$, the mid-point of the new interval is taken as trial eigenvalue and $v(\eta_2)$ is computed. Again if $v(\eta_2) \geq r$, then the eigenvalue is within a new interval $\lambda_r \in [\eta_2, u]$, otherwise $\lambda_r \in [l, \eta_2]$. This procedure is continued with the objective of locating and narrowing the interval within which λ_r is contained. However, the process is terminated if the interval length $(u - l)/2^k$ is as small as we wish, k being the number of bisections. In this work, the minimum interval length is chosen to be $\| A_{n-2} \|_\infty \times 10^{-15}$ where $\| A_{n-2} \|_\infty$ is the row (or infinity) norm and 10^{-15} is the smallest double precision number exactly representable by the computer system used in this work. Actually the initial bound is chosen to be $l = -\| A_{n-2} \|_\infty$ and $u = \| A_{n-2} \|_\infty$ where

$$\|A_{n-2}\|_\infty = \max_i \sum_j |a_{ij}| \qquad (2.23)$$

This follows from the known fact [237,238] that any norm of a matrix defines the interval within which all the eigenvalues of the matrix can be located.

The eigenvalues determined using the above computational procedures are obtained from the computer in descending order of magnitude. They are not exact but

can be made as close to the exact eigenvalues as the machine can allow. The method of bisection incorporated into the procedures is numerically very stable [237] and by its use, it is possible, as has been demonstrated by Wilkinson [236], to separate eigenvalues (of a matrix) that are so close that they agree up to 15 significant decimals.

2.6 Determination of eigenvectors of the composite energy matrix

2.6.1 Introduction

In order to determine the eigenvalues of the real symmetric matrix A, it was necessary to transform it into a tridiagonal matrix A_{n-2}. But the required eigenvectors are those of A and not of A_{n-2}. However they are related through the expression

$$\begin{aligned} \mathbf{y} &= P_1 P_2 \ldots P_{n-2}\mathbf{x} \\ &= (I - 2\frac{\mathbf{u}_1\mathbf{u}_1^T}{2K_1^2})(I - \frac{\mathbf{u}_2\mathbf{u}_2^T}{2K_2^2})\ldots(I - 2\frac{\mathbf{u}_r\mathbf{u}_r^T}{2K_r^2})\mathbf{x}\ldots \end{aligned} \qquad (2.24)$$

where x is the eigenvector of A_{n-2}, corresponding to an eigenvalue λ and y is the eigenvector of A corresponding to the same eigenvalue.

The task at hand then reduces to that of finding the eigenvectors of A_{n-2}. Since the eigenvalues λ_i are not exact, instead of solving the system of homogeneous linear equations

$$(A_{n-2} - \lambda_i I)\mathbf{x} = \mathbf{0} \qquad (2.25)$$

a system of equations in which the zero vector 0 is replaced by b is solved. Thus b is an arbitrary vector chosen so that each of its components is equal to unity [237-239].

One highly recommended strategy for solving Eqns (2.25) is to decompose the coefficient matrix $(A_n - \lambda_i I)$ into a lower triangular matrix L and an upper unit triangular matrix U [237–239]. There after, equations of the type

$$\begin{aligned} L\mathbf{z} &= P\mathbf{b} \\ &= \bar{\mathbf{b}} \qquad (2.27) \\ U\mathbf{x} &= \mathbf{z} \qquad (2.28) \end{aligned}$$

are solved. P is a permutation matrix. Its structure and construction as well as the the procedure for the LU decomposition of a real matrix are described in references [237,239]. In this section are discussed the algorithm for the computation of the final vector x assuming that LU decomposition of A_{n-2} has been achieved.

2.6.2 Eigenvectors of coefficient matrix

Equations (2.27) and (2.28) are used to find the intermediate and final eigenvectors z and x respectively. From the structure of L, it is easy to show that

$$z_i = \frac{b_i - \sum_{j=1}^{i-1} l_{ij} z_j}{l_{ii}} \qquad (2.29)$$

This corresponds to forward substitution in the conventional Gauss elimination procedure. For back substitution and considering Eqn (2.28), with due regard to the structure of U, the elements of x are given by

$$x_i = z_i - \sum_{j=i+1}^{n} u_{ij} x_j \qquad (2.30)$$

The inner products in Eqns (2.29) and (2.30) were accumulated in quadrupole precision but stored as double precision quantities.

Because of the tendency for the computed x_i to be very large, they were normalised so that the largest element (in absolute magnitude) has a value of unity. As a strategy of refining the computed x_i, they are transformed into b_i and the whole process of forward and back substitution repeated. (This is equivalent to going through entire LU decomposition process down to the computation of x_i). In this work, a four-fold iteration routine was adopted for refining the eigenvectors.

2.6.3 Eigenfunctions of total perturbation Hamiltonian

The n eigenvectors of the type x correspond to each of the eigenvalues of the total energy matrix as described in the preceding section. It is a simple matter to transform them into the eigenvectors of the matrix through relations of type indicated in Eqn (2.24). The vectors u_r and quantities $2K_r^2$ are derived from the tridiagonalisation routine. The eigenvectors so obtained were normalised so that each of the vectors would have a length of one. This set of eigenvectors constitute the eigenfunctions of the total perturbation Hamiltonian H'.

2.7 Minimisation of experimentally observed parameters

In the previous chapters, it was seen that the various interaction energies were expressed in terms of energy parameters. The values of the parameters are to be determined experimentally. Nevertheless, it was necessary to optimise the values of these interaction parameters to get a better fit between theoretically determined and experimentally observed energy levels. The conventional way of doing this would be to use the least-square method. However, since it was not possible to express the theoretical energy levels as analyticial functions of the interaction parameters, a modified procedure was adopted. In this section, is described details of the procedure.

The technique consists in inducing shifts in the theoretical energy levels by changing the trial parameters by small amounts one at a time. Comparison of the shifted energy levels with those obtained using some set of trial parameters values on the one hand, and of the energy levels obtained using the trial parameter values and the experimentally observed energy levels on the other, generates a quantity which can easily be optimised. This leads to a system of equations linear in parameter shifts.

Suppose the trial parameters are $P_1^{(0)}, P_2^{(0)}, .., P_n^{(0)}$. Eigenvalues of the system were obtained using this set of parameters. Then, the parameter $P_1^{(0)}$ was changed by a small amount while keeping the rest constant and the energy levels $E_{i1}^{(0)}$ obtained using methods previously described. The value of $P_1^{(0)}$ was restored to its previous value and $P_2^{(0)}$ was then shifted by a small amount to generate another set of eigenvalues E_{i2}. Restoring $P_2^{(0)}$ to its previous value, the process is repeated with $P_3^{(0)}$ and so on.

It is possible therefore to obtain the sum of squares of the deviation D of the calculated energy levels from the experimental ones. The minimisation of D leads to a better estimate of the parameters which are then refined by an iterative process.

If it is supposed that the iteration process is at its k^{th} stage,then representing the $i^{(th)}$ energy level of the various sets of eigenvalues as $E_{i1}^{(k)}$, $E_{i2}^{(k)}$, ... ,$E_{im}^{(k)}$, the theoretical energy level in the neighbourhood of the points $P_1^{(k)}, P_2^{(k)}, ..., P_m^{(k)}$ can

be written as

$$E_i^{(k)} = E_{iT}^{(k)} + (E_{i1}^{(k)} - E_{iT}^{(k)})\Delta P_1^{(k)} + (E_{i2}^{(k)} - E_{iT}^{(k)})\Delta P_2^{(k)} + \ldots + (E_{im}^{(k)} - E_{iT}^{(k)})\Delta P_m^{(k)} \quad (2.31)$$

where the superscript k on the P_j indicate the index of iteration. $E_{iT}^{(k)}$ are the theoretical energy levels obtained using unshifted trial parameter values at the k^{th} iteration. m is the number of parameters. k can be ignored since no confusion shall result in so doing. The deviation δ_i of E_i from experimentally observed $i^{(th)}$ level, E_{ie}, is

$$\begin{aligned}\delta_i &= E_{ie} - E_i \\ &= (E_{ie} - E_{iT}) + (E_{iT} - E_{i1})\Delta P_1 + (E_{iT} - E_{i2})\Delta P_2 + \ldots \\ &\quad + (E_{iT} - E_{ij})\Delta P_j + \ldots + (E_{iT} - E_{im})\Delta P_m\end{aligned} \quad (2.32)$$

Defining the quantity

$$D = \sum_{i=1}^{n} \delta_i \quad (2.33)$$

where n is the number of experimentally observed energy levels. Minimising D, one obtains

$$\begin{aligned}\frac{\partial d}{\partial \Delta P_j} &= \sum_{q=1}^{m}\sum_{i=n}^{n}(E_{iT} - E_{ij})(E_{iT} - E_{iq})\Delta P_q + \sum_{i=1}^{n}(E_{ie} - E_{iT})(E_{iT} - E_{ij}) \\ &= 0\end{aligned} \quad (2.34)$$

Hence

$$\sum_{q=1}^{m}\sum_{i=n}^{n}(E_{iT} - E_{ij})(E_{iT} - E_{iq})\Delta P_q = \sum_{i=1}^{n}(E_{iT} - E_{ie})(E_{iT} - E_{ij}) \quad (2.35)$$

which is a system of equations with m unknowns, and can be represented as

$$M\Delta P = \mathcal{E} \quad (2.36)$$

$j = 1, 2, \ldots, m$. M is a square symmetric matrix of order m and $\mathcal{E}$ is a vector. They are defined as

$$M_{jl} = \sum_{i=1}^{n}(E_{iT} - E_{il})(E_{iT} - E_{ij}) \quad (2.37)$$

$$\mathcal{E}_j = \sum_{i}^{n}\Delta E_i(E_{iT} - E_{ij}) \quad (2.38)$$

ΔE_i being the difference between experimental and theoretical i^{th} energy level. Solution of Eqns (2.35) yields values for ΔP_q. Thus the trial values of the parameters were adjusted and the improved values are

$$P_j = P_j^{(k)} + \Delta P_j^{(k)} \qquad (2.39)$$

The improved values were then used in the $(k+1)^{th}$ the iteration. The iteration process was terminated when adequate convergence of the parameters are obtained. The above procedure incorporates some features of the techniques used by Eremin and Maryakhina [33] and Nara and Schlesinger [247].

In spite of adopting these procedures there could still remain some discrepancy between observed and theoretically predicted energy levels. A measure of this discrepancy is the mean error defined as

$$\mu = \sqrt{\frac{\delta_i^2}{n-m}} \qquad (2.40)$$

where δ_i is the deviation of the theoretically predicted i^{th} level from the experimental, m is the number of free ion parameters and n is the number of observed energy levels [1,37].

2.8 The Computer Programs

2.8.1 Introduction

Many computer programs were written to handle different aspects of the problems being investigated. There were two main categories of programs/subroutines. One category has to do with the programs/subroutines that are specific to a particular ion. The programs and subroutines developed for the calculation of the matrix elements of the energy matrices of Sm^{2+} ions and the W[ ], S[ ], and X[ ] block coefficients fall into this category. Also in this category are the subroutines defining the elements of the energy matrices of Yb^{2+} ions. Since these are specific, and above all, very large in nubmer, details of them will not be given. The other category involve those subroutines that have greater applicability. In this group are subroutines for determining the eigenvalues and eigenvectors of the composite energy matrices and

those for fitting the experimental and theoretical energy levels. A little more will be said about programs/subroutines in the latter category. All the computer programs and subroutines developed in this work, together with tables of W[ ], S[ ] and X[ ] coefficients are available for inspection under a separate cover. The programming language used is Standard Fortran 77.

2.8.2 Program design, development and testing strategies

In the design of the programs, the top-down design approach was adopted. This consists in splitting the problem into its logical parts or modules, each of which was dealt with as a separate entity. Each of the modules was further split into smaller modules until more manageable units were obtained. Programs were written based in these small units and they constitute the subroutines or subprogram of the main programs.

A subroutine or subprogram merely processes an input data (which may be derived from subroutine and produces an output which may be used in another subroutine). Accordingly, each subroutine was tested independently using various driver programs and well-designed data at different stages of constructing the programs.

The system of subroutines were interfaced by means of well-chosen arguments. This intercommunication was done in stages and a testing procedure carried out at each stage.

Eventually the entire system of subroutines were tested together. In the case of subroutines for eigenvalue problems square symmetric matrices of known eigenvalues and/or eigenvectors were used in the tests. Numerous matrices of variable sizes used were obtained from standard textbooks in numerical analysis [236-244]. Excellent agreements were obtained with results stated in textbooks. In cases where the eigenvalues and eigenvectors were not known different forms of checks on the results obtained were done as will be indicated later.

It has to be noted that nearly all computations were done in double precision arithmetic. With IBM 4381 model digital computer double double precision numbers can be held accurately up to sixteen decimal digits. In the determination of residual vectors used in the iterative refinement of parameter shifts, however, quadrupole

precision was used.

2.8.3 Program for the determination of eigenvalues and eigenvectors of composite matrix

The task was divided into three main modules each of which was broken into fairly large constituent modules. The three major modules are (a) construction of the composite perturbation energy matrix (b) evaluation of eigenvalues of the matrix (c) determination of eigenvectors of the matrix. Each of these will be briefly described below. Subroutines/subprograms performing various tasks are indicated. Their arguments are omitted for brevity.

(i) Construction of the composite energy matrix: Composite energy matrices were constructed in either of two ways, depending on the electronic configuration involved. For the $4f^{13}5d$ configuration of Yb^{2+} ions, the composite matrix was constructed within the main program YBF13D. Subroutines which define the values of the relevant coefficients of $F_k(f,d), G_k(f,d), \zeta_{nl}, Dq$ and B_k^q parameters were called by YBF13D and the elements of the matrices computed and summed. In the case of $4f^5 5d$ configuration of Sm^{2+} ions, the composite matrix was also constructed within the main program SMF55D and stored values of coefficients of $F_k(f,f)$, $F_k(f,d)$, $G_k(f,d)$, ζ_{nl}, Dq and B_k^q were accessed from the computer.

(ii) Evaluation of eigenvalues of composite matrix : As earlier indicated, the matrix was first reduced to a tridiagonal form before the eigenvalue evaluation. HOTRED reduces the energy matrix to tridiagonal form. In testing HOTRED, the trace of the original matrix A_0 was compared with the trace A for equality.

EIGVAL actually evaluates the eigenvalues of the tridiagonal matrix. EIGVAL calls an important subroutine BISECT. The latter executes the bisection process as indicated in Section 2.5.3. To do this, it calls STURMS and some other subroutines. STURMS determines the number of agreements in sign between consecutive terms of the Sturm sequence. All these subroutines, at various stages, call the subroutine DPSORT which is a sorting routine that arranges double precision numbers in descending order of magnitude.

Two important strategies adopted in checking the eigenvalues obtained using

the above system of subroutines are as follows: Firstly, the sum of the eigenvalues obtained was compared with the trace of the original composite energy matrix. They must be equal if the evaluation was correctly carried out. Secondly, and as a further check, the product of the eigenvalues was compared with the determinant of the original matrix. The magnitudes must be equal. Difference in sign could arise because of the way the determinant was computed. In this case, the original matrix was decomposed into LU factors [237,239]. The determinant of the original matrix is simply $\pm det$ L since det U = 1. The plus sign is operative if an even number of row, permutations occurred in computing L, otherwise the minus sign is operative [245]. But det L is the product of all the diagonal elements of L. The latter strategy was used during the preparation and testing stages of the programs. The results of these comparisons were excellent and they tended to inspire a lot of confidence as to the effectiveness of the procedures and efficacy of the subroutines.

(ii) Determination of eigenvectors of composite matrix: The main subroutine that performs this task is EIGVEC. Within it, the coefficient matrix is constructed. It then calls other subroutines indicated below.

CRALGO is called by EIGVEC. It factorises the coefficient matrix into a unit upper triangular matrix and a lower triangular matrix. As a check on the effectiveness of the subroutines, the relation $PA - LU$ [239] was verified during the program developmental and testing stages. It calls a specialised subroutine CSORT.

FOWBAK performs the forward and back substitution indicated in Section 2.6.3 in order to obtain the eigenvectors of the tridiagonal matrix. TRAVEC determines the eigenvectors of the composite matrix. It makes use of the output of FOWBAK and the transformation matrices P_i derived from HOTRED.

Each of the above subroutines at some stage calls the subroutine NUSORT which is a sorting routine that returns the largest of a set of absolute numbers. CSORT compares two sets of numbers and its result determines which rows of the coefficient matrix are to be interchanged.

2.8.4 Programs for minimisation interaction parameters

PAROPT is a program based on the main ideas of Section 2.7, designed to minimize the square of the difference between experimental and theoretical energy levels. It calls EGPROB which outputs the eigenvalues of the composite matrix generated with trial parameter values supplied by PAROPT. The latter also calls SIMLEQ which is a subroutine that solves a set of simultaneous linear equations generated by PAROPT and whose coefficients are passed on to it. SIMLEQ also incorporates an iterative refinement of solutions of the equations. It calls FOWBAK, and passes on its output to PAROPT.

Chapter 3

Experimental Methods

3.1 Introduction

Single crystals of rubidium chloride, bromide and iodide were doped with divalent ytterbium (Yb^{2+}) ions using vapour phase diffusion technique. The same method was also used in incorporating divalent samarium (Sm^{2+}) ions into crystals of rubidium and potassium chloride, bromide and iodide. Optical absorption spectra of these ions in the crystals were then measured and analysed. In this chapter, a description of the design features of the apparatus used and the various techniques adopted to obtain the spectra are discussed. Special comments will later be made about heat treatment procedures adopted.

3.2 Incorporation of ions into crystals

3.2.1 Introduction

The single crystals of potassium halides used in this study were obtained from Harshaw Chemical Company, Cleveland, USA while the rubidium halides were supplied by BDH Chemicals Ltd, Poole, England. Metallic ytterbium and samarium were obtained from Rare Earth Products Ltd, Cheshire, a Division of Johnson and Matthey Chemicals Ltd, London. Certified purity level of each sublimed metal ingot was 99.99 %. As a matter of routine, the metal ingots and the crystals were stored in a glove box continuously flushed with a slow stream of dry nitrogen.

Metallic ytterbium and samarium have appreciable vapour pressure (0.00031 — 0.6455 torr) in the temperature range 600^0 C to 900^0 C, in which the melting points of alkali halides lie. This suggests that under suitably arranged thermodynamic conditions, it is possible to incorporate some ytterbium and samarium ions into alkali halide crystals by a vapour phase diffusion process. Table 3.1 shows some of their relevant thermodynamic properties together with those europium and the halides of rubidium and potassium, while Fig 3.1 shows the vapour pressure of all rare earth metals as a function of temperature [5,6,252,253].

Conventional methods of obtaining single crystals of alkali or alkaline earth halides doped with divalent rare–earth ions (RE^{2+}) consists in incorporating some quantities of trivalent rare–earth metal (RE^{3+}) halide into the melt of the desired host crystal. By some reduction process the RE^{3+}) ions are converted to the divalent state. Single crystals are then grown from melt using any of the common crystal growing techniques such as the Czochralski [17,84,116], Kyropoulos [16,20,64,255–257] and the Bridgman [15,86,254,258] methods. As far as this author knows, this is the first time the vapour phase diffusion technique has successfully been used to incorporate Yb^{2+} ions into single crystals of rubidium halides.This is the first time Sm^{2+} ions have been incorporated into crystals of rubidium and potassium halides by this method. Bland and Smith [101] and Bland [6] were the first to successfully incorporate Yb^{2+} ions into crystals of sodium and potassium halides using the above method. However, there has been a previous mention of it [130] in literature as it regards the implantation of Yb^{2+} ions into alkali halides. Apparently, the attempt was not successful because the spectrum identified as Yb^{2+} spectrum in KBr crystals has no obvious resemblance to the usual spectrum of Yb^{2+} ions in octahedral environment. Moreover, the structure of that spectrum appears to be similar to that associated in the same study with Eu^{2+} ions in NaCl crystals.

3.2.2 Design features of primary and secondary diffusion ampoules

The primary diffusion ampoule (PDA) [in Fig 3.2] was made of a special type of stainless steel known as Immaculate V (Chromium 24–26 %, Nickel 19-22 %, Carbon

Table 3.1 Incorporation of Sm^{2+} and Yb^{2+} Ions into Potassium and Rubidium Halide Crystals : Some Thermodynamic Information * *

Host Material	Melting Point of Host Material (^{o}C)	Doping Temperature (^{o}C)	Metal Vapour Pressure at Doping Temperature (torr)		
			Samarium	Europium	Ytterbium
KCl	790	760	0.0148	0.2735	0.6414
KBr	730	705	0.0038	0.0931	0.2596
KI	722	700	0.0034	0.0827	0.2391
RbCl	715	680	0.0020	0.0747	0.1721
RbBr	682	655	0.0011	0.0284	0.1141
RbI	642	610	0.0003	0.0097	0.0388

* * Data on melting point of alkali halides was obtained from the American Institute of Physics Handbook [270] while vapour pressure data were interpolated from tables by Honig [326]

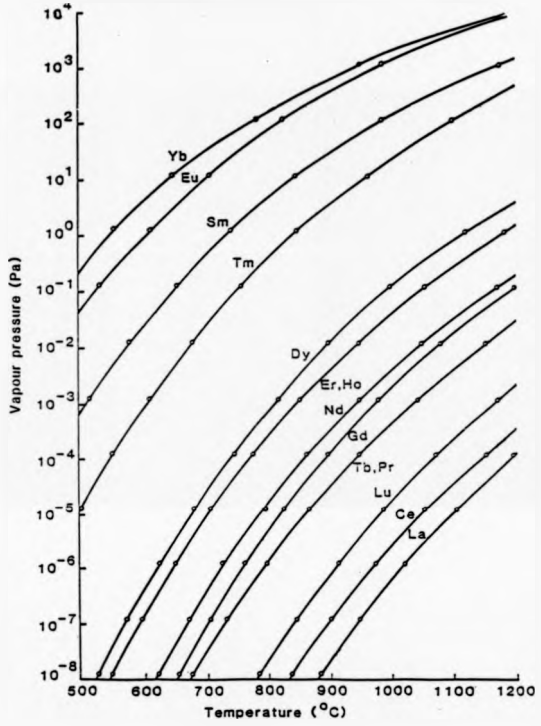

Fig 3.1 Vapour pressure of rare earth metals as function of temperature. (after Hultgren et. al. [253] , Bland [6])

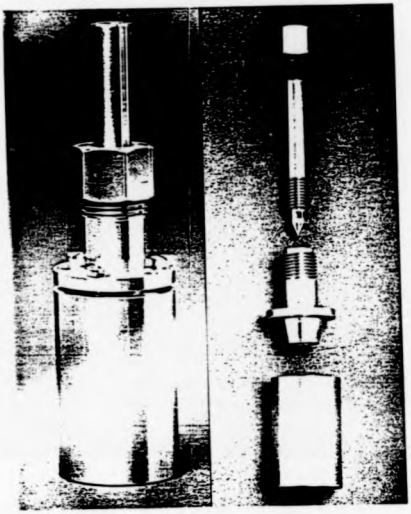

Fig 3.2 Primary diffusion ampoule (PDA)

0.12 % max, Balance Iron) which can withstand a continuous exposure to temperatures up to 1100^0 C for long periods of time, without being degraded. It consists of a body which is a cylindrical container closed at one end, and a top. As shown in Fig 3.3, the top is made up of a hollow cylindrical part (threaded on both the inside and outside) and a truncated conical end with an overlapping metal flap. Both the open end of the body and the conical end of the top are finely machined to form a conical joint. This feature, together with the threaded needle through which the PDA is evacuated constitute the most important features of the device. Provided a rubber 'O' ring with a threaded retain cap are used), the PDA assembly can be evacuated to a pressure as low as 10^{-6} torr. The 'O' ring and its retainer cap are usually removed before the PDA is lowered into the furnace.

The secondary diffusion ampoule (SDA) also consists of a long cylindrical tube closed at one end. At the top part of the SDA there is a water jacket for cooling purposes, and a pumping access. It is made of conventional stainless steel. Its top is a circular stainless steel plug with a central hole which can be sealed by means of 'O' rings and glass-to-metal seal system. Fig 3.3 shows the SDA and its top with a thermocouple passing through the central holes. The thermocouple could be replaced by a stainless steel rod from which is suspended the PDA during doping process.

3.2.3 Characteristics of the high temperature furnace

The furnace is an upright tube furnace which can operate at temperatures up to 1000^0 C, and is connected to a temperature controller (Ether 'Mini' Type 17-90B) capable of holding the temperature constant within $\pm 3^0$ C. Also, in communication with the furnace through a thermocouple sensor is a back off unit which is connected to the temperature controller. The back off unit raises the upper temperature limit of the controller from its original 600^0 C to 1000^0 C.

Fig 3.4 shows a typical variation of temperature of the interior of secondary diffusion ampoule with depths of immersion of thermocouple taken with temperature controller set at 450^0 C and back off unit switched on. The best position for crystals to be placed during doping is within the region of lowest temperature gradient.

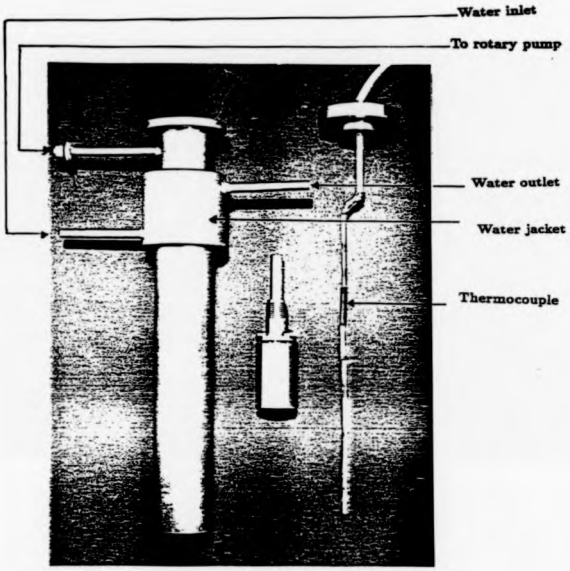

Fig 3.3 Secondary diffusion ampoule (SDA)

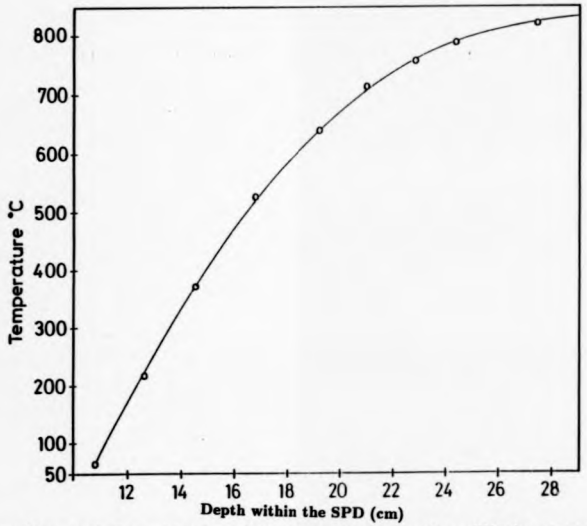

Fig 3.4 Variation of temperature within the secondary diffusion ampoule

Variation of temperature with time at a point 27.7 cm below the top of the SDA, was also measured for different temperature controller settings. A typical result is shown in Fig 3.5 and was taken with temperature controller set at 450^0 C, the back off unit being on. Measurements were made at fifteen minute intervals over six and half hours duration. Temperature stabilization of the system was good at such a high temperature as 809.1^0 C, the range being 6.1^0 C.

3.2.4 Diffusion procedure

A specimen (10 x 6 x 5 mm) of the desired alkali halide crystal host was cleaved off a cuboid of crystals and placed in the PDA while being supported on a molybdenum boat containing about 25 mg of the dopant. The crystals were cleaved in air but all other procedures were carried out in the glove box. Before being lowered into the the SDA which was already being heated (in the furnace) to a constant (doping) temperature, the PDA was evacuated using a diffusion pump. The upper section of the SDA was cooled by means of running water through the water jacket while dry nitrogen gas was used to flush the SPD and the glove box enclosing the furnace for a brief period before they were evacuated by means of a rotary pump. During doping and as long as the SDA is hot, the rotary pump was left to run continuously. Fig 3.6 shows the furnace assembly during doping.

The temperature at which diffusion took place was chosen to be $25^0 - -50^0$ C below the melting point of the intended host crystal. For most halides, diffusion times ranging from 4 hours to 6 hours were used but for rubidium iodide doping was continued for up to 8 hours. This is because the doping temperature for RbI crystals was relatively low (610^0 C). After doping, the PDA was lowered into a dewar of liquid nitrogen. Within three minutes, the PDA had attained the liquid nitrogen temperature (LNT). Quenching of the crystals was considered necessary because it enabled the crystal to cool fast enough to ensure that the impurity ions and other defect centres in the doped crystal were atomically dispersed and uniformly distributed.

Different PDA's were used for different dopants. After each doping session the PDA was cleaned using abrasives and deionised water. A point to note is that the

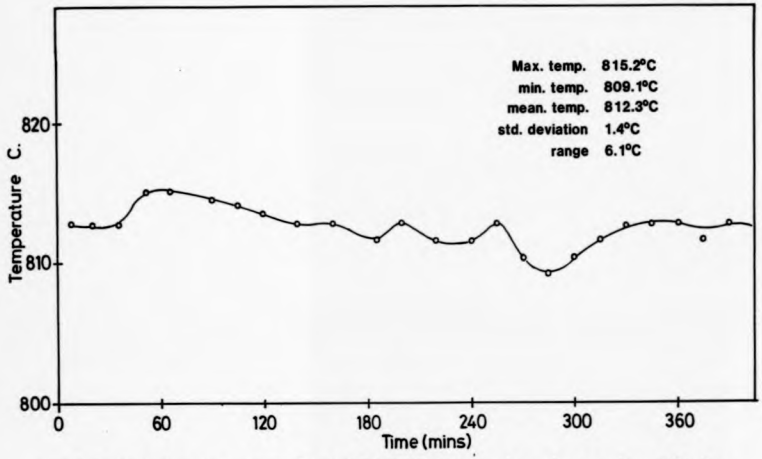

Fig 3.5 Variation of temperature at 27.7cm below the top of secondary diffusion ampoule with time.

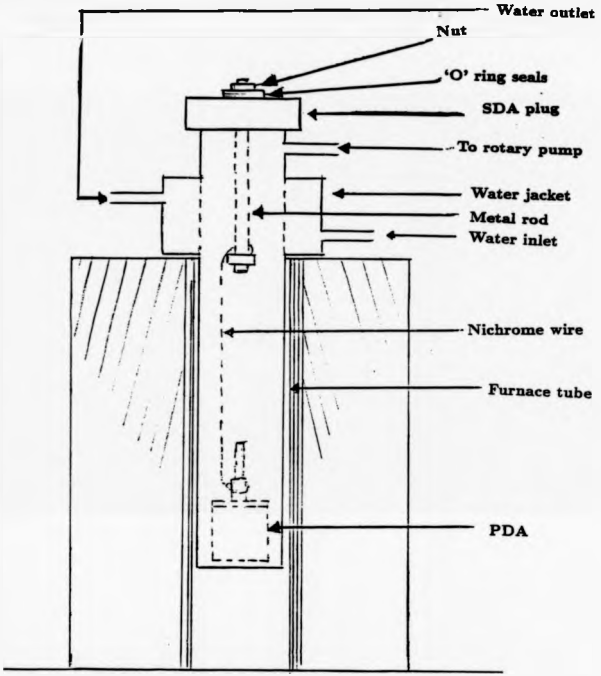

Fig 3.6 Furnace assembly during doping

temperature of the SDA (bottom region) was measured before and after each doping session.

3.3 Thermal Bleaching

Doped samples of crystals obtained using the method just described were usually coloured, except for $RbI : Yb^{2+}$. For the case of $RbCl : Yb^{2+}$ and $RbBr : Yb^{2+}$ samples, the colouration could be heavy, with crystals acquiring deep blue colour. When the optical absorption spectrum of a heavy coloured sample was measured, the F-band was usually limiting and the K– and L_1–bands tended to overlap the low energy bands of Yb^{2+} spectrum. This was particularly critical for $RbCl : Yb^{2+}$ spectrum. On the high energy side and close to the fundamental absorption edge of the spectrum of the crystals and particularly for $RbCl : Yb^{2+}$ system, the Yb^{2+}–bands tended also to overlap with colour centre bands.

For the spectra of samarium–doped crystals, a different kind of problem was encountered. The low energy bands of Sm^{2+} were completely enveloped by the F- and K- bands of the F-centre spectrum. In many cases, promenient bands due to F–centre aggregates appear on the long wavelength side of the F–band. To amiliorate these problems, thermal bleaching technique was incorporated into the standard procedures for handling the crystals.

A freshly doped crystal was first cleaned and cleaved into two portions. One half was then placed in a molybdenium boat in a PDA, the latter being securely screwed up and evacuated. The PDA was then lowered into the SDA, preheated to a constant doping temperature. After a duration ranging from 1 to 2 hours, (the longer duration being for $RbCl : Yb^{2+}$ and $RbBr : Yb^{2+}$ systems) the sample was quenched as indicated above.

After thermal bleaching, $RbBr : Yb^{2+}$ samples would be colourless while those of $RbCl : Yb^{2+}$ crystals would be less heavily coloured. The Sm^{2+} doped crystals assume violet to light brown colouration. The most important result however was that except for $RbCl : Yb^{2+}$ samples, the colour centre–bands in the visible and near UV regions would disappear. For samarium doped samples, the low-energy bands of Sm^{2+} ions would be completely exposed, whereas for $RbCl : Yb^{2+}$, the

L_1–band would completely disappear and the F- and K-bands together with other colour centre bands would be highly reduced in intensity. Fortituously their peak positions become well separated from the Yb^{2+} bands. No difference was found between the spectral positions of well-defined impurity bands before and after thermal bleaching. Previously overlapped bands became well-defined and could be identified unambiguously.

3.4 Optical absorption measurements

3.4.1 Introduction

Optical absorption spectra of all the systems studied were recorded using the Varian DMS-90 UV-Visible spectrophotometer, with wavelength range 190 *nm* to 900 *nm*. Whenever possible, second derivative absorption spectra were also measured. At high and liquid nitrogen temperatures (LNT) a variable temperature optical cell was used. In the next subsection, the design features of the latter will be discussed.

3.4.2 Design features of the variable temperature optical cell

The optical cell consists mainly of the body, the specimen holder and the cell jacket. Fig 3.7 shows the body and the sample holder. The body is a cylindrical tube open at the top end and made of stainless steel. Near its top is a moveable brass plug which fits into the outwardly extending lip of the cell jacket (vide, Fig 3.9) and prevented from making contact with it by means of 'O' ring. Three thermocouples pass through the plug. Screwed to it also is a clipping system which prevents the cylindrical body from slipping down under gravity or reduced pressure, when the cell is being evacuated, and by means of which the vertical position of the sample holder can be raised or lowered. The clipping system consists of a short brass cylinder with an overlapping flap on its top on which the C-shaped brass clip stand. Separating the brass cylinder and the plug is a rubber 'O' ring.

The sample holder is cut from a solid cylinder of Immaculate V stainless steel. Its top part has four grooves while the lower part is cut into a slotted half-cylinder to which three E-shaped knife-edges are screwed (one on either side of the slot and

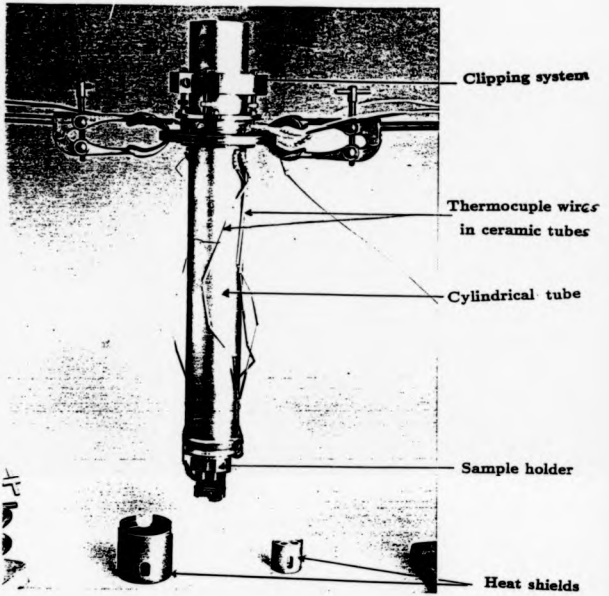

Fig 3.7 Variable temperature optical cell (body and sample holder).

one on the top section). At the bottom section is screwed an down-turned E-shaped stand on which the sample could be made to stand. The knife edges are used to adjust the size of the beam slot, so that samples of various sizes could be used for measurement. A gravity holder, suspended from the top end of the half-cylinder holds the sample in place, without obstructing the path of the beam of radiation. With this set up, the sample has the minimum possible constraint so that it can expand and contract without being damaged. Fig 3.8 shows an enlarged photograph of the sample holder. The stainless steel rails serve as a guide for the slotted copper heat shield (vide Fig 3.7) while the copper rods which actually make contact with the main body of the cell, conducts heat into it and away from the heat shield. Another heat shield made from a short cylinder of stainless steel tube is slotted and covers most of the sample holder as well as the copper shield when it is screwed to the top of the holder. Two of the slots are for thermocouple access while two are the beam slots (vide, Fig 3.7). Two thermocouples were arranged so that their junctions make contact with the crystal, while the third, which is connected to the top region of the sample holder serves as a sensor for the temperature controller. The junction of the bottom thermocouple is separated from the metal frame of the sample holder by means of thin mica sheets and ceramic washers.

The cell jacket (vide Fig 3.9) consists of a cylindrical tube of brass joined to a hollow rectangular box, also made of brass. On opposite faces of the box are two quartz (spectrosil) windows through which radiation beam passes. On another face is welded a tube which serves as a pumping access. Four water channels bored into the base of cell jacket and connected to a copper coil form an integral part of the water cooling system. On the upper part of the cell jacket is a brass tube with a valve and is an inlet for dry nitrogen. A set of two brass plates to which the cell jacket can easily be screwed onto serves as base adapter for the spectrophotometer.

3.4.3 Recording the spectra

Optical absorption spectrum of any sample was measured within two hours of quenching from high temperatures after thermal bleaching. This measure was considered necessary because after 24 hours, the low energy spectral bands tended to

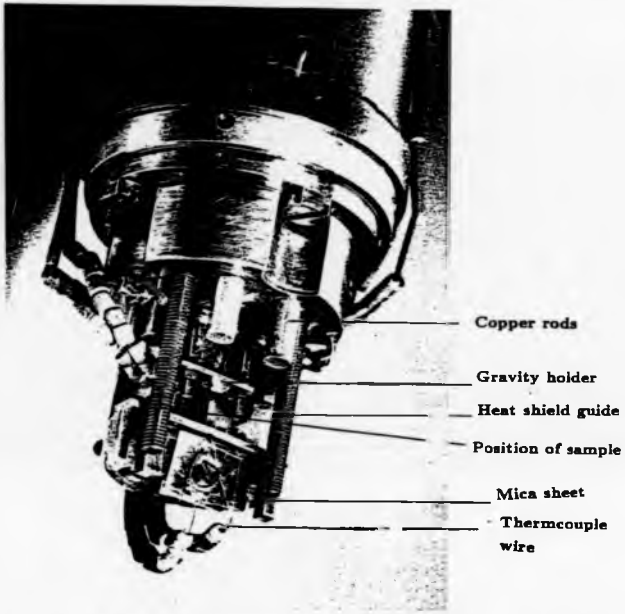

Fig 3.8 Sample holder of optical cell.

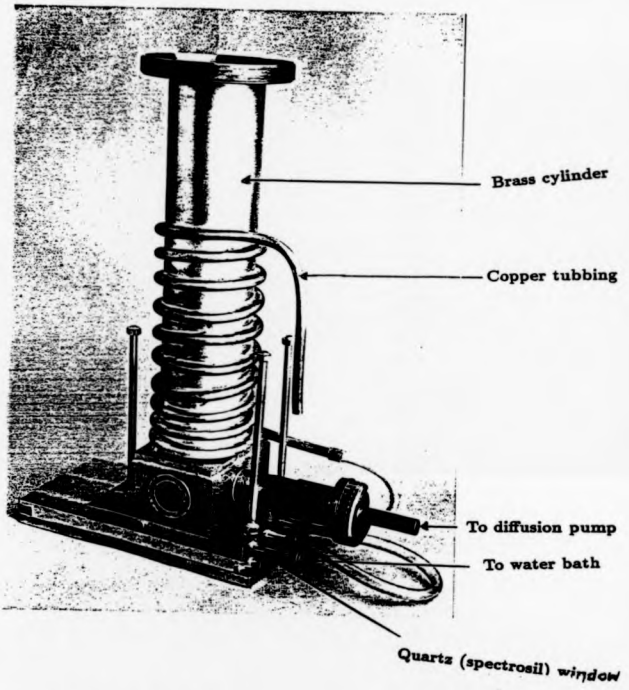

Fig 3.9 Cell jacket of variable temperature optical cell.

shift to lower energies. No such shifts were observed within the first ten hours of quenching of samples.

In order to record the spectrum of a doped sample at room or liquid nitrogen temperatures, the variable temperature optical cell was set up as shown in Fig 3.10, except that the heating coil was replaced by liquid nitrogen. Also, the mica sheet was removed. In all cases, the cell jacket was evacuated by means of diffusion pump. It was necessary to pass water at room temperature round the water cooling system to prevent moisture from condensing onto the quartz spectrosil windows. Usually, room temperature spectrum was recorded before and after measurement at liquid nitrogen temperatures. This check was to ensure that the crystal had undergone no irreversible crystallographic or other forms of transformation during the period of measurement. Peak positions of absorption bands were read off from the corresponding second derivative spectra (where measured). In all cases it was possible to measure spectral positions to within ± 0.25 Å. This means that in the spectral range 16 129 – 20 00 cm^{-1} (620 – 500 nm) the error, μ_ν, in measured spectral position is of the order of $\pm 17\ cm^{-1}$. Whereas in the spectral range 22 222 – 33 333 cm^{-1} (450 – 300 nm) μ_ν is in the order of $\pm$ 40 cm^{-1}, it is about $\pm$ 83 cm^{-1} in the spectral range 33 333 – 50 00 cm^{-1} (300 – 200 nm).

For high temperature measurements, the set up was as in Fig 3.10. Mica sheets separated the heating element from the bottom of the cell tube. In order to retain most of the generated heat within the lower section of the tube, some ceramic balls were poured into it (tube) and glass fibres used to stuff it up. Electric current was supplied to heat element through a 12 V Variac stepdown transformer which was connected to a temperature controller. Before any high temperature was made, the sample cavity was flushed with dry oxygen-free nitrogen and the chamber then evacuated. Cold water was usually pumped from a bath through the water cooling system.

Because of the irregular response of the photodetector of the spectrophotometer at 350 nm at sample temperatures of about 400^0 C and above, absorption spectra of samples could not be recorded at temperatures beyond 380.0^0 C. The irregular behaviour was attributed to the emission of infra–red radiation by the sample and

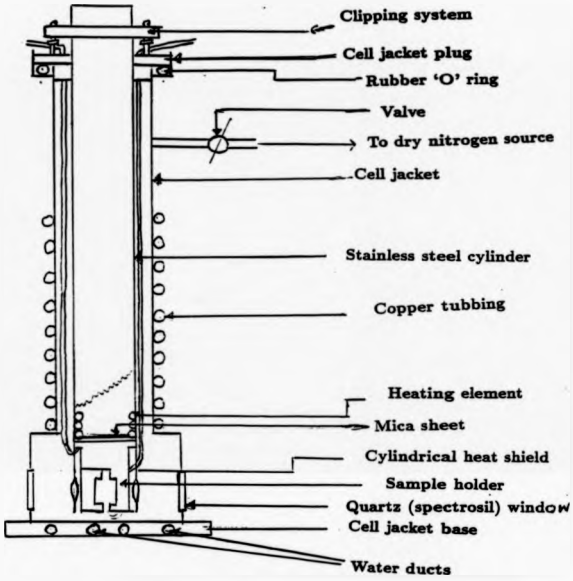

Fig 3.10 Optical cell set up for high temperature measurement.

the body frame of the sample holder. Unfortunately, optical filters which could absorb infra-red radiation and which at the same time are transparent to radiations with wavelengths in the 190–900 nm range could not be found.

Chapter 4

Divalent Ytterbium Ions in Rubidium Halide Crystals

4.1 Introduction

The ground configuration of a Yb^{2+} ion is $4f^{14}$ and is characterised by a single spherically symmetric $^1S_0$ state. When excited however, Yb^{2+} ions exhibit other configurations, the low-lying ones of which include (in increasing order of energy) $4f^{13}5d, 4f^{13}6s$ and $4f^{13}6p$. As has been shown experimentally [99], there are intercommunications among states of these configurations through electronic transitions of Yb^{2+} ions in free space on the event of these ions absorbing photon energies.

In the present study, attention is focussed on the manifestations of electric dipole transitions in Yb^{2+} ions from the ground $4f^{14}(^1S_0)$ state to states of other excited configurations. Such transitions are allowed to the states of $4f^{13}5d$ configuration both on grounds of parity and orbital quantum number selection rules ($\Delta l = \pm 1$). But $4f^{14} \leftrightarrow 4f^{13}6s$ transitions are not allowed on the grounds of the second section rule. Also forbidden but on account of parity selection rule are $4f^{14} \leftrightarrow 4f^{13}6p$ electric dipole transitions. In crystalline environment, therefore $4f^{14}(^1S_0) \leftrightarrow 4f^{13}(6s+6p)$ transitions are unlikely to be strongly manifested through measurements of absorption and/or emission spectrum of Yb^{2+} ions. Nevertheless Bland [6] has suggested that the influence of the ligand ions on Yb^{2+} ions in crystals could lead to some form of transition involving states formed by the interaction of

states of $4f^{13}6s$ configuration with the states of the ligand ions.

Most of the experimentally observed energy bands in the absorption spectra of Yb^{2+} ions in crystals of $RbX, (X = Cl, Br, I)$ are therefore ascribed to parity allowed $4f^{14}(^1S_0) \leftrightarrow 4f^{13}5d$ electronic transitions. In this chapter will be discussed the results of the calculations of the energy level structure of $4f^{13}5d$ configuration of Yb^{2+} ions in octahedral environment and its correspondence or otherwise with the experimentally observed energy levels of Yb^{2+} ions in RbX crystals.

A particularly important point to note is that the site symmetry of these ions in RbX crystals is orthorhombic (point symmetry C_{2v}), since the cubic site occupied by the ion is distorted by the formation of Yb^{2+}– cation vacancy complex, with the vacancy in the < 110 > direction. But as a first order approximation, an octahedral symmetry is assumed in this study. Later in this chapter the adequacy of this approximation shall be examined in the light of experimental data.

As has earlier been noted, this part of the project is an extension of the experimental and theoretical investigation of the energy level structure of Yb^{2+} ions in alkali halides started by Bland and Smith [101]. The theoretical calculations of the energy levels of Yb^{2+} ions in RbX crystals is reported for the first time. Also reported for the first time are the absoprtion spectra of $RbBr : Yb^{2+}$ and $RbI : Yb^{2+}$ systems. That of $RbCl : Yb^{2+}$ crystals has been recorded before [257] but never published.

4.2 Matrix elements of perturbation operators

4.2.1 States of the $4f^{13}5d$ configuration

The predominant interactions that perturb the states of the $4f^{13}5d$ states of Yb^{2+} ions in crystals are Coulomb and exchange, spin-orbit and crystal field interactions. The relative magnitudes of these interactions determine the type of vector coupling scheme by which wavefunctions of the the system can be characterised. For the case at hand, the most appropriate scheme is the J_1j coupling scheme. Accordingly, in free space, the $4f^{13}5d$ configuration of Yb^{2+} ions (which is equivalent to a hole in the $4f$ subshell and a single $5d$ electron and consequently can be regarded as

a two electron system) is characterised by four free-ion energy terms of the form $[^2F_{J_1}5d_{J'}]_J$ where $J_1 = \frac{5}{2}, \frac{3}{2}$, $J' = \frac{5}{2}, \frac{3}{2}$ and J could take integral values from 0 to 6. In all, 20 free–ion energy levels result.

In octahedral crystal field, however, these 20 energy levels are split into 58 crystal field energy levels, which can be associated with functions which transform as the irreducible representations Γ_i (i =1,...,5) of O_h point group. Of these, 6 transform a Γ_1, 5 as Γ_2, 12 as Γ_3, 18 as Γ_4 and 17 as Γ_5. Functions describing the states associated with these levels are of odd parity and each of the irreducible representations Γ_i should have a subscript u. The crystal field energy matrix of order 58 therefore decomposes into five submatrices each of which can be separately diagonalised.

However, it is not actually necessary to diagonalise all five submatrices since electric dipole approximation only allows electronic transitions between the ground state $^1S_0(\Gamma_{1g})$ to the $18\Gamma_{4u}$ states of $4f^{13}5d$ configuration. This is a consequence of the fact that the electric dipole operator $\mathbf{D}$ transforms as the irreducible representation Γ_{4u} of O_h point group. For $\mathbf{D}$ to connect the ground state and a state transforming as Γ_{iu} (i=1,2,...,5) of O_h, the product $\Gamma_{4u} \times \Gamma_{iu}$ must contain the identity representation Γ_{1g} at least once. From Table 4.1 it is clear that only states transforming as Γ_{4u} irreducible representation of O_h point group satisfy this requirement. Therefore electric dipole transitions from the $^1S_0(\Gamma_{1g})$ ground state are allowed only to the $18\Gamma_{4u}$ states of $4f^{13}5d$ configuration of Yb^{2+} ions in octahedral environment.

It is instructive to find out the distribution of these $18\Gamma_{4u}$ states among the four energy terms. One method of doing this is first to obtain the Kronecker product of the form

$$D^{(J_1)} \times D^{(J')} = \sum_{J=|J_1-J'|}^{J_1+J'} D^{(J)} \qquad (4.1)$$

and to use Table 3 in reference [318] to obtain the decomposition of $D^{(J)}$, the irreducible representations of the rotation-inversion group $O(3)$ into the irreducible representations Γ_i of O_h point group. From that table, it can be seen that Γ_{4u} states are not present in the decomposition of $D^{(0)}$ and $D^{(2)}$. Accordingly, in all calculations involving $Yb^{2+}(4f^{13}5d)$ states in octahedral crystal field, states characterised by $J = 0$ and 2 were left out.

Table 4.1 Reduction of the Direct Product of $\Gamma_i \times \Gamma_j$ $(i, j = 1, 2, 3, 4)$ of Irreducible Representation of O Point Symmetry Group into the Irreducible representation of the same Point Group **

Γ_i / Γ_j	Γ_1	Γ_2	Γ_3	Γ_4	Γ_5
Γ_1	Γ_1	Γ_2	Γ_3	Γ_4	Γ_5
Γ_2		Γ_1	Γ_3	Γ_5	Γ_4
Γ_3			$\Gamma_1+\Gamma_2+\Gamma_3$	$\Gamma_4+\Gamma_5$	$\Gamma_4 + \Gamma_5$
Γ_4				$\Gamma_1 + \Gamma_3 + \Gamma_4 + \Gamma_5$	$\Gamma_2 + \Gamma_3 + \Gamma_4 + \Gamma_5$
Γ_5					$\Gamma_1 + \Gamma_3 + \Gamma_4 + \Gamma_5$

** Only the upper half of the table is shown since $\Gamma_i \times \Gamma_j = \Gamma_j \times \Gamma_i$. For O_h point group, a subscript g or u is attached to the irreducible representation depending on whether Γ_i and Γ_j transform as even or odd parity functions according to the following rules:

$$g \times g = g$$

$$g \times u = u$$

$$u \times u = g$$

(After Schläfer and Gliemann [204])

The above considerations give rise to the following sets of crystal wavefunctions.

$$
\begin{aligned}
&|^2F_{\frac{5}{2}}, \tfrac{1}{2}d_{\frac{5}{2}}, JM^{\alpha_2}\Gamma_4\gamma\rangle \quad , J = 6,5,4,3,1 \\
&|^2F_{\frac{5}{2}}, \tfrac{1}{2}d_{\frac{5}{2}}, JM^{\alpha_2}\Gamma_4\gamma\rangle \quad , J = 5,4,3,1 \\
&|^2F_{\frac{5}{2}}, \tfrac{1}{2}d_{\frac{5}{2}}, JM^{\alpha_2}\Gamma_4\gamma\rangle \quad , J = 5,4,3 \\
&|^2F_{\frac{5}{2}}, \tfrac{1}{2}d_{\frac{5}{2}}, JM^{\alpha_2}\Gamma_4\gamma\rangle \quad , J = 4,3,1
\end{aligned}
\qquad (4.2)
$$

These wavefunctions are of the type described by Eqn 2.8. The u subscript on Γ_4 has been dropped since it shall be understood that the states are of odd parity.

4.2.2 Matrix elements of electrostatic Hamiltonian $H_{es}(f,d)$

The relevant electrostatic interaction to be considered in the case of $Yb^{2+}(4f^{13}5d)$ system are those between the $4f^{13}$–core states and the states of $5d$ electron. Matrix elements of $H_{es}(f,d)$ are therefore to be taken between the states described by Eqn (4.2). To do this, the angular parts, f_k^l $(k = 0,2,4)$, of the matrix elements, of the direct Coulomb interaction operators were calculated first in LS coupled basis using procedures outlined in reference [2,170]. In this connection, it was possible to write down the ten terms of the $4f^{13}5d$ configuration as $^{13}PDFGH$. However, note has to be taken of the fact that the configuration can be likened to a system of two non-equivalent electron complimentary to the fd configuration. Because of this, the procedures referenced cannot be used to calculate the g_k^l's, the angular parts of the matrix elements of the exchange interaction operators.

For configurations of almost filled subshells, such as $4f^{13}5d$, the non–vanishing g_k^l's are those for which $k = L$, that is, for singlet states of the configurations. In general, the g_k^l's are given by [192].

$$
\begin{aligned}
g_k^l &= 0\ldots, S = 1 \text{ or } k \neq L \\
g_{k(=L)}^l &= \frac{2(2l+1)(2l'+1)}{2L}\begin{pmatrix} l & l' & L \\ 0 & 0 & 0 \end{pmatrix}^2, S = 0
\end{aligned}
\qquad (4.3)
$$

The calculated term energies , which are expressed in terms of F_k and G_k integrals are:

$$
\begin{aligned}
E[^3H] &= -F_0 - 10F_2 - 3F_4 \\
E[^1H] &= -F_0 - 10F_2 - 3F_4 + 420G_5 \\
E[^3G] &= -F_0 + 15F_2 + 22F_4 \\
E[^1G] &= -F_0 + 15F_2 + 22F_4 \\
E[^3F] &= -F_0 + 11F_2 - 66F_4 \\
E[^1F] &= -F_0 + 11F_2 - 66F_4 + 120G_3 \\
E[^3D] &= -F_0 - 6F_2 + 99F_4 \\
E[^1D] &= -F_0 - 6F_2 + 99F_4 \\
E[^3P] &= -F_0 - 24F_2 - 66F_4 \\
E[^1P] &= -F_0 - 24F_2 - 66F_4 + 70G_1
\end{aligned}
\qquad (4.4)
$$

With the converted integrals being given as F_k and G_k, their coefficients in the above eqnations are designated as f^k and g^k respectively. The values of f^k obtained here differ from those for normal fd configuration by a multiplicative factor -1. These results agree with those obtained by Condon and Shortley [30] by an entirely different method, and to those of Bland [6]. The 3-j and 6-j symbols used in the calculation were obtained from the book by Rotenberg and his colleagues [179], while the D_k's were obtained from Condon and Shortley's book [30].

Transformation of the matrix elements above into those of $H_{so}(f,d)$ in J_1j coupling scheme was achieved through the use of the recoupling relations given by Judd [170]. The values of 9-j symbols used in the computations were obtained from Arima et. al. [184]. As a check, the results of the calculations were compared with the tables of matrix elements for d^9f or $f^{13}d$ configuration obtained by Shortley and Fried [191] by a completely different procedure. The two results are identical.

4.2.3 Matrix elements of spin–orbit operators $H_{so}(f)$ and $H_{so}(d)$

The wavefunctions (4.2) and the methods described in reference [170] were used to calculate the matrix elements of $H_{so}(f)$ and $H_{so}(d)$. Since the $4f^{13}5d$ configuration is complementary to the fd configuration, the substitution $|\psi_1 J_1\rangle = |\bar{a}lj_1\rangle$ was made

so that the results were reduced to

$$\begin{aligned}\langle sl j_1, s'l' j', J_2 M_2^{\alpha_2}\Gamma_2 \gamma \mid H_{ee}(l) + H_{ee}(l') \mid sl j_2, s'l' j'', J_4 M_4^{\alpha_4}\Gamma_4\ \gamma'\rangle \\ = \delta(\Gamma_2,\Gamma_4)\delta(\alpha_2,\alpha_4)\delta(\gamma_2\gamma'')\delta(J_2,J_4)\delta(M_2,M_4)\delta(j_1,j_2)\delta(j',j'') \\ \times \frac{1}{2}\zeta_{4f}[l(l+1) + \frac{3}{4} - j_1(j_1+1)] + \frac{1}{2}\zeta_{5d}[j'(j'+1) - \frac{3}{4} - l'(l'+1)] \quad (4.5)\end{aligned}$$

Note that for the above results are similar to those of the normal fd configuration except that the spin–orbit splitting of the states of f subshell is inverted with respect to that of that configuration [2]. Since H_{ee} is not only diagonal in J and M but also in J_1 and j', only four distinct term energies result. For $4f^{13}5d$ configuration, therefore

$$\begin{aligned}E[^2F_{\frac{7}{2}}, 5d_{\frac{5}{2}}] &= -\frac{3}{2}\zeta_{4f} + \zeta_{5d} \\ E[^2F_{\frac{7}{2}}, 5d_{\frac{3}{2}}] &= -\frac{3}{2}\zeta_{4f} - \frac{3}{2}\zeta_{5d} \\ E[^2F_{\frac{5}{2}}, 5d_{\frac{5}{2}}] &= 2\zeta_{4f} + \zeta_{5d} \\ E[^2F_{\frac{5}{2}}, 5d_{\frac{3}{2}}] &= 2\zeta_{4f} - \frac{3}{2}\zeta_{5d} \quad (4.6)\end{aligned}$$

4.2.4 Matrix elements of crystal field interaction Hamiltonians $H_{cr}(d)$ and $H_{cr}(f)$

The matrix elements of $H_{cr}(d)$ between the basis functions of Eqn (4.2) were calculated as indicated in subsection 2.2.3. They were expressed in terms of Dq and tabulated as DQ matrix. $H_{cr}(f)$ interactions matrices BO4 and BO6 matrices, whose elements were expressed respectively in terms of fourth order B_4^0 and sixth order B_6^0 crystal field parameters. The generalised CG coefficients $(k\Gamma_1, J_2^{\alpha_2}\Gamma_4 \mid J_2^{\alpha_2}\Gamma_4)$ involved in the calculation were obtained from the article by Eremin [228].

Quite remarkably, the results of the above calculations are identical to those obtained by Bland [6] who used an entirely different expression in his computations. On checking the matrices using the procedures adopted by Eremin [228] and Bland [6], a very satisfactory agreement with these earlier works was obtained. For example, on diagonaliaing the DQ matrix, with Dq set to 1, the values obtained were 6 and -4. For BO4 matrix and with $B_4^0 = 1$, the eigenvalues were 1.454545, -0.484848 and -2.909090 while for BO6 matrix, and also with B_6^0 set to 1, the diagonalisation

process gave 8.951045, 3.729603 and -6.713284. These results provided a further evidence of the effectiveness of the computer programs used for the evaluation process.

4.3 Theoretical energy levels of Yb^{2+} ions in octahedral and cubic crystal fields

4.3.1 Introduction

The procedures by which the theoretical energy levels and wavefunctions of the system were obtained have been outlined in Chapter Two. What remains to be done is a description of the various features of the theorectical energy level structure. In this section, such a task is undertaken. Before doing that, however, it is found necessary to indicate how the relative transition intensities were calculated.

4.3.2 Transition intensities

Considerations of the nature of wave functions of an atomic system and the external perturbations applied to it give rise to the selection rules for electronic transitions [98,186,206]. Since the ground state is expressed in LS–coupled functions, it is advisable also to describe the states of the excited configuration in similar basis set. Under the electric dipole approximation, the parity selection rule as well as the $\Delta J = 0, \pm 1$, (in which trasitions from $J = 0$ to $J = 0$ is forbidden), $\Delta M = 0, \pm 1$, $\Delta l = \pm 1$, and the $\Delta S = 0$ selection rules predict that electronic transitions take place only to the $^1P_1$ state of the $4f^{13}5d$ configuration from the $4f^{14}(^1S_0)$ ground state. However, by turning on the spin-orbit interaction operator, states with the same J–values are mixed. Such a mixing results in more than one energy level having appreciable transition intensity. For Yb^{2+} ions in free space, there are three such states, namely: $^1P_1$, $^3P_1$, and $^3D_1$. Under such a circumstance the energy levels corresponding to, say, $^3P_1$ is no longer a pure state. Rather it has a function of the character $^1P_1$ admixed into it. The strength of the transition depends strongly on the coefficient of the admixed function $^1P_1$. If κ_i is the coefficient in front of wavefunction $^1P_1$ in the i^{th} state of the system, the probability of transition to that state, represented by the transition intensity is proportional to κ_i^2.

The above exposition merely illustrates the principle. However, since it is more appropriate to describe the states of $4f^{13}5d$ configuration of Yb^{2+} ions in J_1j–coupled basis functions, a slightly different procedure was adopted. This consists in transforming the $^1P_1$ wavefunction into J_1j-coupled wavefunctions, through Eqn (2.58). The result which corresponds to that in reference 6 is

$$|^1P\rangle = \sqrt{\frac{4}{7}}|^2F_{\frac{7}{2}}, \frac{1}{2}d_{\frac{3}{2}}, 1\rangle + \sqrt{\frac{1}{35}}|^2F_{\frac{5}{2}}, \frac{1}{2}d_{\frac{3}{2}}, 1\rangle + \sqrt{\frac{2}{5}}|^2F_{\frac{5}{2}}, \frac{1}{2}d_{\frac{5}{2}}, 1\rangle \qquad (4.7)$$

It is convenient to redefine $|^1P>$ thus

$$|^1P\rangle = \alpha\,|\,a\rangle + \beta\,|\,b\rangle + \gamma\,|\,c\rangle \qquad (4.8)$$

where $|\,a\rangle$, $|\,b\rangle$ and $|\,c\rangle$ are respectively the J_1j– coupled basis functions of Eqn (4.7) and α, β and γ are corresponding coefficients. To obtain the appropriate transition intensity, it has to be noted that crystal field interaction produces an additional admixing of the states. This results in a considerable redistribution of intensities. Thus the wavefunction of each energy level has to be 'searched' to identify the amount of the $|\,a\rangle$, $|\,b\rangle$ and $|\,c\rangle$ functions admixed to it. The coefficients κ_i in front of each admixed wavefunction is multiplied by the appropriate coefficients α, β or γ, then squared before being multiplied by $(50)^2$. The results are then summed to obtain the relative transition intensity corresponding to the i^{th} state of the system. These relative transition intensities are to be compared with those obtained from actual experiments. Similar procedures are widely used in literature [6,86,228,101].

4.3.3 Main features of theoretical energy spectrum

As has been pointed out, the elements of the various energy matrices were expressed in terms of adjustable parameters F_k $(k = 0, 2, 4)$, G_k $(k = 1, 3, 5)$, ζ_{4f}, ζ_{5d}, Dq and B_k^q $(k = 4, 6)$. F_0 was eventually left out of the calculations since it does not contribute to the structure of the energy levels of the system. Its overall effect is to raise each level by the same amount. Moreover it cannot be reliably calculated. Following Bland and Smith [101] and Bland [6] it was replaced by a quantity Δ which is a measure of the difference between the centre of the Γ_{4u} levels of the $4f^{13}5d$ configuration and the ground state, $^1S_0(\Gamma_{1g})$, of Yb^{2+} ion in octahedral crystal field. More will be said about it in a later section.

In order to calculate the energy levels, values were assigned to these parameters and the matrices summed into a composite matrix which was then diagonalised to obtain its eigenvalues (corresponding to energy levels) and eigenvectors (corresponding to eigenfunctions) of the system. To this end, the computer programs described in Chapter Two were used.

For a start, the Slater-Condon and spin-orbit parameters were assigned the free–ion values obtained by Bryant [99] and shown in Table 5.5. Values of crystal field parameters for the system under study were not known. The strategy adopted was to vary them so as to see how the energy level structure would develop. Because of the apparent connections through crystal field theory, between Dq and B_4^0 on the one hand and between B_4^0 and B_6^0 on the other, it becomes attractive to seek to connect them in one way or another, so that only one of them can be varied at a time. Bland [6] and Bland and Smith [101] owing to a survey of some published work involving both RE^{2+} and RE^{3+} ions in octahedral crystal field find it necessary to make the following approximations

$$\left(\frac{B_6^0}{B_4^0}\right)_{cubic} = -0.20 \qquad (4.9)$$

$$\left(\frac{B_6^0}{B_4^0}\right)_{oct.} = 0.075 \qquad (4.10)$$

$$B_4^0 = \pm(100 + 0.05|Dq|) \qquad (4.11)$$

where in Eqn (4.11) the plus sign applies to the octahedral case and the minus sign to the cubic case.

Using the above approximations and with the Slater-Condon and spin-orbit parameters fixed at their free-ion levels, Dq was varied over a wide range of values in order to find out how the energy levels develop. Fig 4.1 shows the behaviour of the energy levels of the Γ_{4u} symmetry specie derived from $4f^{13}5d$ configuration of Yb^{2+} ions in octahedral environment. The case of cubic environment is shown in Fig 4.2 for completeness. In both figures, the relative transition intensities corresponding to the energy levels at some selected Dq values were indicated as numbers.

It is obvious from the two figures that variations in Dq cause considerable redistribution of transition intensities among the various energy levels. In fact at very low crystal field, $Dq < 200\ cm^{-1}$, most of the lines with high transition intensities

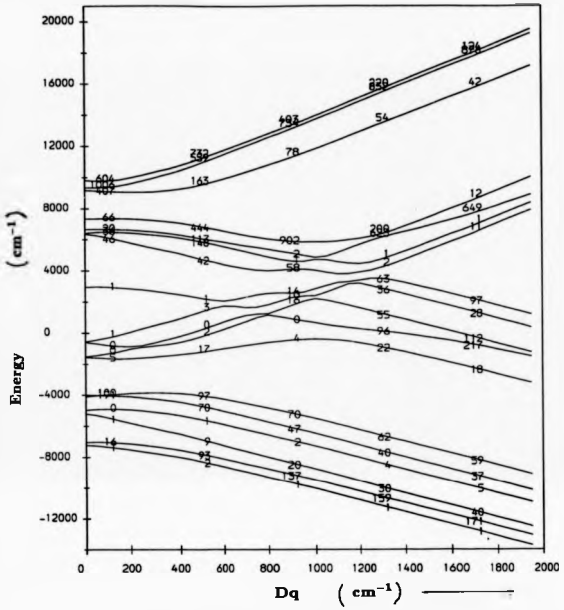

Fig 4.1 Variation of Γ_{4u} energy levels of Yb^{2+} ions with Dq in octahedral crystal field. F_2, F_4, G_1, G_3, G_5, ζ_{4f} and ζ_{5d} are set at free ion values.

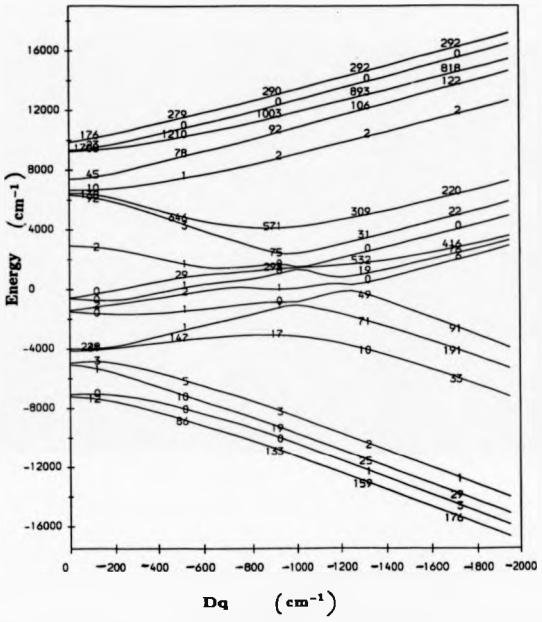

Fig 4.2 Variation of Γ_{4u} energy levels of Yb^{2+} ions with Dq in cubic crystal field. F_2, F_4, G_1, G_3, G_5, ζ_{4f} and ζ_{5d} are set at free ion values.

are located at higher energies. This is expected since two of the three energy levels (those with $J = 1$) to which electronic transitions are possible at zero crystal field are located at higher energies [99]. However at intermediate and higher crystal fields ($800 \leq Dq < 1400\ cm^{-1}$) the intensities become liberally spread throughout the entire spectrum. Interestingly at high crystal fields ($Dq > 1400\ cm^{-1}$) four groups of bands are predicted for Yb^{2+} ions in octahedral or cubic environments.

Bland [6] has studied the effect of the variation of the other adjustable parameters on the energy level structure of the $4f^{13}5d$ configuration of Yb^{2+} ions in octahedral crystal field. The conclusion arrived at was that variations of B_4^0 and B_6^0 do not affect the energy levels considerably but cause an appreciable redistribution of transition intensities. He also finds that reduction by various amounts of F_k and G_k (done independently at fixed values of Dq) results in slight variations in the energy level structure but appreciable intensity redistribution among the energy levels of the system. However, it was decided to study the effect of these parameters on the energy level structure by adopting a different approach.

The procedure consists of assuming a hypothetical situation where only the crystal field interaction was made to bear on the states of the Yb^{2+} ions, the other perturbation interactions being assumed to be effectively zero. These interactions are then 'switched' on, one after the other while Dq was allowed to vary freely. In switching on the Coulomb, exchange, and spin-orbit interactions, the free ion parameters F_k, G_k, ζ_{4f} and ζ_{5d} were used to calculate the appropriate energy levels. As will be seen later, this strategy has the advantage of offering a qualitative picture of the influence of the individual perturbations at different values of crystal field. The insight gained in such a study is particularly valuable in the process of fitting the experimental and theoretical energy levels.

Fig 4.3 shows the variation of the Γ_{4u} energy levels as Dq is varied and when F_k, G_k, ζ_{4f} and ζ_{5d} are all set to zero. The crystal field operators have been allowed to act on the f-electron states by including B_4^0 and B_6^0 through Eqns (4.9 – 4.11). There are two groups of energy levels, each consisting of three closely spaced levels. The two groups correspond to the splitting by the crystal field of the states of the 5d electron into Γ_3 and Γ_5 states, while the fine structure is provided by the

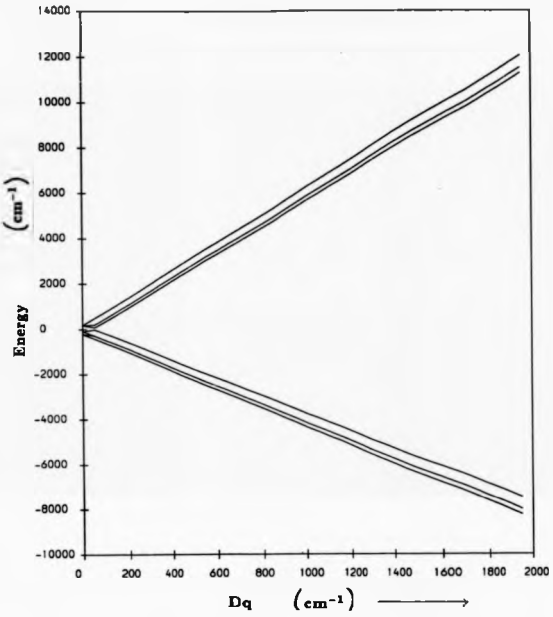

Fig 4.3 Variation of Γ_{4u} energy levels of Yb^{2+} ions with Dq in octahedral crystal field. F_2, F_4, G_1, G_3, G_5, ζ_{4f} and ζ_{5d} are all set to zero.

splitting of f–electron states into three states, Γ_2, Γ_4 and Γ_5. Considerations of the distribution of relative transition intensities (not indicated in the figures) suggest that if only crystal field interactions were acting on the system of electrons, the optical absorption spectrum of the system would consist of two strong, and possibly structured bands.

However by switching on the spin-orbit interaction within the electronic states the $4f$ subshell, one obtains Fig 4.4. Ten energy levels result and they are segregated into groups of two's and three's. Some of the levels are degenerate. It is expected that over a wide range of Dq, optical absorption measurement would yield at least four broad absorption bands (except at $Dq \approx 1100\ cm^{-1}$ about which there would be three) most of which would be structured. On adding the spin–orbit interaction energy between d–electron states, the degeneracy of some of the levels are lifted resulting in fourteen levels. The situation is more complicated as can be seen in Fig 4.5. Basically, there appears to be two MAIN groups of energy levels, each of which is connected to one of the components of the spin–orbit split f-electron states, admixed with the two d–electron states (as in Fig 4.4). The inclusion of spin–orbit interaction of d–electron states results in three subgroups (instead of the previous two) of energies within each main energy group. This strongly suggests that the lower parallel groups of levels within each main energy group depends on $H_{so}(d)$. Instead of four structured bands, there would be at least five (but maximum of six) phonon-broadened absorption bands each of which could be structured, if optical asborption measurement of the system were done. Comparison of Fig 4.1 and 4.5 clearly shows that the general underlying trend and to some extent the limits of the energy level structure of Yb^{2+} ions in octahedral environment are set principally by spin-orbit and crystal field interactions.

It appears that the contributions of the Coulomb and exchange interactions to the energy level structure is to spread the energy levels within the confines almost entirely defined by spin-orbit and crystal field interactions. Suggestions of this nature are afforded by examining Figs 4.6 and 4.7. This spreading effect which results in a general increase in the separation between energy levels within a group and a decrease in inter-groups separation energy is more powerfully demonstrated

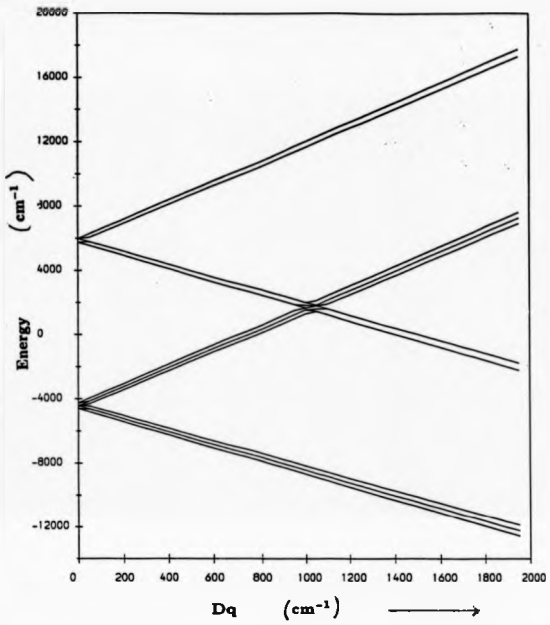

Fig 4.4 Variation of Γ_{4u} energy levels of Yb^{2+} ions with Dq in cubic crystal field. ζ_{4f} is set at free ion value with F_2, F_4, G_1, G_3, G_5 and ζ_{5d} all set to zero.

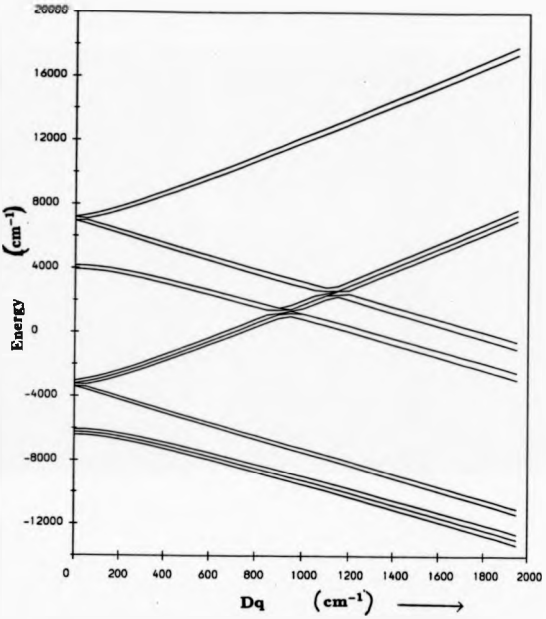

Fig 4.5 Variation of Γ_{8u} energy levels of Yb^{2+} ions with Dq in octahedral crystal field. ζ_{4f} and ζ_{5d} are set at free ion values with F_2, F_4, G_1, G_3, and G_5 all set to zero.

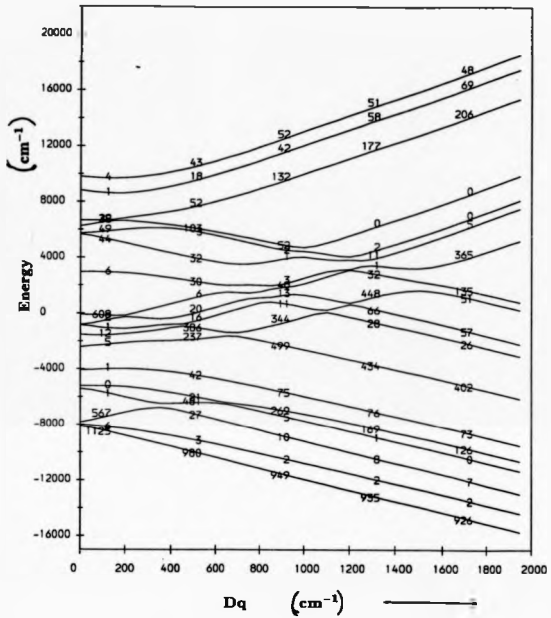

Fig 4.6 Variation of Γ_{4u} energy levels of Yb^{2+} ions with Dq in octahedral crystal field. ζ_{4f}, ζ_{5d}, F_2,and F_4 are set at free ion values with G_1, G_3, and G_5 set to zero.

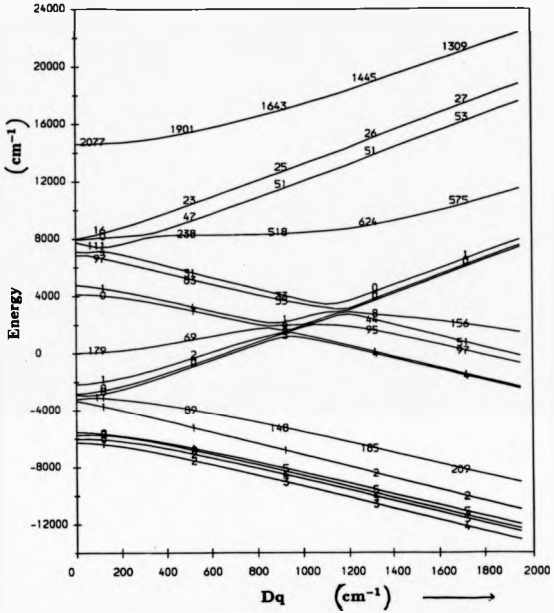

Fig 4.7 Variation of Γ_{4u} energy levels of Yb^{2+} ions with Dq in octahedral crystal field. ζ_{4f}, ζ_{5d}, G_1, G_3, and G_5 are set at free ion values with G_1, G_3, and G_5 set to zero.

in the case where exchange interaction is totally excluded (vide Fig 4.6). It is also interesting to note that the inclusion of either one or both of Coulomb and exchange interactions results in the removal of all degeneracies of the Γ_4 levels.

As will be illustrated later, the insight gained in the above study greatly simplified the grouping of the observed energy levels and the subsequent parameterisation of the systems being studied.

4.4 Optical absorption spectra of Yb^{2+} ions in rubidium halide crystals

Divalent ytterbium ions, incorporated substitutionally into cation lattice site in single crystals of rubidium halides absorb photons of characteristic frequencies which lie within the region of optical transparency of the crystals. These frequencies are host dependent. Fig 4.8 which shows the optical absorption spectra of Yb^{2+} ions in RbI crystals at room and liquid nitrogen (LNT) temperatures. Full line shows the LNT spectrum while the broken trace is the room temperature spectrum. Fig 4.9 shows the second derivative spectrum of the ions in the same host crystals. Measurement of second derivative spectra helps to locate the peak positions of absorption bands more precisely. The absorption and second derivative spectra of Yb^{2+} ions in RbCl and RbBr crystals have essentially the same structure as the corresponding spectra in Figs 4.8 and 4.9, although the spectral location of corresponding bands vary from host to host. For brevity, they are not shown here.

Following Bland and Smith [101] and Bland [6] and in correspondence with the classification of the theoretical energy levels into groups (vide Fig 4.1) the absorption bands in Fig 4.8 have been categorised into four groups, A, B C and D in order of increasing energies. Numbers are attached to each alphabetic label to identify the order of each band within a group, the numbering being from the lowest energy level in each group. For instance, A2 band corresponds to the second energy level in the lowest energy group in Fig 4.1, while A6 corresponds to the sixth (and last) energy level in that group (group A). This assignment is justified in that A2 band is the most prominent of the observed bands (in all the systems) in the low energy side of

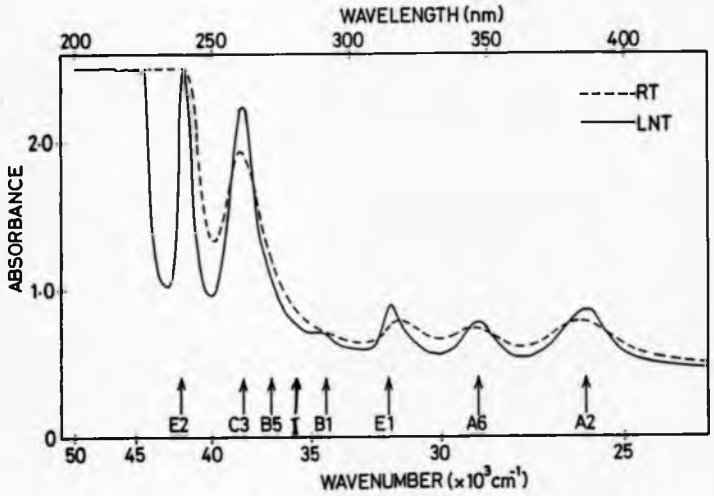

Fig 4.8 Optical absorption spectrum of Yb^{2+} ions in RbI crystals at room and liquid nitrogen temperatures.

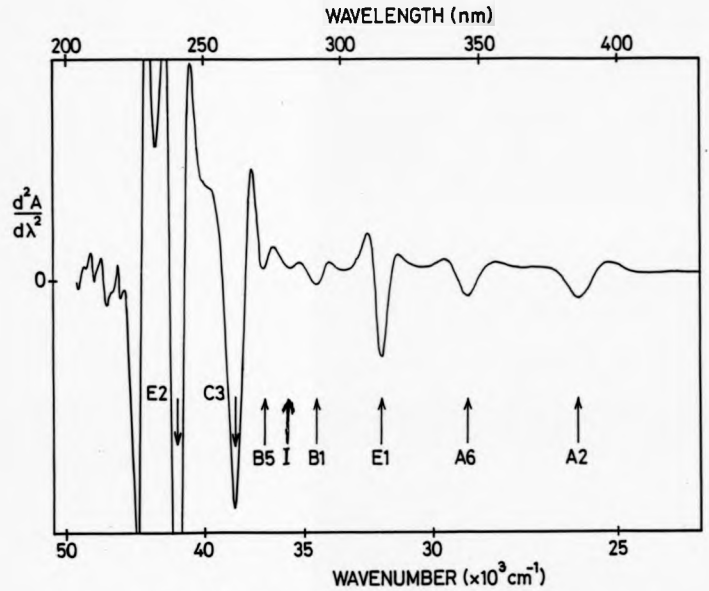

Fig 4.9 Second derivative (absorption) spectrum of Yb^{2+} ions in RbI crystals at liquid nitrogen temperature.

the spectrum while A6 is the next in intensity in both experimental and theoretical spectra.

From comparison of the optical absorption spectra of Yb^{2+} ions in these crystals certain general features clearly emerge. Each spectrum consists of a number of broad absorption bands which maintain discernable relationships with one another in terms of relative energy positions, energy separations and relative transition intensities. The A2 bands in general tend to start from about 25 000 cm^{-1} (400 nm) and could extend to about 27 778 cm^{-1} (360 nm). One interesting feature of these bands is that their peak positions tend to decrease in wave number with increase in cation–anion separation of the host material. These positions are 25 907 cm^{-1} (386 nm) for $RbI : Yb^{2+}$, 26 473 cm^{-1} (377.75 nm) for $RbBr : Yb^{2+}$ and 26 543 cm^{-1} (376.75 nm) for $RbCl : Yb^{2+}$. On the other hand, the peak positions of the strongest energy bands (in the case of $RbI : Yb^{2+}$, it is the band labelled C3 for reasons to be explained later) shift to lower energies with increasing cation-anion separation.

In all the spectra, the intensities of bands A2 and A6 relative to each other follow the same trend, with A2 always stronger in intensity than A6, while the separations between them are fairly constant. They are 2989, 2983 and 2953 cm^{-1} for $RbCl : Yb^{2+}$, $RbBr : Yb^{2+}$ and $RbI : Yb^{2+}$ crystal systems respectively. This fact suggests that A2 and A6 bands belong to the lowest group of levels since Fig 4.1 shows that for Dq values above 600 cm^{-1}, the separation of any two energy levels in the lowest group of energy levels is nearly constant as Dq increases. In general, the B bands tend to be weaker than either the A or C–bands. The latter bands are the strongest in general. In all cases, the D–bands were not observed. It is likely that these bands overlap with the conduction bands of the host crystals or are masked by the tail of the intrinsic absorption edge of the crystals.

Another interesting feature of the spectra is that at LNT all the bands become sharper and the A–bands shift to lower energies while the B–bands shift to higher energies. For the C–bands, the matter is more complicated. In the case of $RbCl : Yb^{2+}$, they shift to high energy side of the spectrum where as for $RbI : Yb^{2+}$ the C3-band shifts to the lower energy side.

It is known that most crystals contract on cooling, causing a decrease in their

lattice parameter, d. The dependence of Dq on d suggests that Dq should increase when d decreases. Fig 4.1 predicts that A-bands should shift to lower energies while C–bands to higher energies at $Dq \geq 1100\ cm^{-1}$. This suggests that Dq for $RbCl : Yb^{2+}$ will likely be in that range. Such characteristics of Fig 4.1, as well as the various features of the spectra already mentioned were used as guide in all identifications of the bands and subsequent estimates of values of Dq.

No mention has yet been made of the bands labelled E1 and E2. As for the spectra of sodium and potassium halide crystals containing Yb^{2+} ions [6], these bands are assigned to absorption by Yb^{2+} ions but their behaviour is different from those of the other bands. Like all other bands in the spectra, they become sharper on cooling the crystal but they shift to higher energies, the shifts generally being larger than those exhibited by the other bands. But the most important feature is that their relative intensities increase as in the series $Cl < Br < I$. For the E2 band, its relative intensity in $RbBr : Yb^{2+}$ is less than in $RbI : Yb^{2+}$. E2 band was not identified in $RbCl : Yb^{2+}$ spectrum, probably because it could overlap with the stronger C–bands.

4.5 Fitting of experimental and theoretical energy levels

The experimentally observed energy bands A-D were ascribed to $4f^{14}(^1S_0) \rightarrow 4f^{13}5d$ Laporte-allowed electric dipole transitions of Yb^{2+} ions in octahedral crystal field. An attempt was made to fit tthe peak energies of these bands to the theoretical levels depicted in Fig 4.1. With the aid of the observed characteristics of the bands for any one host and making reference to Fig 4.1 an initial estimate of Dq was made. To do this the separation between A6 and the strongest of the high energy bands which belong to group C energy levels was equated to 10 Dq. It was found that some considerable discrepancies existed between observed energy levels and those predicted by theory. A decision to vary the energy parameters F_k, G_k, ζ_{4f} and ζ_{5d} was made. A drawback of this strategy is that these parameters outnumber the observed energy levels. To overcome the drawback some approximations were

made. The approximations depend on the assumption that ratios such as $\frac{F_4}{F_2}$, $\frac{G_3}{G_1}$ and $\frac{\zeta_{5d}}{\zeta_{4f}}$ are quite insensitive to changes in the shape of the wavefunctions [1,3] and therefore fixed at free-ion values. Thus the approximations are $F_4 = 0.076232F_2$, $G_3 = 0.127432G_1$, $G_5 = 0.021273G_1$ and $\zeta_{5d} = 0.410481\zeta_{4f}$. By this means, the number of adjustable parameters was reduced to four, namely F_2, G_1, ζ_{4f} and Dq. Approximations such as these are widely used in atomic and crystal spectroscopy [1, 6, 101,40,260].

The study done in subsection 4.3.3 suggests that the separation between A2- and A6–bands depends on F_2, G_1 and ζ_{4f} (through ζ_{5d}) while the separation of B–bands depend mainly on F_2 and G_1. Crystal field parameter Dq and spin-orbit parameter ζ_{4f} mainly determine the separations between A– and C–bands. The procedure for fitting the experimental and theoretical levels revolves on two main steps. Firstly, the adjustable parameters were systematically varied so that the experimentally observed separations between the energy bands and the theoretically determined ones agree as closely as possible.

Secondly, the values of the parameters so determined were used as trial parameters in a computer program designed to minimise the square of the difference between experimental and theoretical energy levels. The design of the program and the computer subroutines used have already been described in Chapter Two. Results obtained for the three systems are shown in Table 4.3 .

It is with these optimised parameter values that the theoretical energy levels of the systems were calculated. They are shown in Tables 4.2(a)–(c). To calculate the (experimental) relative transition intensities, the transition intensity of A2–band was normalised to 100. Evidently, there is a very satisfactory fit between the theoretical and experimental energy levels. However some difference could be observed between the predicted and observed relative transition intenaities of some of the energy levels. In the next section, these results will be discussed.

Table 4.2(a) : Experimental and Theorectical Energy Levels and Relative Transition Intensities of Yb^{2+} Ions in RbI:Yb^{2+} Crystal Matrix. Error is the Difference Between Experimental and Theorectical Levels.

Experimental				Theorectical		
Spectral Band	Energy Level Positions E (cm -1) expt.		Relative Intensity at LNT	Energy Level Positions E (cm -1) theor.	Relative Intensity	Error δ (cm-1)
	RT	LNT				
				46 693	41	
				46 258	615	
				45 323	95	
				38 383	86	
C3	38 462	38 314	434	38 308	1105	+ 6
				38 074	21	
				37 523	69	
B5	36 697	36 765	85	36 766	5	- 1
				36 493	12	
B3	--	36 364	29	36 382	23	- 18
				35 296	6	
B1	--	34 483	24	34 487	11	- 4
A6	28 902	28 860	78	28 868	159	- 8
				28 016	41	
				27 209	0	
				26 407	38	
A2	26 042	25 907	100	25 907	173	0
				25 327	1	

Table 4.2(b) : Experimental and Theoretical Energy Levels and Relative Transition Intensities of Yb^{2+} Ions in RbBr:Yb^{2+} Crystal Matrix. Error is the Difference Between Theoretical and Experimental Levels.

Experimental				Theorectical		
Spectral Band	Energy Level Positions E (cm -1) expt.		Relative Intensity at LNT	Energy Level Positions E (cm -1) theor.	Relative Intensity	Error δ (cm-1)
	RT	LNT				
				48 773	43	
				48 421	703	
				47 335	64	
C4	40 000	40 000	292	40 005	1061	- 5
				39 721	7	
C2	39 139	39 063	141	39 262	91	-199
				38 659	2	
				38 314	29	
				38 144	6	
B3	----	37 313	25	37 331	44	- 18
B2	36 364	36 430	40	36 208	36	+222
B1	35 273	35 398	41	35 487	22	- 89
A6	29 542	29 477	54	29 485	149	- 9
				28 590	37	
				27 778	1	
				26 943	44	
A2	26 560	26 473	100	26 473	160	0
				25 848	1	

Table 4.2(c) : Experimental and Theorectical Energy Levels and Relative Transition Intensities of Yb^{2+} Ions in RbCl:Yb^{2+} Crystal Matrix. Error is the Difference Between Experimental and Theorectical Levels.

Experimental				Theorectical		
Spectral Band	Energy Level Positions E (cm -1) expt.		Relative Intensity at LNT	Energy Level Positions E (cm -1) theor.	Relative Intensity	Error δ (cm-1)
	RT	LNT				
				53 675	18	
				53 463	809	
				52 106	27	
				44 450	13	
C3	43 526	44 101	638	44 085	758	+ 16
				43 356	0	
				43 007	1	
B5	39 216	39 139	106	39 163	91	- 24
				38 456	6	
				37 385	122	
B2	36 866	36 900	81	36 933	244	- 33
B1	35 746	35 810	56	35 763	17	+ 47
A6	29 630	29 532	50	29 492	133	+ 40
				28 560	36	
				27 818	3	
				26 932	76	
A2	26 649	26 543	100	26 543	145	0
				25 830	1	

Table 4.3 Optimised Energy Parameters, $F_2(f,d)$, $G_1(f,d)$, ζ_{4f} and Dq for Yb^{2+} Ions in Rubidium Halide Crystals and Associated Nephelauxetic Ratios β. The Parameter Δ and Lattice Constant, d, are Included in Columns 6 and 10 Respectively.

Crystal	Energy Parameter (cm-1)					Nephelauxetic Ratios			Lattice Constant
Host	F2(f,d)	G1(f,d)	ζ_{4f}	Dq	Δ	β(F2)	β(G1)	$\beta(\zeta_{4f})$	d (Å)
RbI	115.3	108.6	2736.0	931	34483	0.617	0.562	0.927	3.671
RbBr	119.2	120.2	2806.1	1057	35597	0.638	0.622	0.951	3.427
RbCl	122.1	132.7	2811.2	1550	37488	0.654	0.687	0.953	3.291

4.6 Discussion

4.6.1 The $4f^{13}5d$ configuration of Yb^{2+} in $RbX : Yb^{2+}$ systems and optical absorption spectrum

All along, it has been assumed that the observed absorption bands can be ascribed to $4f^{14} \rightarrow 4f^{13}5d$ electronic transitions of Yb^{2+} ions in crystals of rubidium halides. Such an assumption stems from a definite correspondence between experimentally observed energy bands and the theoretical energy levels of the $4f^{13}5d$ configuration of Yb^{2+} ions in octahedral environment. It has also been shown that the theoretical energy levels can be classified into four groups and that the lower three of these correspond to three groups of the observed energy bands. The fourth group of bands could not be observed, possibly because the levels are either masked by the onset of intrinsic absorption edge of the crystals or located in their conduction bands.

The separation of the theoretical energy levels into four distinct groups, particularly at $Dq \geq 1400\ cm^{-1}$ has been a matter of speculation [6,86,101]. In that range of crystal field, the energy levels within the highest as well as within the lowest energy groups maintain constant separations among themselves as Dq is increased. Within that Dq regime also, and for octahedral spectrum $\frac{\partial E}{\partial D_q}$ is + 5.82 ± 0.03 for the highest group of energy levels and -3.88 ± 0.05 for the lowest group. In the cubic case, it is 3.89 ± 0.03 for the highest group and -5.87 ± 0.04 for the lowest. For a system where the crystal field interaction on the d-electron is the most dominant interaction, two energy bands are expected and the corresponding valeus of $\frac{\partial E}{\partial D_q}$ being +6 and -4 for the octahedral case and +4 and -6 for the cubic case [97, 204,210]. Similar results [6, 86, 101] have prompted the suggestion that the system behaves as if the states of the 5d–electron are strongly split by the crystal field and then coupled to the states of the f hole of the $4f^{13}$ configuration. Equivalent models have also been used to explain the broad absorption bands in the spectra of some divalent rare–earth ions in both cubic (8–fold coordinated) and octaheddral (6–fold coordinated) environments [75,76,79,81,84,88–90,104,256,261-263]. In such cases the $4f^{13}$ core states is replaced by the states of $4f^{N}$ core appropriate to the ion being discussed. For example, the two-band structure of the spectrum of diva-

lent europuim (Eu^{2+}) ions in octahedral or cubic crystal field makes the model very attractive, since that is what it predicts. The Γ_3 and Γ_5 states of the $5d$-electron are thought of as being coupled to the ^7F of the $4f^6$ core sub-configuration of the excited $Eu^{2+}(4f^6 5d)$ ion [84,85,90,259,261,262]. As has been pointed out however [80,87] the use of such a model has to be done with care since it only explains the gross features of the observed spectra.

Application of the model to the $4f^{13}5d$ configuration of Yb^{2+} ions in a high octahedral or cubic crystal field gives the same qualitative result as obtained in the theoreticall analysis provided the roles of spin–orbit interaction within the d-electron states and Coulomb and exchange interactions between the $4f^{13}$ and $5d$ electrons are included. The states of the $4f^{13}$ sub-configuration denoted by the lone term ^2F are split into two multiplets $^2F_{7/2}$ and $^2F_{5/2}$ by spin–orbit interaction while the $5d$ electron states are split by the octahedral crystal field into two levels, Γ_3 and Γ_5. However, these cryatal states are further perturbed by $H_{so}(d)$ before being coupled to the states of the $4f^{13}$ core via Coulomb and exchange interactions. These ideas are schematically illustrated by Figs 4.10 and 4.11. It is clear that in octahedral crystal field, the model predicts four groups of Γ_4 levels, the middle two of which could be close to each other. The groups are labelled A', B', C' and D', from the lowest group upwards in that order. Group theoretical considerations predict that there are six Γ_4 levels in group A', five in group B', four in C' and three in D'. Considering group A', levels, the states $^2F_{7/2}$ in crystal field decomposes into the doublets Γ_6, Γ_7 and the quartet Γ_8. Therefore the products

$$\begin{aligned}(\Gamma_6+\Gamma_7+\Gamma_8)\times\Gamma_7 &= \Gamma_1+\Gamma_2+2\Gamma_4+2\Gamma_5\\ (\Gamma_6+\Gamma_7+\Gamma_8)\times\Gamma_8 &= \Gamma_1+\Gamma_2+3\Gamma_3+4\Gamma_4+4\Gamma_5\end{aligned} \qquad (4.12)$$

give 6 Γ_4 levels. Analogous operations for groups B', C' and D' yield results indicated already. For the cubic case, the number of Γ_4 levels in groups A', B', C' and D' are 4, 3, 6 and 5 respectively. All these results agree with the grouping of the energy levels as shown in Figs 4.1 and 4.2. It is no coincidence that this model predicts six energy bands if the Coulomb and exchange interactions were switched off. This prediction is in complete agreement with the result of section 4.3.3, shown in Fig 4.5, in which all other interactions but these two were included. Their inclu-

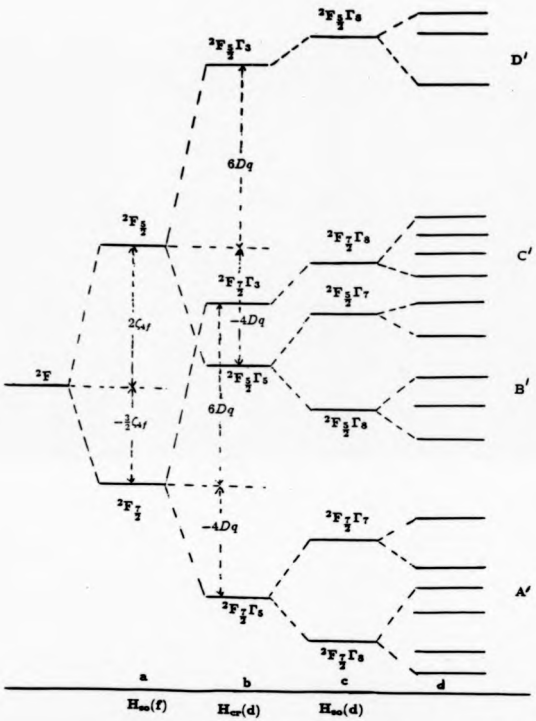

Fig 4.10 Theoretical energy level scheme for $4f^{13}5d$ configuration of Yb^{2+} ions in high octahedral crystal field. (a) $H_{so}(f)$: Spin–orbit interaction within $4f$ subshell. (b) $H_{cr}(d)$: Crystal field interaction on $5d$ states. (c) Spin–orbit interaction within $5d$ subshell. (d) $H_{ee}(f,d)$: Direct Coulomb and exchange interactions between $4f^{13}$ core electrons and the $5d$ electron. (Only Γ_{α} levels are indicated).

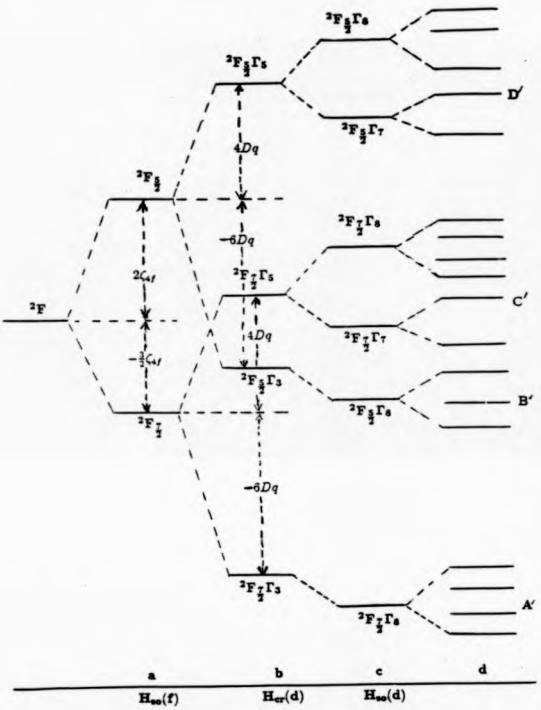

Fig 4.11 Theoretical energy level scheme for $4f^{13}5d$ configuration of Yb^{2+} ions in high cubic crystal field. (a) $H_{so}(f)$: Spin–orbit interaction within $4f$ subshell. (b) $H_{cr}(d)$: Crystal field interaction on $5d$ states. (c) Spin–orbit interaction within $5d$ subshell. (d) $H_{ee}(f,d)$: Direct Coulomb and exchange interactions between $4f^{13}$ core electrons and the $5d$ electron. (Only Γ_{8c} levels are indicated).

sion however tends to spread the energy levels and make the agreement between the model and the results of theoretical calculations complete.

This considerable effect of the operator $H_{ci}(f,d)$ on the eigensystem of the $4f^{13}5d$ configuration of Yb^{2+} ions in an octahedral crystal explains the multiplicity of experimentally observed optical absorption bands and fine structure of some of them as observed by some earlier workers [6,83,86,88,89,101].

In spite of these, a lot of care has to be exercised in applying the model to systems for which $Dq < 1400\ cm^{-1}$. Under such a circumstance, the states of the $5d$–electron can no longer be unambiguously expressed in terms of quantum numbers Γ_i, owing to the closeness of the energy levels in group B' and C', and the possibility of the admixing of the associated wavefunctions. This further justifies the use of free–ion d-electron wavefunctions in the description of the coupling of the $5d$–electrons states to the $4f^{13}$ core states in the computational process.

Nevertheless, using the model, it is easy to appreciate that the initial estimate of Dq can be made with reference to absorption bands in groups A and C or groups B and D, if the latter had been accessible. It therefore serves as a useful guide in the identification of the energy bands. Based on these ideas, the energy level scheme shown in Fig 4.12, is proposed for Yb^{2+} ions in RbX crystals. Intermediate crystal field ($800 \leq Dq \leq 1400\ cm^{-1}$) is assumed. The last three columns show the experimental energy level structure of the ions in $RbX : Yb^{2+}$ crystal systems

It has to be remarked that in the model description, perturbation of the f-states by the crystal field has not been explicitly included. Its inclusion will only alter the energy level positions very slightly [6,101]. Insight into this model (which closely agrees with an earlier scheme proposed by Johnson and Sandoe [80] but wrongly attributed to $4f^15d$ configuration in octahedral crystal field) was obtained from the theoretical analysis of Section 4.3.3.

As has already been noted, there was a satisfactory fit between the experimental and theoretical energy levels. The largest mean error of $180\ cm^{-1}$ was observed for $RbBr : Yb^{2+}$ system. However, there was some noticeable discrepancy between the observed and predicted relative transition intensities. This is particularly so for bands A6 whose observed relative intensity was less than predicted by about

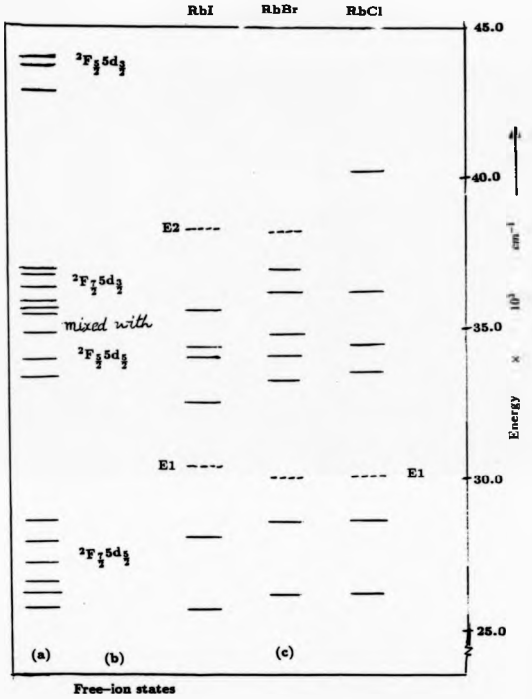

Fig 4.12 Theoretical and experimental energy level structure of Yb^{2+} ions in rubidium halide crystals. (a) Calculated energy levels in RbBr crystals. (b) Corresponding free-ion states. (c) Last three columns show the observed energy levels in the crystal hosts indicated.

a factor of 3 in two the systems studied and about a factor of 2 in one of them. This same trend has been previously observed for Yb^{2+} in sodium and potassium halides [6,101]. As noted in that study also, the experimental relative transition intensities of that band varies as in the spectro-chemical series $Cl^- < Br^- < I^-$. For some other bands, the predicted relative transition intensities were smaller than the experimental ones. However, the agreement between predicted and observed relative transition intensity is particularly good for C3 band in $RbCl : Yb^{2+}$ system.

The discrepancies between predicted and observed relative transition intensities of some bands do not constitute a big surprise since system wavefunctions may not be as accurate as would be desired because of the various approximations made. Prominent among them is the octahedral approximation in which the distortion of the site symmetry of a Yb^{2+} ion by the presence of a charge–compensating cation vacancy in < 110 > direction was ignored. As will be argued in a later section, this may result in some redistribution of transition intensities in the system.

4.6.2 Crystal field parameter Dq

It is interesting to observe that the values of Dq obtained for $RbX : Yb^{2+}$ crystal systems in this study follow the spectro-chemical series of ligand ions: $I^- < Br^- < Cl^-$, as was found by other researchers working on Eu^{2+} and Yb^{2+} ions in alkali halide crystals [85,101]. Earlier, Schäffer and Jorgenson [263] have demonstrated with numerous experimental data involving transition metal ions in molecular complexes and crystals that for a given metal ion Dq increases as in the spectrochemical series

$$I < Br < Cl < S < F < O < N < C \qquad (4.13)$$

Other workers have demonstated the same trend for transition metal complexes [264]. Incidentally, lattice parameter, d for RbX crystals follows the reverse sequence. Therefore another way of interpretting the results is to say that Dq decreases with increasing d, a trend expected on account of the point ion model of crystal field splitting.

However the value of Dq obtained from $RbCl : Yb^{2+}$ matrix was large in comparison with those obtained for $KCl : Yb^{2+}$ and $NaCl : Yb^{2+}$ crystals [6]. It is

expected that Dq for that system would be smaller than in the other alkali chlorides since d for RbCl crystal is larger than those of KCl and NaCl crystals. Reasons were sought for this apparent discrepancy.

One point that comes to mind is that RbCl crystal undergoes a structural transition from sodium chloride to cesium chloride structure at -190^0C [270]. This would mean that cation–anion separation would decrease leading to an increased crystal field interaction. Evidence of such a transition does not seem to exist for the following reasons. The observed spectrum has the features of that of Yb^{2+} ions at sites where they are coordinated with six chloride ions. In cesium chloride structure, the Yb^{2+} ions would be coordinated with eight chloride ions. In such a set up, band A6 would be absent, but more importantly the room temperature spectrum would be markedly different in structure from the spectrum at LNT. The main differences observed are the sharpening of the bands and shifts in spectral positions of the bands when the crystal goes from room to liquid nitrogen temperatures. These changes are expected and the other systems studied show the same changes (vide Section 4.4).

A more attractive point of view is that Yb^{2+} ions in substitutional sites are separated from the chloride ions by a significantly shorter distance than rubidium ions are from the anions. This is because the radius of Rb^{+} ion is 1.47 Å while that of Yb^{2+} ion is 0.93 Å [252]. On substitution therefore, the six ligand anions will have to adjust their positions to accommodate the new neighbour, resulting in a reduction of the effective cation-anion distance, R, and hence in an increase in the crystal field interaction. However, the value of R is also influenced by the presence of charge– compensating vacancy [64,273] thereby making matters more complex. An objection to the above view, is that the values of Dq for $RbBr:Yb^{2+}$ and $RbI:Yb^{2+}$ would also be very large in comparison to Yb^{2+} ions in other bromides and iodides. But it has to be remembered that the radius of chloride ion is 1.81 Å as compared with 1.95 and 2.2 Å for bromide and iodide ions respectively. Any local contraction at the site of Yb^{2+} in these crystals will definitely be much smaller than in RbCl crystals. Nevertheless, the possibility of local contraction or expansion of cation impurity-anion distance in some crystals has often been evoked by many workers to

explain observed effects related to crystal field interaction [64,75,134,274-278].

In spite of the trend shown above for Dq values obtained for Yb^{2+} in RbX crystals, there is a marked departure from the expected proportionality expected between Dq and R^{-5}, on the basis of the point-ion model of crystal field theory. A plot of Log Dq against Log d shows a big scatter around a straight line. However, it is recognised that d is not an adequate approximation to R. But no estimate has yet been made for R for Yb^{2+} ions in alkali halide crystals. Ruiz-Mejia C, and his colleagues [273,306] have calculated R for Eu^{2+} in alkali halides. They find that R is less than d by $0.167d_{RbCl}$, $0.147d_{RbBr}$ and $0.124d_{RbI}$ in $RbCl : Eu^{2+}$, $RbBr : Eu^{2+}$ and $RbI : Eu^{2+}$ systems respectively where d_{RbX} are lattices parameters of RbX crystals. (vide Table 4.3). Allowing for similar same percentage reductions, the effective Yb^{2+}–anion distances R, of 2.74, 2.932, 3.209 Å were estimated for $RbCl : Yb^{2+}$, $RbBr : Yb^{2+}$ and $RbI : Yb^{2+}$ respectively. Despite this adjustment (as shown in Fig 4.13) the large scatter was only slightly reduced. But if one assumes a reduction in Yb^{2+}-anion distance for only $RbCl : Yb^{2+}$ system to the degree indicated above while ignoring possible reductions in R for the other systems, a good fit is obtained. The straight line has a gradient of -1.80 ± 0.02 which is small in magnitude compared with the expected value of -5 on the basis of point ion model. This result however has to be viewed with extreme caution because there is no reason to believe that R and d will have the same value for $RbBr : Yb^{2+}$ and $RbI : Yb^{2+}$ systems, even though they are expected to differ very much for $RbCl : Yb^{2+}$ crystal matrix.

The deviation of experimental data from the predictions of point ion model of crystal field theory is not surprising since the inadequacy of the theory has long been recognised [279]. Numerous experimental results involving transition metal ions with nd^N open shells (n=3,4,5) indicate that covalency and the exchange forces due to the charge clouds of the central ion and those of the ligand ions make important contributions to the value of Dq [223,281–287].

In the case of rare–earth metal ions, with partially filled $4f^N$ subshells, it has been shown [4,75,288-292] that covalency (which involves transfer of some charge from the ligands to the rare earth metal ions), overlap of $4f^N$ orbitals with like-spin

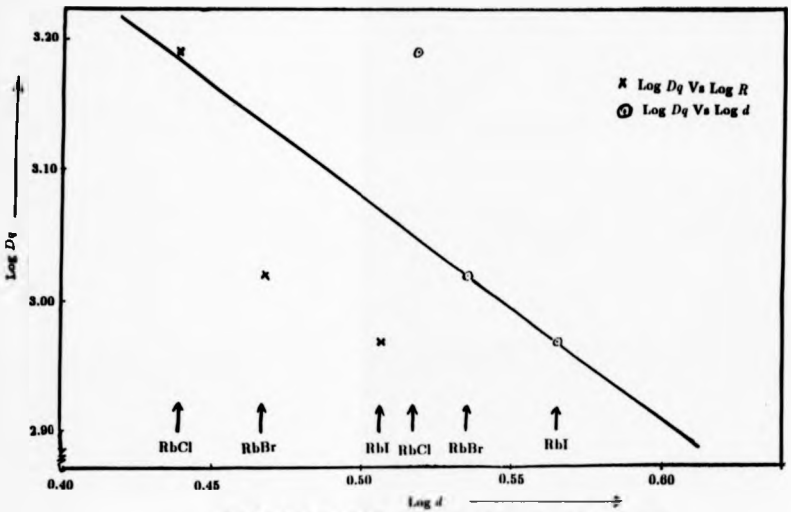

Fig 4.13 Relationship between Log Dq and Log d for Yb^{2+} ions in RbX (X = Cl, Br, I) crystals.

ligand orbitals and also of the orbitals of $5p^6 6s^2$ subshells and those of ligands, make important contributions to crystal field splitting of free ion levels of ions in crystalline environment. Such contributions are however less than observed for transition metal ions in molecular complexes or crystal matrix, owing to the extra shielding of the $4f^N$ subshell afforded by the $5p^6 6s^2$ subshells. It will be expected that the energy levels of the $4f^{13}5d$ configuration of Yb^{2+} ions in crystalline environment will be definitely affected by these factors too and hence the deviations of the measured Dq–values from the point-ion crystal field model. This deviation has also been found for Eu^{2+} and Yb^{2+} in some alkali halides [6,85,101].

The comments above, however do not invalidate the results obtained in this study. This is because as Anderson [293] and Hüfner [4] point out, even though Eqn (3.32) does not represent all the major interactions involved in crystal field splitting, the parametrisation scheme ensures that the other interactions such as covalency, overlap and electrostatic shielding are taken up into Dq, B_2^0 and B_4^0.

Another parameter determined in this work which has to do with crystal field interaction is Δ (vide Table 4.3). Using the values of Δ for the systems studied, it was found that the depression of the centre of gravity of the Γ_{4u} levels of $4f^{13}5d$ configuration as the ions go into crystals is 7 802 cm^{-1} for $RbCl : Yb^{2+}$, 9 693 cm^{-1} for $RbBr : Yb^{2+}$ and 10 807 cm^{-1} for $RbI : Yb^{2+}$. Again these quantities follow the spectro–chemical series of ligand ions

$$Cl^- < Br^- < I^-$$

Incidentally these depressions increase as lattice parameter d increases. It appears that the depressions are connected with the spectral displacements to lower energies of the A2– and A6– bands with increase in d.

Bland [6] and Bland and Smith [101] find a linear dependence of Δ on d for Yb^{2+} ions in sodium and potassium halides. No such dependence was found in this study for the same reasons that Log Dq deviates from a proportionality relationship with Log d.

4.6.3 Reduction of free-ion parameters

The values obtained for F_2, G_1 and ζ_{4f} as shown in Table 4.3 are smaller than the free–ion values obtained by Bryant [99]. Many research workers [6,82,101,259,294] who have studied the excitation of RE^{2+} ions (in crystals) involving states of $4f^N5d$ configurations have found it necessary to use F_k, G_k and ζ_{4f} values smaller than free-ion estimates. Wealkiem [259] uses electrostatic parameters 50 % of their free ion values in order to obtain a fit between theory and experiment in his study of $CaF_2 : Eu^{2+}$ system while Alig and his colleagues [82] use F_k and G_k values 60 % of their free-iron values for $SrCl_2 : Tm^{2+}$ system. Bland [6] and Bland and Smith [101] use Slater-Condon parameters, F_2 and G_1 and spin–orbit parameters ranging in value from 0.56 to 0.91 % of free–ion values for Yb^{2+} ions in sodium and potassium halides. Much less reduction in free–ion F_k and ζ_{4f} parameters have been found for some RE^{3+} ions in crystals, in which excitations involving $4f^N \leftrightarrow 4f^N$ transitions were studied [295-298].

An explanation to these results could be obtained from the conclusions drawn from many studies on optical absorption of transition metal complexes. In these works and reviews of them, it has been observed that theoretical results could only be fitted with experimental spectra if the free–iron values of Slater–integrals (F^k) or Racah parameters [B,C] were assumed to be reduced sometimes by as much as 50 % [263,264,280–285].

This reduction in electrostatic parameters of transition metal ions in molecular complexes or crystals below their free-iron values is known as nephelauxetic (cloud–expanding) effect [263]. It is assumed that since the partically filled $3d^N$ orbitals of the transition metal ions are unshielded from the surrounding ligand ions, two types of covalency are possible. One type, central–field covalency, concerns the expansion of the radial wavefunctions of the $3d^N$ electrons owing to the presence of the ligands. This leads to shifts in the charge clouds from ligand to central ion and vice-versa. As a result there is a reduction in the effective positive charge of the atomic core and hence a reduction in the oxidation number of the central ion.

The second type, symmetry–restricted covalency has to do with the delocalization of the partially filled $3d^N$ orbitals of the central ion. These orbitals interact with

those of the ligand ions, forming molecular orbitals. In this respect, only orbitals of the same symmetry type interact [283-286,299]. Both types of covalency lead to changes in the charge density of the central ion / ligand ions complex and an overall decrease in Coulomb energy of the central ion. This is reflected in smaller F_k or B and C values, than in free ion states.

Schäffer and Jorgensen [263] have defined the nephelauxetic ratio β as the ratio of a phenomenological electrostatic (inter– electronic) parameter for a central iron in a molecular complex to its free–ion value. They have developed an emperical sequence regarding the value of β for the same ion in different bonding environments. The sequence of liganda in decreasing order of β is [283]

$$\text{no ligand} > F^- > H_20 > Cl^- > Br^- > I^- > 0^{2-} \qquad (4.14)$$

This is known as the nephelauxetic series. Incidentally, the values of β calculated for each of the parameters F_2, G_1 and ζ_{4f} follow the sequence $Cl^- > Br^- > I^-$, which agrees with the series (Eqn 4.14) above.

4.6.4 Adequacy of octahedral approximation

It has been mentioned that the Yb^{2+} ions are incorporated substitutionally into the cation sublattice and that this requires cation vacancies to be associated with them on a one-to-one basis in order to balance the local charge at the vicinity of the Yb^{2+} ions. The assumption has been that for a Yb^{2+} ions at a substitutional site, the charge compensating vacancy is located at a nearest neighbour cation site. Fig 1.5 shows that there are twelve such inequivalent sites. As far as the author knows, there is no direct evidence in literature to confirm this assumption. But results of studies involving other divalent ions in crystals of sodium chloride structure tend to strengthen it. ESR involving Mn^{2+} ions in NaCl crystals [134] and of Eu^{2+} ions in a variety of alkali halide crystals [15,16,20,300–305] have shown that the most preferred mode of charge compensation is the association of the divalent impurity ion with an alkali–ion vacancy at the nearest neighbour cation site in $< 110 >$ direction. It has also been found that the emitting state of Sm^{2+} ions in many alkali halides crystals are those of substitutional Sm^{2+} ions at orthorhombic sites [64,69,140,307–309]. The site symmetry of the impurity is therefore taken to be

orthorhombic point symmetry (C_{2v}).

Corroborative as these results are to earlier dielectric loss and ionic conductivity studies of a variety of divalent ions in alkali halides which lead to the strong suggestions that the formation of divalent ion-cation vacancy is the major charge compensating mechanism [135–137,309-312], it appears reasonable to assume that the same model is applicable to Yb^{2+} ions in alkali halides. However one must not loose sight of the observation by Brown and his colleagues [276] that for RE^{3+} ions in alkali–earth fluorides, the site of the charge compensating defect (in this case F^- ion) in the crystal lattice depends on the difference between the radii of the substitutional RE^{3+} ion and the host ion. The larger this difference the more remote the location of the charge compensator would be from the RE^{3+} ion, and hence the lower the symmetry at the site of the impurity ion. Applying this to the case of Yb^{2+} ions in alkali halide crystals, one is tempted to accept the possibility that the compensating positive–ion vacancy may be far removed from the site of the Yb^{2+} ion particularly as the difference between the radii of Yb^{2+} and Rb^+ is large (0.54 Å). However the structure of the optical absorption spectra of Yb^{2+} ions in RbX crystals do not in any fundamental way differ from those of Yb^{2+} ions in sodium and potassium halide crystals [6], the host cations of which have radii that do not differ very much from that of Yb^{2+} ions. The temptation is stronger therefore to assign the same site symmetry to Yb^{2+} ions in crystals of all alkali halides studied. An orthorhombic (C_{2v}) symmetry is therefore assumed for Yb^{2+} ions in RbX crystals. The most direct way of testing this assumption would be an electron spin resonance study but incidentally, Yb^{2+} ion is diamagnetic.

Working on the above assumption, group theoretical arguments suggest that the 58 crystal field levels of $4f^{13}5d$ configurations of Yb^{2+} ion in O_h crystal field will be split into 140 levels classified into four symmetry species (Γ_{2u} , i = 1,2,3,4) each of which consists of 35 levels. The ground state $^1S_0(4f^{13})$ would transform as Γ_{1g}, the identity representation of C_{2v} point group. Electric dipole transitions are possible from the ground $^1S_0(\Gamma_{1g})$ state to each of the 35 Γ_{1u}, Γ_{3u} and Γ_{4u} states, giving a total of 105 spectral lines as can be deduced from Table 4.4. But these large numbers of spectral lines (bands) were not observed.

Table 4.4 Reduction of the Direct Product of $\Gamma_i \times \Gamma_j$ $(i, j = 1, 2, 3, 4)$ of Irreducible Representation of C_{2v} Point Symmetry Group into the Irreducible representation of the same Point Group **

Γ_i / Γ_j	Γ_1	Γ_2	Γ_3	Γ_4
Γ_1	Γ_1	Γ_2	Γ_3	Γ_4
Γ_2		Γ_1	Γ_4	Γ_3
Γ_3			Γ_1	Γ_2
Γ_4				Γ_1

** Only one half of the table is shown since $\Gamma_i \times \Gamma_j = \Gamma_j \times \Gamma_i$. Odd and even parity assignment rules indicated in Table 6.1 also apply here. In C_{2v} symmetry, the electric dipole moment transforms as Γ_{1u}, Γ_{3u} or Γ_{4u}. So electric dipole transitions from $^1S_0(\Gamma_{1g})$ groung state is possible only to Γ_{1u}, Γ_{3u} or Γ_{4u} state.

One explanation for this is that the orthorhombic distortion of the site symmetry of Yb^{2+} in the crystal do produce actual splitting of the lines but that the splittings are so small that they become obscured by the broad spectral envelope of the bands due to octahedral splittings. If this suggestion is correct, one is then surprised at the largely symmetric nature of the observed bands, particularly the low energy bands. It is expected that if the perturbation potential contribution due to the orthorhombic distortions were big enough to cause some splitting, the wave functions should have changed significantly enough to redistribute the transitive intensities among the spectral components of individual bands. Such redistribution of intensities could have produced structured bands. However, the fact that the charge compensating vacancies randomly occupy the 12 inequivalent nearest neighbour cation sites could play some part in neutralising the effect such asymmetric distribution of spectral transition intensities. Consequently what is observed is largely an octahedral optical absorption spectrum.

In view of the argument above and of the fact that there was a significantly satisfactory agreement between the theoretically predicted energy levels and experimentally observed spectra, one is convinced that to a first order, the octahedral approximation is adequate for the systems studied. This approximation has in the past been successfully used for spectra of Eu^{2+} in alkali halides [84–85] and of Yb^{2+} in sodium and potassium halides [6,101].

4.6.5 Additional Remarks

It has already been mentioned that E1- and E2- bands are associated with photon absorption by Yb^{2+} ions in the crystals. However as has been satisfactorily explained by Bland [6], these bands are not ascribed to $4f^{13}5d$ configuration. Rather, they are thought to arise from electronic transitions to molecular orbitals (MO's) formed from ($4f^{13}6s$) configuration of Yb^{2+} ions and the $(n+1)s$, ($n = 3, 4, 5$, for Cl^-, Br^-, I^- ions respectively) orbitals of halide ions, co-ordinated to the substitutional Yb^{2+} ions. In this model, the $6s$ atomic orbitals are conceived as being much more susceptible to the perturbing influence of the ligand ions than the $4f^{13}$ states which are strongly split by spin–orbit interaction. As a result, whereas the $4f^{13}$

states remain largely unperturbed by the crystalline environment, the $6s$ atomic orbitals overlap with the unoccupied $(n+1)s$ orbitals of the ligand ions in a σ–type interaction to form bonding (σ) and anti-bonding (σ^*) MO's as depicted in Fig 4.14.

As a rule, the ns^N orbitals of either the central or ligand ions in an octahedral environment transform as Γ_{1g}, the irreducible representation of the O_h point group, while the electron orbitals of np^N, and d^N subshells transform as Γ_{4u}, and $\Gamma_{3g}+\Gamma_{5g}$ respectively. The $6s(\Gamma_{1g})$ orbitals of Yb^{2+} ions are more likely to interact with the $(n+1)s(\Gamma_{1g})$ orbitals of the ligand ions since they are of the same symmetry specie and also closer together in energy terms, than the rest of the ligand orbitals. As a result, a σ– type bonding occurs. In this connection two sets of bonding MO's are expected, namely $4f^{13}(^2F_{7/2})6s\sigma(\Gamma_{1g})$ and $4f^{13}(^2F_{5/2})6s\sigma(\Gamma_{1g})$ orbitals, with the latter being located at higher energies.

It is the electronic transitions to these bonding MO's that give rise the E1– and E2– bands. Since this type of interaction is thought of as overlap or mixing of wavefunctions in such a way as to modify the character of the basic eigenstates, it is possible that the selection rules for electronic transition from the ground states of the $4f^{14}$ configuration of Yb^{2+} ions become relaxed particularly as the octahedral sites of the ions are distorted. If this is so, the degree of overlap (or mixing) of the wavefunctions will to some extent determine the strength of electronic transition to the admixed orbitals.

The above model reasonably explains the observations made in this study. Firstly electronic transitions to bonding MO's are expected to anion dependent. Implied in this statement is the suggestion that the more covalent the complex, YbX_6, the stronger will be the overall transition strength. Indeed it was found that for any of the bands, say E1-band, the transition intensity relative to A2-band in all the spectra of the systems studied varies in the accordance with the spectro–chemical series of ligand ions $Cl^- < Br^- < I^-$ This means that the electronic transitions to the more covalent complexes are much more enhanced than in the less covalent complexes. Table 4.5 shows the energy level positions of the E1– and E2– bands both at RT and LNT. E2-band was not observed in $RbCl:Yb^{2+}$ crystals. The last column gives the separation between E1 and E2 bands measured at LNT. In the

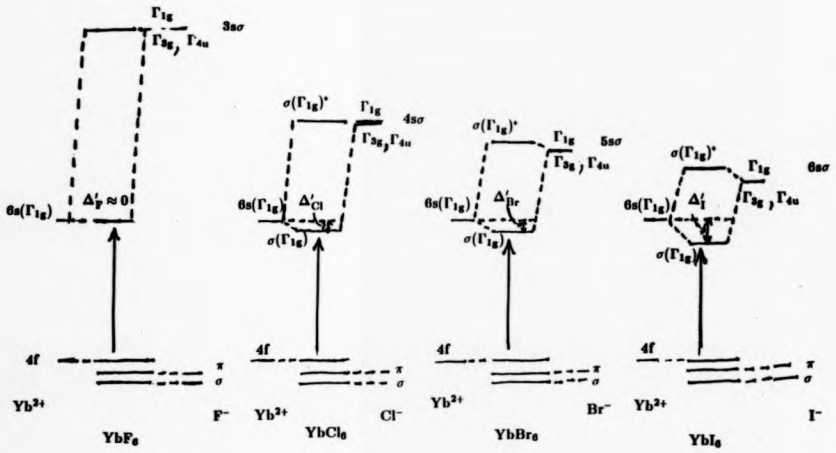

Fig 4.14 A schematic representation of the formatiom of bonding and antibonding molecular orbitals for Yb^{2+} ions octahedrally co-ordinated to various halogen ions. (after Bland [6])

Table 4.5 Spectral Positions and Relative Transition Intensities of E1- and E2-Bands in the Absorption Spectra of $RbX : Yb^{2+}$ $(X = Cl, Br, I)$ Crystals at RT and LNT. $\nabla(E1, E2)$ is the Separation between E1- and E2- bands at LNT.

Crystal Host	E- Band Spectral Position (cm^{-1}) RT	E- Band Spectral Position (cm^{-1}) LNT	E- Band Relative Intensity at LNT	E- Band Spectral Position (cm^{-1}) RT	E- Band Spectral Position (cm^{-1}) LNT	E- Band Relative Intensity at LNT	$\nabla(E1, E2)$ (cm^{-1})
RbI	31 496	31 771	100	–	41 667	493	9 896
RbBr	30 912	31 299	36	41 667	41 580	223	10 281
RbCl	31 056	31 546	28	–	–	–	—

table, the relative intensities recorded were calculated relative to the A2-band of the relevant spectra. Thus the entry against E1-band for the host crystal RbBr refers to the intensity of that band relative to A2-band of $RbBr : Yb^{2+}$ spectrum measured at LNT. This makes comparison across spectra easy.

Secondly, the calculated spectral positions of the $^2F_{7/2}s_{1/2}$ and $2F_{5/2}s_{1/2}$ energy terms of the $4f^{13}6s$ configuration of Yb^{2+} ions are comparable to the spectral positions of E1 and E2-bands. In this respect, it can noted that the J_1j–coupled states $(^2F_{7/2}s_{1/2})_{J2}$, $(J_2 = 3, 4)$ are located at 35 033 and 34 660 cm^{-1} respectively above the ground state of the $4f^{14}$ configuration while the states $(^2F_{5/2}s_{1/2})_{J2}$ $(J_2 = 2, 3,)$ are located respectively at 44 858 and 45 157 cm^{-1} [99] . When compared with spectral locations of the E-bands, one can appreciate the relation between the latter and the free ion energy levels of the $4f^{13}6s$ configuration if about 3000 cm^{-1} is substracted from free ion level positions. Such depressions in free ion levels as Yb^{2+} ions enter substitutional lattice sites are attributable to crystal field effects or effects of the co-ordinating environment. More remarkably, the separation between the gravimetric centre of the two high lying doublets and that of the low-lying states is 10 161 cm^{-1} which is comparable to the separation of the E-bands. This strengthens the assignment of the E1-band to the orbital $4f^{13}(^2F_{7/2})6s\sigma(\Gamma_{1g})$ and E-2 band to $4f^{13}(^2F_{5/2})6s\sigma(\Gamma_{1g})$ orbital.

Related to these is the anion dependence of the separation between E1 and E2 bands. As can be seen from Table 4.5, it is greater for $RbBr : Yb^{2+}$ spectrum than for $RbI : Yb^{2+}$ spectrum. However it is difficult to make the comparisons across the $RbX : Yb^{2+}$ series since that for $RbCl : Yb^{2+}$ spectrum could not be measured.

It is worth commenting on the bands labelled I in Fig 4.8 and 4.9. The band is also present in the spectrum of $RbCl : Yb^{2+}$ crystals. In the case of $RbCl : Yb^{2+}$ system, the I-band is located at 40 816 cm^{-1} (254 nm) while in the case of $RbI : Yb^{2+}$ crystals it is loacated at 35 524 cm^{-1} (281.5 nm). Whereas in the latter system, the I-band is due to an unknown impurity present in the nominally pure crystal of RbI, its real origin in the former system is not certain. To start with, in the absorption spectrum of the nominally pure crystal of RbCl, there is a broad though weak impurity band at 40 984 cm^1 (245.0 nm) at LNT. It may be misleading to

ascribe the I-band to whatever impurity is present in the nominally pure crystal for the following reasons. The I-band in the $RbCl : Yb^{2+}$ spectrum is much more intense than the 244 nm band in the nominally pure crystal of RbCl. The spectra of $RbCl : Eu^{2+}$ and $RbCl : Sm^{2+}$ at LNT were examined to find out whether absorption bands occurred at 244 nm. In the case of $RbCl : Eu^{2+}$ spectrum, the band, if present, would be completely enveloped by the broad structured high energy bond of Eu^{2+} ions in the crystal. However, what can be called a 'blip' at 245 nm was identified. Nevertheless, it is difficult to attach any serious importance to it since no absorption band was found at about 244 nm in the $RbCl : Sm^{2+}$ spectrum. It appears therefore that the 244 nm band in RbCl spectrum is due to an unstable impurity to which the I-band of $RbCl : Yb^{2+}$ may not be directed ascribed. In spite of this, the behaviour of that band under different conditions suggests that it may still be linked with the impurity causing the 244 nm band in nominally pure RbCl crystal. The intensity of the I-band relative to either the A2- or C3- bands in the $RbCl : Yb^{2+}$ spectra at RT and LNT varies from sample to sample. The relative intensity is greater in the spectra of samples that are heavily coloured than in the spectra of those that are lightly coloured. In this respect, attention has to be drawn to the fact that all attempts at obtaining $RbCl : Yb^{2+}$ crystals with acceptable level of concentration of Yb^{2+} ions resulted in crystal samples attaining deep blue colouration. The absorption spectra of such samples consist of a variety of colour centre bands in near–infra red, visible and ultra violet. By a process of thermal bleaching, most of the colour centre bands, except the F–, K– and those close to the absorption edge of the crystal were removed. The remaining colour centre bands were reduced in intensity, including the I-band. It was not possible to bleach the colour centres completely as was done for other crystal systems studied, including $RbCl : Sm^{2+}$. Because of this, it was very difficult to unequivocally establish the identity of the I-band in $RbCl : Yb^{2+}$ spectrum .

The high colourability of RbCl crystals in ytterbium atmosphere and the difficulty of thermally bleaching the colour centres in $RbCl : Yb^{2+}$ crystals suggests the possibility of a reaction between some of the Yb^{1+} ions and the unknown unintentional impurity Another possibility is an association between the Yb^{2+} ions and the

unknown impurity in RbCl crystals. A common impurity in synthetic single crystals of alkali halides is the hydroxyl (OH^-) ion. Etzel and Patterson [314] and Etzel [315] have demonstrated conclusively that the colourability and optical properties of synthetic alkali halide crystals are affected (though to varying degrees) by the concentration of OH^- ions in the crystals. Consequently, some absorption bands in the ultra violet have been ascribed to OH^- ions in sodium and potassium halide crystals, while some others have been ascribed to H^-–centres which result from a reaction between the intentionally introduced cation impurities with the OH^- ions (giving rise to the U-bands).

It is here suggested that the 244.0 nm band in RbCl crystals may be due to OH^- ions which greatly enhance the colourability of the crystals in ytterbium atmosphere. The difficulty of bleaching the colour centres by a thermal process suggests that the OH^- ions may be associated with some of the Yb^{2+} ions in some way, the number being in association, getting reduced by thermal bleaching. This is a possible explanation for the observed reduction in the relative transition intensity of the I-band in $RbCl:Yb^{2+}$ crystals.

4.7 Conclusions

In this study, it has been shown that it is possible to incorporate Yb^{2+} ions into RbX (X = Cl, Br, I) crystals by heating the crystals in ytterbuim atmosphere at elevated temperatures. The broad absorption bands of Yb^{2+} ions in the crystals are ascribed to electric dipole transitions from the ground state ($^1S_0(\Gamma_{1g})$) of the $4f^{14}$ configuration to the $18\Gamma_{4u}$ levels of $4f^{13}5d$ configuration of the ions in octahedral environment.

Using J_1j–coupled basis functions for the $4f^{13}5d$ configuration, intermediate coupling calculations demonstrate that there is a satisfactory fit between experimental and theoretical spectra of Yb^{2+} in these crystals by assuming that Yb^{2+} ions occupy substitional lattice sites of effective octahedral symmetry. However, the Slater–Condon F_k, and G_k parameters as well as the spin–orbit parameters ζ_{4f} and ζ_{5d} (through ζ_{4f}) needed to obtain satisfactory fit were observed to be less than the free-ion parameter values determined by Bryant [99]. The reduction in these

values is thought to be due to nephelauxetic effects associated with the presence of co–ordinating ligands. This is more so as the nephelauxetic ratios determined for each of the parameters F_2, G_1 and ζ_{4f} follow the nephelauxetic series of Schäffer and Jorgensen.

Computer experiments on the evolution of the Γ_{4u} levels of the $4f^{13}5d$ configuration of Yb^{2+} ions in octahedral crystal field suggests that the contribution of the electrostatic (direct Coulomb and exchange) interactions to the energy level structure is to spread the energy levels within the confines almost entirely determined by the spin–orbit and crystal field interactions. As the model description of the interaction scheme based on the above result and groups theoretical considerations emphasise, the role of direct Coulomb and exchange interactions is very important in the low and intermediate crystal field ($Dq < 1400\ cm^{-1}$) regimes.

Quite interesting is the observation that the depression of the centre of gravity of the free ion levels that giving rise to the Γ_{4u} levels of Yb^{2+} ions in the rubidium halide series follows a spectro-schemical series ($Cl^- < Br^- < I^-$) of ligand ions. An equally interesting observation is that in the same halide series, the experimentally determined values of Dq follow the above series in reverse direction, namely: $Cl^- > Br^- > I^-$.

In addition to the $4f^{13}5d$ absorption bands of Yb^{2+} ions, a pair of bands was observed in the spectra of each of $RbBr : Yb^{2+}$ and $RbI : Yb^{2+}$ crystals and one in $RbCl : Yb^{2+}$ crystals, which have been ascribed to electronic transitions to bonding molecular orbitals formed by the mixing of the $4f^{13}6s$ wavefunctions and the (n+1)s orbitals of the ligand ions. In fact the observed relative transition intensities of any of the bands pairs depends on the degree of covalency of the host material being larger in more covalent halide hosts than in the more ionic crystals.

Chapter 5

Divalent Samarium Ions in Potassium and Rubidium Halide Crystals

5.1 Introduction

Divalent samarium ions, as has been pointed out, show two distant spectra both in absorption and fluorescence when incorporated into substitutional lattice sites in crystals. The more widely studied of these series consists of weak intense bands which have been attributed to parity-forbidden $4f^6 \leftrightarrow 4f^6$ transitions Sm^{2+} ions. In free space, the ground manifold of the $4f^6$ configuration is ^7F_J ($J = 0, 1, ..6,$), the lowest being the state with $J = 0$. In cubic crystalline environment this ground state is a singlet $\Gamma_{1g}(^7F_0)$ and the next excited state is a triplet $\Gamma_{4g}(^7F_1)$. The rest of the levels of the manifold are however split into several crystal levels.

If however the Sm^{2+} ions occupy substitutional lattice sites with point symmetry lower than octahedral or cubic, as is the case with the application of uniaxial stress on $CaF_2 : Sm^{2+}$ crystals or with a charge compensating cation vacancy in the nearest neighbour or next nearest neighbour position as in the case of $KCl : Sm^{2+}$ system, many more energy levels are observed experimentally [275,64]. The multiplicity of levels is due to further splitting of the crystal field levels at lower symmetry

sites.

It is the parity-allowed electronic transitions from the ^7F_J manifold of levels of the $4f^6$ configuration to the first excited $4f^55d$ configuration that give rise to the second series of bands, that is, the strong broad absorption bands observed, in the visible and ultraviolet region, in the spectra of Sm^{2+} ions in crystals. Because of the complexity of the $4f^55d$ configuration, only a single fairly detailed theoretical calculation of the energy levels of Sm^{2+} ions in crystals exists [104]. As far as the author knows, up to date, there is no comprehensive theoretical analysis of the free ion spectra of SmIII leading to proper parametrisation of the observed spectra. What exist are estimates of Slater-Condon parameters $F_k(f,f), F_k(f,d), G_k(f,d)$ and spin-orbit parameters ζ_{nl} $(n = 4, 5, l = f, d)$ through interpolation from values of these parameters for other ions. From the foregoing, it is clear that detailed theoretical analysis of the energy levels of the $4f^55d$ configuration of $MeX : Sm^{2+}$ $(M_e = K, Rb, X = Cl, Br, I)$ systems has not been reported before. In this chapter, therefore, are presented, details of such a calculation, undertaken with the hope of obtaining a theoretical spectrum that reproduces the gross features of the absorption spectra of $MeX : Sm^{2+}$ systems. Outlined in the next section are details of the assumptions and the approximations made in the study

Reported also are the absorption spectra of $MeX : Sm^{2+}$ crystals. The spectra of $RbBr : Sm^{2+}$ and RbI:Sm^{2+} are reported for the first time. Interestingly, the incorporation of Sm^{2+} ions into the crystals was successfully done through a vapour phase diffusion process. The spectra presented here are so far the only ones reported for alkali halide crystals doped with Sm^{2+} ions using this technique.

5.1.1 Assumptions and approximations made in the theoretical calculation

Inevitably, certain assumptions and approximations have to be made in a calculation involving a system as complex as the one under study. Among the assumptions are that the most prominent bands observed in the absorption spectra of $MeX : Sm^{2+}$ crystals are due to electric dipole transitions from the ground state of Sm^{2+} ions in the crystals to $4f^5(^6FH)5d$ sub–configuration, and that LS coupling scheme is

valid among states of terms with highest spin multiplicity (i.e. ^6FH) of the $4f^5$ configuration. The first assumption not only leads to a truncation of the $4f^5 5d$ configuration so that attention is confined not only to the states derived from the sextets terms of $4f^5$ configuration but also enables the program of calculation to ignore states derived from $4f^5(^6P)$ sub–configuration. The neglect of the ^6P term in the calculation is justified on the grounds that the free ion assignment of the states of $4f^5(^6P)5d$ sub–configuration shows that the lowest of the states is located at 51 160.8 above the ground state of the $4f^6$ configuration [102]. Having noted that, the point has to be acknowledged that the crystal field interaction may not only lower states of the sub–configuration thereby making them accessible for observation in the ultra violet region of the spectra but also cause a mixing of those states with the lower lying states. Nevertheless, it is hoped that such a sub-configuration mixing would be minimal. The second assumption makes possible the use of the Yanase-Kasuya coupling scheme for rare-earth ions in crystal field in the calculation program.

Another of the important approximations is that the electrostatic interaction between the odd-parity $4f^5d$ and $4f^56s$ configurations could be neglected. The justification for this comes from the fact that such an interaction is a second-order effect, being much smaller than crystal field, spin-orbit and direct electrostatic and exchange interactions which are the principal pertubation interactions that determine the energy levels of Sm^{2+} ions in the crystals. In addition to this, the inclusion of configuration interaction will not only increase considerably the size of the energy matrices but also introduce multiple interaction parameters whose values have to be determined. Unavoidably the model proposed makes use of 13 energy parameters including $F_k(f,f), F_k(f,d), G_k(f,d)$, ζ_{nl}, Dq and B_k^0 parameters. Increasing the number of energy parameters in a situation where there are comparatively few observed absorption bands makes reliable determination of parameter values very difficult. Practical considerations therefore dictate that configuration interaction should be included when refinement of the calculation becomes necessary.

Equally important is the approximation based on a model of Sm^{2+} ions occupying substitutional lattice sites in alkali halide crystals with the site symmetry being distorted by the presence of an alkali ion vacancy in the $< 110 >$ direction. In this

connection, the octrahedral approximation made earlier in respect of Yb^{2+} ions in $RbX : Yb^{2+}$ crystals is applicable. The orthorhombic distortion is therefore assumed to pr duce only slight shifts in energy level positions of the Sm^{2+} ions.

5.2 Matrix elements of interaction Hamiltonians

5.2.1 The states of the $4f^5(^6FH)5d$ sub–configuration of Sm^{2+} ions in octahedral crystal field

In free space, the $4f^5(^6FH)5d$ sub–configuration of Sm^{2+} ions gives rise 20 energy multiplets in the LS coupling scheme. These are $^{5,7}FGHIK$ from $4f^5(^6H)5d$ sub–configurations, and $^{5,7}DFGH$ from $4f^5(^6F)5d$ sub–configuration. In all, these give rise 112 theoretical energy levels.

The situation is different however when the ion situates in crystals. Under such a circumstance, and following Yanase-Kasuya coupling formalism, the 5d electron states are thought to split into crystal states describable in terms of the irreducible representations, Γ_d, of the symmetry of H_{cr}. Thus in octahedral environment, these states are described by the irreducible representations Γ_3 and Γ_5 of O_h point group as quantum numbers. The core electron states couple with Γ_3 and Γ_5 states giving rise to the final crystal states denoted by the irreducible representations Γ_i (i = 1,2,..,5) of O_h point group. Group theory predicts that of the 450 crystal levels derived $4f^6(^6FH)5d$ from the sub–configuration under study, 45 each transform as Γ_{1u} and Γ_{2u}, 90 as Γ_{3u} and 135 each as Γ_{4u} and Γ_{5u} functions. To arrive at this, use was made of the definition of the basis functions as in expression 2.9 as well as Table 3 in reference [318] and Table 4.1 of this work.

In the Yanase-Kasuya coupling scheme and by the definition 2.9, it is easy to derive the values of the quantum numbers as follows: S_2 ($= S_1 + s$) takes values 2 or 3 since $S_1 = 5/2$ for the sub–configuration terms. L_1 could take values 3 or 5. Therefore, for final crystal functions transforming according to the irreducible representations Γ_i of O_h there can be described 8 groups of basis functions categorised as

$$
\begin{aligned}
&|((\tfrac{5}{2}\tfrac{1}{2})^7 H] J_2, \Gamma_d, \alpha_2 \Gamma_i \gamma\rangle \quad ; \; J_2 = 8, 7, ..., 2 \\
&|((\tfrac{5}{2}\tfrac{1}{2})^6 H] J_2, \Gamma_d, \alpha_2 \Gamma_i \gamma\rangle \quad ; \; J_2 = 7, 6, ..., 3 \\
&|((\tfrac{5}{2}\tfrac{1}{2})^7 F] J_2, \Gamma_d, \alpha_2 \Gamma_i \gamma\rangle \quad ; \; J_2 = 6, 5, ..., 1 \\
&|((\tfrac{5}{2}\tfrac{1}{2})^5 F] J_2, \Gamma_d, \alpha_2 \Gamma_i \gamma\rangle \quad ; \; J_2 = 5, 4, ..., 1
\end{aligned}
\tag{5.1}
$$

In all cases $\Gamma_d = \Gamma_3, \Gamma_5$.

The assumption that only electric dipole transitions from the ground state Γ_{1g} are permitted reduces the size of the energy matrices from 450 to 135 since such transitions can only terminate at the $135\Gamma_{4u}$ levels.

5.2.2 Calculation of matrix elements of electrostatic Hamiltonian $H_{es}(f,f)$

The matrix elements of the electrostatic interaction Hamiltonian between the $4f^5$ core configuration were obtained from tables by Nielson and Koster [196] and checked with that from Wybourne [173]. The term energies are given as in Equation (2.5). Hence

$$E[^6F] = 10E^0 \tag{5.2a}$$

$$E[^6H] = 10E^0 - 9E^3 \tag{5.2b}$$

The $10E^0$ is common to all energy terms of the $4f^N$ configuration and makes no contribution to the structure of the configuration. As a result, it is dropped from the calculation. E^k has been expressed in terms of $F_k(f,f)$ by Racah [95]. Using the inter–conversion expressions, the term energies can be written as

$$E[^6F] = 0 \tag{5.3a}$$

$$E[^6H] = -15F_2(f,f) - 18F_4(f,f) + 273F_6(f,f) \tag{5.3b}$$

5.2.3 Matrix elements of electrostatic interaction Hamiltonian $H_{el}(f,d)$

The effective Hamiltonian for direct Coulomb and exchange interaction defined by Eqn (2.2) can be rewritten for the case of $4f^5 5d$ configuration of Sm^{2+} ions as

$$H_{el}(f,d) = \sum_{k}^{\infty}[Of^k(f,d)F_k(4f,5d) + Og^k(f,d)G_k(4f,5d)] \qquad (5.4)$$

where

$$Of^k(f,d) = D_k Of_k'(f,d) \qquad (5.5a)$$

$$Og^k(f,d) = D_k Og_k'(f,d) \qquad (5.5b)$$

are the effective operators. The operators Of_k' and Og_k' are defined by Eqns (2.3) and (2.4) and D_k values by Condon and Shortley [30] for fd configuration. In particular

$$Of^2(f,d) = 70\sqrt{6}\mathbf{U}_f^{(2)}.\mathbf{u}_d^{(2)} \qquad (5.6a)$$

$$Of^4(f,d) = 126\sqrt{55}\mathbf{U}_f^{(4)}.\mathbf{u}_d^{(4)} \qquad (5.6b)$$

$$Og^k(f,d) = -\frac{1}{2}D_k\sum_{r=0}^{4}[Y_r\mathbf{U}_f^{(r)}.\mathbf{u}_d^{(r)} + Z_r\mathbf{V}_f^{(1r)}.\mathbf{v}_d^{(1r)}] \qquad (5.6c)$$

where Y_r and Z_r are coefficients. If the matrix elements of the scalar operator $\mathbf{U}_f^{(r)}.\mathbf{u}_d^{(r)}$ between the basis fucntions (7.1) are denoted as Q_r and those of $\mathbf{V}_f^{(1r)}.\mathbf{v}_d^{(1r)}$ as Q_{1r}. The coefficients of G_k in the energy matrices can be written as

$$g^k(f,d) = -\frac{1}{2}\sum_{r=0}^{4}[Y_{kr}Q_r + Z_{kr}Q_{1r}] \qquad (5.7)$$

with the coefficients $Y_{kr} = D_kY_r$, $Z_{kr} = D_kZ_r$ are shown in Table 5.1. The last row in the table headed by index m_r gives the multiplicative constants with which each element of each column has to be multiplied to get the actual Y_{kr} and Z_{kr} coefficients. Entries in this and subsequent tables are read as follows: each negative entry is preceded by a minus sign. All numbers (or factors) enclosed in parenthesis ( ) should have their square root taken. Thus $Y_{53} = -77\sqrt{15}$ while $Z_{31} = 36\sqrt{70}$

In order to calculate Q_r and Q_{1r}, the methods of reference [75] were used. Values of the reduced matrix elements, RME, $\langle\psi_1\|\mathbf{U}_f^{(r)}\|\psi_3\rangle$ were obtained from tables by

Table 5.1 Table of Coefficients Y_{kr} and Z_{kr}

	$D_k \underline{Y}_r = \underline{Y}_{kr}$				$D_k \underline{Z}_r = \underline{Z}_{kr}$				
r / k	1	2	3	4	0	1	2	3	4
1	2	6	3	1	4	8	24	12	4
3	3	-11	-8	4	16	12	-44	-32	16
5	-33	55	-11	1	88	-132	220	-44	4
m_r	3(70)	5(6)	7(15)	9(55)	3(35)	3(70)	5(6)	7(15)	9(55)

Table 5.2 Reduced Matrix Elements of Unit Tensor Operator $U^{(r)}$ Between Coupled States of $f^5(^6FH)$ Sub_configuration * *

Tensor Operators → / Coupled States ↓ $^{S\ L}_{1\ 1}$, $^{S\ L}_{3\ 3}$	$U^{(1)}$	$U^{(2)}$	$U^{(3)}$	$U^{(4)}$	$U^{(5)}$	$U^{(6)}$
^6F ^6F	1	$\frac{1}{3}$	-1	$\frac{1}{3}$	1	$\frac{1}{3}$
^6F ^6H	0	$\frac{-2(\ 77)}{21}$	$\frac{1(\ 77)}{7}$	$\frac{-1(455)}{21}$	0	$\frac{1}{3}(14)$
^6H ^6H	$\frac{1(770)}{14}$	$\frac{-1(2002)}{42}$	0	$\frac{2(\ 91)}{21}$	$\frac{-1(\ 91)}{7}$	$\frac{1}{21}(595)$

* * After Nielson and Koster (1963). Only upper triangle of the $U^{(r)}$ matrix is given above For reflected cases, values are the same both in magnitude and sign.

Nielson and Koster's tables [196]. In available literature, no tables of the RME's $\langle\psi_1\|V^{(1r)}_{\gamma}\|\psi_3\rangle$ seem to exist for $N = 5$, $l = 3$, $r = 2,3,4$. Using Eqn (2.101) in reference [1], therefore, the RME of $V^{(1r)}$ between basis functions characterised by the quantun numbers $S_1 = 5/2, L_1, L_3 = 3,5$ were calculated. The coefficients of fractional parentage (cfp) used in these calculations were obtained from the tables of Nielson and Koster [196]. Results of the calculation are shown in Table 5.3

Inevitably, the W[ ] block coefficients involved in the calculation of Q_r and Q_{1r} were calculated using integer arithmetic and stored in the computer. Their calculation involves vector coupling coefficients $\langle\Gamma_i\gamma_i\Gamma_j\gamma_j|^{\alpha_3}\Gamma_4\gamma\rangle$, $i,j = 1,2,...,5$ and the transformation coefficients $< J_2M_2|^{\beta_3}\Gamma_i\gamma_i >$ and $< lm|\Gamma_j\gamma_j >$. The former were obtained from tables by Griffith [215] while the latter set from tables by Leushin [214]. As earlier noted in Chapter 4, the 3-j symbols were obtained using a library of computer subroutines. In all, there are three main categories of W[ ] coefficients corresponding to

$$
\begin{aligned}
&W[d(\Gamma_3)J_3, d(\Gamma_3)J_4 : {}^{\alpha_3\alpha_4}\ \Gamma_4 r] \quad , r = 0,1,...,4,\ J_3, J_4 = 1,2,...,8\\
&W[d(\Gamma_3)J_3, d(\Gamma_3)J_4 : {}^{\alpha_3\alpha_4}\ \Gamma_4 r] \quad , r = 1,...,4,\ J_3, J_4 = 1,2,...,8\\
&W[d(\Gamma_3)J_3, d(\Gamma_3)J_4 : {}^{\alpha_3\alpha_4}\ \Gamma_4 r] \quad , r = 0,1,...,4,\ J_3, J_4 = 1,2,...,8 \qquad (5.8)
\end{aligned}
$$

Each of the first and last categories consists of five different tables while the remaining category contains four. These tables are presented in a separate cover because of their bulk. Eventually five energy matrices respectively expressed in terms of $F_k, (k = 2,4)$ and G_k $(k = 1,3,5)$ resulted and were stored in the computer.

5.2.4 Matrix elements of spin–orbit interaction Hamiltonians

In order to obtain the matrix elements of $H_{so}(f)$ and $H_{so}(d)$, the procedures of reference [75] were also closely followed. In the case of the matrix elements of $H_{so}(d)$, the S[ ] block coefficients had to be calculated. Note has to be taken, however, that the spin orbitals are characterised by half–integral J_1-values in the range $\frac{1}{2}$–$\frac{15}{2}$. By implication, Γ_{J_1} are the doubly-valued irreducible representations Γ_j $(j = 6,7,8)$ of the octahedral double group. Whereas the transformation coefficients $< J_1M_1|^{\phi}\Gamma_{J_1}\gamma_{J_1} >$ were obtained from tables by Leushin [214], the vector

Table 5.5 Reduced Matrix Elements of Double Tensor Operator $V^{(1r)}$ Between Coupled States of $f^5(^6FH)$ Sub_configuration *

Double Tensor Operators / Coupled States $^{S\ L}_{1\ 1}$ $^{S\ L}_{3\ 3}$	$V^{(10)}$	$V^{(11)}$	$V^{(12)}$	$V^{(13)}$	$V^{(14)}$	$V^{(15)}$	$V^{(16)}$
^6_F ^6_F	$\frac{1}{2}(210)$	$\frac{1}{10}(210)$	$\frac{1}{30}(210)$	$\frac{-1}{10}(210)$	$\frac{1}{30}(210)$	$\frac{1}{10}(210)$	$\frac{1}{30}(210)$
^6_F ^6_F	0	0	$\frac{-1}{15}(330)$	$\frac{1}{10}(330)$	$\frac{-32}{77}(78)$	$\frac{2}{11}(78)$	$\frac{13}{35}(15)$
^6_F ^6_F	$\frac{1}{2}(330)$	$\frac{1}{2}(33)$	$\frac{1}{30}(2145)$	0	$\frac{1}{15}(390)$	$\frac{-1}{10}(390)$	$\frac{53}{1155}(102)$

* Only upper triangle of $V^{(1r)}$ matrix is given above. Reflected elements of lower triangle are equal to corresponding elements in the upper traingle.

coupling coefficients $< \Gamma_j\gamma_j\Gamma_i\gamma_i|^{\alpha_k}\Gamma\gamma >$ are not available in the same quantisation scheme adopted in this study. Accordingly, they were calculated using the isomorphic correspondence between crystal wave functions characterised by Γ_j and spherical harmonics.

The principle of isomorphism used here rests on the premise that crystal wave functions characterised by the irreducible representation Γ of the point group symmetry of the crystal field Hamiltonian can be connected on one to one basis to wave functions (expressible in spherical harmonics) of the ions in free space. As Abragam and Pryce [317] point out, in O_h point symmetry Γ_4 functions are p-like since they behave like the p^N functions of the free ion or atom. Implied in the above statement is the correspondence between the components of Γ_4 functions to the components of the orbital angular momentum 1 ($l = 1$). It was Dixon [316] who first drew attention of the author to the possible use of the isomorphic principle to connect the doubly-valued functions Γ_6 and Γ_8 to spherical harmonic functions of half integral order. Details of how this was achieved, the calculation of the vector coupling coefficients and the resulting tables are presented in Appendix A.

The resulting S[ ] block coefficients were grouped into three main categories, namely :

$$\begin{aligned} &S(\Gamma_3 J_2 \Gamma_8 J_1 : {}^{\alpha_2\alpha_3}\Gamma_4 g) \quad , J_1 = \tfrac{1}{2}, \tfrac{3}{2}, ..., \tfrac{15}{2} \\ &S(\Gamma_5 J_2 \Gamma_8 J_1 : {}^{\alpha_2\alpha_3}\Gamma_4 g) \quad , J_1 = \tfrac{1}{2}, \tfrac{3}{2}, ..., \tfrac{15}{2} \\ &S(\Gamma_5 J_2 \Gamma_7 J_1 : {}^{\alpha_2\alpha_3}\Gamma_4 g) \quad , J_1 = \tfrac{3}{2}, \tfrac{5}{2}, ..., \tfrac{15}{2} \end{aligned} \qquad (5.9)$$

In all cases, $J_2 = 1, 2, ..., 8$. Making use of an equation analogous to Eqn (30) of reference [75], and the S[ ] block coefficients, the matrix elements of $H_{ee}(d)$ were calculated.

5.2.5 Matrix elements of crystal field interaction Hamiltonians $H_{cr}(d)$ and $H_{cr}(f)$

In the Yanase-Kasuya coupling scheme, the matrix elements of $H_{cr}(d)$ are not only independent of the quantum numbers $S_1, S_2, S_4, L_1, L_2, J_2$ and J_4 but also diagonal

in Γ_d. The matrix elements of $H_{cr}(d)$ between the basis functions (5.1) reduce to

$$\begin{aligned} < \Gamma_3 | H_{cr}(d) | \Gamma_3 > &= 6Dq \\ < \Gamma_5 | H_{cr}(d) | \Gamma_5 > &= -4Dq \end{aligned} \qquad (5.10)$$

in the case of Sm^{2+} ions in octahedral crystal field. For cubic crystal field (with 8-fold co-ordinated ligand ions) the signs in the equations above are reversed.

In octahedral or cubic crystal fields $H_{cr}(f)$ can be partitioned into two effective operators $\Theta^{(k)}_{\Gamma_1}$ $(k = 4, 6)$. The matrix elements of these operators between the basis functions (5.1) involve the X[ ] block coefficients. Whereas the transformation coefficients, $\langle kq \mid \Gamma_1 a_1 \rangle$, appearing in the definition of X[ ] block coefficients were obtained from Eqns (2.6) and (2.7), the rest of the coefficients were obtained from sources cited as for W[ ] and S[ ] block coefficients. Two classes of X[ ] block coefficients, each consisting of two tables, result. They include

$$\begin{aligned} &X[J_2 J_4(\Gamma_3) : k\Gamma_1 \; {}^{\sigma_2\sigma_4}\Gamma_4] \quad , k = 4, 6 \\ &X[J_2 J_4(\Gamma_5) : k\Gamma_1 \; {}^{\sigma_2\sigma_4}\Gamma_4] \quad , k = 4, 6 \end{aligned} \qquad (5.11)$$

In each case $J_2, J_4 = 1, 2, ..., 8$. The coefficients were stored in the computer from where they were later accessed..

It was possible, therefore, to construct two matrices, one each in terms of B^0_k parameters $(k = 4, 6)$ which were then stored in the computer.

5.3 Theoretical energy levels

5.3.1 Relative transition intensities

In order to calculate the relative transition intensities of the spectral bands, it is important to look closely at the electric dipole selection rule for transition between the terminal eigenstates in the Yanase-Kasuya coupling scheme. The wavefunctions describing the eigenstates of the ground manifold of the $4f^{N+1}$ configuration can then be written as

$$| 4f^{N+1}(S_g L_g) J_g \; {}^{\sigma}\Gamma_g \mu \rangle = \sum_{M_g=-J_g}^{J_g} \langle J_g M_g \mid {}^{\sigma}\Gamma_g \mu \rangle \, | 4f^{N+1}(S_g L_g) J_g M_g \rangle \qquad (5.12)$$

while the perturbed eigenstates of the $4f^N5d$ configuration in crystal environment have as wavefunctions, the linear combinations of the basis functions defined in expression (2.9). However, Yanase [104] and Asano [75] have shown that the matrix element of the electric dipole moment between an eigenstate of the ground manifold and an eigenstate of an excited configuration is given

$$\begin{aligned}
&\langle 4f^{N+1}(S_gL_g)J_g :^{\omega}\Gamma_g\mu) \mid (-e\sum_{i=1}^{N+1}(x_\eta)_i \mid 4f^N[(S_1s)S_2L_1]J_2,\Gamma_{l'} :^{\alpha_2}\Gamma\gamma\rangle \\
&= \delta(S_g,S_2)(-e)\langle 4f\|r\|5d\rangle[L_g,J_2]^{\frac{1}{2}}\sqrt{N+1}(f^{N+1}S_gL_g\{\mid f^N(S_1L_1)fS_gL_g\rangle \\
&\quad\times(-1)^{S_g+J_g+L_1+l_f}\begin{Bmatrix} 3 & J_2 & J_g \\ S_2 & L_g & L_1 \end{Bmatrix} \\
&\quad\times\sum_{M_2M_gm_fm_{l'}}(-1)^{J_2+M_g+m_f}\begin{pmatrix} J_2 & 3 & J_g \\ M_2 & m_f & -M_g \end{pmatrix}\begin{pmatrix} 2 & 1 & 3 \\ m_{l'} & \eta & -m_f \end{pmatrix} \\
&\quad\times\langle l'm_{l'}(\Gamma_{l'})J_2M_2 \mid^{\alpha_2}\Gamma\gamma\rangle\langle J_gM_g \mid^{\omega}\Gamma_g\mu\rangle
\end{aligned} \tag{5.13}$$

where

$$\begin{aligned}
\langle l'm_{l'}(\Gamma_{l'})J_2M_2 \mid^{\alpha_2}\Gamma\gamma\rangle &= \sum_{\gamma_{J_2}\gamma_{l'}}\langle l'm_{l'} \mid \Gamma_{l'}\gamma_{l'}\rangle\langle J_2M_2 \mid^{\beta_2}\Gamma_{J_2}\gamma_{J_2}\rangle \\
&\quad\times\langle\Gamma_{J_2}\gamma_{J_2}\Gamma_{l'}\gamma_{l'} \mid^{\alpha_2}\Gamma\gamma\rangle
\end{aligned} \tag{5.14}$$

$\eta = 0, \pm 1$ is the component of light polarization and

$$\begin{aligned}
(x_{\pm1})_i &= \mp\frac{(x_i + iy_i)}{\sqrt{2}} \\
(x_0)_i &= z_i
\end{aligned}$$

(x_i, y_i, z_i) being the cartesian co-ordinates of the i^{th} electron. The sixth factor to the right of Eqn (5.13) is the coefficient of fractional parentage and the RME

$$\langle 4f\|r\|5d\rangle = \langle 3\|\mathbf{C}^{(1)}\|2\rangle\int_0^\infty[R_{4f}(r)][R_{5d}(r)]r^3dr$$

is the radial part of the transition matrix element.

For Eqn (5.13) not to vanish, the inequalities

$$|J_2 - J_g| \leq 3 \leq J_2 + J_g \tag{5.15}$$

must be satisfied as can be deduced from the triangular condition on the 6-j symbol [104]. Since the ground state of Sm^{2+} $(4f^N)$ ions is characterised by $J_g = 0$,

electronic transitions from the ground state are permitted only to states with $J_2 = 3$. Additionally, the selection rule $\Delta S = 0$ is implied in the delta function in Eqn (5.13). Using these selection rules, the relative transition intensities for the spectral lines were calculated as outlined below.

Electric dipole transitions take place to eigenstates admixed to the functions

$$|[(S_1 s)3, L_1]3, \Gamma_d, {}^{2S+1}\Gamma_4 \gamma\rangle \ , \ L_1 = 3, 5, \ \Gamma_d = \Gamma_3, \Gamma_5$$

The transition probability for any level is not only proportional to the square of the coefficient appearing in the linear combination of admixed functions but also to the square of the matrix elements of the electric dipole moment. The admixed coefficients are obtained from the calculated system of eigenvectors of the composite matrix. For each of the admixed basis functions noted above, a composition factor χ_{Γ_s} was determined using Eqn (5.13). These factors are shown in Table 5.4. It is possible therefore to obtain the product $\kappa\chi_{\Gamma_s}$ which gives the amount of the basis functions characterised by $J = 3$, $S = 3$ admixed with a given eigenstate. The relative transition intensity for a given level then is the number $(50\kappa\chi_{\Gamma_s})^2$ as was done in the study of $RbX : Yb^{2+}$ systems.

5.3.2 Main features of theoretical energy spectrum

A procedure analogous to that described in section 4.3.3 was adopted in calculating the energy levels of Sm^{2+} ions in octahedral and cubic crystal fields. Because up to date, no consistent estimates of the set of parameters $F_k(f,d)$, G_k(f,d), ζ_{4f} and ζ_{5d} exists, their values were interpolated from those of seven doubly ionised rare earth metals obtained from various sources. Table 5.5 indicates the seven ions their free-ion parameters, and the sources from which they were obtained. Graphs from which the esimates of the parameter values for Sm^{2+} ions were interpolated are shown in Figs A.1 – A.6 in Appendix A. In those graphs, the Slater–Condon and spin–orbit parameters for six divalent rare–earth ions in free space were plotted against the number of optically active electrons, N, in the core sub–configuration, $4f^N$. Since for Sm^{2+} $N = 5$, it was an easy matter to estimate the values of these paramaters for the ion through interpolation from the graphs.

Table 5.4 Composition Factors χ_{Γ_4} for the States $|[(3,\frac{1}{2})3,L_1]3,\Gamma_d,^{\alpha_2}\Gamma_{4a}\rangle$,

$L_1 = 3,5$; $\Gamma_d = \Gamma_3, \Gamma_5$.

Geneology of Eigenstate			Composition factor
$4f$– Electron Sub–space ($L_1 = 3,5$)	$5d$– Electron Sub–space	α_2	χ_{Γ_4}
^6F	Γ_5	1	0.2564644
		2	0.2007149
		3	0.3626954
	Γ_3	1	0.3440831
		2	0.1813477
^6H	Γ_5	1	0.3214951
		2	0.2516096
		3	0.4546628
	Γ_3	1	0.431331
		2	0.2273312

Table 5.5 : Free Ion Parameter Values for $4f^N5d$ Configuration of some Divalent Rare_Earth Ions. Values are in cm^{-1}.

Free Ion	N	$F^k(f,d)$		$G^k(f,d)$			ζ_{4f}	ζ_{5d}	Reference
		F^2	F^4	G^1	G^3	G^5			
Ce^{2+}	1	185.0	22.7	303.4	34.8	4.50	637.0	656.0	29
Pr^{2+}	2	182.0	21.4	283.0	32.6	4.35	767.0	734.0	29
Eu^{2+}	6	182.2	17.7	222.3	24.4	4.61	1181.0	898.0	36
Tb^{2+}	8	193.0	17.1	171.6	22.9	3.20	1549.0	1053.0	327
Er^{2+}	11	195.4	20.1	213.1	25.9	3.43	2383.0	1089.8	328
Tm^{2+}	12	195.0	18.6	216.5	31.5	5.27	2639.4	1131.0	34
Yb^{2+}	13	186.8	14.4	193.2	24.6	4.11	2950.2	1211.0	99
Sm^{2+}	5	181.6	18.3	236.0	26.3	3.73	1060.0	860.0	* *

* * Estimates obtained

However direct Slater-Condon integrals $F_k(f,f)$ for the $4f^5$ configuration of Sm^{2+} ions were obtained from Wybourne [1]. They are $F_2 = 370.0\ cm^{-1}$, $F_4 = 51.08\ cm^{-1}$, $F_6 = 5.591\ cm^{-1}$ Approximations similar to those leading to Eqn 4.9 give the ratio $(B_6^0/B_4^0)_{cubic}$ as -0.25. Consequently

$$(B_6^0/B_4^0)_{oct} = 0.094 \qquad (5.16)$$

Eqn (4.11) was used to connect Dq and B_4^0 parameters.

By varying Dq over a large range of values while keeping the other energy parameters constant at their estimated free–ion values, it was possible to study the evolution of the Γ_{8u} energy levels of $4f^5(^6FH)5d$ sub–configuration of Sm^{2+} ions. Fig 5.1 shows that the energy levels are very closely spaced and that at any of the two extremes of the theoretical spectrum, the levels are parallel even at low Dq values ($Dq < 600\ cm^{-1}$). At Dq values of about $1600\ cm^{-1}$ two groups of parallel levels emerge, each group diverging from the other. Evidently, the energy levels at such high Dq regime appear to be predominantly determined by the crystal field. The quantity $\frac{\partial E}{\partial Dq}$ is about -3.98 ± 0.01 for the lower group of parallel levels and 5.97 ± 0.01 for the upper group. These values compare favourably with the expected values of -4 and $+6$ respectively.

More information could have been obtained from Fig 5.1 if the distribution of relative transition intensities among the energy levels were indicated. Because of this, the figure was divided into eight units based on the following procedure. Although each of the energy levels for a given Dq, value is described by a wavefunction which is a linear combination of basis functions such as given in Eqn (5.1), the classification of the levels is based on the groupings indicated therein. Thus eight groups of energy levels emerge since for each of the four groups of functions, there are two subgroups corresponding to $\Gamma_4 = \Gamma_3, \Gamma_5$. For ease of identification, therefore, the groups of energy levels are labelled 1 to 8, starting with the lowest group. Figs 5.3(a)–5.3(b) show these groups of energy levels for the octahedral crystal field. In all the figures, the numbers indicated the relative transition intensities for the levels indicated.

An inspection of these figures indicates that at any Dq value, four sets of 'clustered' levels characterised by high relative transition intensities can be observed. As

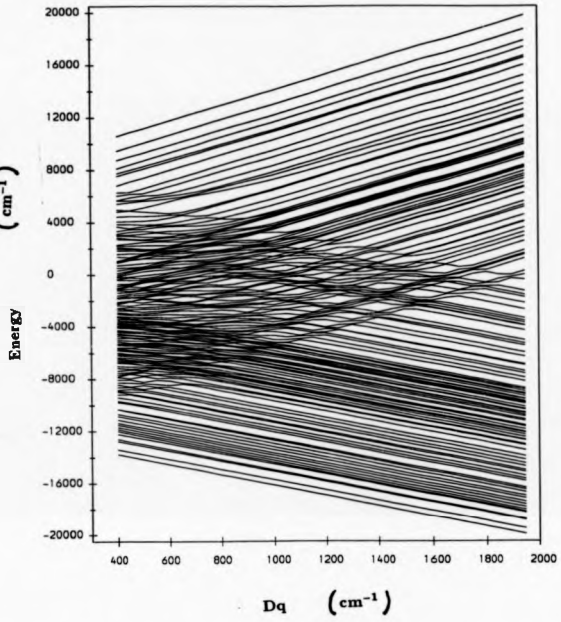

Fig 5.1 Variation of Γ_{4u} energy levels of Sm^{2+} ions with Dq in octahedral crystal field. F_2, F_4, G_1, G_3, G_5, ζ_{4f} and ζ_{5d} are set at estimated free ion values.

PAGINATION
ERROR

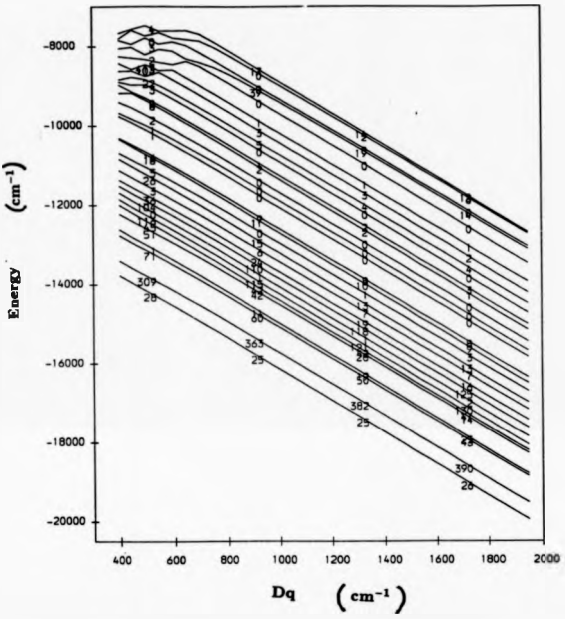

Fig 5.3(a) Variation of Group 1 of Γ_{4u} energy levels of Sm^{2+} ions with Dq in octahedral crystal field. F_2, F_4, G_1, G_3, G_5, ζ_{4f} and ζ_{5d} are set at estimated free ion values.

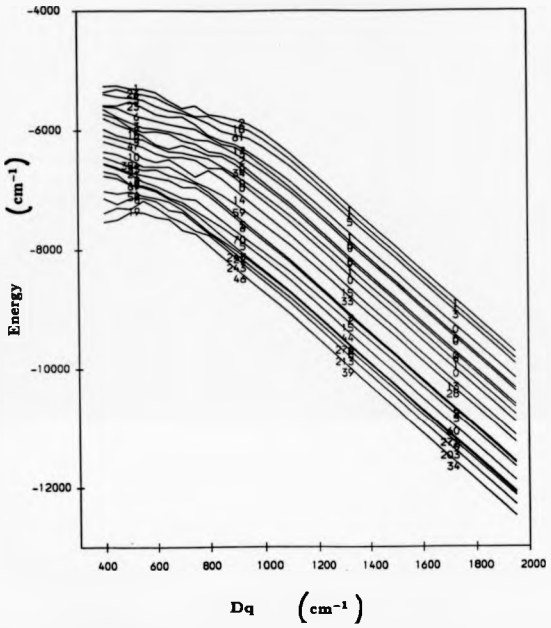

Fig 5.3(b) Variation of Group 2 of Γ_{4u} energy levels of Sm^{2+} ions with Dq in octahedral crystal field. F_2, F_4, G_1, G_3, G_5, ζ_{4f} and ζ_{5d} are set at estimated free ion values.

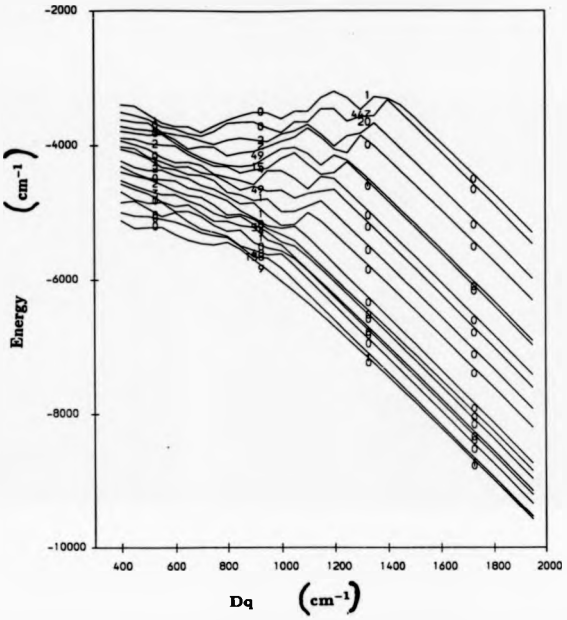

Fig 5.3(c) Variation of Group 3 of Γ_{4u} energy levels of Sm^{2+} ions with Dq in octahedral crystal field. F_2, F_4, G_1, G_3, G_5, ζ_{4f} and ζ_{5d} are set at estimated free ion values.

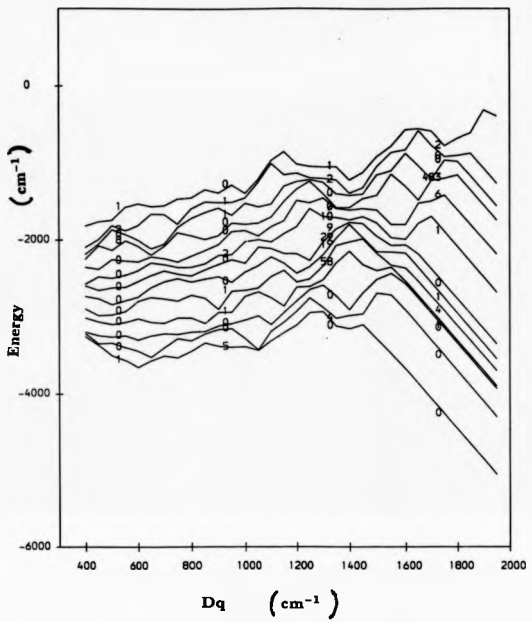

Fig 5.3(d) Variation of Group 4 of Γ_{4u} energy levels of Sm^{2+} ions with Dq in octahedral crystal field. F_2, F_4, G_1, G_3, G_5, ζ_{4f} and ζ_{5d} are set at estimated free ion values.

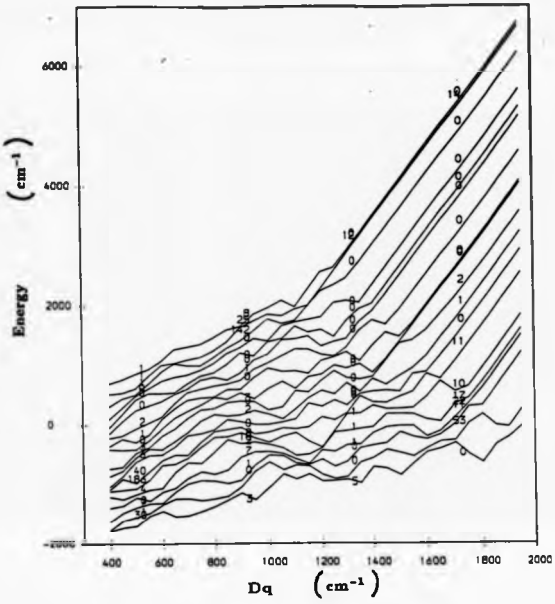

Fig 5.3(e) Variation of Group 5 of Γ_{1u} energy levels of Sm^{2+} ions with Dq in octahedral crystal field. F_2, F_4, G_1, G_3, G_5, ζ_{4f} and ζ_{5d} are set at estimated free ion values.

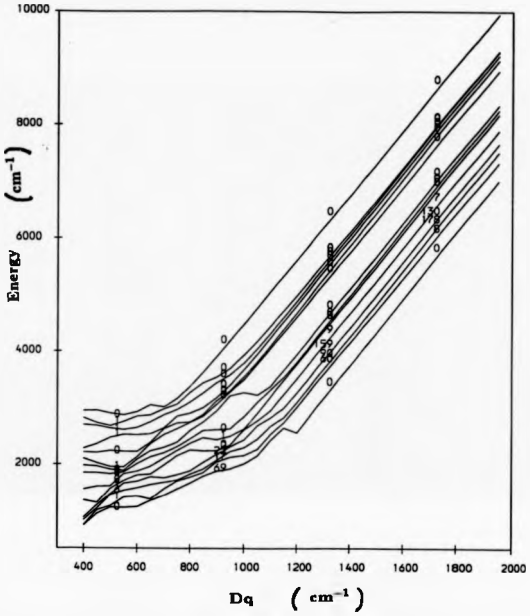

Fig 5.3(f) Variation of Group 6 of Γ_{4u} energy levels of Sm^{2+} ions with Dq in octahedral crystal field. F_2, F_4, G_1, G_3, G_5, ζ_{4f} and ζ_{5d} are set at estimated free ion values.

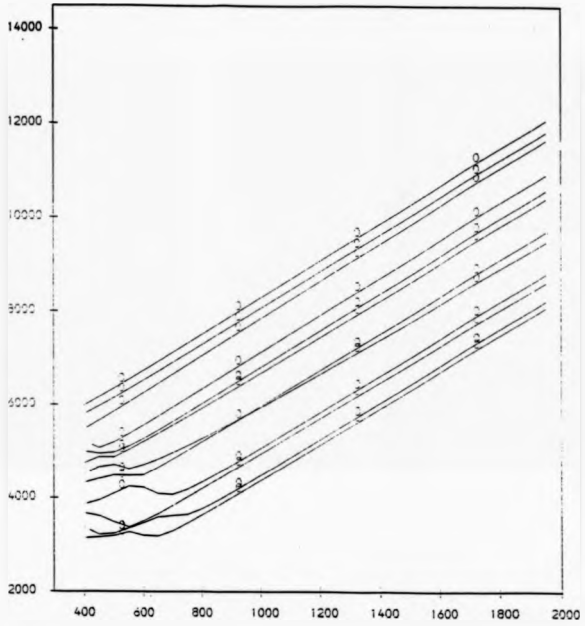

Fig 5.3(g) Variation of Group 7 of Γ_{4u} energy levels of Sm^{2+} ions with Dq in octahedral crystal field. F_2, F_4, G_1, G_3, G_5, ζ_{4f} and ζ_{5d} are set at estimated free ion values.

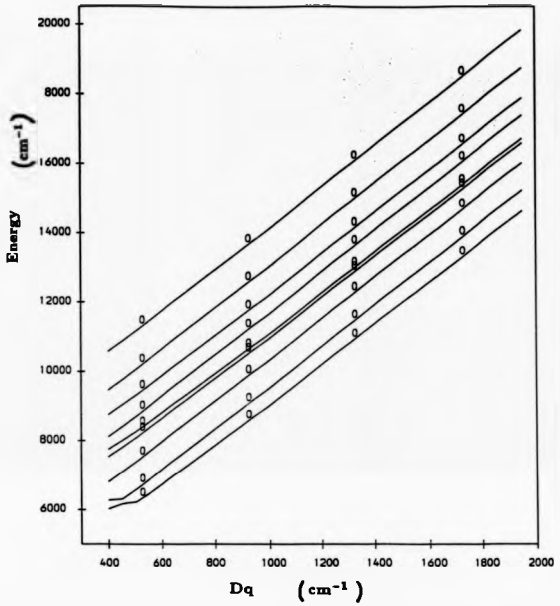

Fig 5.3(h) Variation of Group 8 of Γ_{4u} energy levels of Sm^{2+} ions with Dq in octahedral crystal field. F_2, F_4, G_1, G_3, G_5, ζ_{4f} and ζ_{5d} are set at estimated free ion values.

an illustration, at intermediate crystal fields ($800 < Dq < 1400\ cm^{-1}$)) the first three sets are located in groups 1–3 of energy levels (vide Figs 5.3(a)–5.3(c)). At $Dq = 1300\ cm^{-1}$, part of the third set is located among group 4 energy levels. The fourth set of levels of high transition intensities are found partly in group 5 and partly in group 6 at $Dq = 900\ cm^{-1}$ but in group 6 at $Dq = 1300\ cm^{-1}$. Clearly indicated in these figures is the redistribution of transition intensities with changes in Dq. Remarkabaly, the redistribution appears to be in form of shifts in the upper clusters to higher energies as Dq increases with little spreading of intensities among the energy levels.

Obviously, the clustering of energy levels with high relative transition intensities into four sets indicates that if an optical absorption spectrum of Sm^{2+} in an octahedral environment were measuerd, four groups of energy bands are expected. As a result of the small separations of some of the energy levels, some of the observable levels would overlap giving rise to broad structured absorption bands. In fact, throughout the entire range of Dq values, the four classes of bands would be evident. What is different though are the relative positions and separations of the hypothetical bands. For example, at $Dq = 500\ cm^{-1}$ (low Dq regime), the strongest of the lowest energy levels is separated from the strongest of the third set of energy levels of high transition intensities by about $7300\ cm^{-1}$ while at $Dq = 900\ cm^{-1}$ (intermediate Dq regime) the separation is about $10\ 000\ cm^{-1}$. At $Dq = 1300\ cm^{-1}$, this separation is about $13\ 250\ cm^{-1}$. However at intermediate and high Dq regimes, the separation between the strongest of the lowest group of energy levels and the centre of the second set of 'clustered' levels with high relative transition intensities is fairly constant at about $7500\ cm^{-1}$.

From this point, the sets of 'clustered' energy levels of high relative transition intensities shall be designated as A', B', C' and D' sets of energy levels in order of increasing energy. Continuing with the description of the characteristics of the theoretical spectrum, an interesting feature that can be observed throughout the entire range of Dq values is the considerable concentration of relative transition intensity in the A' group of bands. Indications are that in the hypothetical absorption spectrum of Sm^{2+} ions in octahedral crystal field, at least two distinctively separate

absorption bands are expected with the one lying higher in energy being structured and lower in intensity than the lower band.

5.4 Absorption Spectra of Sm^{2+} ions in potassium and rubidium halide crystals

The absorption spectra of Sm^{2+} ions in rubidium bromide crystals at room and liquid nitrogen temperatures are shown in Fig 5.4. Full line shows the spectrum recroded at LNT while broken line shows RT spectrum. Fig 5.5 on the other hand shows the second derivative spectrum of the same crystals. The absorption spectra as well as the second derivative spectra of Sm^{2+} ions in potassium and rubidium chloride and iodide and in potassium bromide resemble very closely those shown in Figs 5.4 and 5.5. An inspection of the absorption spectra indicates that they consist of intense broad bands located in the visible and ultra-violet. Even at RT, six groups of bands are identifiable for chloride and bromide host crystals while for the iodides, the resolution of the second RT band into two clear bands at LNT makes the similarity between the spectra very clear. The term group of bands is used deliberately because the B,C,D and G bands, which are structured, can be decomposed into component bands. Hence the labels B1, B2,..., D1, D2,.... By measuring the second derivative spectra of the crystals, it was possible to locate the positions of the component bands. The RT spectra resemble very closely those (also recorded at RT) of $KX : Sm^{2+}$ $(X = Cl, Br, I)$ systems obtained by Karapetyan et al [317] and of $KCl : Sm^{2+}$, $KBr : Sm^{2+}$ and RbCl:Sm^{2+} systems obtained by Johnson and Sandoe [80].

As can be seen from Fig 5.4, the absorption bands sharpen considerably and the groupings of the bands become more evident when the crystals are cooled to LNT. The resolution of the fine structure of the bands permit a convenient labeling procedure which consists in attaching a number to alphabets A, B, C,D, G, E to identify prominent peaks or sufficiently resolved shoulders of the bands. One remarkable observation is that in both the potassium and rubidium halide series, the low temperature fine structure of the high energy bands (particularly the C

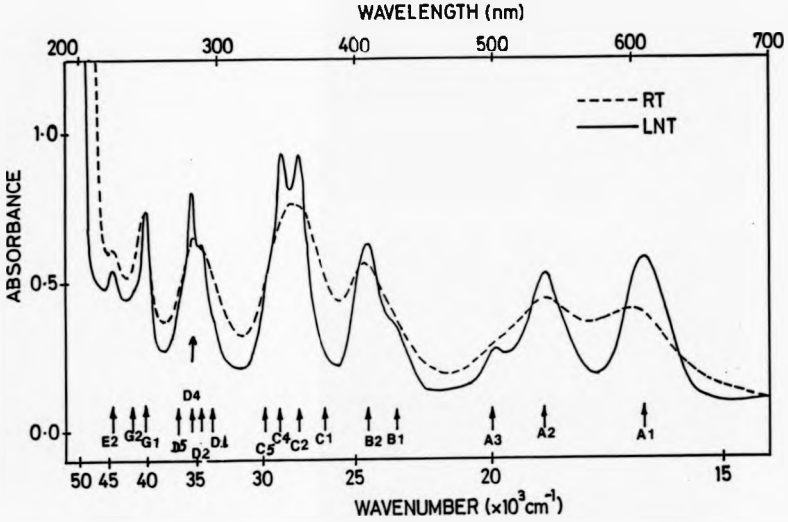

Fig 5.4 Optical absorption spectrum of Sm^{2+} ions in RbBr crystals at room and liquid nitrogen temperatures.

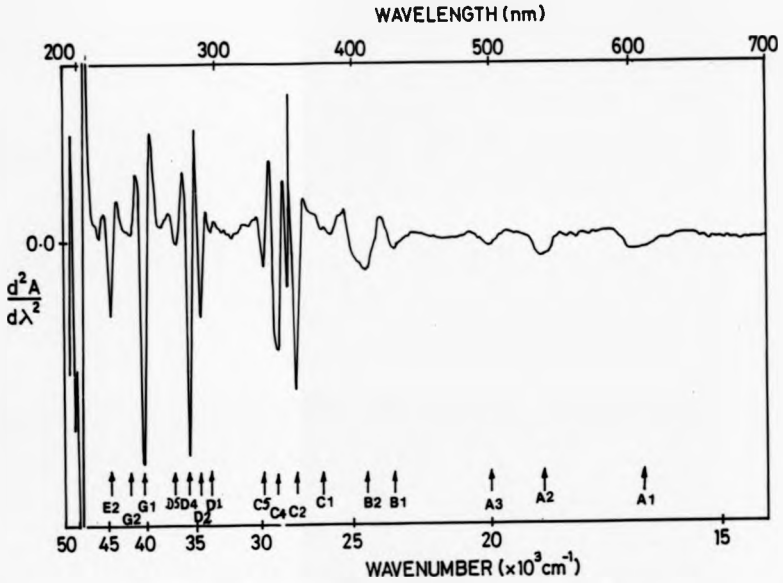

Fig 5.5 Second derivative (absorption) spectrum of Sm^{2+} ions in RbBr crystals at liquid nitrogen temperature.

and D-bands become more pronounced in the progression from chlorides through bromides to iodides. In general, A-bands are located in the spectral region 14 706 cm^{-1} (640 nm) to 20 833 cm^{-1} (480 nm) while the B-bands commence at about 21 739 cm^{-1} (460 nm) and terminate at about 26 316 cm^{-1} (380 nm). The rest of the bands in the spectra lie in the ultra violet.

Apart from the narrowing of the width of the various bands in each of the spectra as a consequence of cooling the crystal, other interesting behaviours were observed. On cooling the crystals to LNT from RT, the spectral positions of the A- and B-bands shift to lower energies (longer wavelengths) whereas C and D bands in general shift to higher energies (shorter wavelenghts).

Another aspect of the displacement behaviour of the spectral positions relates to the relative sensitivity of the A-bands to temperature change. Clearly indicated in Figs 5.5 is the fact that A1-bands undergo a greater spectral displacement than A2-bands as the crystals cool, which leads to a net increase in the separation of the two bands. Although temperature induced shifts of the spectral positions of the G1-band is only slight for the chlorides and bromides, they are more substantial for the iodides. The shifts are towards lower energies as the crystal is cooled from RT to LNT.

In each spectrum of the entire series, the intensity of a given band, say A1, relative to another, say B1 remains fairly the same throughout, with C2- and/or C4 -bands being always the strongest. A striking feature is that at RT, band A2 is slightly more intense than band A1 but at LNT, the reverse is the case. All these observations are summarised in Tables 5.6(a) and 5.6(b) for the spectra of $KX : Sm^{2+}$ and $RbX : Sm^{2+}$ crystals respectively.

Quite remarkably, for a given cation series (i.e. $KX : Sm^{2+}$ or $RbX : Sm^{2+}$), the A-, B- and G-bands shift towards lower energies with increase in lattice parameter d. For example, an A-band in $KCl : Sm^{2+}$ system is located at higher energies than the corresponding band in $KBr : Sm^{2+}$ system while the same band in the latter system is located at higher energies than the corresponding A-band in $KI : Sm^{2+}$ system. Also the displacement of the higher energy bands (C- and D-bands) with increase in d follows the same trend. In this regard notice has to be taken that for

Table 5.6(a) Spectral Positions of Main Bands in the Absorption Spectra of KX : Sm^{2+} ($X = Cl, Br, I$) Crystals at Room and Liquid Nitrogen Temperatures

Host Crystal	Spectral Position (cm^{-1})					
	KCl		KBr		KI	
Band	RT	LNT	RT	LNT	RT	LNT
A1	16 502	16 340	16 447	16 276	16 129	15 785
A2	18 484	18 416	18 450	18 349	18 051	17 857
A3	20 121	19 822	20 000	19 782	–	19 268
B1	–	23 095	23 041	23 041	22 676	22 472
B2	24 510	23 866	24 510	24 213	23 866	23 781
B3	–	24 631	–	24 570	–	–
C1	–	27 435	–	–	–	–
C2	29 155	29 412	27 701	27 933	25 253	26 076
C3	29 762	30 075	–	–	25 974	26 316
C4	30 581	30 912	28 986	29 028	26 991	27 027
C5	31 646	31 949	29 851	30 120	–	27 548
D1	34 364	34 722	33 670	33 784	–	30 411
D2	–	36 036	34 364	34 783	32 787	32 841
D3	36 496	36 900	–	–	–	–
D4	37 313	37 594	35 336	35 714	33 727	33 898
D5	–	–	36 630	37 037	34 542	34 843
G1	40 161	40 040	40 080	40 000	39 841	39 526
G2	–	41 710	–	41 408	–	40 984
E1	- -	–	–	–	30 864	31 299
E2	44 298	44 346	44 248	44 298	37 665	38 023

Table 5.6(b) Spectral Positions of Main Bands in the Absorption Spectra of $RbX:Sm^{2+}$ ($X = Cl, Br, I$) Crystals at Room and Liquid Nitrogen Temperatures

Host Crystal	Spectral Position (cm^{-1})					
	RbCl		RbBr		RbI	
Band	RT	LNT	RT	LNT	RT	LNT
A1	16 611	16 447	16 502	16 393	16 234	15 949
A2	18 657	18 587	18 587	18 553	18 116	18 034
A3	–	19 960	—	19 920	–	19 531
B1	–	23 229	–	23 229	—	22 624
B2	24 631	24 390	24 631	24 390	23 923	23 923
B3	–	24 570	–	24 752	–	–
	–	–	26 455	26 525	–	–
C1	–	27 248	26 882	27 174	–	–
	–	28 902	–	–	–	–
C2	29 326	29 630	27 624	27 894	25 873	26 042
C3	–		–	–	–	26 455
C4	30 395	30 489	28 902	28 944	26 774	26 882
C5	31 250	31 447	29 586	29 851	27 510	27 548
						28 090
	–	–	–	32 895	–	–
D1	–	–	33 445	34 014	31 596	31 949
D2	–	35 336	34 305	34 542	32 468	32 797
D3	36 101	36 166	–	–	–	–
D4	36 969	37 175	35 336	35 524	33 557	33 670
D5	38 023	38 168	36 364	36 799	34 423	34 602
G1	40 404	40 323	40 323	40 241	39 841	39 683
G2	–	42 017	–	41 929	–	41 322
E1	–	–	–	–		30 395
E2	44 248	44 444	44 444	44 643	36 969	37 175

any alkali halide series of $d_{Cl} < d_{Br} < d_I$ (where the subscripts indicate the halide crystal refererd to) and that for any anion series $d_{Li} < d_{Na} < d_K < d_{Rb}$ [121,270].

On the other hand, for any halide series, A-, B- and G- bands shift to higher energies, while C- and D- bands shift to lower energies with increase in lattice constant. Thus a given A-band in $RbCl : Sm^{2+}$ spectrum is located at a higher energy than the corresponding band in $KCl : Sm^{2+}$ spectrum, whereas a given C- or D- band is located at lower energies in $RbCl : Sm^{2+}$ spectrum than in $KCl : Sm^{2+}$ spectrum. To enhance comparison of a spectrum in the two series with another, the separations of the major experimentally observed bands have been compiled in Table 5.7. The findings noted above are in complete agreement the reported structure and behaviour of the spectra of $KX : Sm^{2+}$ and $NaX : Sm^{2+}$ crystal systems [50,63], although the behaviour of the D and G bands was never noted

Some comments must be made, however, about the low temperature second derivative spectra recorded for $KCl : Sm^{2+}$, $KBr : Sm^{2+}$ and $RbCl : Sm^{2+}$ crystal systems. The unresolved structure of the A1- and A2- bands show clearly in the spectra of $KCl : Sm^{2+}$ while in that of $RbCl : Sm^{2+}$ and $KBr : Sm^{2+}$ crystals, the unresolved structure of the A1-band of the absorption spectra manifests itself. This behaviour was only observed, however, in those crystal samples with substantially high concentration of Sm^{2+} ions. Since there was no attempt to measure the concentration of the ions in each sample, the relative concentration could only be judged by the relative intensities of a given band, say A1-band, in the spectra produced for the samples being compared. A close look at A1-band recorded for $KCl : Sm^{2+}$ reveals that the low energy side of the band is not smooth and could be made up of a superposition of many unresolved bands.

5.5 Fitting of experimental and theoretical energy levels

Working on the assumption that the experimental absorption spectra of $KX : Sm^{2+}$ and $RbX : Sm^{2+}$ crystals can be ascribed to $4f^6 \rightarrow 4f^5 5d$ transitions of Sm^{2+} ions, attempts were made to fit the experimental energy levels to the theoretical ones.

Table 5.7 Separation of Some Selected Absorption Bands in the Spectra of $KX : Sm^{2+}$ and $RbX : Sm^{2+}$ ($X = Cl, Br, I$) Crystals at Liquid Nitrogen Temperatures

	Spectral Position (cm^{-1})					
Host Crystal	KCl	KBr	KI	RbCl	RbBr	RbI
Band Pairs						
A1,A2	2 076	2 082	2 076	2 140	2 160	2 080
A1,A3	3 482	3 515	3 484	3 513	3 527	3 582
A1,B1	6 755	6 765	6 687	6 782	6 836	6 675
A1,B2	7 815	7 937	7 996	7 943	7 997	7 974
A1,C2	13 628	11 657	10 291	13 183	11 501	10 093
A2,C4	12 496	10 679	9 170	11 902	10 391	8 848
B1,D2		11 742	10 369		11 313	10 173
B1,D3*	13 670			12 937		
B2,D4	13 439	11 501	10 117	12 785	11 134	9 747
C2,D2	6 624	6 850	6 765	–	6 648	6 755
C2,D3*	7 353			6 536		
C3,D3	6 690					
C4,D4	6 682	6 686	6 871	6 686	6 580	6 788
A1,G1	23 700	23 724	23 741	23 876	23 848	23 734
B1,G1	16 945	16 959	17 054	17 094	17 012	17 059
E1,E2	–	–	6 724	–	–	6 780

* D3–bands in the chlorides series correspond to D2 bands in the bromide and iodide series

This consists in seeking agreement between the spectral positions of A', B', C' and D' sets of theoretical energy levels (bands) and experimental groups of bands A, B, C and D.

To do this, numerical experiments were performed using computer with a view to finding the dependence of A', B', C' and D' groups of energy levels on variations of the energy parameters $F_k(f,d)$, $G_k(f,d)$, ζ_{4f} and ζ_{5d}. It was found that the separations of A' group of levels depend critically on ζ_{4f} but slightly on ζ_{5d}, $G_k(f,d)$ and $F_k(f,d)$. However the separations of A' and B' levels depend critically on both $F_k(f,d)$ and $G_k(f,d)$ which also determine the separations of C' and D' groups of levels. As for the separations between A' and C' as well as between B' and D' groups of levels, they depend mainly on Dq and ζ_{4f}.

The same procedure of keeping $F_k(f,d)$ and $G_k(f,d)$ ratios constant at their estimated free ion values, as was done for $4f^{13}5d$ configuration, was used so as to reduce the number of adjustable parameters. Thus $F_4(f,d) = 0.1007709F_2(f,d)$, $G_3(f,d) = 0.1114406G_1(f,d)$ and $G_5(f,d) = 0.015805G_1(f,d)$ with B_4^0 and B_6^0 connected to Dq through Eqns (4.11) and (5.16). Consequently the five parameters $F_2(f,d)$, $G_1(f,d)$, ζ_{4f}, ζ_{5d} and Dq were varied in order to obtain a satisfactory fit between theoretical and experimental energy levels.

Using the established dependence of the theoretical energy levels on these parameters as a guide, it was possible to systematically vary the latter so that the separations of the individual energy levels are as close as possible to the separations of corresponding energy bands. In this way, a set of trial parameters were obtained for each of the crystal systems. The trial parameters were then used in the set of FORTRAN computer programs designed to minimise the squares of the differences between the experimental and theoretical energy levels. The set of optimised parameter values for each crystal system is given in Table 5.8. Theoretical energy levels were calculated using these parameters. Tables of calculated energy levels and relative transition intensities for the systems studied cannot be presented here because of their bulk. For most of the observed energy levels in all the systems studied, the deviation of the theoretical from the experimental spectral energies were in the range $0 - 400\ cm^{-1}$. There were, however, a few energy levels for which deviations

Table 5.8 Optimised Energy Parameters $F_2(f,d)$, $G_1(f,d)$, ζ_{4f}, ζ_{5d} and Dq for Sm^{2+} Ions in Potassium and Rubidium Halide Crystals. Parameter Δ_{Sm} and Lattice Constant d are included.

Crystal	Energy Parameters (cm^{-1})						Lattice Constant
Host	$F_2(f,d)$	$G_1(f,d)$	ζ_{4f}	ζ_{5d}	Dq	Δ_{Sm}	d (Å)
KCl	256.7	263.6	1172.4	953.5	1320.2	34 264	3.146
KBr	255.6	254.7	1171.8	980.0	1158.8	33 425	3.300
KI	245.6	250.0	1170.4	970.1	989.0	32 171	3.533
RbCl	256.2	257.8	1174.5	1005.9	1267.4	34 095	3.291
RbBr	254.8	255.4	1177.4	952.8	1109.6	33 369	3.427
RbI	254.2	248.6	1178.3	963.8	954.7	32 238	3.671

as large as 800 cm^{-1} occured. This is particularly so for D2 and D5 bands in the spectrum of $RbBr : Sm^{2+}$ crystals. The mean errors (μ's, as defined in section 2.8) were calculated and they are 367 cm^{-1}, 294 cm^{-1}, and 423 cm^{-1} for $KCl : Sm^{2+}$, $KBr : Sm^{2+}$ and $KI : Sm^{2+}$ systems respectively. For the rubidium halide series, they are 284 cm^{-1}, 464 cm^{-1} and 382 cm^{-1} respectively for $RbCl : Sm^{2+}$, $RbBr : Sm^{2+}$ and $RbI : Sm^{2+}$ system.

On the whole, the agreement between the experimental and calculated energy level positions is quite satisfactory. This can be viewed against the background that the theory of atomic spectra applied in this work is an approximation which introduces an inherent uncertainty of 100—200 cm^{-1} into the results [1,86]. Additional error could also be introduced by the crystal field theory. Nevertheless, for some of the energy level assignments, discrepancies exist between the calculated and observed relative transition intensities.

5.6 Discussion

5.6.1 The $4f^5(^6FH)5d$ sub–configuration of Sm^{2+} ions and the optical absorption spectra of $KX : Sm^{2+}$ and $RbX : Sm^{2+}$ crystals

All the optical absorption bands observed in the spectra of $KX : Sm^{2+}$ and $RbX : Sm^{2+}$ crystals are ascribed to photon absorption by Sm^{2+} ions. Each spectrum consists of six groups of bands labelled A-, B-, C-, D-, E- and G- bands. Furthermore the structure of the spectra are alike and corresponding bands behave in a similar way on cooling. To further strenghten the conclusion that the spectra are of common origin, attention is drawn to the striking similarity between the separation of any given pair of bands in one spectrum and of corresponding bands in the other spectra. Across the entire series, and as clearly illustrated in Table 5.7, the separations between a given pair of A-bands are nearly similar. The same can be said of the following band pairs: (A1,B1), (A1,B2), (C2,D2), (C4,D4) and (B1,G1).

In the theoretical study of the $4f^5(^6FH)5d$ sub–configuration of Sm^{2+} ions in octahedral crystal field, four sets of clustered energy levels which have high relative transition intensities were predicted. Consequently, it was concluded that the

absorption spectrum corresponding to that sub–configuration would consist of four groups of bands, some of which would be structured. In pursuance of that prediction, the experimental A-bands are here assigned to the lowest set of theoretical bands (that is, the A' group of levels) while the B-bands are assigned to the next higher set, the B' group of levels. To justify this assignment, it can be noticed that the separation between the strongest of the A' bands and the gravimetric centre of the B' group of bands is between 7300 cm^{-1} (for Dq = 900 cm^{-1}) and 7500 cm^{-1} (for higher Dq values). These values compare favourably with the separations of A1- and B- bands shown in Table 5.7, if it is borne in mind that the comparison is only a rough one. A more direct comparison would involve obtaining the centre of the B-bands first before calculating the separation. However this was not done since more detailed fitting of the energy bands to the theoretical spectrum was carried out.

Continuing with the band assignments one again has to recognise the similarity between the separation of the theorectiacl A' and C' bands on the one hand and the experimental A and C bands on the other. As mentioned in Section 5.3.2, for the theorectical energy spectrum and at Dq = 900 cm^{-1}, this separation is about 10 000 cm^{-1} while it is about 13 250 cm^{-1} at Dq = 1300 cm^{-1}. Again, these values compare favourably with the separations of the band pairs (A1, C2) on the one hand and (A2, C4) on the other (vide Table 5.7). The increase in the separation of the theoretical bands with increase in Dq can be likened to the increase in the separations of A- and C- bands with decrease in lattice parameter d.

Because of these and the fact that in general A-bands shift to lower energies and C-bands to higher energies as the crystals are cooled from RT to LNT (such displacements being attributed to increased Dq owing to reduction in d), it is attractive to assign the C-bands to the of theoretical C' group of energy bands. Also, in view of the similarity between the separations of the B- and D-bands on the one hand and of the B' and D' on the other, the latter being assigned to the experimental D–bands.

A question arises as to the precise way the groups of experimentally observed bands are related to the components of $4f^5 5d$ configuration of Sm^{2+} ions in octa-

hedral environment. The answer is sought in the correspondence already established between these groups of bands and the theoretically predicted A', B', C', and D' bands of the $4f^5(^6FH)5d$ sub-configurations. Evidently, the observed A-, B-, C- and D- bands are connected with that sub-configuration. To further buttress the connection, recourse is made to the coupling scheme used in the theoretical calculation. The lowest group of experimental bands, the A-bands can be assigned to the states

$$|[(\tfrac{5}{2}\tfrac{1}{2})S_2 = 3, L_1 = 5]J_2 = 3, \Gamma_5; {}^{\alpha_2}\Gamma_{4u}\gamma\rangle,\ \alpha_2 = 1,2,3 \qquad (5.17)$$

while the C-bands can be assigned to states

$$|[(\tfrac{5}{2}\tfrac{1}{2})S_2 = 3, L_1 = 5]J_2 = 3, \Gamma_5; {}^{\alpha_2}\Gamma_{4u}\gamma\rangle,\ \alpha_2 = 1,2. \qquad (5.18)$$

By these assignments it is never suggested that these bands are characterised only by these pure basis functions. Rather, the idea being conveyed is that functions of this type contribute most to the characteristics of the bands, particularly, their spectral positions. Definitely, the bands depict the energy level positions characterised by linear combinations of pure basis functions. Other basis functions most likely to contribute to the spectral positions and intensities of the A- and C-bands through admixing by spin-orbit interactions and possibly the odd components of the crystal field potential operators are those for which $S_2 = 2$ replaces $S_2 = 3$ in the expressions above. It is possible therefore to obtain a rough estimate of the value of $10Dq$ for any of the crystal systems studied. On the average, this is given by the separation of the gravimetric centres of the A-bands and C-bands.

Following a similar argument the other groups of experimental bands can be assigned to states for which $L_1 = 3$ replaces $L_1 = 5$ in expression (5.17) (for B–bands) and expression (5.18) (for D–bands). The separation of the centres of gravity of B- and C- bands gives another rough estimate of $10Dq$. In general, the two estimates of $10Dq$ are not the same although, they are of the same order of magnitude as have previously been indicated by Johnson and Sandoe [80] in their semi-quantitative study of RT spectra of some alkali halides doped with Sm^{2+}. For each crystal system, the two estimates are different. However they indicate a range of values within or close to which the true $10Dq$ value can be located. An important inference to be drawn from the different $10Dq$ estimates is that inter-electronic interactions are

important in determining the energy level positions of Sm^{2+} ions in the crystals studied.

An additional justification for assigning the B-bands to states derived from $4f(^6F)5d$ sub–configuration comes from the evidence that in trivalent samarium salts, the spectral positions of states of predominantly ^6F (90% or above) in character are located in energy terms, at 5767 cm^{-1}, 6305 cm^{-1} 7049 cm^{-1}, 8001 cm^{-1}, 9078 cm^{-1} and 10 469 cm^{-1} above $4f^5(^6H_{5/2})$ ground state of $4f^5$ configuration of Sm^{3+} ions. A simple average puts the centre of gravity of the observed $4f^5(^6F)$ states at 7778 cm^{-1} above the $4f^5(^6H_{5/2}$ ground state. This value compares well with the separation of the B-bands from A1- band as indicated in Table 5.7. Moreover, the study by Nara and Schlesinger [67] indicates that the lowest observed groups of levels of the ^6F_J multiplets of Sm^{3+} ions in CaF_2 are located at between 6357 and 6757 cm^{-1} above the $^6H_{5/2}$ ground state. Band assignments analogous to the ones made here have previously been made for the first three bands in the absorption spectra of Sm^{2+} ions in CaF_2, SrF_2 and BaF_2 crystals by Yanase [104].

With observed absorption bands assigned in this way to the $4f^5(^6FH)5d$ sub–configuration of Sm^{2+} ions, a clear picture emerges. The electronic states of the $4f^5(^6FH)$ core sub–configuration are seen to couple through electrostatic interaction (of direct Coulomb and exchange type) to the states γ_3, γ_5 of the 5d electron, which are strongly perturbed by the octahedral crystal field. The grouping of the energy bands (and hence observed energy levels) is determined mostly by the electrostatic interaction between pairs of electrons in the $4f^5$ core electron system and crystal field interaction. The spreading out of the energy levels and hence the occurrence of many absorption bands result from the direct Coulomb and exchange interactions between the $4f^5$ core electrons and the lone 5d electron as well as spin orbit interactions within the electron systems of the two sub-shells. This is depicted schematically in Fig 5.6 for the octahedral crystal field. Because of the very large number of states and also because spin-orbit and direct Coulomb and exchange interactions are of the same order of magnitude, their effects are grouped together in the schematic diagrams. In the above representations attempts were made to reflect the fact that the theoretical energy levels do in fact overlap. Obviously there are many

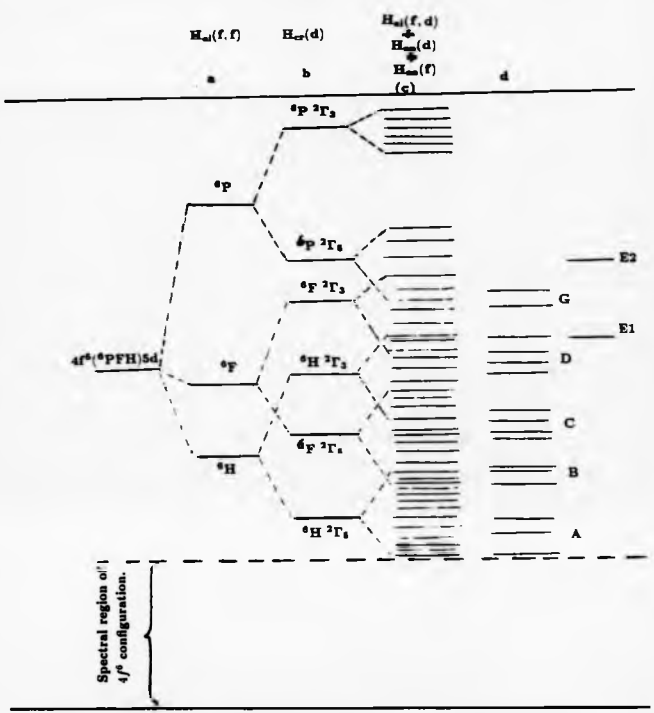

Fig 5.6 Theoretical energy level scheme for $4f^6(^6PFH)5d$ sub-configuration of Sm^{2+} ions in octahedral crystals field. Effects of various perturbation interactions are illustrated. (a) Electrostatic interaction within $4f^5$ electron system, $H_{el}(f,f)$, (b) Crystal field perturbation on d-electron states $H_{cr}(d)$, (c) Combined effects of direct Coulomb, exchange and spin-orbit interactions, $H_{el}(f,d) + H_{so}(nl)$.

more energy levels than indicated in the last but one column. The last column depicts the typical structure of an experimental spectrum. The suffix 2 on Γ_3 or Γ_5 only indicates that the functions are characterised by spin half associated with the 5d electron. Johnson and Sandoe [80] do in fact suggest an analogous scheme for the $4f^5(^6FH)5d$ sub–configuration of Sm^{2+} ions in CaF_2 crystals. The scheme suggested here is more extensive than those of the authors referred to above because of the inclusion of the $4f^5(^6P)5d$ sub–configuration. The justification for including the latter will be given in the next subsection.

Of the 450 energy levels predicted with the aid of the above model and group theory, symmetry selection rule permits electronic transitions to only $135\Gamma_{6u}$ levels from the $^7F_0(\Gamma_1 g)$ ground state of $4f^6$ configuration. Even at that, only a few of these can be observed because of the additional selection rules discussed in section 5.3.1. (vide Eqn 5.15). Fig 5.7 shows the experimental energy level structure of the $4f^5(^6PFH)5d$ and $4f^5(^6FH)6s$ sub–configurations of Sm^{2+} in $KX : Sm^{2+}$ and $RbX : Sm^{2+}$ crystals. As will be made clear later, the levels labelled E1 and E2 are ascribed to the latter sub–configuration while the rest of the levels belong to the former.

The theoretical calculations done in this study were based on the above model. Judging from the correspondence so far established between the theoretical spectrum of the $4f^5(^6FH)5d$ sub–configuration and the observed absorption spectra of Sm^{2+} ions in the six alkali halide crystals, it is evident that the model successfully explains the gross features of the observed spectra in spectral regions below 40 000 cm^{-1}. Having said that, it is instructive to comment on the occurrence of three well resolved absorption bands in the lower regions of the spectrum. It has been suggested by some authors [63,80] that the resolution of these bands (the A-bands) into three and the elaborate fine structure of the other bands are evidence of crystal field splitting due to the orthorhombic distortion of the octahedral symmetry at the site of the Sm^{2+} ions arising from the charge compensating vacancies. In other words, the octahedral approximation usually applied to $4f^N5d$ configurations of rare earth ions in alkali halide crystals may break down in the instance of Sm^{2+} ions. That the multi-band nature of the lower part of the spectrum is expected from the theoretical

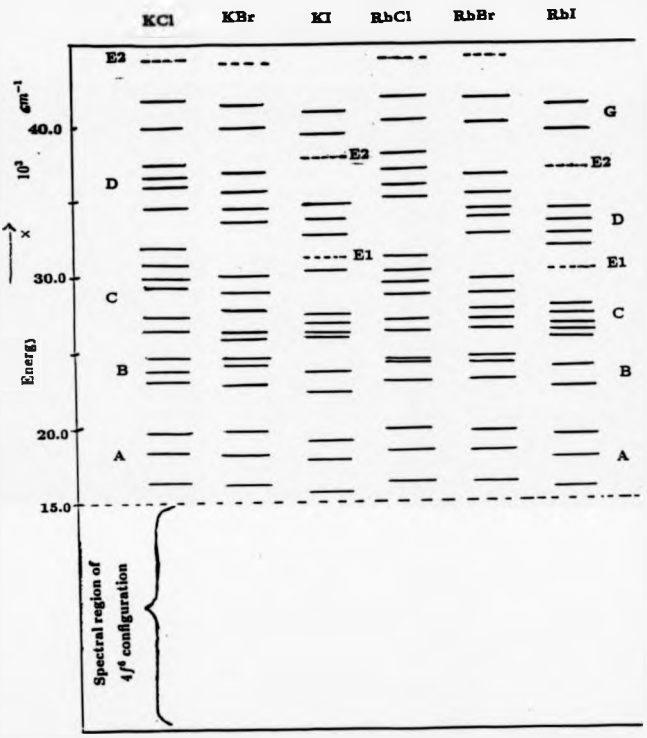

Fig 5.7 Experimental energy level structure of the $4f^5(^6PFH)5d$ and $4f^5(^6FH)6s$ sub-configurations of Sm^{2+} ions in KX and RbX (X = Cl, Br, I) crystals. Levels labeled E1 and E2 correspond to electronic transitions to states of $4f^5(^6FH)6s$ sub-configuration from the $^7F_0(4f^6)$ ground state while the rest correspond to transitions to the states of the $4f^5(^6PFH)5d$ sub-configuration. (See text.)

analysis is very evident. What is not expected however is that A2-band would have a comparable transition intensity as A1-band. Theory predicts that levels corresponding to A2-band would have relative transition intensities about one-third in magnitude of that of a level corresponding to A1-band. The possible reasons for such a discrepancy between predicted and observed spectral intensities will be discussed in a later section. Judging from the closeness of the predicted energy levels with high relative intensities, it is expected that in the high energy region of the spectrum, structured absorption bands would be obtained experimentally. The observed structure of the experimental spectra are therefore predicted by theory based on the octahedral approximation.

Attention may now be drawn to the fine structure exhibited by the A1-band and A2-bands in the second derivative spectra of $KCl : Sm^{2+}$ and A1 band in the those of $KBr : Sm^{2+}$ and $RbCl : Sm^{2+}$ crystals. They are interpreted as due to vibronic interactions. Although the temperature at which measurements were made was too high for the vibronic bands to appear in the absorption spectra, evidence of their occurrence was picked up in the second derivative spectra. Earlier observation of elaborate vibronic spectra of Sm^{2+} ions in alkali halide crystals have been made at 10 K [64] and 4.2 K [63]. It is not possible at athis stage for further interpretation to be given to the fine structure bands since they were not observed in the absorption spectra.

5.6.2 The G and E Absorption bands

In previous studies of optical absorption by Sm^{2+} ions in some alkali halide crystals absorption bands corresponding to those labelled G1 have not been positively identified even though they may be present in the spectra studied [50,80]. The insight gained through studying their behaviour across the two alkali series at room and liquid nitrogen temperatures has made possible their identification as Sm^{2+} bands. Obviously they do not belong to the $4f^5(^6FH)5d$ sub–configuration of Sm^{2+} ions. Nevertheless, they are ascribed to $4f^5(^6P)5d$ sub–configuration for the following reasons. Throughout the two alkali series, the intensity of the G1-band relative to that of the nearby C- and D-bands is nearly constant indicating that they are Sm^{2+}

bands. Although the temperature induced displacements of the G1-band is small for a few of the crystal systems the trend for all the systems studied is towards lower energies as the crystal is cooled from RT to LNT. Moreover, the G1 bands as well as the G2-bands share with the A-bands and to some extent the B-bands the trend towards lower spectral energies with increase in d for any given alkali series. Also illuminating is the fact that as with the A- and B- bands, the G-bands lie at higher energies in $RbX : Sm^{2+}$ systems than in corresponding halide host among $KX : Sm^{2+}$ systems.

All these suggest that G1-bands may be the lowest band of the $4f^5(^6P)5d$ sub–configuration of Sm^{2+} ions in the crystals. In free space, the lowest observed energy level of $4f^5(^6H)5d$ sub–configuration is located at 26 283.55 cm^{-1} relative to the ground state of the $4f^6$ configuration [102]. But in the crystal series studied, the lowest energy bands observed experimentally lie at energies ranging from 15 785 cm^{-1} (for $KI : Sm^{2+}$ crystals) to 16 447 cm^{-1} (for $RbCl : Sm^{2+}$ crystals). This means that crystal field effects cause a depression of the centre of the sub–configuration by an amount in the order of 10 160 cm^{-1}. Allowing for a depression of such a magnitude for the $4f^5(^6P)5d$ sub–configuration (although it is recognised that there may be differential sub–configurational shifts), one would expect the lowest energy level of that sub–configuration in alkali halide-crystals to be at about 41 000 cm^{-1} since it is at 51 160.8 cm^{-1} in free space [102,72]. Considering the approximations made, this value compares well with the spectral positions of the G1-bands relative to the ground state of the $4f^6$ configuration (vide Tables 5.6(a), (b)).

A search for an additional justification was, however, made. Wybourne[74] , using experimental data from various sources, on the absorption and fluorescence spectra of trivalent samarium salts measured at liquid helium temperatures identifies an energy level of Sm^{3+} ions located at 23 780 cm^{-1} above the lowest energy level of $4f^5(^6H)$ sub–configuration. The wave functions describing that level comprises a linear combination of LS-coupled basis functions whose components include 35% $^6P_{3/2}$ multiplet. A next higher level predicted to be located at 25 035 cm^{-1} above the $4f^5(^6H_{5/2})$ ground state and which is strongly $^6P_{3/2}$ (65%) in character was not experimentally observed. The similarity between the separations of the G1-

band from A-band with the energy level of Sm^{2+} ion lying at 23 780 cm^{-1} above the ground state of the $4f^6$ configuration further justifies this assignment of the G-bands.

The G-bands can therefore be associated with basis functions of the form

$$|[(\frac{5}{2}\frac{1}{2})S_2 = 3, L_1 = 1]J_2 = 3, \Gamma_5; ^{\alpha_2}\Gamma_{4\alpha}7\rangle \ , \ \alpha_2 = 1,2,3 \qquad (5.19)$$

The bands correspnding to the states

$$|[(\frac{5}{2}\frac{1}{2})S_2 = 3, L_1 = 1]J_2 = 3, \Gamma_3; ^{\alpha_2}\Gamma_{4\alpha}7\rangle \ , \ \alpha_2 = 1,2 \qquad (5.20)$$

were not observed experimentally. They are likely to lie in the vacuum ultra violet.

Because E2 band is present in all the spectra of the crystals studied and also because in any given host crystal, its transition intensity bears a constant relation to any of the other bands, it is here associated with photon absorption by Sm^{2+} ions in the crystals. The spectral position of the band is host dependent. In general, its position is displaced to lower energies as d increases, a trend also exhibited by A-, B- and G- bands. (Notice however that the trend is disrupted in $RbX : Sm^{2+}$ series by E2 band in $RbBr : Sm^{2+}$ system lying at slightly higher energies than in $RbCl : Sm^{2+}$ system: (vide Table 5.6(b)). In spite of this, it does not share with these other groups of bands the temperature induced displacement towards lower energies as the crystal is cooled from RT to LNT. Rather, in all cases, the E2 bands are displaced to higher energies in such circumstances. This may be indicative of the sensitivity of the E2 band to changes in the crystal field potential.

The puzzle of the origin of the band is sought in the occurrence in the spectra of Sm^{2+} in the iodide crystals of a band labelled E1. The separations of this band from E2 in the spectra of Sm^{2+} ions in the iodide series are comparable to the separations of A1- and B1- bands in those spectra. (vide Table 5.7). Unless this comparability is a coincidence, it strongly suggests that the E-bands have some connection with the ^6FH energy terms $4f^5$ configuration. One way this can occur is through the $4f^56s$ configuration. Nominally, electric dipole transition to states of this configuration from the ground configuration, $4f^6$ is forbidden on the grounds of the $\Delta l = \pm 1$ selection rule. As pointed out in the discussion on the $4f^{13}6s$ configuration of Yb^{2+} (subsection 4.6.5) this selection rule may break down owing to the orthorhombic

distortion of the octahedral symmetry at the site of the Sm^{2+} ions. It was observed that the relative transition intensity of an E2 band occurring in the spectrum of an iodide host crystal when compared with A1-band is greater than that of any E2 band in spectrum of either the bromide or chloride hosts crystals. In $KX : Sm^{2+}$ series, the relative intensities of the E2 bands follow the spectro–chemical series of ligand ions :

$$Cl < Br < I$$

This points to a possibility of covalency playing a central role in the occurrence of the E-bands. If this is the case, a model analogous to that used to explain their occurrence in the spectra of Yb^{2+} ions in RbX crystals is proposed here.

Following the arguments of subsection 4.6.5, the $6s$ atomic orbitals of Sm^{2+} ions are thought to form bonding (σ) and anti-bonding ($\sigma*$) MO's with the $(n+1)s$ atomic orbitals of the ligand halogen ions. The only difference in the details of the interactions involving Sm^{2+} and Yb^{2+} ions comes through the sub–states of the $4f^N$ core configuration. In the case of Sm^{2+} ions, the ${}^6H_{J_1}$ ($J_1 = 5/2, 7/2, ..., 15/2$) and ${}^6F_{J_1}$ ($J_1 = 1/2, 3/2, ..., 11/2$) core multiplets couple with bonding MO's to form the bonding states $4f^5({}^6H)6s\sigma(\Gamma_{1g})$ and $4f^5({}^6F)6s\sigma(\Gamma_{1g})$. It is the electronic transitions to these states that cause the absorption experimentally observed. On this model it is expected that the E-bands will exhibit greater relative intensity in the more covalent crystals than in the more ionic ones. For the $KX : Sm^{2+}$ crystals, this was observed as noted earlier. In the case of $RbX : Sm^{2+}$ systems however, the E2-band shows the greatest relative transition intensity in $RbI : Sm^{2+}$ crystals but its intensity in the spectrum of $RbBr : Sm^{2+}$ is slightly less than that $RbCl : Sm^{2+}$ crystal system. Table 5.9 illustrates these points. Unfortunately the E1-band was not identified in the spectra of chloride and bromide host crystals. If the model proposed is correct, they are expected to lie within the D-bands in these spectra and their transition intensities are expected to be low.

5.6.3 Adequacy of the theoretical analysis

Having established a qualitative and semi-quantitative agreement between the proposed model and the experimental spectra, it remains to examine the results of the

Table 5.9 Spectral Positions and Relative Transition Intensities of E1- and E2-Bands in the Absorption Spectra of $KX : Sm^{2+}$ and $RbX : Yb^{2+}$ ($X = Cl, Br, I$) Crystals at RT and LNT. $\nabla(E1, E2)$ is the Separation Between E1- and E2- bands at LNT.

Crystal	E– Band			E– Band			
	Spectral Position (cm^{-1})		Relative Intensity	Spectral Position (cm^{-1})		Relative Intensity	$\nabla(E1, E2)$
Host	RT	LNT	at LNT	RT	LNT	at LNT	(cm^{-1})
KCl	–	–	–	44 298	44 346	16	–
KBr	–	–	–	44 248	44 298	27	–
KI	30 864	31 299	48	37 665	38 023	79	6 724
RbCl	–	–	–	44 248	44 444	46	–
RbBr	–	–	–	44 444	44 643	26	–
RbI	–	30 395	42	36 969	37 175	75	6 780

detailed theoretical analysis of the spectra of $KX : Sm^{2+}$ and $RbX : Sm^{2+}$ crystals. It has already been noted that a satisfactory agreement was found between calculated and experimental energy levels of Sm^{2+} ions in the entire crystal series. In extreme cases deviations of up to 800 cm^{-1} were found. For systems of this type involving broad absorption bands the deviations are not adverse. Considering that the mathematical techniques adopted in the calculation procedures are approximate, with inherent errors associated with them as mentioned in section 5.5, the agreement is good.

It is in no way being suggested however that such inherent errors can explain all the observed deviations as well as the discrepancies between the predicted and observed relation transition intensities of some of the bands. In all the crystals, the most intense absorption bands were observed among the C-bands. Predicted spectra for the chloride crystal systems show that the theoretical level corresponding to C2-band is the strongest. In all the other crystal systems, the predicted relative transition intensity of the theoretical level corresponding to A1-band is the most intense.

Recalling the approximations and assumptions made in the theoretical calcualtions, it can be easily appreciated that the trauncation of the $4f^5 5d$ configuration may in part account for the deviations and discrepancies. It is quite possible for the wavefunctions of electrons in the higher lying levels of the configuration to be admixed to the wave functions of those in the $4f^5(^6FH)5d$ sub–configuration. Since it has been shown that the G-bands can be ascribed to the $5f^5(^6P)5d$ sub–configuration, it is natural to expect that the wavefunction of electrons in those sub-levels may overlap or mix with those of electrons in the lower states. Such mixing could result in some shifts in energy level positions and also some changes in the distribution of transition intensities. This is more so for the upper levels of the $4f^5(^6FH)5d$ sub-configuration.

In his analysis of the spectra of trivalent samarium salts, Wybourne[74] identifies some higher-lying quartets ^4DFGH terms of $4f^5$ configuration admixed with those of the lowest sixtets ^6FH. Because the admixed wavefunctions are small, they are unlikely to introduce any serious limitations to the model adopted in this study.

However, their influence could result in small modifications in the observed transition intensities since the latter are very sensitive to wave function distortions. Also identified in that study some quartets, ^4FGI, lying below the ^6P_J manifold, but over 8000 cm^{-1} above the highest level of the ^6P_J manifolds. Inclusion of the states of these multiplets will greatly complicate the problem but it is not difficult to appreciate that the coupling of any of these quartet states to the states of the 5d–electron in a crystal results in wavefunctions of the type expressed in Eqn (5.1), with $S_2 = 1, 2$. Electric dipole transition to such states from the ground state of the $4f^6$ configuration are forbidden in view of the $\delta(S_g, S_2)$ selection rule.

What could happen, however, is that the states of these sub–configurations could become admixed with the states of interest through spin-orbit interaction. Such a mixing could also result from the orthorhombic distortion of the octahedral site symmetry of the Sm^{2+} ions. Considering the extent of agreement between experimental and theoretical energy level positions, it appears that the most likely effect of the $4f^5(^4FGI)$ sub-configuration could be some re-distribution of transition intensities. Any changes in energy level positions resulting from such a may not be significant.

Another facet of the problem relates to the fact that the absorption spectra were obtained at LNT. But the calculation scheme assumes that the observed spectra result from electronic transitions from the $^7F_0$ ground state of Sm^{2+} ions. Fluorescence spectroscopic studies reveal that the ground states is separated from the next excited state, $^7F_1$, by about 261.0 cm^{-1} in $RbBr : Sm^{2+}$ [69], 288.1 cm^{-1} in $KCl : Sm^{2+}$ 288.9 cm^{-1} in $KBr : Sm^{2+}$ 287.6 cm^{-1} in $RbCl : Sm^{2+}$ [64] crystals. It is possible that at LNT, the $^7F_1$ level of Sm^{2+} ions in these crystals become thermally populated. Thermal population of a state of energy E_n follows the Boltzmann law: $exp(-E_n/kT)$ and if $E_n < kT$, occupation of levels of energy E_n becomes possible. Using the value of k given by Dieke [3] it can be seen that at energy levels of 54 cm^{-1} or smaller above the ground state could be occupied at 77 K. It is, therefore, 'unsafe' to assume that all the observed $4f^6 \rightarrow 4f^55d$ transitions originate from the $^7F_0$ ground state. Experimental observations have shown that some absorption bands in $CaF_2 : Sm^{2+}$ become slightly more intense with increase temperature while some others diminish in intensity [62]. Indeed, similar observations were made in respect

of the A1- and A2- bands since as noted earlier, A2 bands tend to be slightly more intense than A1 bands at RT while at LNT, the reverse is the case.

These facts do not however invalidate the model used in the calculation and the assignments of bands made for the following reasons. Group theoretical analysis shows that electric dipole transitions originating from the $^7F_1(\Gamma_{4g})$ state of Sm^{2+} ions in octahedral environment are allowed to the

$$35\Gamma_{1u} + 90\Gamma_{3u} + 135\Gamma_{4u} + 135\Gamma_{5u}$$

states of the $4f^5(^6FH)5d$ sub–configuration. Consideration of such transitions into the theoretical calculations introduces formidable difficulties. However, not much will be gained by their inclusion since the basic structure of all the spectra at RT are maintained at LNT. Moreover, Dieke[3], points out that for an electronic transition from a thermally populated level about 246.4 cm^{-1} above the ground state of an ion, the transition intensity measured at LNT is about 10^{-2} times what it should have been if the transitions had taken place from the ground state. This is corroborated by the evidence that the spectral intensity of the 14 118 cm^{-1} fluorescence line in the spectrum of $CaF_2 : Sm^{2+}$ crystals was reduced by a factor of 10^2 and that the 14 353 cm^{-1} line in $SrF_2 : Sm^{2+}$ spectrum by a factor of 11, when the sample temperatures were increased from 4.2 K to 77 K [62].

In view of the above, one can conclude that at LNT transitions originating from the thermally populated energy levels will be weak. Their most likely effect will be a modification of the distribution of transition intensities from what they would have been if those levels were depopulated.

Using the octahedral approximation, it has been established that the multi-band structure of the spectra of Sm^{2+} ions in alkali halide crystals is expected. Also predicted by theory are the observed band groupings. It appears unnecessary therefore to invoke the orthorhombic distortion of the octahedral symmetry at the site of the ions to explain any of the main features of the spectra. However, because of the very large number of quantum states of the $4f^5(^6FH)5d$ sub-configuration which happen to lie close to each other, it cannot be ruled out that crystal field potentials of odd order associated with the C_{2v} point group could modify the wave functions of the electrons in these states [318]. A possible consequence of the admixing of wave

functions associated with these states is a re–distribution of transition intensities of the various energy levels. The contention here ins that the effect of the orthorhombic distortion on the energy level positions of Sm^{2+} ions in these crystals will likely be slight. The major influence may consist, in some intensity re–distribution according to the degree of overlap of the wavefunctions of the optically active electrons.

5.6.4 Crystal field effects

Some explanation is hereby sought for the observed spectral displacement of the A-, B- and G- bands to lower energies as the lattice parameter d increases for a given alkali metal series. It can be recalled that similar observation was made in respect of A2- and A6- bands in the spectra of $RX : Yb^{2+}$ crystals. In that case, it was possible to obtain the difference between the centre of gravity of the free-ion states giving rise to the Γ_{4u} crystal levels and the centre of gravity of these levels in the crystals. Such a quantity constitutes a configurational depression since the centre of gravity of the levels in a crystal is lower. Results indicate that configurational depression increases as d increases. The conclusion reached was that the differential configurational shift may be connected with spectral displacements of the A2- and A6-bands in the spectra of Yb^{2+} ions as d increases.

Although the gravimetric centres of Γ_{4u} levels of Sm^{2+} ions in each of the crystal systems were obtained, such a direct connection as above could not be established in the case of Sm^{2+} spectra since the actual centre of gravity of the $4f^5(^6FH)5d$ sub-configuration of free Sm^{2+} ions is not known. However, if the conclusion in respect of Yb^{2+} ions is correct, one is lead to suggest that the same trend as it regards configurational depression may apply in the case of Sm^{2+} ions in the crystals studied.

Also found was that for a given anion series, an opposite effect takes place. In general, spectra displacement of A-, B- and G-bands to higher energies with increase in d was observed. This evidently complicates the picture and suggests that configurational depression may have no simple relationship with d. Ivoilova and Leushin [321] conclude from results of their analytical studies that exchange interactions between the $4f^{13}5d$ electrons of Yb^{2+} ions and those the ligand fluoride

ions account partly for the observed dependence of shifts in the centre of gravity of the $4f^{13}5d$ configuration of Yb^{2+} ions in MeF_2 crystals (Me = Ca, Sr, Ba). This is indirectly linked with an earlier suggestion that the observed spectral displacements of the low energy bands of Sm^{2+} ions in KX and NaX crystals with changes in d may be connected with covalency effects [63].

For any of the alkali series, the value of Dq obtained in respect of Sm^{2+} ions follows the spectro–chemical series already established for Yb^{2+} ions in RbX crystals in subsection 4.6.2. Plots of Log Dq against Log d show a linear relationship between the two quantities for each alkali series as shown in Fig 5.8. From these graphical representations, it was concluded that $Dq \propto d^{r_p}$ where r_p is -2.428 ± 0.005 for the potassium series and -2.424 ± 0.004 for the rubidium series. These r_p^{th} power laws deviate he expected proportionality of Dq with d^{-5} on account of the point ion model crystal field theory. In subsection 4.6.2, some reasons were adduced for the failure of that model to predict the values of Dq for the $4f^{13}5d$ configuration of Yb^{2+} ions in RbX crystals. Similar explanations apply in the case of Dq values for the $4f^{5}5d$ configuration of Sm^{2+} ions in KX and RbX crystals.

5.6.5 Slater-Condon and spin orbit parameters

The values of the energy parameters F_2, G_1, ζ_{4f} and ζ_{5d} that give the best fit between theoretical and experimental energy levels for each of the crystal systems (as shown in Table 5.8) are host dependent. In general, the F_2 and G_1 values follow the familiar spectrochemical series of ligand ions but in reverse order. Thus $Cl > Br > I$. No clear trend was however obtained for the values of ζ_{4f} and ζ_{5d}. In the past, the dependence of the values of these parameters on crystal host has manifested itself in the form of differential reduction of their values from what they are known to be in free space. As discussed in subsection 4.6.3 in respect of Yb^{2+} ions in RbX crystals, such reductions have been attributed to nephelauxetic effect. Although the values of these parameters depend on host in the case of Sm^{2+} ions, they are in general greater than the interpolated estimates attributable to free Sm^{2+} ions. It is acknowledged that those estimates serve only as trial parameters and that it is not strictly correct to regard them as the free ion values. Nonetheless, the values obtained for them in

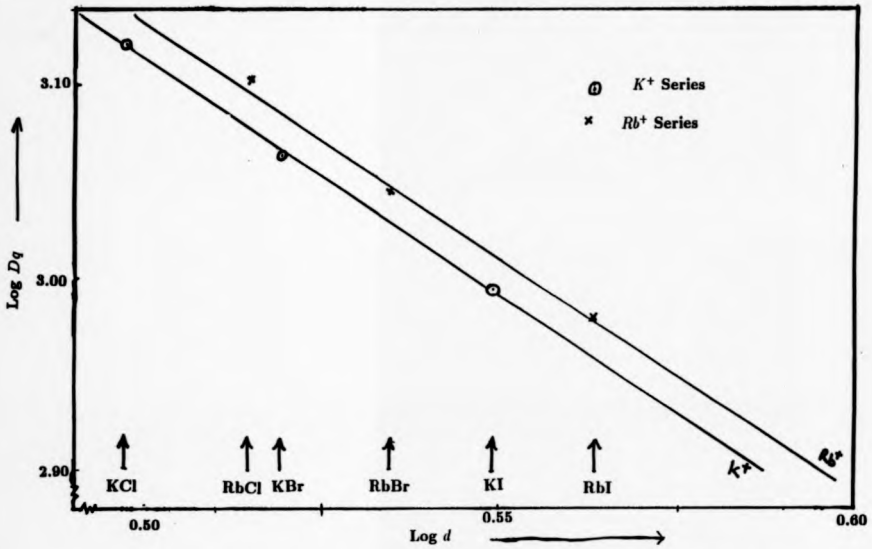

Fig 5.8 Relationship between Log Dq and Loq d for Sm^{2+} ions in KX and RbX (X = Cl, Br, I) crystals.

the parametrisation process are in the range expected for Sm^{2+} ions in free space. On the basis of this, it is a matter for speculation to suggest that the up to 40% reduction in Slater-Condon parameters observed for $4f^{13}5d$ configuration of Yb^{2+} in this study and for corresponding mixed configurations of Yb^{2+}, Eu^{2+} and Tm^{2+} ions in other studies [6,82,101,259] as these ions enter a crystal, have not been observed for Sm^{2+} ions. Such a speculation is fraught with some difficulties, particularly as it has been shown that the parameter values are host dependent.

In their discussions of the electronic states of Eu^{2+} ions in CaF_2 crystals, Yanase and Kasuya [92] and Asano and Nakao [76] find no need to make allowance for reduction in F_k, and G_k parameters owing to nephelauxeteic effect. In those studies as well as in that of Yanase[104] in which he discusses the coarse structure of the spectra of Sm^{2+} ions in CaF_2 crystals, the assumption is made that the main contribution of the operator $H_{ai}(f,d)$ to the energy of the system is through the isotropic exchange interaction. This results via the double tensor operator $\mathbf{V}_f^{(10)}$. The anisotropic exchange interaction (contributed through the double tensor operators $\mathbf{V}_f^{(1k)}$ $(k = 1,...,4)$) is believed to partially cancel the contribution by the direct Coulomb interaction. It is to this partial cancellation that the previously observed reduction in G_k and F_k parameter values are ascribed. Even though in this study, the Yanase-Kasuya model was used in defining the basis functions describing the states of $4f^5 5d$ configuration of Sm^{2+} ions, there was no explicit assumption that such a partial cancellation mechanism is operative. The analysis of the spectra follows a different procedure to those of the other authors.

Having noted that, the possibility of the nephelauxetic reduction of F_k, G_k and ζ_{5d} values being absorbed in the calculation procedure cannot be overlooked. This follows from the fact that any element of an energy matrix consists of two parts, the radial and angular parts. F_k, G_k ζ_{4f} and ζ_{5d} parameters are among the radial parts of interest. Attention is here drawn to the fact that the calculation procedure involves the introduction of the generalised W[ ] and S[ ] coefficients in order to reflect the coupling of the $5d$ electron states to the crystal lattice. Because these coefficients are in general less than unity, the angular components of the matrix elements of the direct and exchange interaction matrices as well as of $H_{ao}(d)$ matrix

will be smaller than what they would have been if the calculations were done in pure LS coupling scheme. As a result, optimised values of F_k, G_k and ζ_{5d} may not reflect any significant reduction due to nephelauxetic effect as is the case in those studies cited above.

5.7 Conclusions

Apparently for the first time, Sm^{2+} ions have been successfully incorporated into KX and RbX crystals by diffusing samarium vapour into the crystals at high temperatures. Each Sm^{2+} ions occupies a substitutional lattice site which is distorted from octahedral symmetry by the presence of a charge compensating cation vacancy in the $< 110 >$ direction.

Excitation of the Sm^{2+} ions in these crystals with radiation in the visible and ultraviolet range leads to absorption spectra consisting of six groups of broad bands. By defining the electronic states of the $4f^5(^6FH)5d$ sub–configuration of Sm^{2+} ions in the Yanase-Kasuya coupling scheme, theoretical analysis of these spectra which ignores the orthohombic distortion of the site symmetry of the Sm^{2+} ions establishes a correspondence between the predicted groups of energy levels and the experimental spectra. On the basis of this the first four groups of bands in each of these spectra were ascribed to electronic transitions from the $^7F_0$ ground state of $4f^6$ configuration to the states of $4f^5(^6FH)5d$ sub-configuration. Also predicted by the theoretical calculations is the multi-band nature of the absorption spectra. A model was proposed which satisfactorily explains the gross features of the observed spectra and further extends the band assignments to the higher lying G-bands which are ascribed to $4f^6(^7F_0) \rightarrow 4f^5(^6P)5d$ transitions.

Even though $4f^6 \rightarrow 4f^56s$ electronic transitions are not allowed, in the electric dipole approximation they could become allowed through the distortion of the site symmetry of the Sm^{2+} ions and/or through a mechanism in which the states of the $6s$ electron are strongly perturbed by the crystalline environment. The occurrence in the spectra of the E-bands is attributed to this type of mechanism. A model which adequately explains this conceives the $6s$ atomic orbitals as overlapping with the $(n+1)s$ atomic orbitals of the ligand ions resulting in the formation of σ bonding

and $\sigma*$ anti–bonding MO's.

Detailed analysis of the absorption spectrum of each of the crystal systems shows a satisfactory agreement between the predicted and observed energy level positions. Discrepancies between the calculated and observed relative transition intensities are explained on the basis of the approximations and assumptions made in the theoretical calculations. It is believed that better agreement between theory and experiment could be obtained if the electronic states of the $4f^5(^6P)5d$ sub–configuration were included in the calculation. As a refinement to this work, this is suggested for future work. For more significant improvement to be obtained, a reliable way of estimating the effect of the orthohombic distortion on intensity distribution has to be devised. Further refinement could be achieved if the absorption spectra are measured at temperatures lower than 77 K, preferably 4.2 K. This will eliminate the chance of higher levels of the ^7F_J manifold of the $4f^6$ configuration being thermally populated.

The values of Dq obtained for Sm^{2+} ions in the crystals not only show a dependence on the nature of the anions of the host crystal but also follows an r_p^{-5} power relationship with lattice parameter d, for a given alkali metal series, r_p being -2.428 ± 0.005 for the potassium series and -2.424 ± 0.004 for the rubidium series.

Equally host dependent are the values of Slater-Condon and spin orbit parameters that give the best fit between experiment and theory for each of the crystal hosts. The values of F_2 and G_1 follow the same spectrochemical series as Dq.

Chapter 6

The Effect of Thermal Annealing on the Absorption Spectra of $RbBr : Yb^{2+}$ Crystals

6.1 Introduction

All along, the orthorhombic distortion of the octahedral crystal field at the site of the substitutional Yb^{2+} ions has been ignored. It has been found that the octahedral approximation used is quite reasonable. But at a point during the study, it was considered worthwhile to check out this approximation using a certain procedure. When a crystal is doped at a high temperature and then quenched, it is assumed that the incorporated impurity ions are frozen in at that state and at the sites in which they were at doping temperature. Consequently they are assumed to be atomically dispersed within the crystal, each impurity ion being out of range of the influence of the others.

However, it is now clear that in the case of a divalent impurity ion in an alkali halide crystal, at room and lower temperatures, a cation vacancy is needed most probably at a cation lattice site close to the site of the substitional impurity ion so as to preserve local charge neutrality. But at high temperatures (about 300 ^{0} C) it has been shown [301] that for Eu^{2+} in $KCl : Eu^{2+}$ system, any charge

compensation need not be localized and that the effective local symmetry of the substitutional impurity ion is octahedral. The vacancies are conceived as moving in such a manner that they are not attached to any particular impurity ion. Using the above experimental evidence as a guide, it was decided to check the possibility of obtaining the high temperature spectra of $RbX : Yb^{2+}$ (X=I, Br, Cl) crystals and of comparing them with those of quenched crystals measured at room and liquid nitrogen temperatures. While in pursuit of this idea, it was recognised that the effect of thermal broadening of the absorption bands could obscure the weak bands, particularly the B-bands. Nevertheless, it was hoped that the high temperature spectra could be detailed enough to make comparison possible.

Although the results of the high temperature measurements that followed were inconclusive, the chance finding that the room temperature spectrum of $RbX : Yb^{2+}$ crystal cannot be recovered after measurements were done at temperatures above 200^0 C opened up new grounds for investigation. Indeed, there was evidence that Yb^{2+} ions exist in different phases in these crystals at different elevated temperatures.

In this chapter, therefore the background to this evidence is reported and the results of subsequent experiments performed using $RbBr : Yb^{2+}$ single crystals subjected to a variety of heat treatments are also reported and discussed.

6.2 Background to heat treatment experiments

6.2.1 High temperature spectra of $RbBr : Yb^{2+}$ crystals

The high temperature experiments were designed to measure the absorption spectra of Yb^{2+} ions in $RbX : Yb^{2+}$ crystals using the optical absortpion cell already described. It was hoped that the site symmetry of the Yb^{2+} ions would approximate more closely to the octahedral symmetry assumed in the calculations. Incidentally, the room temperature spectrum of the crystals changed after measurements at temperatures above 200^0 C. Further measurements became difficult because on subsequent measurements, previous high temperature spectra could not be recovered. It was suspected therefore that the crystals could have changed in form as

the temperature was being raised. A decision was taken to obtain spectra at high enough temperature as 550^0 C since the same situation as that noted above was observed at about 350^0 C.

Unfortunately, the absorption spectra of the crystals at temperatures above 375^0 C could not be measured using the Varian DMS-90 UV - visible spectrophotometer. This was because infra-red radiation was emitted by both the framework of the optical cell and the sample and this made the response of the photo cell of the spectrophotometer unreliable. There was also prospects of damage to the machine. However, the high temperature spectra of $RbBr : Yb^{2+}$ crystals are reported below.

As the temperature of the crystal was being raised, A2 and A6-bands of Yb^{2+} in $RbBr : Yb^{2+}$ crystals started to shift to shorter wavelengths while the C4 band started to shift to longer wavelengths. The B-bands however became enveloped within the long wavelength edge of the C-bands. But the phenomenon of interest started at about 200^0 C at which temperature the A-bands started to shift to longer wavelengths and this latter trend continued until a temperature of 358^0 C was reached. Above this temperature no further measurements were taken for reasons already explained. Fig 6.1 shows the spectra of a $RbBr : Yb^{2+}$ crystal at four different temperatures. It illustrates clearly the points previously made. Another interesting finding is that when the spectrum of a sample cooled slowly from a temperature above 200^0 C to room temperature was measured, the original room temperature spectrum (vide Fig 6.1, trace (a)) could not be reproduced. Fig 6.2 illustrates this point. It shows the spectra of the sample of $RbBr : Yb^{2+}$ cooled to room temperature from 252^0 C and 354^0 C. It can be seen that the same bands appear as in the original room temperature spectrum but that these bands are shifted in position. For example the A-bands shift to longer wavelengths while E-bands to shorter wavelengths with the B-bands becoming better resolved. But when the spectrum of the sample was measured at LNT after being slowly cooled from 354^0 C, the difference between the spectrum of the quenched crystal and that of the slow cooled sample becomes more striking. To illustrate this, Fig 6.3 shows the spectrum of the slow cooled sample recorded at LNT. Evidently additional absorption bands have appeared. In fact each of the bands A2, A6, E1 and E2 appears to have a

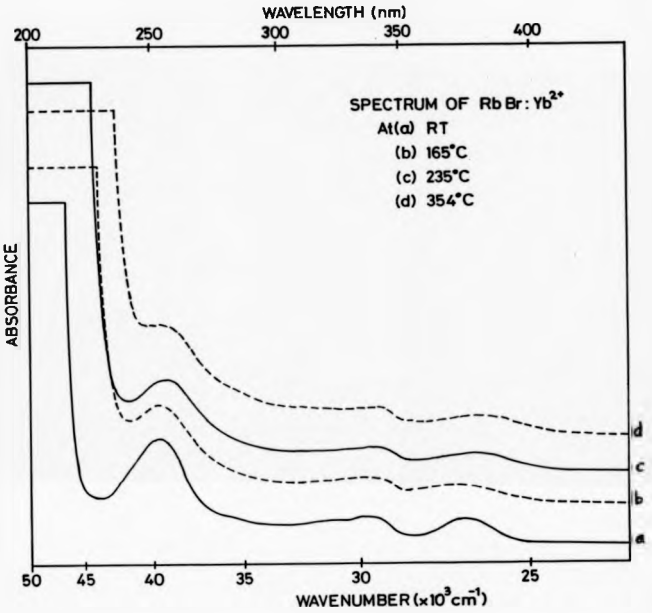

Fig 6.1 Optical absorption spectra of $RbBr : Yb^{2+}$ crystals at different temperatures.

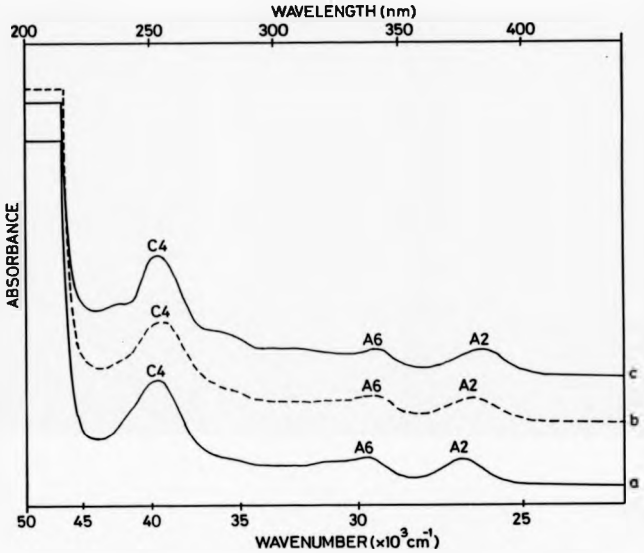

Fig 6.2 Room temperature optical absorption spectra of a $RbBr : Yb^{2+}$ crystal slowly cooled from (b) 252^0 C (c) 354^0 C . (a) is room temperature spectrum of a freshly doped sample.

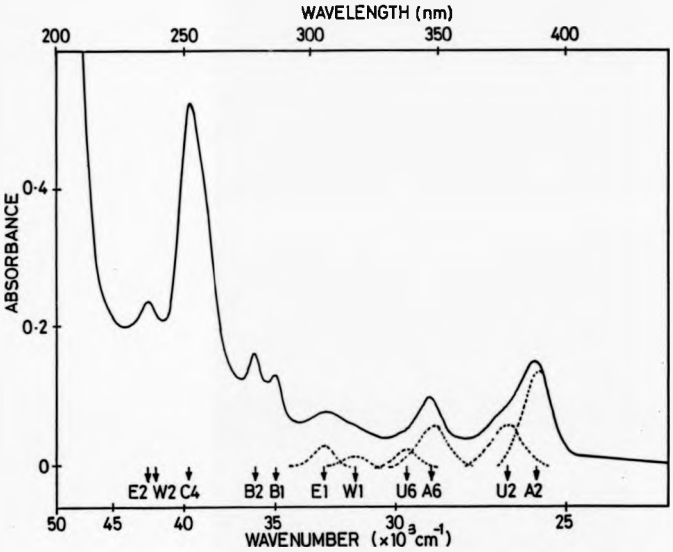

Fig 6.3 Optical absorption spectrum at liquid nitrogen temperature of a $RbBr : Yb^{2+}$ crystal at slow cooled from 354° C to room temperature.

companion band designated as U2, U6, W1 and W2 in Fig 6.3. The dotted traces in the figure show the decomposed low energy bands if the background absorption is subtracted. An estimate of the intensity of U6 band relative to U2 band gives values of 43 and 100 which are comparable to values of 49 and 100 for A6 and A2 bands respectively, in the spectrum of the quenched crystal. Quite remarkably, for the spectrum in Fig 6.3, the intensity of A2-band relative to U2-band is 100:42 while that of A6-band relative to A6-band is 100:42 also.

Tables 6.1 and 6.2 summarise the highlights of the results of this section. Included for comparison are columns for positions of bands in the spectra of quenched crystals at both RT and LNT. The last column in Table 6.1 give the separation of the A2 and C4 bands and is denoted by the parameter ∇. The same parameter values are given in the last row of Table 6.2. It is worth noting that when the slow cooled sample was heated to 600^0 C for two hours and quenched, the original room and liquid nitrogen temperature spectra were reproduced.

6.2.2 Interpretation and discussion of the results of the high temperature measurements

It has been noted that at temperatures below 200^0 C but above room temperature, there is a compression of the Yb^{2+} bands in the spectra of $RbBr : Yb^{2+}$ as evidenced by relative shifts in A- and C- bands in opposite directions. Heating a sample of the crystal causes an increase in its lattice parameter d and hence the crystal field strength $10Dq$ is expected to decrease. Taking a hint from the coupling scheme schematically represented by Fig 4.10, the parameter ∇ is seen to be related to $10Dq$ in the sense that the two parameters change in the same direction. In the temperature range mentioned above, $10Dq$ is therefore expected to have decreased. Thus the decrease in the value of ∇ reported in the last section is expected.

But the increase in ∇ at temperatures above 200^0 C to values above its room temperature value runs against this line of reasoning since it is expected to decrease further. One explanation for this could be that the oxidation state of the ytterbuim ions could have changed. The fact that the basic structure of the spectrum of Yb^{2+} ions in octahedral environment was still observed eliminates this possibility. A more

Table 6.1 Spectral Positions of A2-, A6- and C4-Bands of Yb^{2+} Ions in RbBr : Yb^{2+} Crystal Matrix at Different Elevated Temperatures.

Last column gives values of ∇ Parameter.[1]

Measurement Temperature °C	Spectral Positions						
	A2-band		A6-band		C4-band		∇
	Wavelength λ (nm)	Spectral Energy ϵ (cm^{-1})	Wavelength λ (nm)	Spectral Energy ϵ (cm^{-1})	Wavelength λ (nm)	Spectral Energy ϵ (cm^{-1})	$\times 10^3 cm^{-1}$
RT	375.5	26 631	337.0	29 674	251.0	39 841	13.21
165	372.0	26 882	336.0	29 762	251.0	39 841	12.96
235	377.0	26 525	341.0	29 326	252.0	39 683	13.16
252	377.0	26 525	341.0	29 326	252.0	39 683	13.16
354	380.0	26 316	341.5	29 283	252.0	39 683	13.37

[1]Spectral positions were not obtained from second derivative spectra.

Table 6.2 Positions of Absorption Bands of Yb^{2+} ions in a sample of RbBr : Yb^{2+} Crystals Slow Cooled from 252°C and 354°C and Measured at Room and Liquid Nitrogen Temperatures. [1]

	Room Temperature Spectrum						Liquid Nitrogen Temperature Spectrum			
	QSDT		SCS252		SCS354		QSDT		SCS354	
Band	Wavelength λ (nm)	Spectral Energy ϵ cm^{-1}	Wavelength λ (nm)	Spectral Energy ϵ cm^{-1}	Wavelength λ (nm)	Spectral Energy ϵ cm^{-1}	Wavelength λ (nm)	Spectral Energy ϵ cm^{-1}	Wavelength λ (nm)	Spectral Energy ϵ cm^{-1}
A2	375.5	26 631	380.5	26 281	384.5	26 008	377.5	26 490	388.5	25 740
U2	—	—	—	—	—	—	—	—	377.0	26 525
A6	337.0	29 674	341.5	29 283	342.0	29 240	339.0	29 499	347.0	28 818
U6	—	—	—	—	—	—	—	—	338.0	29 586
E1	321.0	31 153	—	—	308.0	32 468	319.5	31 299	307.0	32 573
W1	—	—	—	—	—	—	—	—	317.0	31 546
B1	281.0	35 587	—	—	284.0	35 211	282.5	35 398	286.0	34 965
B2	—	—	—	—	276.0	36 232	273.5	36 563	278.0	35 971
C4	251.0	39 841	252.0	39 683	251.5	39 761	250.5	39 920	252.0	39 683
W2	—	—	—	—	—	—	—	—	239.5	41 754
E2	240.0	41 667	239.0	41 841	238.0	42 017	241.0	41 494	235.5	42 463
	$\nabla = 13210 cm^{-1}$		$\nabla = 13402 cm^{-1}$		$\nabla = 13753 cm^{-1}$		$\nabla = 13430 cm^{-1}$		$\nabla = 13943 cm^{-1}$	

KEY: QSDT Sample quenched from doping Temperature
SCS252 Same sample heated to 252°C and slow cooled to room temperature
SCS354 Same sample heated to 354°C and slow cooled to room temperature

[1] No second derivative spectra were measured for this sample.

likely explanation seems to be that the co-ordination environment of the Yb^{2+} ions at these elevated temperatures could have changed to a lattice configuration not very different from their co-ordination environment when the crystal was quenched from doping temperature. In this respect, the increase in ∇ shows that the co-ordinating ions may be separated from the substitional ion by a smaller distance. A possible test of this idea would be to cool the sample to room temperature and again observe the spectrum, hoping that whatever changes that had taken place would still be stable. That the original room temperature spectrum was not recovered when the sample was cooled from 354^0 C to room temperature strengthens the above model. There exists the possibility, therefore, that precipitates of $YbBr_2$ crystals or crystallites or some other precipitate complexes involving association of Yb^{2+}, Br^- or even Rb^+ ions could have been formed. In whatever association Yb^{2+} ions must have entered, one point seems to be evident, and that is, that at least some of the Yb^{2+} ions occupy an environment that is effectively octahedral since the basic octahedral spectrum is still observed.

The additional energy bands observed in the LNT spectrum (vide Fig 6.3) of the slow cooled sample suggests that the Yb^{2+} ions could exist in two separate coordination environments. The positions of U2, U6 and W1 bands are almost the same as those of A2, A6 and E1 - bands in the LNT spectrum of a quenched crystal. That the B and C bands do not have obvious 'comparison' bands could be because the possible companion bands are overlapped by them. If the above proposition is correct, the U- and W- bands are then very likely to be due to Yb^{2+} ions in a coordinating environment similar to that of Yb^{2+} ions in quenched samples, while the other bands now labelled A2, A6, E1 and so on are due to Yb^{2+} ions in a different coordination environment.

To further this view is the fact that on heating the same slow cooled $RbBr : Yb^{2+}$ crystal sample to a temperature of 600^0 C, for two hours and quenching it, the original spectra both at RT and LNT are recovered. It can be argued that at 600^0 C, the Yb^{2+} ions have again got dispersed within the crystal and that at some temperature the precipitate structures or complexes giving rise to the spectra shown in Fig 6.3 become unstable. The above propositions motivated the experiments

reported in the next section.

6.3 Precipitate formation and dissolution kinetics

6.3.1 Introduction

The exposition made in the last section strongly suggests the possibility of Yb^{2+} ions existing in two separate phases in the sample of $RbBr : Yb^{2+}$ cooled slowly from 354^0 C. To test this proposition two different types of experiments were undertaken. One type attempts to answer the question as to whether it is the slow-cooling process that caused the formation of what is now suspected to be precipitate complexes and whether at temperatures below 600^0 C such structures/complexes could still be formed even if the crystal sample is quenched. The other experiment was designed to answer the question as to the temperature range outside which the complexes or precipitate structures become unstable and so dissolve.

In this section, the procedure for carrying out these experiments and the results obtained are outlined.

6.3.2 Experiments on formation of precipitate structures

In line with question one raised above, the following experimental procedure was adopted. A sample of $RbBr : Yb^{2+}$ crystal quenched from doping temperature was heated for two hours at a chosen temperature in the range 50^0 C – 550^0 C and quenched again. The spectrum of the sample was recorded at both RT and LNT. The same sample was again heated for two hours at the doping temperature before being quenched again, the idea being to dissolve any precipitates or complexes formed. Room and liquid nitrogen temperature spectra of the quenched sample were again taken. Using the same sample the procedure was repeated at different annealing temperatures in the range already indicated. However there was one difficulty with this method. A sample used in this way tends to loose some of the Yb^{2+} ions particularly during annealing at doping temperatures. To ameliorate this problem, a large sample was doped and cleaved into two along its length. Each half was used separately as described above. The order of doing the experiments was

such that each sample was used for temperature within the upper and lower halves of the temperature range.

Results of the experiments show that the structure of the spectrum of $RbBr : Yb^{2+}$ crystal and the positions of the absorption bands depend on annealing temperature. Fig 6.4 indicates the room temperature spectra of the $RbBr : Yb^{2+}$ twin samples at five different annealing temperatures. In all, the experiments were done at thirteen different annealing temperatures. Choice of the spectra in Fig 6.4 depends on whether they are representative of those at temperatures close to the annealing temperature at which it was produced or whether it provides a new information. The main feature depicted is the high sensitivity of the A2 and A6-bands to annealing temperatures. Whereas for an annealing temperature of 150^0 C, A2 band is displaced to lower energies by 298 cm^{-1} from its position for freshly doped crystal, it is displaced also to lower energies by 723 cm^{-1} for annealing temperature of 325^0 C. The A6 band also experiences appreciable displacements to the red at these temperatures. Other features include the shift of E1 band to higher energies and the change in the structure of the high energy bands at annealing temperatures above 300^0 C.

However, the LNT spectra of the same samples annealed at temperatures indicated in Fig 6.4 reveal a lot more of what structural changes have taken place in the spectra as a result of thermal ageing of the crystal. These are clearly illustrated in Fig 6.5. Evidently, the most striking structural changes start to occur at an annealing temperature of 325^0 C. At that temperature, apart from an increased shift in the positions of A- and E1- bands, the companion U- and W- bands appear. In fact,thereafter, there is a progressive increase in the intensities of the U2, U6 and W1-bands, relative to A2, A6 and E1 bands respectively as annealing temperature increases. The spectrum at 450^0 C annealing temperature atests to this fact. To illustrate this point further, Fig 6.6 shows the LNT spectrum of a sample annealed at 500^0 C. Clearly, the intensities of the A- and E-bands are comparable to those of the companion U- and W- bands respectively.

Another point emerging from these results is that at an annealing temperature of 550^0 C, the spectrum (either at room or liquid nitrogen temperature) is restored

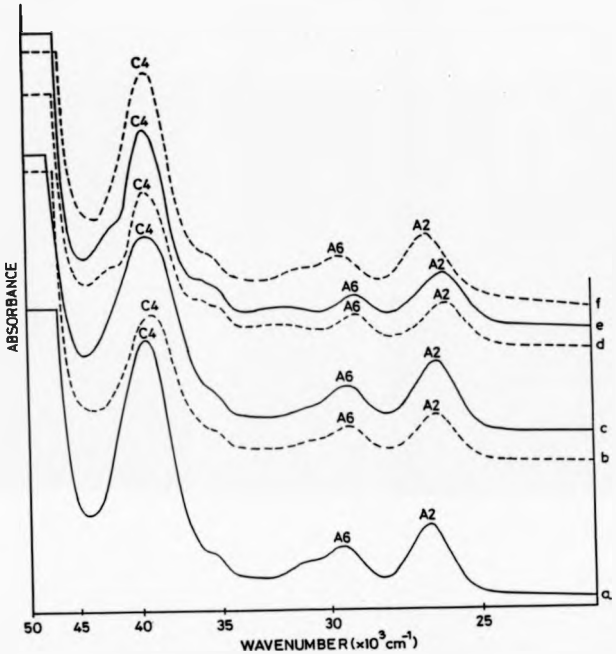

Fig 6.4 Room temperature optical absorption spectra of $RbBr : Yb^{2+}$ twin crystals quenched from different annealing temperatures.Crystals were quenched from (a) Doping temperature (b) 150° C (c) 300° C (d) 325° C (e) 450° C (f) 550° C .

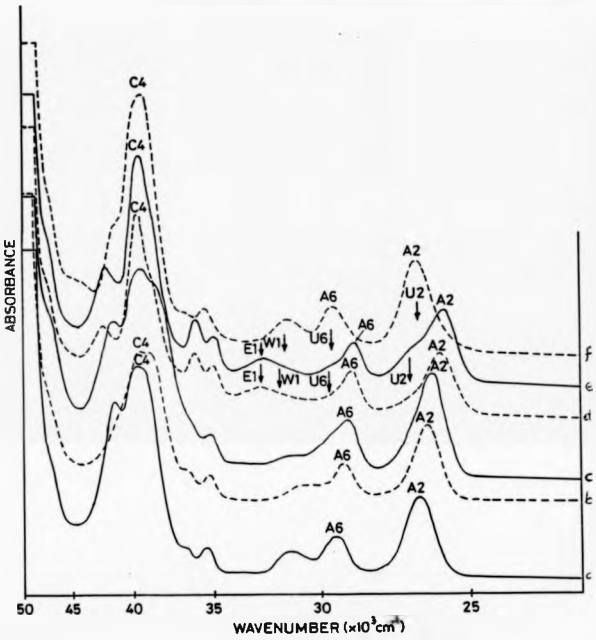

Fig 6.5 Liquid nitrogen temperature optical absorption spectra of $RbBr:Yb^{2+}$ twin crystals quenched from different annealing temperatures. Crystals were quenched from (a) Doping temperature (b) 150° C (c) 300° C (d) 325° C (e) 450° C (f) 550° C .

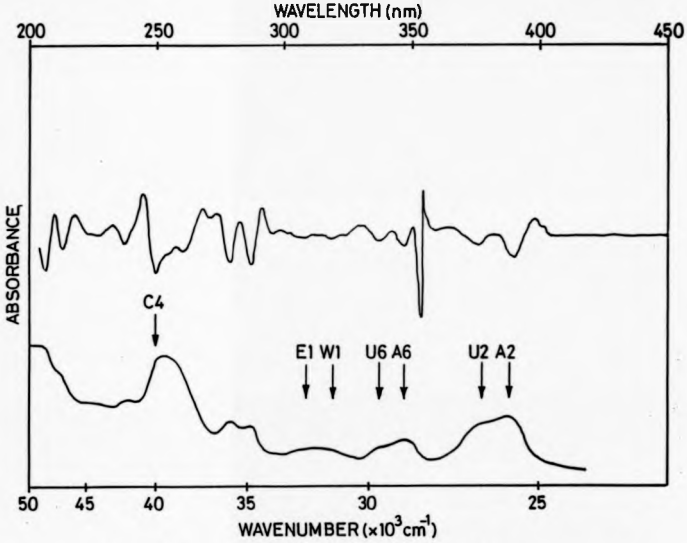

Fig 6.6 Absorption spectrum measured at liquid nitrogen temperature of a $RbBr : Yb^{2+}$ crystal annealed at and quenched from 500^0 C to room temperature.

to that of a freshly doped sample. This can be seen by comparing traces (f) and (a) in Fig 6.5.

Table 6.3 shows the positions of A2 and C4-bands at various annealing temperatures while Fig 6.7 depicts graphically the spectral positions of the A2-band of the room temperature spectra at these temperatures. The positions marked x and connected to other points by broken lines are not experimental points. Their significance will be discussed in the section on discussion.

6.3.3 Experiments on dissolution of precipitate structures

The second type of experiment was carried out as follows. A sample of $RbBr : Yb^{2+}$ crystal quenched from doping temperature was again heated at doping temperature for one hour and slowly cooled to room temperature. Slow cooling consists in lowering the temperature of the furnace to 500^0 C at a rate of 50^0 C/hour. After two hours at that temperature, the furnace was switched off and allowed to cool to room temperature. This took about fourteen hours. The sample of crystal was then heated to a chosen temperature in the range 50^0 – 550^0 C for two hours and quenched. Measurement absorption spectra at RT and LNT were then made and the procedure repeated for another annealing temperature. Only one sample was used throughout. The recorded LNT absorption spectra are displayed in Fig 6.8 for fair representative annealing temperatures. The figure includes the spectrum of the slow cooled sample.

Obviously there is a remarkable similarity between the spectrum of the sample slow cooled from doping temperature and that slow cooled from 354^0 C obtained during the high temperature measurements. The main difference between them, however, is that the companion bands observed in the latter case are much more pronounced than in the former. From Fig 6.8, it appears that constant temperature annealing at temperatures of 250^0 C and below does not affect the structure of the bands and that there are only minor shifts in the positions of the A- and E- bands. At an annealing temperature of 300^0 C, a real change appears as the U2-, U6- and W1-bands gain in intensity at the expense of the A2-, A6- and E1-bands. This trend continues until a temperature of 550^0 C is reached at which the normal Yb^{2+}

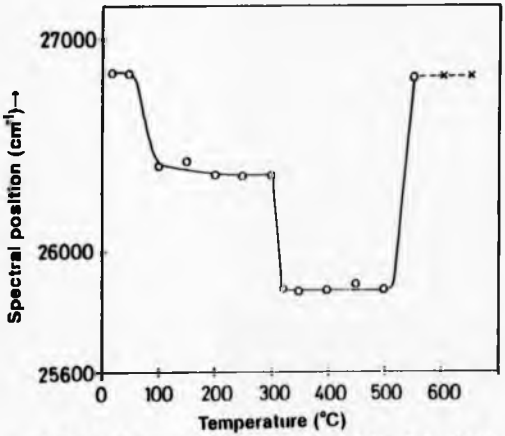

Fig 6.7 Variation of the spectral position of the A2-band at room temperature in the spectra of $RbBr:Yb^{2+}$ crystals quenched from different annealing temperatures.

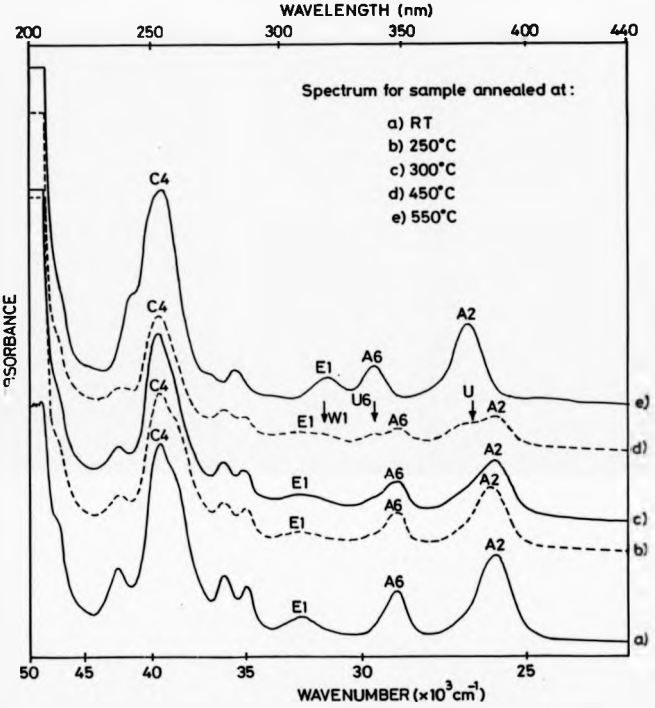

Fig 6.8 Absorption spectra measured at liquid nitrogen temperature of a $RbBr : Yb^{2+}$ crystal slow cooled from doping temperature and annealed at and quenched from different elevated temperatures.

Table 6.3 Spectral Positions of A2 and C4 Bands at Room and Liquid Nitrogen Temperatures for Different Annealing Temperatures in the Formation Kinetics Experiments

Annealing Temperature °C	Spectral Positions				▽ at LNT
	A2-band		C4-band		
	RT $\times 10^3 cm^{-1}$	LNT $\times 10^3 cm^{-1}$	RT $\times 10^3 cm^{-1}$	LNT $\times 10^3 cm^{-1}$	$\times 10^3 cm^{-1}$
20	26.60	26.47	40.00	40.00	13.53
50	26.56	26.49	40.00	39.92	13.43
100	26.28	26.25	39.92	39.92	13.67
150	26.30	26.20	39.92	39.76	13.56
200	26.25	26.16	40.00	39.76	13.60
250	26.25	26.09	39.92	39.76	13.67
300	26.25	26.04	39.92	39.84	13.80
325	25.87	25.79	39.84	39.76	13.97
350	25.87	25.77	39.92	40.00	14.23
400	25.87	25.74	39.92	39.84	14.10
450	25.89	25.72	39.76	39.84	14.12
500	25.87	25.69	39.84	40.04	14.35
550	26.58	26.53	39.92	40.00	13.47

spectrum of a freshly doped sample of $RbBr : Yb^{2+}$ crystal is recovered (compare Figs 6.8(a) and 6.8 (f)).

Table 6.4 gives the positions of the A2-band at both RT and LNT for the spectra corresponding to various annealing temperatures; while Fig 6.9 graphically illustrates the shifts in the spectral position, measured at RT, of the A2–band at these temperatures. As in Fig 6.7, the points marked x and connected by broken lines are not experimental points.

6.4 Interpretation of results and discussion

The results of the last section indicate that thermal ageing of a sample of $RbBr : Yb^{2+}$ crystal causes changes in the absorption spectrum of the crystal and that the structural change in the spectrum depends on the annealing temperature. Four temperature zones can clearly be identified; namely from room temperature to 50^0 C, 100^0 – 300^0 C, 325^0 – 500^0 C and 550^0 C – doping temperatures. Since the spectra obtained for the two temperature ranges RT – 50^0 C and 500^0 C — doping temperatures are similar it can be assumed that the Yb^{2+} ions experience the same type of coordination environment in both temperature ranges. In this case the Yb^{2+} ions are assumed to be dispersed within the crystal and are associated with cation vacancies to form I-V dipoles. It is also possible that some of the dipoles form aggregates in pairs or higher or order aggregates like trimers. However, Yb^{2+} ions in dispersed state corresponds to the model used for the calculation and the effective symmetry suggested by the results of the computation is octahedral. Divalent ytterbium ions in this type of lattice configuration in which they are dispersed within the crystal shall be designated as type I complex.

In the temperature range 100^0 – 300^0 C Yb^{2+} ions very likely experience a coordination environment different from that of type I complex. Evidence of this comes from the finding that the A2- and A6- bands of the spectrum of $RbBr : Yb^{2+}$ crystal annealed at a temperature in this range shift to longer wavelengths with small shifts of C4-band, resulting in an increase in ∇. As previously explained an increase in ∇ is indicative of an increase in $10Dq$. However, the overall structure of the spectrum is still preserved which means that the effective site symmetry of the

Table 6.4 Spectral Positions of A2 Band at Room and Liquid Nitrogen Temperatures for Different Annealing Temperatures in the Dissolution Kinetics Experiments

Annealing Temperature °C	Spectral Positions			
	RT		LNT	
	Wavelength λ (nm)	Spectral Energy $\epsilon(cm^{-1})$	Wavelength λ (nm)	Spectral Energy $\epsilon(cm^{-1})$
20	385.25	25 957	387.75	25 790
50	385.00	25 974	387.50	25 806
100	385.00	25 974	385.50	25 940
150	385.50	25 940	386.50	25 873
200	385.25	25 957	385.50	25 940
250	385.50	25 940	386.25	25 907
300	385.50	25 940	387.75	25 806
350	386.50	25 873	388.50	25 740
400	386.50	25 873	388.50	25 740
450	386.00	25 907	389.00	25 708
500	386.00	25 907	389.00	25 708
550	376.00	26 631	376.50	26 560

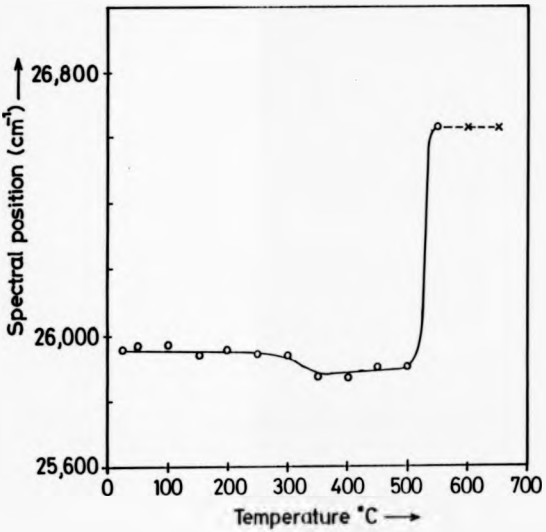

Fig 6.9 Variation of the spectral position of the A2–band (measured at room temperature) in the spectra of sample of $RbBr : Yb^{2+}$ crystal slow cooled from doping temperature but annealed and quenched from different temperatures.

Yb^{2+} ions could approximate to octahedral.

Further evidence in support of the proposition that some form of precipitation takes place when the sample is heated in this temperature regime comes from the fact that the absorption spectra obtained for this temperature range (vide Figs 6.4 and 6.5) are very similar both in structure and band positions to that of a time–aged sample of $RbBr : Yb^{2+}$ kept under laboratory conditions for 23 months. Fig 6.10 clarifies this point. The time–aged sample had no previous thermal history. Within a time scale of 23 months Yb^{2+} ions could move in the crystal by a diffusive process during which some form of aggregation of the ions in the crystal could take place. The precipitate structure or complex formed in this temperature regime shall be designated as type II complex.

What really are type II complexes? A promising candidate for consideration is the Suzuki phase of Yb^{2+} ions in RbBr. Firstly, like the dihalide-type plate-like precipitate phase, it is metastable and can even be formed at room temperature over a period of time. Secondly, Sors and Lilley [151] have established that a condition for the formation of the Suzuki phase of a divalent impurity cation in an alkali halide crystal is that the ratio of the radius R^{2+} of the divalent impurity ion to R^{+} that if the alkali ion be less than or equal 1.2 . For the case at hand, the ratio is less than unity. Insufficient as the above condition may be, the model is further strengthened by the evidence that the paramater ∇ is larger than for the Yb^{2+} ions dispersed in the crystal. For Suzuki phase precipitates, the separation between the divalent impurity ion and an anion is smaller than in the host crystal matrix since the anions in the unit cell are displaced towards the cations. Actually, it has been found experimentallay that for the case of LiF:MgF_2 system, the displacement, δ of F^{-} ions towards the Mg^{2+} is 0.01d [149] while for $NaCl : CdCl_2$ system δ= 0.014d [319]. Moreover, although less importantly, the formation of Suzuki phase of Eu^{2+} in RbBr crystals has been reported.

Finally the octahedral structure of the spectrum is preserved in this annealing temperature regime. In the Suzuki phase, the Yb^{2+} ions are each coordinated to six bromide ions as in $RbBr : Yb^{2+}$ crystal system with no precipitates. The unit cell of the stiochiometric unit $6RbBr : YbBr_2$ is basically face centred cubic. In other

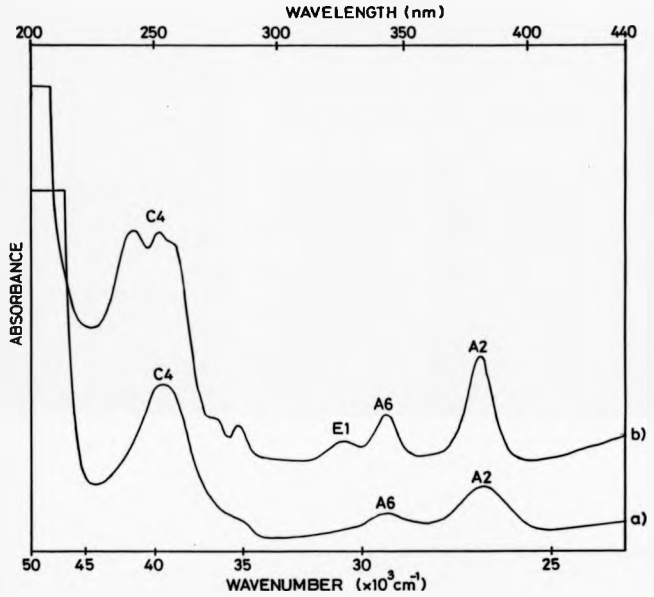

Fig 6.10 Absorption spectra of a sample of $RbBr : Yb^{2+}$ crystal stored under laboratory conditions for 23 months. (a) Room temperature spectrum. (b) Liquid nitrogen spectrum.

words, the site symmetry of a divalent impurity ion in the Suzuki phase is effectively octahedral.

It is the view of the present author, therefore, that the formation of the Suzuki phase of Yb^{2+} in $RbBr : Yb^{2+}$ crystals could be responsible for the absorption spectra observed in the temperature 100^0 – 300^0 C. However, this assignment is tentative and needs confirmation through further investigation.

In the 325^0 – 500^0 C temperature regime, results of the thermal ageing experiments show that the paramter ∇ is further increased indicating that there is an increase in the value of $10Dq$. Although the overall structure of the octahedral spectrum is preserved when the U- and W- bands are subtracted from the spectrum, the increase in ∇ is suggestive of change in the environment of the Yb^{2+} ions. The likely conclusion is that after thermal annealing in this temperature range, some of the Yb^{2+} ions are coordinated in an environment that is close to octahedral symmetry but in which the Yb^{2+} ions are separated from the Br^- ions by a distance smaller than $\frac{a}{2}$ (d = 6.854 Å). Divalent ytterbium ions are therefore, considered to be involved in some form of precipitate state which shall be designated as type III complex. Interpreting the U- and W- companion bands as being due to type I complexes then completes the proposition that the spectra of $RbBr : Yb^{2+}$ system produced this range of annealing temperatures are due to Yb^{2+} ions in two separate phases.

The model therefore envisages that type III complex is a stable phase in the temperature range 50^0 – 300^0 C as can be deduced from the results of the dissolution experiments. In that temperature range, most of the Yb^{2+} ions in the slow cooled sample are in the stable phase and only show signs of dissolution at about 300^0 C. As was found that at this latter temperature, the U- and W- companion bands start to appear and grow in intensity progressively with temperature increase until a temperature of 500^0 C at which their intensities become comparable to those of the A2-, A6- and E1- bands. At 550^0 C and above, the spectrum of type I complex is reproduced, and in this case the A- and E- bands can be said to be coincident with the companion bands.

Looking at the model from the point of view of formation kinetics, it can be

said that type III complex could not be formed at temperatures below 300^0 C. Being a stable structure, it probably requires higher activation energy for formation than could be thermally generated at those temperatures. At about 325^0 C the increased displacement of A2- and A6- bands and the appearance of the U- and W- companion bands suggest a phase transition which indeed is sharp. This means a sudden transformation in the precipitate phase of the Yb^{2+} ions from a type II complex to type III complex. However increase in 'formation' temperature causes fewer Yb^{2+} ions to be in type III complex since the intensities of U- and W- bands relative to A and E1- bands respectively increase with temperature. At 550^0 C there appears to be little chance of type III complex forming. In the 325^0 – 500^0 C temperature range therefore, type III complex is unstable. These two view points are consistent with the model of type III complex as a stable precipitate at temperatures below 300^0 C which coexist with type I complex structures in the temperature range 300^0 – 500^0 C.

It is being suggested that type III complex is a small precipitate involving Yb^{2+} ions, in which these ions experience a coordination environment that is effectively octahedral. In addition, the separation of Yb^{2+} and Br^- ions in this complex would be smaller than that between the same ions in type I complex.

The question arises as to what type of precipites type III complexes are. A likely response is that they probably consist of $YbBr_2$ precipitates. Generally dihalides of divalent metal ions are known to be stable substances. Knowledge of the crystal structure and lattice parameters of $YbBr_2$ could have been of great help in proposing a definitive model. Unfortunately, the information is not available as noted earlier. Judging by the sizes of Yb^{2+} and Br^- ions, the Wyckoff radius ratio $\frac{r_{cation}}{r_{anion}}$ (= 0.477) is greater than 0.41 which is the minimum value of the ratio of oppositively changed ions to be 6-fold coordinated in a crystal matrix [320]. It is therefore quite possible that $YbBr_2$ has crystal structure which is a distorted form NaCl structure. For obvious reasons of charge balance, $YbBr_2$ may not be isomorphic with NaCl.

However, this dilemma can only be resolved by studying the morphology of the precipitates using optical or electron microscopy in conjunction with X-ray diffraction techniques. It must be noted that attempts were made to obtain micrographs

of the precipitate structures in the samples studies using the ultra-fot microscope. The precipitates could not be identified. One difficulty in this regard was that the process of cleaning and polishing the samples interfer with the results. Doping of samples using the metal-vapour phase diffusion technique as done in this study has the advantage that the ions do not diffuse far into the bulk of the crystal. From the point of view studying precipitate structures using X-ray diffraction technique or microscopy this is a disadvantage. Absorption spectra of well polished doped samples only showed very weak bands, indicating that most of the Yb^{2+} ions had been removed during the polishing process..

It is, therefore, suggested that any further study of the precipitate structures of Yb^{2+} in alkali halide crystals should employ bulk doping techniques so that optical or electron microscopy and X-ray diffraction techniques can easily be incorporated into the study design.

In line with the models discussed above, some picture can now be created of the kinetic processes involving Yb^{2+} ions in $RbBr : Yb^{2+}$ crystal during the high temperature measurements. Increased temperature of the crystal causes motion of the lattice ions, including the Yb^{2+} ions. Although Yb^{2+} ions are heavy, diffusion can be facilitated through jumps to cation vacancy sites. At temperatures in the range $100^0 - 300^0$ type II complexes are easily formed. Being identified as Suzuki phase of Yb^{2+} ions in $RbBr : Yb^{2+}$ which are metastable, type II complexes offer a fairly easy route to the aggregation of Yb^{2+} ions to a more stable structure which would probably require higher activation energy to form. For the Suzuki phase of Yb^{2+} ions to form, only some rearrangement of the cations (both host and impurity) and the extrinsic cation vacancies was required. This would more easily be achieved than a dissociation of cation vacancies and an aggregation of Yb^{2+} and Br^- ions to form a more stable structure.

At higher temperatures however, this becomes possible. The Suzuki phase was no longer a necessary route. This Suzuki phase was no longer a necessary route. This explains why high temperature annealing of a freshly doped sample at temperatures above 325^0 C followed by quenching produced the same effect on the absorption spectrum as cooling the sample slowly from 354^0 C. Slow cooling process, there-

fore was not the cause of the change in the spectrum of the sample used for the high temperature measurement. Samples quenched from comparable temperatures gave the same result. To obtain high temperature spectrum corresponding to Yb^{2+} was dispersed in substitutional lattice sites, it would have been necessary to do measurements at temperatures of 550^0 C or above.

6.5 Conclusions

Divalent ytterbuim ions exist in three separate phases in $RbBr : Yb^{2+}$ crystals, in the temperature range 20^0 – 500^0 C. These phases are designated as type I, type II and type III complexes. In type I complex, ytterbium ions are dispersed in the crystal lattice and occupy substitutional cation sites Each Yb^{2+} ion is in association with a cation vacancy in a nearest neighbour or next nearest neighbour cation site, thereby forming a I-V dipole. Type II complex is tentatively identified as the metastable Suzuki phase of Yb^{2+} ions in the $RbBr : Yb^{2+}$ crystal system. Anticipating that the effective local symmetry of Yb^{2+} ions in the crystal of $YbBr_2$ is octahedral or distorted octahedral, type III complex is tentatively assigned as a precipitate of $YbBr_2$ in $RbBr : Yb^{2+}$ system. An additional proviso is that the separation of Yb^{2+} and Br^- ions be smaller in $YbBr_2$ crystals than in $RbBr : Yb^{2+}$ system.

Slow cooling of a sample of $RbBr : Yb^{2+}$ crystal from doping temperature to room temperature results in the formation of a precipitate structure of type III. But when a freshly doped sample of $RbBr : Yb^{2+}$ is heated to a temperature of about 354^0 C and cooled slowly to room temperature the formation of type I and type III complexes result, the two phases of Yb^{2+} ions co-existing in the crystal.

Constant temperature annealing for a two hour period, of the sample of $RbBr : Yb^{2+}$ at a temperature range of 100^0 – 300^0 C produces a precipitate structure identified as type II complex. But in the temperature regime 300^0 – 500^0 C thermal annealing process for the same duration causes the formation of two separate phases of Yb^{2+} ions, in $RbBr : Yb^{2+}$. The two co-existing phases are type I and type III complexes.

When a sample of $RbBr : Yb^{2+}$ crystal slow cooled from any temperature below

and including the doping temperature or a freshly doped sample of the same crystal is heated to a temperature of 550^0 C or above, and quenched, only type I complex results. Type III complexes are stable structures at temperatures below 300^0 C. In the temperature regime 300^0–500^0 C however some can be converted to type I complexes, the amount being converted depending on the annealing temperature.

From the foregoing, it can be concluded that any high temperature absorption spectrum at temperatures above 50^0 C and below 500^0 C will not represent that of Yb^{2+} ions dispersed in substitional lattice sites. Rather it will represent that of Yb^{2+} ions in association with other ions and lattice vacancies in the crystal in form of type II or type III complexes noted above.

Chapter 7

Concluding Remarks and Summary

7.1 Introduction

This chapter contains some remarks on the kinetics of the formation of rare–earth impurity centres and the associated colour centres in alkali halide crystals . Since thermal bleaching procedure was adopted to eliminate the colour centres, a possible bleaching mechanism is suggested. The chapter concludes with a summary of the main findings of this work.

7.2 Incorporation of Sm^{2+} and Yb^{2+} ions into KX and RbX crystals

The doping process consists in heating the host crystals to temperatures between 25^0 – 50^0 C below their melting points in metal vapour. At such temperatures it is easy for the rare earth metal (RE) atoms to be deposited on the surface of the crystals. A chemical process ensures during which the RE atom is ionised by losing two electrons. Thus

$$RE_{atom} \rightarrow RE^{2+} + 2e^- \qquad (7.1)$$

The ion then diffuses into the crystal to occupy a substitutional cation site. At the same time, the electrons injected into the crystal diffuse further into the bulk of

the crystal. A number of possible processes may take place. Normally at elevated temperatures, intrinsic cation and anion vacancies are formed in equal numbers within the crystal [106,121]. The thermal process may be represented as

$$MeX \rightleftharpoons Me^{+} + X^{-} + \square + \bigcirc \qquad (7.2)$$

where $\square$ and $\bigcirc$ are cation and anion vacancies respectively. The alkali (Me^{+}) and halogen (X^{-}) ions which have left the lattice sites diffuse within the crystal. They could take up appropriate vacancy sites and some could diffuse to the surface and recombine.

With the introduction of a RE^{2+} into the crystal extra cation and anion vacancies are created as it takes up a cation site. As a result there are a large number of both intrinsic and extrinsic vacancies. The electrons injected into the crystal easily become trapped at the site of the anion vacancies to form F-centres. Thus

$$\bigcirc + e^{-} \rightleftharpoons \textcircled{F} \qquad (7.3)$$

where $\textcircled{F}$ represents the F–centre

Since two electrons are injected for every rare earth atom that becomes ionised, many more F–centres are likely to be formed than RE impurity centres. The latter are very heavy and can diffuse only a short distance (0.5mm to 1.0mm) [6] into the crystal during doping while the electrons, being light, can easily diffuse into the bulk regions of the crystal.

At elevated temperatures, the impurity ions as well as the F-centres are dispersed within the crystal. In order to maintain the local charge balance at the site of a RE^{2+} impurity ion, a cation vacancy is proposed to situate at the nearest or next nearest neighbour cation site [134 142]. On quenching the crystals to RT, the impurity and colour centres are frozen in at their sites at high temperatures.

7.2.1 Thermal Bleaching Mechanism

Heating doped crystals of $RbBr : Yb^{2+}$, $RbI : Yb^{2+}$, $RbX : Sm^{2+}$ and $KX : Sm^{2+}$ to doping temperatures destroys the F-centres and other colour centres in these crystals. The concentration of colour centres in $RbCl : Yb^{2+}$ crystals is considerably

reduced by such a process. At such temperatures, thermal generation of cation and anion vacancies again takes place. It is possible that an F-centre dissociates into an anion vacancy and an electron according to the reverse reaction indicated in Eqn (7.3). The vacancy can be reoccupied by a halogen ion thereby destroying the defect centre at that locality while the electron can easily reduce an alkali ion by the latter capturing it. This is more likely to take place in regions close to the surface or close to an internal crack or surface. In fact a doped coloured crystal which has been heated for a few minutes (about 20 minutes) shows a large clear zone and a receeding inner coloured bulk region. The reduced ion can then be deposited in the surface as an atom which again could inject an electron into the crystal and re-enters the crystal. Whichever of the two processes (reduction and re-oxidation) predominates determines the degree and effectiveness of the bleaching procedure. The reduction and re-oxidation process can be represented as

$$Me^{+} + e^{-} \rightleftharpoons Me_{atom} \qquad (7.4)$$

Such a mechaniam as this still maintains the charge balance within the crystal.

It is also possible for some of the RE^{2+} ions to become reduced by capturing two electrons. This probably explains the reduced relative intensity of the absorption bands due to RE^{2+} ions after thermal bleaching since such a reduction is indicative of reduced impurity ion concentration. However during the short periods of thermal bleaching it seems that the reduction of the alkali ions predominates.

7.3 Summary

7.3.1 Energy level structure of $4f^N5d$ configurations of Sm^{2+} and Yb^{2+} ions in RbX and KX crystals

In the main, the broad absorption bands in the spectra of $RbX : RE^{2+}$ ($RE^{2+} = Yb^{2+}, Sm^{2+}$) and $KX : Sm^{2+}$ crystals are ascribed to $4f^{N+1} \rightarrow 4f^N5d$ ($N = 5$ for Sm^{2+}, $N = 13$ for Yb^{2+}) transitions of the RE^{2+} ions in the crystal. Although the RE^{2+} ions occupy cation lattice sites, whose symmetry is C_{2v}, it can be assumed that the effective symmetry at the site is octahedral, O_h, with an orthorhombic

distortion. Using such an approximation and two different models for the coupling of the wavefunctions of the electrons of Yb^{2+} and Sm^{2+} ions, it was possible to establish a satisfactory fit between experiment and theory

In the case of Yb^{2+} ions, J_1j–coupled basis functions were used for the theoretical calculations and the results demonstrate conclusively that the multi–band structure of the experimental spectra are due to spin–orbit, direct Coulomb and exchange perturbation interactions acting on the electron system of the Yb^{2+} ions. The reduced numerical value of the energy integrals F_k, G_k and ζ_{nl} associated with these interactions when compared with the free ion values are explained as due to nephelauxetic effect. This is an interaction model which adduces a certain degree of delocalization of the electrons of the central ion with the consequential overlap of their wavefunctions with those of the ligand ions. Implied in this model is the role covalency and the overlap processes which are expected to be more important in les ionic crystals than the more ionic ones. Incidentally, the observed reductions follow the nephelauxetic series proposed by Sch"affer and Jorgenson [262] and further supports the explanation.

It was possible to establish a definite correspondence between the spectra of $RbX : Sm^{2+}$ and $KX : Sm^{2+}$ crystals and a theoretical spectrum computed using a model suggested by Yanase and Kasuya [92] for Eu^{2+} ions in CaF_2 crystals. Assumed to be strongly perturbed by the crystal field in this model, the 5d electron states are better described in terms of crystal wavefunctions γ_3 and γ_5 which then couple with the electronic states of the $4f^5$ core configuration with the highest multiplicity. The coupling is through the direct Coulomb and exchange interactions. It is the strong crystal field interaction and the electrostatic interaction $H_{ee}(f,f)$ however that define the observed groups of bands. Nevertheless, it was found that the structure of the band groups in the experimental spectra are due to the effects of spin–orbit interactions $H_{so}(f)$ and H_{so}(d) as well as direct Coulomb and exchange interactions H_{ee}(f,d).

On the whole the detailed calculations for each of the crystal systems show reasonably good agreement with the experimental data. There are however, explainable discrepancies between the computed and observed relative transition intensities of

some of the assigned bands. The discrepancies are attributed to the effects of some of the approximations made in the calculation.

For any given alkali metal series, the Dq values obtained for the $4f^N5d$ configurations of Sm^{2+} and Yb^{2+} ions in the crystal systems studied decrease as the ionicity of the crystal host decreases; that is, according to the sequence $Cl > Br > I$. When viewed from the point of view of lattice parameter d, Dq values for the two electronic systems increase as d decreases. In the case of crystals containing Sm^{2+} ions, a definite r_p^{th} ($p = K, Rb$) power law: $Dq \propto d^{r_p}$ was established for each alkali metal series, with $r_K = -2.428 \pm 0.005$ and $r_{Rb} = -2.424 \pm 0.004$. Also found is the fact that the centre of gravity of the $4f^{13}5d$ configuration of Yb^{2+} ions shifts to lower energies as the ion enters the crystals. For $RbX : Yb^{2+}$ crystals, the established configurational depression increases as d increases. Although it was not possible to estimate the depressions of the centre of the $4f^5(^6FH)5d$ sub-configuraiton of Sm^{2+} ions in the crystals, indications are that a similar relationship exists between sub-configurational depressions and d

7.3.2 $4f^{N+1} \rightarrow 4f^5 6s$ transitions in $RbX : Yb^{2+}$, $RbX : Sm^{2+}$ and $KX : Sm^{2+}$ crystals

Observed also in the optical spectra of Sm^{2+} and Yb^{2+} ions in the RbX and KX, crystals are additional absorption bands whose behaviour is anion dependent. For example, their transition intensities relative to any given band in the spectra increases as the degree of covalency of the host crystal increases for any given alkali metal series. In other words the relative intensities follow spectro–chemical sequence: $Cl < Br < I$. To explain the occurrence and behaviour of these bands, attention is called to the possibility of the $6s$ atomic orbitals of the RE^{2+} ions overlapping with the $(n+1)s$ atomic orbitals of the ligand ions to form bonding (σ) and anti-bonding ($\sigma*$) MO's which couple with the substates of the $4f^N$ configuration. Electronic transitions to the bonding MO's are possible on the grounds that the electric dipole selection rules could break down owing to the orthorhombic distortion of the site symmetry of the RE^{2+} ions.

7.3.3 Precipitate complexes in thermally annealed crystals of $RbBr : Yb^{2+}$

Divalent ytterbuim ions were found to exist in RbBr crystals in three separate phases. One phase corresponds to Yb^{2+} ions dispersed within the crystal with each ion associated with a cation vacancy. They are referred to as type I complex and are produced when the doped crystal is quenched from a temperature greater than 550^0 C. On the other hand, when a crystal containing type I complexes is heated at a temperature below and including 300^0 C and then quenched, type II complex structures result. The latter is tentatively identified as the Suzuki phase of Yb^{2+} ions in RbBr crystals, which is a metastable precipiate phase of a fairly complex stiochiometry.

At temperatures above 325^0 C but below 550^0 C a precipitate atructure designated as type III is formed. Dissolution experiments show that type III complex is a stable precipitate at temperatures below 300^0 C. However above that temperature, it starts to dissolve giving rise to type I complex with which it co-exists and which grows in at its (type II complex's) expense until a temperature of 550^0 C is reached. Complete dissolution of type III complex phase is achieved at this temperature. It is possible that type III complex is a precipiate of $YbBr_2$ formed during thermal annealing at the temperature ranges indicated. Confirmatory identification of the precipiate structures however require some microstructural or crystallographic studies of thermally annealed $RbBr : Yb^{2+}$ crystals. The study could also be extended to other $RbX : Yb^{2+}$ crystals.

Appendix A

Calculation of Vector Coupling Coefficients

$\langle \Gamma_j \gamma_j \Gamma'_p \gamma_p \mid^{\beta} \Gamma_i \gamma_i \rangle$, $j = 6, 7, 8$; $i = 1, 2, ..., 5$, $\Gamma'_p = \Gamma_6, \Gamma_7, \Gamma_8$

The calculation of the vector coupling (overlap) coefficients rests on the premise that there is an isomorphic correspondence between crystal wavefunctions characterised by the irreducible representations, Γ_j, of the cubic double group (O') and spherical harmonic functions of half–integral order. Abragam and Pryce [317] point out that in the cubic or octahedral symmetry, the Γ_4 functions transform as the p^N functions of the free atom or ion. Accordingly, the following correspondences can be made between the components of Γ_4 functions and the components of the orbital angular momentum, l ($l = 1$), of an electron in the p orbit:

$$\begin{aligned} |\Gamma_4 1\rangle &\sim |p1\rangle \\ &= |11\rangle \\ |\Gamma_4 0\rangle &\sim |p0\rangle \\ &= |10\rangle \\ |\Gamma_4 -1\rangle &\sim |p-1\rangle \\ &= |1-1\rangle \end{aligned} \qquad (A.1)$$

Similar isomorphic correspondences have been established between the Γ_3 and Γ_5 functions of the describing the motion of a single d electron in cubic, octahedral crystal fields [215,318,323]. Dixon [316] drew the attention of the author to the possibility of using the isomorphic principle to connect the doubly valued functions Γ_6 and Γ_8 to spherical harmonics of half–integral order. The following correspondences were therefore made:

$$\begin{aligned} |\Gamma_6 \alpha'\rangle &\sim |\tfrac{1}{2}\tfrac{1}{2}\rangle \\ |\Gamma_6 \beta'\rangle &\sim |\tfrac{1}{2}\tfrac{-1}{2}\rangle \end{aligned} \qquad (A.2)$$

and

$$
\begin{aligned}
|\,\Gamma_8\kappa\rangle &\sim |\,\frac{3}{2}\frac{3}{2}\rangle \\
|\,\Gamma_8\lambda\rangle &\sim |\,\frac{3}{2}\frac{1}{2}\rangle \\
|\,\Gamma_8\mu\rangle &\sim |\,\frac{3}{2}\frac{-1}{2}\rangle \\
|\,\Gamma_8\nu\rangle &\sim |\,\frac{3}{2}\frac{-3}{2}\rangle
\end{aligned}
\qquad (A.3)
$$

It was possible therefore to couple the functions

$$
|\,J_1M_1\rangle\,|\,J_1'M_1'\rangle = \sum_{JM}(J_1J_1'M_1M_1'\,|\,J_1J_1'JM)\,|\,JM\rangle \qquad (A.4)
$$

The coefficients under summation sign are Clebsch–Gordon (CG) coefficients which are connected to 3-j symbols of Wigner [2,165]. For the purpose of this calculation, values of the CG coefficients were obtained from the book by Heine [324]. From a comparison of the linear combination of these functions and the definitions of the $|\,\Gamma_i\gamma_i\rangle$ $(i = 1,2,...,5)$ functions in terms of spherical harmonics, the vector coupling coefficients

$$
\langle\Gamma_j\gamma_j\Gamma_F\bar{\gamma}_F\,|^\beta\,\Gamma_i\gamma_i\rangle
$$

$(j = 6,7,8,\ i = 1,2,...,5,\ \Gamma_F = \Gamma_6,\Gamma_7,\Gamma_8)$, were written down. Results of the calculations are shown in Tables A5.1 – A5.6.

Quite interestingly, the entries in these tables agree in every case with the values (but not always with the phase factor) of the coefficients derived from the tables by Koster, et. al. [216]. In the latter tables, a system of quantisation in which the components of the Γ_i functions are expressed in cartesian co–ordinates was used. For conversion to the system of quantisation used in this study, the following relations were used [215].

$$
\begin{aligned}
|\,\Gamma_4 1\rangle &= \frac{-i}{\sqrt{2}}(\Gamma_4 x + i\Gamma_4 y) \\
|\,\Gamma_4 0\rangle &= i\Gamma_4 z \\
|\,\Gamma_4 -1\rangle &= \frac{i}{\sqrt{2}}(\Gamma_4 x - i\Gamma_4 y)
\end{aligned}
\qquad (A.5)
$$

The sign differences in the results arise from the difference in the sign conventions used in the computations. However, these latter tables were not used in this work. Tables A5.1 – A5.6 were used instead.

Table A5.1 Vector Coupling Coefficients $< \Gamma_6 a \Gamma_8 b \mid \Gamma_4 c >$, $\Gamma_4 = \Gamma_1, \Gamma_4$

$\Gamma_6 \times \Gamma_8$		Γ_1	Γ_4		
		a_1	1	0	-1
α'	α'	0	1	0	0
	β'	$\frac{1}{2}(2)$	0	$\frac{1}{2}(2)$	0
β'	α'	$-\frac{1}{2}(2)$	0	$\frac{1}{2}(2)$	0
	β'		0	0	1

Table A5.2 Vector Coupling Coefficients $< \Gamma_6 a \Gamma_7 b \mid \Gamma_5 c >$, $\Gamma_5 = \Gamma_2, \Gamma_5$

$\Gamma_6 \times \Gamma_7$		Γ_2	Γ_5		
		a_2	1	0	-1
α''	α''	0	1	0	0
	β''	$\frac{1}{2}(2)$	0	$\frac{1}{2}(2)$	0
β''	α''	$-\frac{1}{2}(2)$	0	$\frac{1}{2}(2)$	0
	β''		0	0	1

Table A5.3 Vector Coupling Coefficients $< \Gamma_6 a \Gamma_8 b \mid \Gamma_7 c >$, $\Gamma = \Gamma_3, \Gamma_4, \Gamma_5$

$\Gamma_6 \times \Gamma_8$		Γ_3		Γ_4			Γ_5		
		θ	ϵ	1	0	-1	1	0	-1
α'	κ	0	$\frac{1}{2}(2)$	0	0	0	0	$\frac{1}{2}(2)$	0
	λ	0	0	$-\frac{1}{2}$	0	0	0	0	$-\frac{1}{2}(3)$
	μ	$\frac{1}{2}(2)$	0	0	$-\frac{1}{2}(2)$	0	0	0	0
	ν	0	0	0	0	$-\frac{1}{2}(3)$	$\frac{1}{2}$	0	0
α''	κ	0	0	$\frac{1}{2}(3)$	0	0	0	0	$-\frac{1}{2}$
	λ	$\frac{1}{2}(2)$	0	0	$\frac{1}{2}(2)$	0	0	0	0
	μ	0	0	0	0	$\frac{1}{2}$	$\frac{1}{2}(3)$	0	0
	ν	0	$\frac{1}{2}(2)$	0	0	0	0	$-\frac{1}{2}(2)$	0

Table A5.4 Vector Coupling Coefficients $< \Gamma_7 a \Gamma_7 b \mid \Gamma_i c >$, $\Gamma_i = \Gamma_1, \Gamma_4$

$\Gamma_7 \times \Gamma_7$		Γ_1	Γ_4		
		a_1	1	0	-1
α''	α''	0	1	0	0
	β'	$\frac{1}{2}(2)$	0	$\frac{1}{2}(2)$	0
β''	α''	$-\frac{1}{2}(2)$	0	$\frac{1}{2}(2)$	0
	β''	0	0	0	1

Table A5.5 Vector Coupling Coefficients $< \Gamma_7 a \Gamma_8 b \mid \Gamma_i c >$, $\Gamma_i = \Gamma_3, \Gamma_4, \Gamma_5$

$\Gamma_7 \times \Gamma_8$		Γ_3		Γ_4			Γ_5		
		θ	ϵ	1	0	-1	1	0	-1
α''	κ	$\frac{1}{2}(2)$	0	0	$\frac{1}{2}(2)$	0	0	0	0
	λ	0	0	0	0	$-\frac{1}{2}(3)$	$-\frac{1}{2}$	0	0
	μ	0	$-\frac{1}{2}(2)$	0	0	0	0	$-\frac{1}{2}(2)$	0
	ν	0	0	$\frac{1}{2}$	0	0	0	0	$-\frac{1}{2}(3)$
β''	κ	0	0	0	0	$-\frac{1}{2}$	$-\frac{1}{2}(3)$	0	0
	λ	0	$-\frac{1}{2}(2)$	0	0	0	0	$\frac{1}{2}(2)$	0
	μ	0	0	$\frac{1}{2}(3)$	0	0	0	0	$\frac{1}{2}$
	ν	$\frac{1}{2}(2)$	0	0	$-\frac{1}{2}(2)$	0	0	0	0

Table A5.6 Vector Coupling Coefficients $< \Gamma_2 a \Gamma_3 b \mid \Gamma_1 c >$, $\Gamma_i = \Gamma_1, \Gamma_2, \Gamma_3$

$\Gamma_2 \times \Gamma_3$		Γ_1	Γ_2	Γ_3	
		a_1	a_2	θ	ϵ
κ	κ	0	0	0	0
	λ	0	$\frac{1}{2}$	0	$\frac{1}{2}$
	μ	0	0	0	0
	γ	$\frac{1}{2}$	0	$\frac{1}{2}$	0
λ	κ	0	$\frac{1}{2}$	0	$-\frac{1}{2}$
	λ	0	0	0	0
	μ	$-\frac{1}{2}$	0	$\frac{1}{2}$	0
	ν	0	0	0	0
μ	κ	0	0	0	0
	λ	$\frac{1}{2}$	0	$-\frac{1}{2}$	0
	μ	0	0	0	0
	ν	0	$-\frac{1}{2}$	0	$\frac{1}{2}$
ν	κ	$-\frac{1}{2}$	0	$-\frac{1}{2}$	0
	λ	0	0	0	0
	μ	0	$-\frac{1}{2}$	0	$-\frac{1}{2}$
	ν	0	0	0	0

Table A8.6 (contd.) Vector Coupling Coefficients $< \Gamma_8 a \Gamma_8 b \mid^{\phi} \Gamma_i c >$.

$^{\phi}\Gamma_i = {}^{2}\Gamma_4, {}^{2}\Gamma_4$

$\Gamma_8 \times \Gamma_8$		$^{1}\Gamma_4$			$^{2}\Gamma_4$		
		1	0	-1	1	0	-1
κ	κ	0	0	0	0	0	$-\frac{1}{4}(10)$
	λ	0	0	0	0	0	0
	μ	$\frac{1}{10}(30)$	0	0	$-\frac{1}{20}(30)$	0	0
	ν	0	$\frac{3}{10}(5)$	0	0	$\frac{1}{10}(5)$	0
λ	κ	0	0	0	0	0	0
	λ	$-\frac{1}{5}(10)$	0	0	$-\frac{3}{20}(10)$	0	0
	μ	0	$-\frac{1}{10}(5)$	0	0	$\frac{3}{10}(5)$	0
	ν	0	0	$\frac{1}{10}(30)$	0	0	$-\frac{1}{20}(30)$
μ	κ	$\frac{1}{10}(30)$	0	0	$-\frac{1}{20}(30)$	0	0
	λ	0	$-\frac{1}{10}(5)$	0	0	$\frac{3}{10}(5)$	0
	μ	0	0	$-\frac{1}{5}(10)$	0	0	$-\frac{3}{20}(10)$
	ν	0	0	0	0	0	0
ν	κ	0	$\frac{3}{10}(5)$	0	0	$\frac{1}{10}(5)$	0
	λ	0	0	$\frac{1}{10}(30)$	0	0	$-\frac{1}{20}(30)$
	μ	0	0	0	0	0	0
	ν	0	0	0	$-\frac{1}{4}(10)$	0	0

Table A5.6 (contd.) Vector Coupling Coefficients $< \Gamma_\beta a \Gamma_\delta b \mid^\phi \Gamma_\epsilon c >$,

$^\phi\Gamma_\epsilon = {}^1\Gamma_5, {}^2\Gamma_5$

$\Gamma_\beta \times \Gamma_\delta$		$^1\Gamma_5$			$^2\Gamma_5$		
		1	0	-1	1	0	-1
κ	κ	0	0	0	$-\frac{1}{4}(6)$	0	0
	λ	0	$\frac{1}{2}$	0	0	$\frac{1}{2}$	0
	μ	0	0	$-\frac{1}{2}(2)$	0	0	$\frac{1}{4}(2)$
	ν	0	0	0	0	0	0
λ	κ	0	$-\frac{1}{2}$	0	0	$\frac{1}{2}$	0
	λ	0	0	0	0	0	$\frac{1}{4}(6)$
	μ	0	0	0	0	0	0
	ν	$\frac{1}{2}(2)$	0	0	$\frac{1}{4}(2)$	0	0
μ	κ	0	0	$\frac{1}{2}(2)$	0	0	$\frac{1}{4}(2)$
	λ	0	0	0	0	0	0
	μ	0	0	0	$\frac{1}{4}(6)$	0	0
	ν	0	$-\frac{1}{2}$	0	0	$\frac{1}{2}$	0
ν	κ	0	0	0	0	0	0
	λ	$-\frac{1}{2}(2)$	0	0	$\frac{1}{4}(2)$	0	0
	μ	0	$\frac{1}{2}$	0	0	$\frac{1}{2}$	0
	ν	0	0	0		0	$-\frac{1}{4}(6)$

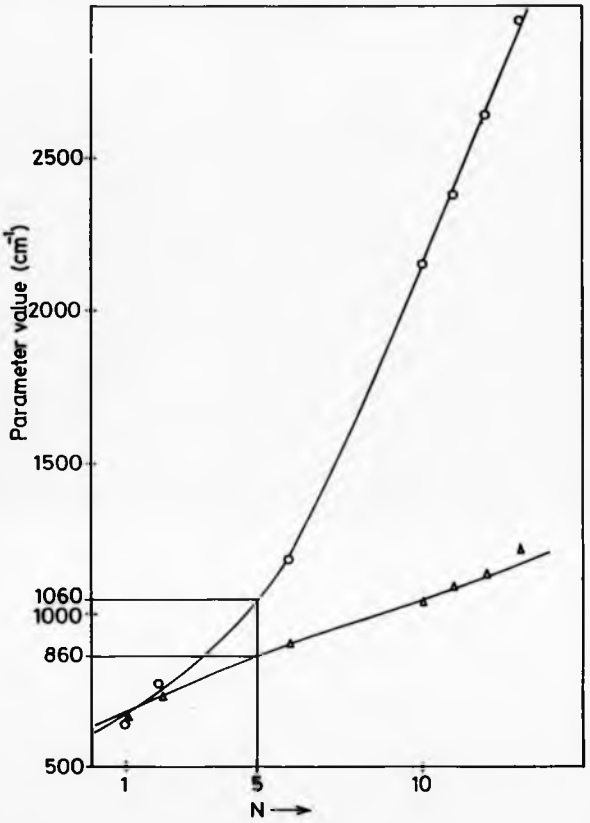

Fig A5.1 A plot of values of ζ_{4f} and ζ_{5d} against N, the number of equivalent electrons, for $4f^N5d$ configuration of 6 divalent rare-earth ions in free state. Interpolated values of ζ_{4f} and ζ_{5d} for free Sm^{2+} (N = 5) ions are respectivaly 1060 cm^{-1} and 860 cm^{-1}.

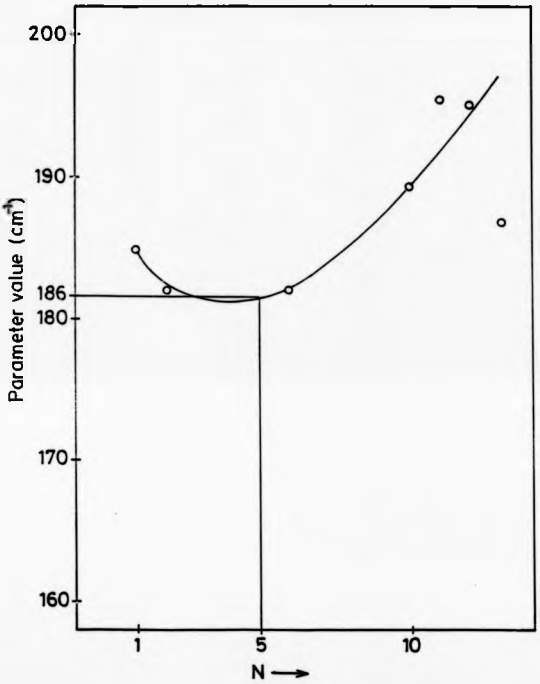

Fig A5.2 A plot of values of F_2 against N, the number of equivalent electrons, for $4f^N5d$ configuration of 6 divalent rare-earth ions in free state. Interpolated value of F_2 for free Sm^{2+} (N = 5) ions is 181 cm^{-1}.

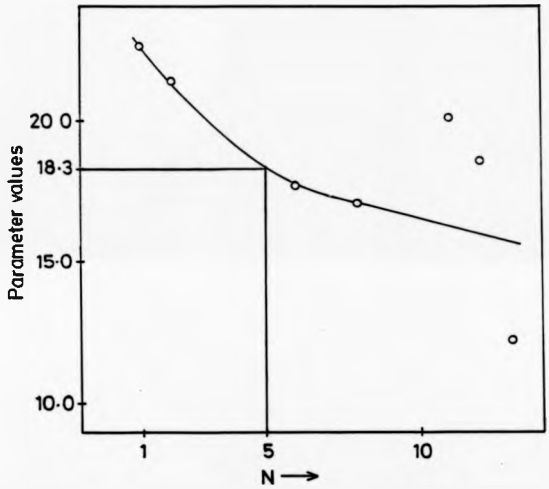

Fig A5.3 A plot of values of F_4 against N, the number of equivalent electrons, for $4f^N5d$ configuration of 6 divalent rare-earth ions in free state. Interpolated value of F_4 for free Sm^{2+} (N = 5) ions is 18.3 cm^{-1}.

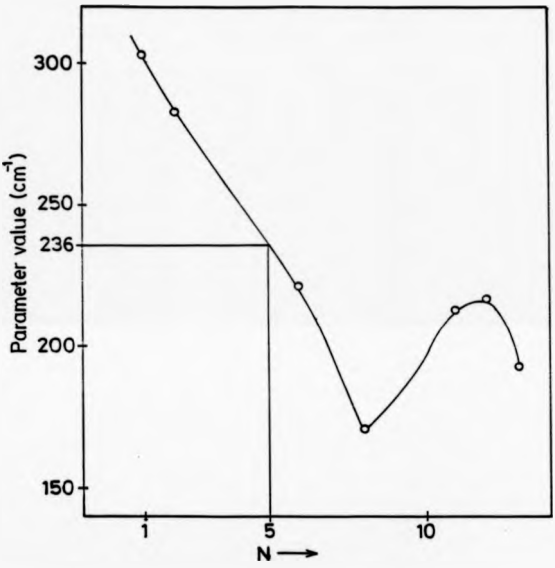

Fig A5.4 A plot of values of G_1 against N, the number of equivalent electrons, for $4f^N5d$ configuration of 6 divalent rare-earth ions in free state. Interpolated value of G_1 for free Sm^{2+} (N = 5) ions is 236.0 cm^{-1}.

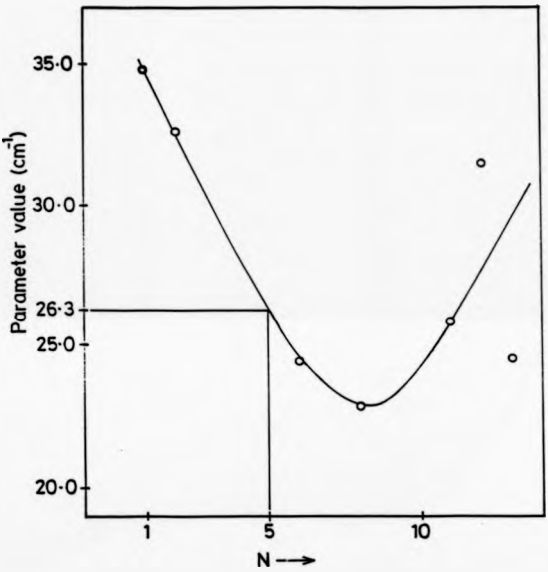

Fig A5.5 A plot of values of G_3 against N, the number of equivalent electrons, for $4f^N5d$ configuration of 6 divalent rare-earth ions in free state. Interpolated value of G_3 for free Sm^{2+} (N = 5) ions is 26.3 cm^{-1}.

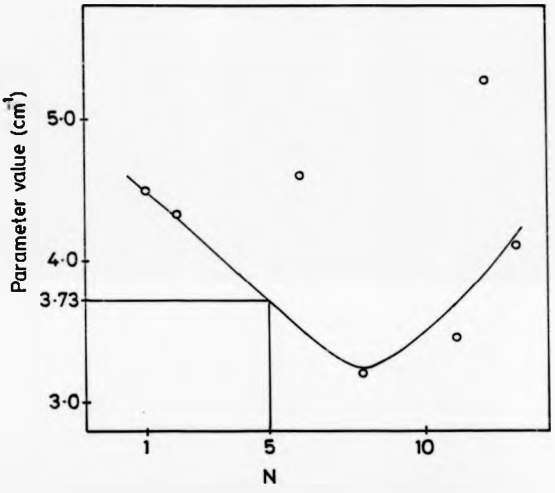

Fig A5.6 A plot of values of G_5 against N, the number of equivalent electrons, for $4f^N5d$ configuration of 6 divalent rare-earth ions in free state. Interpolated value of G_5 for free Sm^{2+} (N = 5) ions is 3.73 cm^{-1}.

.2 References

1 Wybourne, B. G., 'Spectroscopic Properties of the Rare Earths', John Wiley and Sons Inc. N.Y. (1965)

2 Cowan, R. D. 'The Theory of Atomic Structure and Spectra' University of California Press Berkeley Los Angeles, (1981)

3 Dieke, G. H. 'Spectra and Energy Levels of Rare Earth Ions in Crystals' John Wiley and Sons Inc N.Y. (1968)

4 Hüfner, S., 'Optical Spectra of Transparent Rare-Earth Compounds, Academic Press Inc. N.Y. (1978)

5 Spedding, F. H., in 'The Rare Earths' (eds) F.H. Spedding and H.H. Daane, John Wiley and Sons Inc. N.Y. (1961)

6 Bland, S., (Unpublished PhD Thesis, University of Warwick) 1985

7 Hayes, E. and Twidell, J. W., J. Chem. Phys. 35 1521 (1961)

8 Hayes, W. et al, Proc Phys Soc (London) 81, 371 (1963)

9 Kiss, Z. J., Phys. Rev. 127 718 (1962)

10 McClure, D. S. and Kiss, Z. J., J. Chem. Phys. 39 3251 (1963)

11 Kiss, Z. J. and Yocom, P. N., J. Chem. Phys. 41 1511 (1964)

12 Sabisky, E. S., J. Chem Phys. 41 892 (1964)

13 Sabisky, E. S. and Anderson, C. H. Phys. Rev. 148 194 (1966)

14 Anderson, C. H. and Sabisky, E. S. Phys Rev. 178 177 (1969)

15 Nair, P. C., et al., J. Phys. Chem. Solids. 29 2183 (1968)

16 Muñoz, E. P., et al., J. Chem. Phys 62 3416 (1975)

18 Low, W. Phys. Rev. 118 1608 (1960)

19 Kiss, Z. J. et al, Phys Rev 137 A1749 (1965)

20 Aguilar, G. S. et al, J. Chem. Phys 60 4665 (1974)

21 Kirton, J. and White A. M. Phys Rev 178 543 (1969)

22 Murao, T. et al, J. Chem. Phys 42 993 (1965)

23 Shen, Y. R. and Bloemberger, Phys Rev. 133 (1964)

24 Zakharcheynya, B. P. et al, Opt. and Spectroscopy 18 563 (1965)

25 William, H. et al, Phys Rev. 132 (1963)

26 Weber, M. J. and Bierig R. W., Phys. Rev. 134 A1492 (1964)

27 Bierig, R. W., et al, Phys. Rev. 134 A1504 (1964)

28 McLaughlan, S. D. et al, Phys. Rev. 146 344 (1966)

29 Goldschmidt, Z. B., in 'Handbook on the Physic and Chemistry of Rare–Earths', Vol 1 – Metals. (Eds) Gschneider, Karl and Eyring, LeRoy, North-Holland Publishing Company Amsterdam, (1978)

30 Condon, E. U. and Shortley G. H. 'The Theory of Atomic Spectra' Cambridge University Press, Cambridge 1979

31 Goldschmidt, Z. B. in Block F. et al, (eds) Spectroscopc and Group Theoretical Methods in Physics North-Holland Publications Company, Amsterdam (1968)

32 Carnall, W. T. et al, J. Chem. Phys 49 4424, 4443, 4450 (1968)

33 Eremin, M. V. and Maryakhina, O. I., Optics and Spectroscopy 26 479 (1969)

34 Sugar, J., J. Opt. Soc. Am. 60 454 (1970)

35 Sugar, J. and Kaufmann, V., J. Opt Soc. Am. 62 562 (1972)

36 Sugar, J. and Spector, N. J. Opt. Soc. Amr 64 1484 (1974)

37 Judd, B. R. Rep. Prog Phys 48 907 (1985)

38 Freed, S. Phys Rev. 38 2122 (1931)

39 Freed, S. and Katcoff S. Physics 15 17 (1948)

40 Butement, F. D. S. Transc Faraday Soc. (London) 44 617 (1948)

41 Feofilov, P. P., Optics and Spectroscopy 6 150 (1959)

42 Kaplyanskii, A. A. and Feofilov, P. P., Optics and Spectroscopy 13 129 (1962)

43 Feofilov, P. P. and Kaplyanskii, A. A.,Optics & Spectroscopy 12 272 (1962)

44 Low, W., J. Chem. Phys. 37 30 (1962)

45 Kiss, Z. J., Phys. Rev. 127 718 (1962)

47 Rabbiner, N. Phys. Rev. 130 502 (1963a)

48 Rabbiner, N. Phys. Rev. 132 224 (1963b)

49 Kaplyanskii, A.A., et al., Optics and Spectroscopy 14 351 (1963)

50 Karapetyan, V.E., et al., Optics and Spectroscopy 14 236 (1963)

51 Hoogschagen, J. and Gorter, C. J., Physica 14 197 (1948)

52 Sayre, E. V., and Freed, S., J. Chem. Phys. 23 2060 (1955)

53 Satten, R. A., J. Chem. Phys. 21 637 (1953)

54 Dieke, G. H. and Crosswhite, H. M., J. Opt. Soc. Am. 46 885 (1956)

55 Dieke, G. H. and Hall, L. A., J. Chem. Phys. 27 465 (1957)

56 Dieke, G. H. and Leopold, L., J. Opt.Soc. Am. 47 944 (1957)

57 Dieke, G. H. and Sarup, R., J. Chem. Phys. 29 741 (1958)

58 Magno, M. S. and Dieke, G. H., J. Chem. Phys. 37 2354 (1962)

59 Weakliem, H. A. and Kiss, Z. J., Phys. Rev., 157 277 (1967)

60 Loh, E., Phys. Rev. 147 332 (1966)

61 Dieke, G. H. and Sarup, R., J. Chem. Phys. 36 371 (1962)

62 Wood, D. L. and Kaiser, W. Phys Rev. 126 2079 (1962)

63 Kaplyanskii, A. A. and Feofilov, P. P., Optics and Spectroscopy 16, 144 (1964)

64 Bron, W. E. and Heller, W. R,. Phys Rev. 136 A1433 (1965)

65 Mahbub'ul Alam, A. S. M. and Di Bartolo, Balbaaaars., J. Chem. Phys. 47 3790 (1967)

66 Brecher, C., et al., Phys Rev 155 178 (1967)

67 Nara, H., and Schesinger, M., Phys. Rev. B3 58 (1971)

68 Loh, E. Phys Rev. 154 270 (1967a)

69 Loh, E. Phys Rev. 158 273 (1967b)

70 Pollack, S. A., J. Chem. Phys 40 2751 (1964)

71 Al'tshuler, N. S. et al, Soviet Physics - Sol. State 11 2921 (1970)

72 Martin, W. C., et al., 'Atomic Energy Levels— The Rare–Earth Elements', US Department of Commerce ,Washington DC, (1978)

73 Guzzi, M. and Baldini, G., J. Luminescence 6 270 (1973)

74 Wybourne, B. G., J. Chem. Phys. 36 2301 (1962)

75 Asano, S., J. Phys. C : Solid State 12 4081 (1979)

76 Asano, S.and Nakoa, Y., J. Phys. C : Solid State 12 4095 (1979)

77 Runciman, W. A. and Stager, C. V., J. Chem. Phys. 37 196 (1962)

78 Axe, J. D. and Sorokin, P. P. Phys Rev 130 945 (1963)

79 Loh, E. Phys Rev 175 533 (1968)

80 Johnson, K. E. and Sandoe, J. N., J. Chem. Soc. 4 1674 (1969)

81 Reisfeld, R. and Glasner, A. J. Opt Soc. Am. 54 5839 (1964)

82 Alig, R. C. et al, J. Chem Phys. 59 5837 (1973)

83 Tsuobi, T., et al J. Luminescense 24/25 305 (1981)

84 Hernandez, A. J. et al, J. Chem. Phys 72 198 (1980)

85 Hernandez, A. J. et al, J. Phys Soc. Japan 50 225 (1981)

86 Piper, T. S. et al, J. Chem. Phys 46 1353 (1967)

87 Kisliuk, P., et. al, Phys. Rev. 171 336

88 Loh, E. Phys Rev. 184 348 (1969)

89 Loh, E. Phys Rev. 137 1846 (1973)

90 Freiser, M. J., et al., J. Appl. Phys. 39 (1968)

91 Eremin, M. V., Optics and Spectroscopy 26 317 (1969)

92 Yanase, A. and and Kasuya, T., Suppl. of the Progress of Theoretical Phys. No. 46 338 (1970)

93 Racah, G., Phys. Rev. 62 438 (1942)

94 Racah, G., Phys. Rev. 63 367 (1943)

95 Racah, G., Phys. Rev. 76 1352 (1949)

96 Bethe, H., Ann. Physik, 3 133 (1929) Engish Translation: 'Splitting of Terms in Crystals' by Consultant Bureau Inc., NY

97 Ballhausen, C. J., 'Introduction to Ligand Field Theory', McGraw-Hill Book Company, NY, (1962)

98 Douglas, E. B. and Hollingsworth, C. A., 'Symmetry in Bonding and Spectra', Academic Press Inc, N Y ,(1985)

99 Bryant, B. W., J. Opt. Soc. Am. 55 771 (1965)

100 Kirton, J. and McLaughan, S. D., Phys. Rev. 155 279 (1967)

101 Bland, S. W. and Smith, M. J. A., J. Phys. C : Solid State Physics 18 1525 (1985)

102 Dupont, A., J. Opt.Soc. Am. 57 867 (1967)

103 Becher, J., Unpublished PhD Thesis, John Hopkins University, Baltimore, USA (1965)

104 Yanase, A. J., J. Phys. Soc. of Japan 42 1680 (1977)

105 Knox, R. S. and Teegarden, K. in 'Physics of Colour Centres' (Ed) Fowler W. B., Academic Press, N.Y. (1968)

106 Mott, N. F. and Gurney, R. W. 'Electronic Processes in Ionic Crystals' 2nd Ed. Dover Publications Inc N.Y. (1964)

107 Konitzer, J. D. and Markham, J. J., Phys Rev. 107, 685 (1957)

108 Konitzer, J. D. and Markham J. J., J. Chem Phys 32 843 (1960)

109 Pick, H. Nuovo Cimento Suppl. 10 498 (1958)

110 Hutchinson, C. A., Phys Rev 75 1769 (1949)

111 Hutchinson, C. A. and Noble, G. A., Phys Rev. 87 1125 (1952)

112 Compton, W. D. and Rabin, H., in Solid State Physics Vol 16 (Eds) F. Seitz and D. Turnbull, Academic Press, N.Y. (1964)

113 Townsend, P. D. and Kelly, J. C. "Colour Centres and Imperfections in Insulators and Semiconductors" Chartto Windus, London, (1973)

114 Fowler, W. B. in Physics of Colour Centres (Ed) Fowler W. B., Academic Press, N.Y. (1968)

115 Markham, J. J., "F-centres in Alkali Halides" Solid State Supplement 8 (ed), F. Seitz, and D. Turnbull, Academic Press, N.Y. (1966)

116 Chiarotti, G. and Grassano, U.M. Phys Rev Lett. 16 124 (1966)

117 Delbecq, C. et al, J. Chem. Phys 19 574 (1951)

118 Fuch, D. Phys Rev. 111 387 (1958)

119 Kanzig, W. and Woodruff, I. O., J. Phys. Chem. Solids 9 70 (1958)

120 Castner, T. G. and Kanzig, W. J., J Phys Chem. Solids 3 (3/4) 178 (1957)

121 Schulman, J. H. and Compton, W. D., "Colour Centres in Solids", Pergamon Press, Oxford (1963)

122 Jawad, K. I. and Smith, M. J. A. Phil Mag., B37 585 (1978)

123 Spector, H. N. et al, J. Chem. Phys 46 2676 (1967)

124 Wood, R. F., and Opick U., Phys Rev. 162 736 (1967)

125 Wood, R. F. and Gilbert, R. Phys Rev 162 746 (1967)

126 Lüty, Fritz, in "Physics of Colour Centres" (Ed) Fowler, W. B. Academic Press, N.Y. (1968)

127 Henderson, B. "Defects in crystalline solids" Edward Arnold (Publishers) Ltd London (1972)

128 Seitz, F., Phys Rev 83 134 (1954)

129 West, E. J. and Compton, W. D., Phys Rev 108 (1957)

130 Radhakrishna, S. and Chowdari, B.V.R. Phys Stat. Sol. A12 557 (1972)

131 Rosenberger, F. and Lüty F. Solid State Communication 7 249 (1969)

132 Etzel, H. W. and Schulman, J. H., J. Chem. Phys 22 1549 (1954)

133 W. Maenhout van der Vorst, Physica 24 996 (1958)

134 Watkins, G. D, Phys Rev 113 79 (1959)

135 Cook, J. S. and Dryden J. S., Aust. J. Phys. 13 260 (1960)

136 Cook, J. S. and Dryden J. S., Proc Phys Soc (London) 80 479 (1962)

137 Dryden, J. S., J. Phys. Soc. Japan 18 Suppl. III 129 (1963)

138 Pascual, J. L. et al, J. Luminescance 17 325 (1978)

139 Kynew, K. and Tabakova V., Optics and Spectroscopy 32 288 (1974)

Hernandez, J. et al, Japanese J. Applied Physics 18 533, (1979)

140 Brabury, R. G. and Wong, E. Y., Phys. Rev. B 4 690 (1971)

141 Aguilar, G. S., et al., J. Chem. Phys. 60 4665 (1974)

142 Watkins, G. D. Phys Rev 113 91 (1959)

143 Aguilar, G. S., et al., J. Chem. Phys. 62 1197 (1975)

144 Rubio, J. O., et al., J. Chem. Phys. 63 4222 (1975)

145 Miyake, S. and Suzuki K. J. Phys Soc. Japan 9 702 (1954)

146 Suzuki, K. J., Phys Soc. Japan 10 794 (1955)

147 Suzuki, K. J., Phys Soc Japan 13 179 (1958)

148 Suzuki, K. J., Phys Soc. Japan 1 67 (1961)

149 Lilley, E. and Newkirk J. P., J. Material Science 2 567 (1967)

150 Chapman, J. A. and Lilley E. J., Material Science 10 1154 (1975)

151 Sors, A. I. and Lilley E., Phys. Stat. Sol. A27 467 (1975)

152 Sors, A. I. and Lilley E., Phys. Stat. Sol. A32 533 (1975)

153 Garcia, J. M., et al., Phys. Rev. B21 5012 (1980)

154 Lopez, F. J. et al., J. Luminescence 26 129 (1981)

155 Aguilar, M. G. et al., Solid State Communication 44 141 (1982)

156 Medrano, C. P., J. Luminescence 29 223 (1984)

157 Lopez, F. J. et al, Phys. Rev. B22 6428 (1980)

158 Rubio, J. O. et al, Phys. Rev. B24 4847 (1981)

159 Slater, J. C., Phys. Rev. 34 1293 (1929)

160 Slater, J. C., 'Quantum Theory of Atomic Structure, Vols I & II', McGraw–Hill Book Company, NY (1960)

161 Racah, G. Phys Rev 61 186 (1942)

162 Racah, G. and Stein J., Phys. Rev. 156 58 (1967)

163 Racah, G., Group Theory and Spectroscopy, Springer Tracts in Modern Physics Vol 37 Berlin:Springer-Verlag (1965)

165 Judd, B. R., Operator Techniques in Atomic Spectroscopy McGraw Hill Book Company N.Y. (1963)

166 Judd, B. R., Proc Roy Soc (London) A250 562 (1959a)

167 Judd, B. R., Proc Phys Soc (London) 74 330 (1959b)

168 Judd, B. R., and Louden R. Proc. Roy. Soc. (London) A251 127, 1959

169 Judd, B. R., Phys. Rev 141 4 (1966)

170 Judd, B. R., Phys Rev 125 613 (1962)

171 Judd, B. R., and Armstrong L., Proc Roy Soc. A309 185 (1969)

172 Wybourne, B. G., J. Chem. Phys. 35 340 1961

173 Wybourne, B. G., J. Chem. Phys. 36 2295 (1962)

174 Wybourne, B. G., J. Math. Phys. 4 354 (1963)

175 Wybourne, B. G., J. Chem. Phys. 40 1457 (1964)

176 Wybourne, B. G., Phys. Rev. 137 A364 (1965)

177 Sharp, R. T., Am. J. Phys. 28 116 (1960)

178 Messiah, A. 'Quantum Mechanics' (Translated by) J. Potter, North Holland Publishing Company, Amsterdam (1965)

179 Rotenberg, M. et al, 'The 3-j and 6-j symbols' The Technology Press, MIT, Cambridge, Massachusetts. (1959)

180 Wigner, E. P. in 'Quantum Theory of Angular Momentum', (Eds) Biedenharn, L. C. and H. van Dam. Academic Press. N.Y. (1965)

181 Edmonds, A. R., 'Angular Momentum in Quantum Mechanics', (2nd) Princeton University Press, N.Y. (1960)

182 Shores, Bruce W. and Menzel, D. H., 'Principles of Atomic Spectra', John Wiley and Sons Inc, N.Y. (1968)

183 Gerlock, M., 'Magnetism and Ligand Field Analysis', Cambridge University Press, Cambridge. (1983)

184 Arima, A., et al., Progress of Theoretical Physics vol II 143 (1954)

185 Matsunobu, H. and Takebe H., Progress in Theoretical Physics 14 589 (1955)

186 Bransden, B. H. and Joachain, C. J., 'Physics of Atoms, and Molecules' Longman, London (1983)

187 Smith, K. and Stephenson, J. W., Argonne National Laboratory Reports ANL-5776 (1957) and ANL-5860 (1958)

188 Koozekanani, S. H., '9j Symbols' (Engineering Publications, Ohio State University), Columbus (1972)

189 Racah, G. J., Optical Society of America 50 408 (1960)

190 Callahan, W. R., J. Opt Soc. Am. 53 695 (1963)

191 Shortley, G. H. and Fried, B., Phys. Rev. 54 739 (1938)

192 Shortley, G. H. and Fried B., Phys Rev 54 749 (1938)

193 Racah, G. Physica 16 651 (1950)

194 Racah, G. Phys. Rev. 61 537 (1942)

195 Cowan, R. D. and Kenneth A. L., J. Opt Soc. Am. 55 502 (1965)

196 Nielson, C. W., and Koster, G. F., 'Spectroscopic Coefficients for the p^n, d^n and f^n configurations, MIT press Cambridge, Mass. 1963

197 Fano, U. and Racah, G. 'Irreducible Tensorial Set' Academic Press Inc. N.Y. 1959

198 Trees, R. E. Phys Rev 83 756 1951

199 Rajnak, K., J. Opt Soc. Am. 55 126 (1965)

200 Rajnak, K., J. Chem. Phys 43 8 1965

201 Wong, E. Y., J. Chem Phys 38 976 (1963)

202 Lomont, J. S., 'Applications of Finite Groups', Academic Press. N.Y. (1959)

203 Knox, R. S. and Gold, A., 'Symmetry in the Solid State', Benjamin, N.Y. (1964)

204 Schläfer, Hans L. and Gliemann, Gunter, 'Basic Principles of Ligand Field Theory' (Trans) David, F. Ilten., John Wiley and Sons Ltd, NY, (1969)

205 Elliott, J. P. and Dawber, P. G., 'Symmetry in Physics Vol I', Principles and simple applications' The McMillan Press Ltd (1979)

206 Bassani, F. and Parravicinc, G. P., 'Electronic States and Optical Transitions In solids', (Ed) R.A. Ballinger Pergamon Press Oxford 1975

207 Sugano, S., et al., 'Multiplets of Transition-Metal Ions in Crystals' Academic Press N.Y. (1970)

208 Druzhinin, V. V., Optics and Spectroscopy 22 446 (1967)

209 Druzhinin, V.V. et al., Soviet Physics - Solid State 7 2023 (1966)

210 Sugano, S. et al, J. Phys Soc. Japan 13, 880 (1958)

211 Bell, D. G., Rev. Mod Phys 26 311 (1954)

212 Altmann, S. L. and Bradley, C. J., Phil. Trans. of Roy. Soc. (London) A255 (1963)

213 Altmann, S., L, and Cracknell, Revs. of Mod. Phys. 37 (1965)

214 Leushin, A. M., 'Tables of Functions Transforming According to Irreducible Representations of Crystallographic Point-Groups', (in Russian) Nauka Press, Moscow (1968)

215 Griffith, J. S., 'Theory of Transition-Metal Ions', Cambridge University Press, Cambridge (1964)

216 Koster, G. F., et al, 'Properties of the Thirty Two Point Groups', MIT Press Cambridge, Mass. (1963)

217 Starostin, N. V., Optics and Spectroscopy 23 260 (1967)

218 Starostin, N. V., Optics and Spectroscopy 25 (1970)

219 Tsuboi, T. J., Phys. C.- Solid State Phys 14 4727 (1981)

220 Judd, B. R., J. Chem. Phys. 66 3163 (1977)

221 Nara, H. and Schlesinger M. Phys Rev B3 58 (1971)

222 Low, W. 'Paramagnetic Resonance in Solids' in Solid State Supplement 2 Academic Press, N.Y. (1960)

223 McClure, D. S., Solid State Physics Vol.9 (Ed), F. Seitz and D. Turnbull. Academic Press, N.Y. (1959)

224 Vetri, G. and Bassani, F., Nuovo Cimento 55B 504 (1968)

225 Elliot, R. J. and Stevens, K. W. H., Proc. Roy. Soc (London) A215 437 (1953)

226 Biedenhani, L. C., J. Math. and Phys. 31 287 (1952)

227 Elliott, J. P., Proc Roy Soc (London) A218 345 (1953)

228 Eremin, M. V., Optics and Spectroscopy 29 53 (1970)

229 Hutchings, M. T., in Solid State Physics Vol. 16. (Eds) F. Seitz, and D. Turnball, Academic Press 1959

230 Kaasman, A., J. Chem. Phys. 53 4118 (1970)

236 Wilkinson, J. H.,'The Algebraic Eigenvalue Problem', Oxford University Press, London (1965)

237 Ortega, J. M. and Poole W. G., 'An Introduction to Numerical Methods for Differential Equations', Pitman Publishing Inc. Marshfield, Massachusetts (1981)

238 Cohen, A. M., in: 'Numerical Analysis', in Cohen, A. M.(Ed) McGraw-Hill Book Company (UK) Ltd. Maidenhead England. (1973)

239 Ralston, A. and Rabinowitz P., 'First Course in Numerical Analysis', McGraw-Hill Book Company, Singapore (1978)

240 Dodes, A. Irving, 'Numerical Analysis for Computer Science', North-Holland Inc. N.Y. (1978)

241 Kelly, Louis, Handbook of Numerical Analysis and Applications. Addison-Wesley Publishing Company Reading, Massachusetts (1967)

242 Phillips, G. M. and Taylor P. J., Theory and Applications of Numerical Analysis: Academic Press London (1973)

243 Khabaza, I. M., Numerical Analysis Pergamon Press, Oxford (1965)

244 Chapra, Stem C. and Raymond P., Canale Numerical Methods for Engineers with Personal Computer Applications, McGraw-Hill Book Company, N.Y. (1985)

245 Vandergraft James S., Introduction to Numerical Computing, Academic Press, N.Y. 1978

246 Eremin, M. V. and Maryakhina, O. I., Optics and Spectroscopy 26 479 (1969)

247 Nara, H., and Schlesinger M., J.Phys C. Solid State Physics 5 606 (1972)

249 Ellis, T. M. R., A Structured Approach to Fortran 77 Programming, Addison-Wesley Publishing Company London (1982)

250 Monro, D. M., Fortran 77, Edward Arnold, London, (1982)

251 Balfour, A. and Marwick D.H., Programming in Standard Fortran 77. Heinemann Educational Books Ltd, London (1979)

252 Weast, R. C., (Ed) 'CRC Handbook of Chemistry and Physics', 55 Edition, CRC Press Inc. Florida (1974–75)

253 Hultgren, P., et al, 'Selected Values of the Thermodynamic Properties of the Elements", American Society for Metals, Ohio, (1973)

254 Lauer, H. U. et al, J. Chem. Phys. 65 3108 (1976)

255 Rubio, J. O. et al, J. Chem. Phys. 63 4222 (1975)

256 Aguilar, G. S. et al, J.Chem. Phys. 62 1197 (1975)

257 Wagner, M. and Bron W. E., Phys. Rev. 139 A223 (1965)

258 Rubio, J. O. et al, J.Chem. Phys. 61 5273 (1974)

259 Weakliem, H. A., Phys Rev. B6 2743 (1972)

260 Judd, B. R., Proc Roy. Soc. (London) A228 120 (1959)

261 Chase, L. L., Phys. Rev. B2 2308 (1970)

262 Dimmock, J. O. et al, J. Applied Phys. 41 1088 (1970)

263 Schäffer, C. F. and Jorgensen C. K., J. Inorganic and Nuclear Chemistry 8 143 (1958)

264 Wood, D. L. et al, J. Chem. Phys 39 890 (1963)

270 American Institute of Physics Handbook (2nd Ed.) McGraw-Hill Book Company, NY (1963)

271 Chakravarty, A. S., 'Introduction to Magnetic Properties of Solids', John Wiley & Sons, NY, (1980)

272 Muñoz, P., et al., J.Chem. Phys. 62 3416 (1975)

273 Ruiz-Mejia, C., et al., J.Chem.Phys. 73 60 (1980)

274 Rubio, J. O. et al, J.Chem. Phys 73 53 (1980)

275 Kaplyanski, A. A. and Przhevuskii, A. K., Optics and Spectroscopy 20 577 (1966)

276 Brown, M. R. et al, J. Chem. Phys 50, 891 (1969)

277 Sch'affer, C. E., J. Inorganic and Nuclear Chemistry 8 149 (1958)

278 Kiss, Z. J., Phys Rev. 137 A1749 (1965)

279 van Vleck J. H., J.Chem.Phys 3 803, 807 (1935)

280 Owen, J., Proc Roy Soc. (London) S227 183 1955

281 Tanabe, Y. and Sugano S., Phys Soc. Japan 11 864 (1956)

282 Tin Kham, M., Proc Roy Soc. (London) A236 5 35, 549 (1956)

283 Jorgenson, C.K., in: Solid State Physics 13 375, Academic Press, N.Y. (1962)

284 Jorgenson, C. K., Progress in Inorganic Chem. 4, 73 (1962)

285 Jorgenson, C. K., Progress in Inorganic Chem. 4, p73 (1962)

286 Ferguson, J., Progress in Inorganic Chem. 12 159 Interscience, N.Y. (1970)

287 Gerlock, M., Magnetism and Ligand Field Analysis, Cambride University Press, Cambridge, (1983)

288 Barker, J. M. et al, Proc. Roy Soc. A308 403 (1968)

289 Ellis, M. M. and Newman D. J., J.Chem.Phys 47 1986 (1967)

290 Ellis, M. M. and Newman D. J., J.Chem.Phys 49 4032 (1968)

291 Bishton, S. S. et al, J.Chem. Phys. 47 4133 (1967)

292 Curtis, M. M. et al., J.Chem.Phys. 50 1077 (1969)

293 Anderson, C. H., in: Crystals with Fluorite Structure, Hayes, W. (ed) Clarendon Press, Oxford (1974).

294 Weakliem, H. A. et al, Phys. Rev. B2 4354 (1970)

295 Wong, E. Y. and Richman, L, J.Chem. Phys. 36 1889 (1961)

296 Wong, E. Y. and Richman, L, J.Chem. Phys. 37 2270, 2498 (1962)

297 Wong, E. Y. et al, J. Chem. Phys 39 786 (1963)

298 McLaughin, R. P. and Conway, J. G., J.Chem. Phys. 38 1037 (1963)

299 Alig, R. C., R.C.A. Review 36 125 (1975)

300 Rohrig, R., Phys. Lett. 16 20 (1965)

301 Pandey, S. D., J. Chem. Phys. 47 3094 (1967)

302 Pandey, S. D., Chem. Phys. Lett. 3 46 (1969)

303 Rubio, J. O. et al, J. Phys 61 5273 (1974)

304 Rubio, J. O. et al, J. Chem. Phys 63 4222 (1975)

305 Aguilar, G.S. et al, J. Chem. Phys 62 1197 (1975)

307 Bradbury, R. E. and Wong, E. Y., Phys. Rev. B4 694 (1975)

308 Bradbury, R. E. and Wong, E. Y., Phys. Rev. B4 702 (1975)

309 Grimley, T. B., J. Chem. Phys 17 496 (1949)

310 Breckenbridge, R. C., J. Chem.Phys. 18 913 (1950)

311 Lidiard, A. B., in: Defects in Crystalline Solids: Report on the Conference on Defects in Crystalline Solids held at University of Bristol by Physical Society (1954)

312 Lidiard, A. B., Phys. Rev. 94, 29 (1954)

313 Bassani, F. and Fumi F. G., Phil. Mag. 45, 228 (1954)

314 Etsel, H. W. and Patterson, D. A., Phys. Rev. 112 1112 (1958)

315 Etsel, H. W., Phys. Rev. 118 1150 (1960)

316 Dixon, J. M., Private Communication

317 Abragram, A. and Pryce, M. H. L., Proc. Roy. Soc. A 205 135 (1951)

318 Abragram, A. and Bleaney, B., 'Electron Paramagnetic Resonance of Transition Ions', Dover Publication, NY (1986)

319 Tolman, K., Czech. J. Phys. 13 296 (19630) quoted in Lilley, E. and Newkirk, J. B., J. Material Science 2 567 (1967)

320 Goodman, C. H. L., Lecture notes on 'Structure and Properties of Non–Metallic Solids', given at the University of Warwick, Coventry, (1984)

321 Ivoilava, E. K. and Leushin, A. M., Soviet Physics : Solid State 22 601 (1980)

322 Donnay, J. D. H. and Donnay, Gabrielle, 'Crystal Data: Determinative Tables', Published by American Crystallographic Association (1963)

323 Stevens, K. W. H. and Bates, C. A., in D. J. Craik, (Ed) 'Magnetic Oxides, Part 1', John Wiley & Sons Ltd, NY, (1975)

324 Heine, Volker, 'Group Theory in Quantun Mechanic', Pergamon Press, Oxford, (1964) 1484 (1974)

326 Honig, R. E., R C A Review, 23 567 (1962)

327 Meiders, Th A. M. van Kleef and Wyart, J. F., Physica 61 443 (1972)

328 Wyart, J. F., et al., Physica Scripta 9 323,325 (1974)

THE BRITISH LIBRARY DOCUMENT SUPPLY CENTRE

TITLE

Optical Spectra and Energy Levels of Divalent Ytterbium and Samarium Ions in Some Alkali Halides

AUTHOR

Ihebrodike Maurice Mejeha

INSTITUTION and DATE

the University of Warwick 1988

Attention is drawn to the fact that the copyright of this thesis rests with its author.

This copy of the thesis has been supplied on condition that anyone who consults it is understood to recognise that its copyright rests with its author and that no information derived from it may be published without the author's prior written consent.

THE BRITISH LIBRARY
DOCUMENT SUPPLY CENTRE
Spa, Wetherby
West Yorkshire
United Kingdom

REDUCTION X 20

CAMERA 8

D86232